Advances in atmospheric drag force modeling for satellite orbit prediction and density estimation

by

Vishal Ray

B.S., Indian Institute of Technology (IIT) Bombay, 2017

M.S., Indian Institute of Technology (IIT) Bombay, 2017

M.S, University of Colorado Boulder, 2020

A thesis submitted to the

Faculty of the Graduate School of the

University of Colorado in partial fulfillment

of the requirements for the degree of

Doctor of Philosophy

Ann and H.J. Smead Department of Aerospace Engineering Sciences

2021

Committee Members:

Daniel J. Scheeres, Chair

Eric Sutton

Marcin Pilinski

Tomoko Matsuo

Jay W. McMahon

Ray, Vishal (Ph.D., Aerospace Engineering Sciences)

Advances in atmospheric drag force modeling for satellite orbit prediction and density estimation

Thesis directed by Prof. Daniel J. Scheeres

Atmospheric drag is the largest nongravitational perturbing force acting on low altitude low Earth orbit (LEO) satellites and debris, and the modeling and estimation of drag effects is a limiting problem in the prediction of their orbits over time. The primary sources of uncertainties in drag modeling are introduced due to the atmospheric density and the drag-coefficient. On top of the stochastic variations in atmospheric density, which drive the magnitude of the drag force, there are systematic variations in the drag coefficient due to satellite specific factors and atmospheric conditions. These include satellite attitude shifts, variations in ambient atmospheric parameters such as temperature, molecular composition, and the satellite wall temperature. Thus, even with increasing accuracy of semi-empirical models for the atmospheric density, there remain model uncertainties and time variations in the effective coefficient of drag that affect the satellite's motion, which are not captured using the standard constant drag coefficient model. Though physics-based models of the drag-coefficient can be used to calculate the time-variations in the drag-coefficient, a gap in knowledge of input parameters across orbital regimes and space weather conditions limits their use in operational orbit determination.

This work develops new estimation-based methods to capture the time variations in the drag-coefficient due to attitude changes and orbital motion using Fourier-series expansions. Before implementing these high-fidelity models of drag, a thorough analysis of aliasing effects in estimates of nongravitational force coefficients due to arbitrary truncation of geopotential models is carried out. This allows an informed choice of geopotential degree and order during orbit determination. Improvement in the orbit determination and prediction of simulated and real satellites is demonstrated with the proposed Fourier models. A framework to invert physical parameters from the Fourier coefficient estimates is developed to provide better constraints on physics-based models of

the drag-coefficient.

Atmospheric densities derived from satellite tracking data are used in calibration of atmospheric models that are in turn used for orbit determination as well as scientific studies of the Earth's atmosphere. But the derived densities are subject to biases in the assumed drag-coefficient. An important goal of this work is to break out of this circular problem and provide a way to estimate atmospheric densities unbiased by the drag-coefficient. Leveraging the physics of the problem and the Fourier coefficient models, a method to estimate accurate local atmospheric densities at a sub-orbital cadence is developed and reduction in density biases is shown using simulated and real tracking data. Lastly, the new drag-coefficient models are applied to analytical theories of orbital motion in an atmosphere.

Dedication

To my wonderful parents for being the amazing people they are

Acknowledgements

Dedicating a few years of your life to an academic degree, especially one which is perceived to be an isolating effort, can quickly begin to take its toll when you set out to undertake this journey alone. But I have been extremely fortunate in my life to be surrounded by simply the best people I could have asked for. First and foremost, I just could not have done this without the unflinching support of Prof. Scheeres. He has supported me in every undertaking, believed in my capabilities when I have been unsure myself and provided me with opportunities that few are lucky to have. He truly has our best interests at heart. My committee has been really helpful in my research with their constructive feedback. Prof. McMahon's and Prof. Matsuo's classes have informed the methods that I have used in my research. I have really enjoyed my collaborations with Dr. Pilinski and Dr. Sutton, and our discussions have saved me a ton of time while trying to figure out things from scratch. I would like to thank Suood Alnaqbi for his hard work on processing of the Spire GPS data, and Prof. Penina Axelrad and Shaylah Mutschler for their support in that effort. It has been such a pleasure working with Dr. Siamak Hesar throughout my time here; thank you for being such a kind mentor. I have found a sense of belonging among other grad students here at CU. I am so glad Valerie and I share our research focus and have similar interests; working together on community projects would not have been so enjoyable without her. There are so many friends that I could write another thesis for, just thanking them for being part of my life and turning not-so okay days into beautiful memorable ones. You guys are like sunshine, lighting up a gloomy cloudy day! Last but not the least, none of this would have been possible without the support of my parents and my brother. I cannot overstate how blessed I feel to have you as my family.

Contents

Chapter

Tables

Table

Figures

Figure

Chapter 1

Introduction

1.1 Earth's debris environment

In 1957, with the launch of Sputnik 1, a new era began for humanity—the space age. Since then, satellite technology has permeated almost every aspect of our lives, revolutionizing the way modern society functions. The protection of our world's collective space assets is a shared interest of all of humanity.

As with the discovery of any new resource, swift utilization without a lot of thought dedicated to sustainability, due to the seeming abundance of given resource, was what happened to outer space as well. In the nearly 65 years following the launch of the first satellite, we have added around 23000 objects that are more than 10 centimeters in size [106]; and that is just the number of objects that are being tracked and cataloged for collision avoidance purposes. Fig. 1.1 shows the rapidly growing total number and mass of objects in Earth orbit officially cataloged by the US Space Surveillance Network. With the object population in certain low Earth orbit (LEO) belts reaching a critical spatial density [57], accurate real-time monitoring as well as prediction of satellite positions into the future has emerged as a problem of utmost importance for orbit maintenance and collision avoidance. The relevance of tracking accuracy is underscored by the 2009 collision between a derelict Kosmos and an active Iridium satellite. In recent years, with the launch of mega-constellations of commercial satellites such as SpaceX's Starlink, the number of near misses that would increase the debris population by thousands of more objects has been quickly rising, especially in the absence of traffic rules, communication protocols between different

satellite operators and the potential lack of transparency regarding conjunction events [2]. Along with active debris remediation strategies and developing policies regarding norms of behaviour in space, improving tracking accuracy of space objects is necessary to prevent catastrophic collisions of active maneuverable satellites.

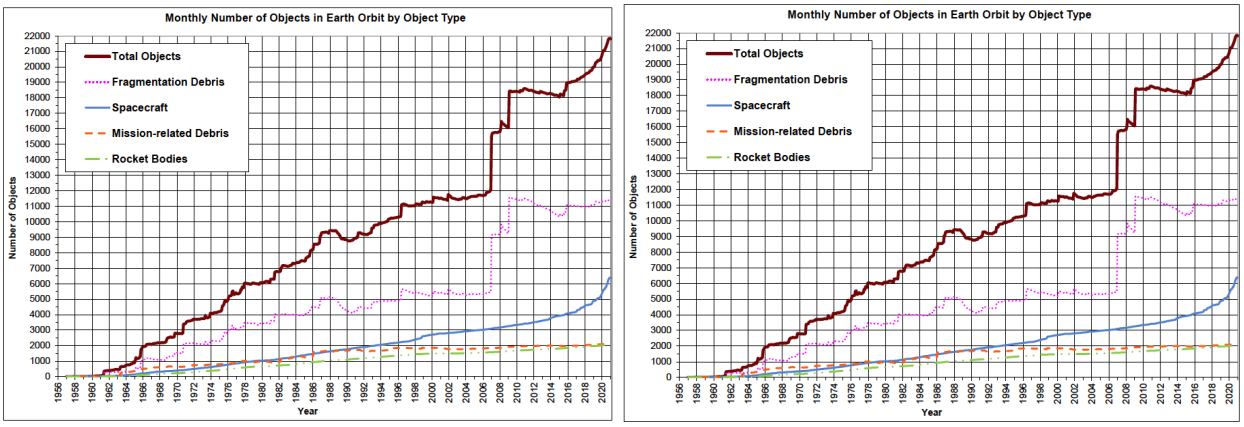

(a) (b)

Figure 1.1: (a) Monthly number of objects in Earth orbit, (b) Monthly mass of objects in Earth orbit officially cataloged by US Space Surveillance Network as of 5 Jan 2021; figure courtesy NASA Orbital Debris Quarterly news [83]

1.2 Satellite drag environment

The modeling of perturbing forces acting on a satellite is a key component of orbit determination and prediction. Atmospheric drag is the largest perturbing force for low altitude LEO satellites and uncertainty in its parameters remains the foremost contributor to prediction errors in this orbit regime [44]. Even though high-fidelity non-conservative force models used in conjunction with empirical accelerations meet current requirements in terms of orbit fit residuals, the prediction accuracy may still degrade rapidly due to inherent assumptions in the modeling and estimation of force parameters such as the drag coefficient [84].

Drag is one of the three atmospheric forces acting on the satellite, the other two being lift and side forces. The lift and side force coefficients are usually an order of magnitude smaller than the drag coefficient [25] and can be ignored as a first approximation without significant loss in

accuracy. The drag force ($\boldsymbol{a_{drag}}$) acting on a satellite is given by

$$\boldsymbol{a_{drag}} = -\frac{1}{2}\rho C_d \frac{A_{ref}}{m} v_r^2 \hat{\boldsymbol{u}}, \tag{1.1}$$

where ρ is the atmospheric neutral density, C_d is the drag coefficient, v_r is the relative velocity of the satellite w.r.t the atmosphere, $\hat{\boldsymbol{u}}$ is the unit vector in the relative velocity direction, m is the mass of the satellite and A_{ref} is the reference cross-sectional area. Considering the mass and relative velocity of the satellite with respect to the atmosphere to be known and combining the drag coefficient and the reference cross-sectional area, the primary uncertainties in the drag force are introduced due to density and drag coefficient models. It should be noted here that this work is concerned with the drag force on satellites due to the neutral atmosphere. Charged particles in the ionosphere can induce an ionospheric drag on satellites that may become important when very high precision is required for the orbit determination process [11]. The key issues remaining in upper atmospheric drag modeling are discussed in detail in Thayer et al. (2021) [125].

In most of the orbit determination applications, the drag coefficient is estimated as a constant, similar to the cannonball model for the radiation coefficient in solar radiation pressure (SRP) [60]. But the drag coefficient is a highly variable quantity, the value of which is governed by the physics of gas-surface interactions in orbit. The systematic variations in drag coefficient are driven by satellite specific factors such as attitude shifts which change the angle of the flow with respect to the surface and satellite wall temperature, as well as atmospheric conditions such as molecular composition and ambient temperature. It is important to take a look at the state-of-the-art drag coefficient models to understand the existing issues with drag coefficient calculations.

1.3 Current state of upper atmospheric density models

The Earth's upper atmosphere or thermosphere, around 100-1000 km above the Earth's surface, is a dynamic system with variations resulting due to interactions with the Sun as well as the lower atmosphere. The upper atmospheric density is primarily driven by space weather drivers—solar and geomagnetic activity; both the solar extreme ultraviolet (EUV) radiation and

the interactions of particles from the Sun with the geomagnetic field inject energy into Earth's atmosphere. A high solar activity or higher number of solar particles entering the geospace causes heating and subsequent expansion of the atmosphere to higher altitudes leading to an increase in the thermospheric density and therefore, satellite drag. This complex dependence of the density on space weather has been historically captured in thermospheric models such as the widely used NRLMSISE-00 [93] in satellite operations through F10.7 and Ap proxies for the solar and geomagnetic activity respectively. But the space weather effects on the atmospheric density are not fully captured by these proxies which introduces errors in the density output of these models. The use of newer solar and geomagnetic indices has reduced the density uncertainties in the JB2008 atmospheric model compared to MSIS and Jacchia models [125].

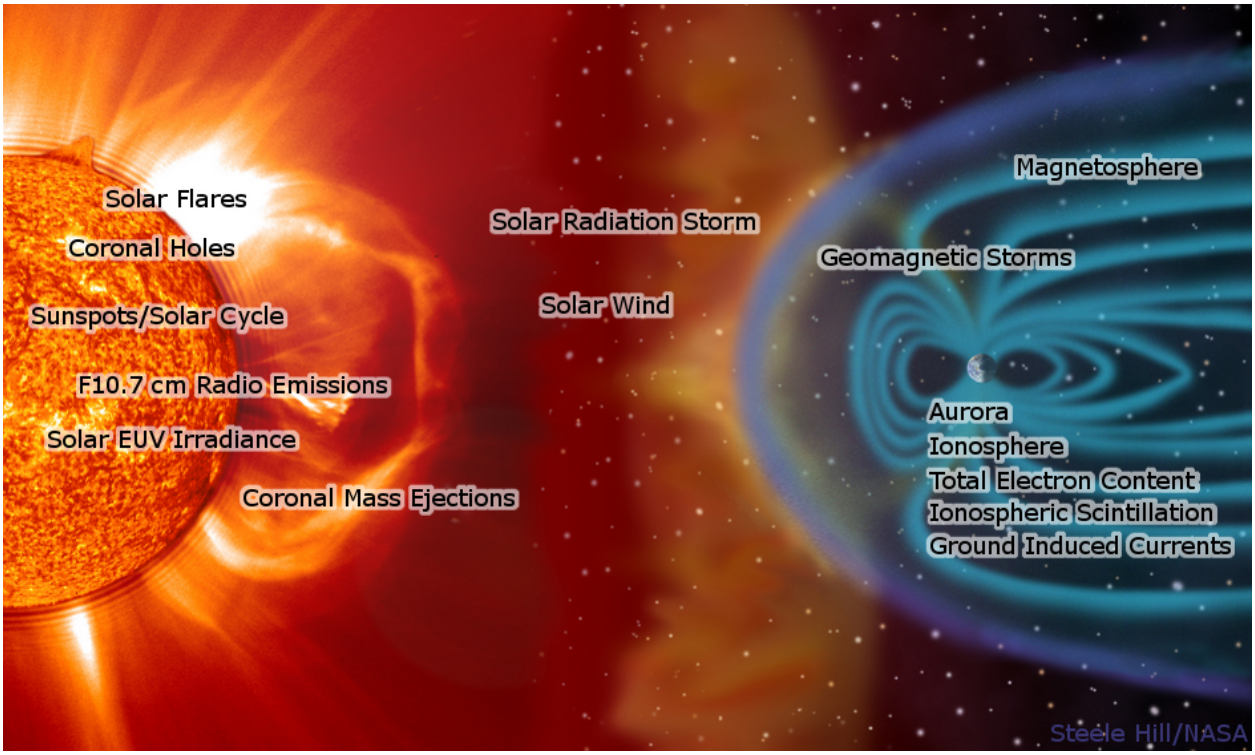

Figure 1.2: Interaction of the geospace with the Sun; figure courtesy NOAA

In the last two decades, there have been significant advances in atmospheric density modeling, thanks to the measurements from instruments onboard satellites such as CHAMP (2000-2010),

GOCE (2009-2012) and GRACE (2002-2017) complementing orbital decay data and ground-based measurements [25, 29]. Estimates of atmospheric densities from satellite data not only allow the calibration of semi-empirical atmospheric density models used in orbit determination but provide invaluable insights into the evolution of Earth's atmosphere [30] and its causes such as anthropogenic factors [50]. A key science goal identified by the National Research Council decadal survey for solar and space physics [20] is to analyze changes in our planetary environment and identify underlying causes. The derivation of decadal changes in the thermospheric densities using satellite data forms an important component in achieving that goal. Therefore, any biases in the derived densities have far reaching consequences from both engineering and scientific perspectives. One of the primary biases is introduced in the inversion of atmospheric densities from satellite data as a result of simplifying assumptions pertaining to the drag coefficient [29].

Atmospheric densities can be derived from satellite drag primarily through two approaches - accelerometers and orbit tracking data; both are directly affected by the error in the drag coefficient used in the inversion. With the accelerometer data from satellites such as CHAMP and GOCE being available to the scientific community, the discrepancy between the densities derived from satellites and existing atmospheric models have become more evident. GOCE densities had to be rescaled by a factor of 1.25 to match the High Accuracy Satellite Drag Model (HASDM) [7, 26]. Corrections to HASDM [117] are made in real time from observed drag effects on satellites but the derived densities are again ambiguous to a factor of the drag coefficient being used, though the calibration satellites are supposed to have stable ballistic coefficients. Using more realistic drag coefficients, it was estimated that the Jacchia 71 model (based on measurements using a drag coefficient of 2.2) overestimates density by nearly 23% and the MSIS 90 model by 15% [12, 78]. It is important to be able to separate the density variations from the drag-coefficient variations while estimating the satellite drag.

1.4 Current state of drag-coefficient modeling

Since closed-form solutions of drag coefficient were derived by Cook [19] for simple shapes at the advent of space age, it has been long estimated as a constant in the orbit determination process, also known as the cannonball model [60]. But the drag coefficient can vary significantly in orbit due to its dependence on satellite specific factors such as satellite orientation with respect to atmospheric flow and ambient parameters such as molecular composition and temperature. Earlier, the errors in atmospheric density model overshadowed the errors due to drag coefficient in orbit determination. But with reduction in orbit determination errors due to atmospheric density, improved models of the drag coefficient have become necessary.

Until a few years back, most of the research in drag coefficient modeling focused on the development of gas-surface interaction models (GSIMs) that are based on actual physics that govern the atmospheric flow around the satellite [19, 80, 79]. But estimates of the parameters that are used in these models are strongly dependent on the solar-atmospheric coupling [81] and are available only for specific atmospheric conditions and altitudes [88, 77]. Advances towards the use of GSIMs for a larger subset of orbital regimes and ambient conditions have been made possible as a result of models proposed for parameters such as energy accommodation coefficient that characterizes the energy of flow emitted from the satellite wall [96, 71, 95, 132, 131]. The second important area of research has been focused on utilizing numerical methods for drag coefficient modeling. Numerical methods such as test particle Monte Carlo (TPMC) and direct simulation Monte Carlo (DSMC) [5] are more accurate than analytical GSIMs since they can account for factors such as overshadowing and multiple reflections, but unfortunately suffer from a large computational burden. The resolution of this problem has been found in machine-learning techniques that use numerical methods to generate data for 'training' computationally tractable models [71, 72, 119]. These resultant models are functions of a selected input parameter set which is dependent on satellite properties and orbital regime, and therefore specific to the satellite under consideration. In particular, response surface models (RSM) developed in such a manner have been shown to

improve orbit prediction for GRACE [72] and provide better density estimates from accelerometer data onboard CHAMP and GRACE [73].

In order to ensure a transition from a cannonball model to these higher-fidelity models for the general orbit determination community, some pertinent issues need to be addressed. One of the drawbacks of using such models across the LEO regime is that they are not generic but have to be developed for individual satellites. The other issue common to most drag coefficient models is that input parameters to these models are not always known accurately. One possible solution is to use semi-empirical models developed for parameters such as energy accommodation coefficient [96, 71] in conjunction with response surface models. Even then, other parameters such as the angular spread of the remitted flow still remain unknown. In addition, inputs to these models such as concentrations of different atmospheric species will carry biases of the atmospheric density model used to calculate them.

The issue of observability of input parameters is encountered while incorporating high-fidelity drag coefficient models in the filtering methodology for orbit determination. Many of these input parameters change over time in orbit and cannot be estimated in the filter since they are not directly observable. Therefore, unless accurate models are available for the input parameters across all orbital regimes and satellite shapes, developing a physics-based drag coefficient model applicable for all LEO altitudes is difficult. Consequently, many real satellites still utilize the cannonball model, i.e., estimate the drag coefficient as a constant, in orbit determination applications. This calls for a modeling approach that can condense the physics associated with the drag coefficient into observable quantities that can then be estimated in a filter. Estimation-based empirical models of the drag coefficient can potentially capture frequencies associated with periodic variation of the drag coefficient in orbit due to repeating attitude and ambient parameters. The estimates of free parameters associated with such models can provide information that can ultimately be used to improve the input parameter space of machine-learning models. They can also provide better orbit determination performance than the standard cannonball model that assumes the drag coefficient to be a constant with minimal implementation overhead.

1.5 Thesis statement and outline

The importance of accurate modeling of the drag-coefficient in orbit determination and atmospheric density inversion from drag data and the current need for a framework to estimate time-variations in the drag-coefficient from satellite tracking data leads us to the following thesis statement.

Thesis: Advances in drag coefficient modeling, specifically development of models whose parameters can be estimated through satellite tracking data, will lead to improvements in dynamic orbit prediction of all low Earth orbit (LEO) satellites and knowledge of gas-surface interaction (GSI) parameters. In addition, they will be useful in removing biases in current thermospheric density models introduced during the process of density inversion from satellite drag.

The primary focus of this thesis is developing a high-fidelity drag-coefficient model for further applications. In order to understand the nature of drag-coefficient dependence on various satellite and orbit factors, the physics of gas-surface interactions need to be studied. Chapter 2 discusses the GSIMs that are used to calculate the drag-coefficient variations in this work. Processing of satellite tracking data in a filtering framework requires careful consideration of various aspects such as the filtering method, time systems, coordinate systems and force models. An outline of satellite orbit determination relevant to this thesis is provided in chapter 3. Unmodeled forces in the filter dynamics are absorbed by the parameters being estimated. Arbitrary truncation of gravitational force models can corrupt drag and solar radiation pressure (SRP) coefficients leading to larger than anticipated errors in orbit prediction. A thorough understanding of these effects is required before implementing high-fidelity models of drag-coefficient as discussed in chapter 4. Chapter 5 details the derivation of estimation-based models that capture higher-order frequencies in the drag-coefficient using Fourier series expansions. Improvements in orbit determination and prediction are demonstrated with the developed models using simulated cases with increasing complexity

and real tracking data. A framework to obtain better constraints on a given GSIM from the estimates of drag-coefficient variations is developed in chapter 6. Drag-coefficient estimates and subsequent derivation of GSIM parameters are dependent on the atmospheric model being used. Any improvements in drag force modeling will require better estimates of both drag-coefficient and density. But due to the nature of the drag-force, the orbit determination filter cannot distinguish between biases in the drag-coefficient and density. Leveraging the developments of chapters 5 and 6 and existing work in literature [135], a method to decorrelate density and drag-coefficient biases is presented in chapter 7. The Fourier-series models proposed here allow a time-varying representation of the drag-coefficient in analytical theories of orbital motion in an atmosphere. Chapter 8 re-derives the widely used King-Hele theory [51] to allow for drag-coefficient variation.

1.6 Contributions

The main contributions of this work are summarized below

- Quantified aliasing effects of higher-order gravitational harmonics into nongravitational force coefficients and mapped out required geopotential truncation orders across the LEO altitude regime.
- Developed estimation-based Fourier drag-coefficient models that can capture time-variations in the drag-coefficient due to attitude and orbital motion and a framework to incorporate them in the orbit determination methodology.
- Demonstrated improvements in orbit determination and prediction on simulated and real tracking data with the developed drag-coefficient models.
- Performed a comprehensive observability analysis to understand the specific Fourier coefficients that can be estimated for the different models and various satellite shapes.
- Derived closed-form solutions for the nominal Fourier coefficients for the diffuse reflection incomplete accommodation (DRIA) model of drag-coefficient; this allows an understanding

of what frequencies are non-zero in orbit given the satellite shape and material properties.

- Developed a framework to invert GSIM parameters from estimated Fourier coefficients that can potentially be used to constrain GSIM uncertainties across the LEO regime.
- Developed a method to estimate local atmospheric densities, unbiased by the drag-coefficient, by leveraging the Fourier drag-coefficient models and GSIMs.
- Demonstrated improvements in filter density model corrections using simulated and real tracking data.
- Derived a modified analytical theory of satellite orbital motion in an atmosphere with time-varying drag-coefficient.

1.7 Publications

1.7.1 Journal papers

- V. Ray, D.J. Scheeres, S. Alnaqbi, K.W. Tobiska, S.G. Hesar, A framework to estimate local atmospheric densities with reduced drag-coefficient biases, *submitted to Space Weather*
- [104] V. Ray, D.J. Scheeres, M. Pilinski, Inverting gas-surface interaction parameters from Fourier drag-coefficient estimates for a given atmospheric model, *Advances in Space Research*, vol. 68, no. 4, 2021, pp. 1902-1927. DOI: 10.1007/s40295-019-00200-4
- [102] V. Ray, D.J. Scheeres, King-Hele orbit theory for periodic orbit and attitude variations, *Monthly Notices of the Royal Astronomical Society*, vol. 501, 2020, pp. 1168-1187. DOI: 10.1093/mnras/staa3630
- [101] V. Ray, D.J. Scheeres, Gravitational force model aliasing with nongravitational force coefficients in dynamic prediction, *Journal of Guidance, Control and Dynamics*, vol. 43, no. 11, 2020, pp. 1984-1997. DOI: 10.2514/1.G005001

- [100] V. Ray, D.J. Scheeres, Drag-coefficient model to track variations due to attitude and orbital motion, *Journal of Guidance, Control and Dynamics*, vol. 43, no. 10, 2020, pp. 1915-1926. DOI: 10.2514/1.G004854

- [103] V. Ray, D.J. Scheeres, S. Hesar, M. Duncan, A Drag Coefficient Modeling Approach Using Spatial and Temporal Fourier Expansions for Orbit Determination, *Journal of the Astronautical Sciences*, vol. 67, 2020, pp. 1139-1168. DOI: 10.1007/s40295-019-00200-4

1.7.2 Conference papers

- V. Ray, D.J. Scheeres, S. Alnaqbi, Decorrelating density and drag-coefficient through attitude variations, *Advanced Maui Optical and Space Surveillance Technologies Conference*, Maui, HI, 2021.

- V. Ray, D.J. Scheeres, Eric K. Sutton, Marcin Pilinski, Density estimation using second-order Gauss-Markov processes, *AAS/AIAA Spaceflight Mechanics Conference*, Virtual, 2021, AAS 21-340.

- V. Ray, D.J. Scheeres, Performance metrics for Fourier drag models in low Earth orbit determination and prediction, *Advanced Maui Optical and Space Surveillance Technologies Conference*, Virtual, 2020.

- V. Ray, D.J. Scheeres, King-Hele orbit theory for periodic orbit and attitude variations, *AAS/AIAA Astrodynamics Specialist Conference*, Virtual, 2020, AAS 20-542.

- V. Ray, D.J. Scheeres, Aliasing of unmodeled gravity effects in estimates of non-conservative force coefficients, *Advanced Maui Optical and Space Surveillance Technologies Conference*, Maui, HI, 2019.

- V. Ray, D.J. Scheeres, An estimation-based drag-coefficient model for tracking variations due to attitude and orbital motion, *AAS/AIAA Astrodynamics Specialist Conference*, 2019, Portland, ME, AAS 19-754.

- V. Ray, D.J. Scheeres, Improved drag coefficient modeling with spatial and temporal Fourier coefficient expansions: theory and application, *Advanced Maui Optical and Space Surveillance Technologies Conference*, Maui, HI, 2018.

1.7.3 Conference abstracts

- V. Ray, S. Alnaqbi, D.J. Scheeres, Atmospheric density inversion from Spire orbit tracking data, *American Geophysical Union (AGU) Fall Meeting*, 2021.

- V. Ray, D.J. Scheeres, Development of an algorithm to estimate unbiased local atmospheric densities, *American Geophysical Union (AGU) Fall Meeting*, 2021.

- V. Ray, D.J. Scheeres, Simultaneous estimation of density and Fourier drag-coefficient, *American Geophysical Union (AGU) Fall Meeting*, 2020.

- V. Ray, D.J. Scheeres, Eric K. Sutton, A Fourier-series modeling approach to develop corrections to atmospheric density and drag coefficient in orbit, *American Geophysical Union (AGU) Fall Meeting*, 2019.

1.7.4 Invited talks

- Development of drag-coefficient models for more accurate orbit prediction and thermospheric density estimation, AGU Fall Meeting Union SEED Session U009 - Student Engagement to Enhance Development, 2020.

- Drag coefficient modeling using Fourier expansions, International Space Weather Action Team (ISWAT), G2A03-Satellite Aerodynamic Modeling, 2020.

- A Fourier series representation of drag coefficient for improved orbit determination in LEO, SSA Operators' Workshop, 2018.

Chapter 2

Gas-surface interaction models (GSIMs)

This chapter provides the details of the GSIMs that have been used in this work. Numerous GSIMs have been proposed in literature for predicting the drag coefficient of simple shapes. A comprehensive review on the subject can be found in Livadiotti et al. (2021) [58] and Prieto et al. (2014) [99]. This work uses two GSIMs to calculate the drag-coefficient variations in orbit. The exact nature of the GSIMs used does not significantly affect the developments in this work since the models proposed in subsequent chapters estimate higher-order variations in drag coefficient through empirical parameters from tracking data. Both the GSIMs used in this work attempt to account for a fraction of the satellite surface being covered by atomic oxygen (contaminated) with the rest of the surface being clean. The first model [77] does this by using a linear combination of a diffuse reflection complete accommodation model for the contaminated fraction and a quasi-specular model for the clean fraction. The second model [131] assumes a diffuse reflection incomplete accommodation (DRIA) for the clean surface.

2.1 Sentman-Schamberg model

The first model is a linear combination of Sentman's model [113] for diffuse reflection and Schamberg's model [111] for specular reflection. The choice of these two models is based on the availability of closed form analytical expressions of drag coefficients for the geometries considered and the estimates of parameters used in these expressions from satellite measurements [88, 81]. Sentman's model considers the random thermal motion of the ambient atmosphere which becomes

a crucial factor in improving the accuracy of the estimated drag coefficients as demonstrated by the comparison of density data from CHAMP and HASDM [122]. But Sentman's model is based on the assumption of a purely diffuse reemission. The nature of reemission is determined by surface contamination. From laboratory measurements it is known that as surface contaminants decrease, the energy accommodation also decreases and the quasi-specular nature of the reemission increases [110, 42]. Harrison and Swinerd (1996) [43] performed multiple satellite analyses using the Nocilla model [86] for reemission to conclude that the reemission is in a direction halfway between specular and diffuse at 800-1000 km altitudes. Though it is known that at lower altitudes with higher surface contamination, the reemission is nearly diffuse and it becomes quasi-specular for higher altitudes, the transition is not well defined or modelled. Instead of using two separate models for the two regimes, we attempt to model the transition using a linear combination of models [77] applicable for the two types of reemission. The fraction assigned to each model uses the semi-empirical satellite accommodation model (SESAM) [96]. The two models are described below.

2.1.1 Sentman's model for diffuse reflection

Sentman's model of gas-surface interaction is based on the assumption of completely diffuse reemission. Outside this assumption, it is an exact theory and makes use of the Maxwellian velocity distribution function to compute the force due to impingement and reemission of the particles. It incorporates the thermal motion of the particles along with the bulk velocity.

The drag-coefficient for a spherical object can be calculated as follows-

$$C_d = \frac{4s^4 + 4s^2 - 1}{2s^4}\mathrm{erf}(s) + \frac{2s^2 + 1}{\sqrt{\pi}s^3}e^{-s^2} + \frac{2\sqrt{\pi}}{3}r, \tag{2.1}$$

and the drag-coefficient of a flat plate with one side exposed to the flow inclined at an angle ψ with the incident velocity vector is given by,

$$C_d = \frac{A}{A_{ref}}\left(\frac{e^{-\gamma^2 s^2}}{s\sqrt{\pi}} + \gamma Z\left(1 + \frac{1}{2s^2}\right) + \frac{\gamma}{2}r\left(\gamma\sqrt{\pi}Z + \frac{1}{s}e^{-\gamma^2 s^2}\right)\right). \tag{2.2}$$

where $Z = 1 + \frac{2}{\sqrt{\pi}} \int_0^{\gamma s} e^{-t^2} dt$, $\gamma = \cos\psi$, s is the molecular speed ratio, r is the velocity ratio between the incident and reemitted particles, A_{ref} is a reference area and A is the actual area of the plate.

The molecular speed ratio is defined as the ratio of the bulk speed and the most probable speed of the gas molecules,

$$s = \frac{V_i}{\sqrt{\frac{2RT}{M}}}, \tag{2.3}$$

where R is the ideal gas constant, M is the mean molar mass and T is the ambient temperature.

Ideally, the drag coefficients of individual molecular species should be calculated separately and summed up. But the error in calculating the drag coefficients with a mean molecular mass is only $\sim 0.1\%$ [131] for lower altitudes. This approximation degrades in accuracy with increasing atmospheric temperatures and as the shape becomes more slender and elongated.

The bulk velocity (V_i) is the velocity of the satellite relative to the incident flow stream. An accurate analysis would demand taking into account complex atmospheric dynamics but a fair assumption is to take the velocity relative to the co-rotating atmosphere,

$$\mathbf{V_i} = \mathbf{v} - \omega_\mathbf{e} \times \mathbf{r}, \tag{2.4}$$

where $\mathbf{v}$ refers to the inertial velocity of the satellite, $\omega_\mathbf{e}$ is the angular velocity vector of Earth given by $[0, 0, 7.292 \times 10^{-5}]$ rad/s and $\mathbf{r}$ is the position vector of the satellite in the inertial frame. The maximum observed deviations from this assumption are of the order of 40 % leading to a drag uncertainty of 5% [82].

The ratio of velocities of reemitted and incident particles r (note that the reemission velocity is the most probable velocity) in Eq. 2.2 can be calculated from the energy accommodation coefficient and is given by [25],

$$r = \sqrt{\frac{1}{2}[1 + \alpha(\frac{4RT_w}{V_i^2} - 1)]}, \tag{2.5}$$

where T_w denotes the satellite wall temperature and α denotes the energy accommodation coefficient.

Sentman's model is a fairly accurate representation of the gas surface interactions in the lower altitudes (150 km-300 km) [77] based on the evidence of diffuse reemission stated earlier. But the assumption of a completely diffuse reemission degrades its accuracy for application in higher altitudes where the energy accommodation is lower and the reemission has an increasing quasi-specular component. Since the parameters for quasi-specular reemission can be difficult to determine, we use a specular reemission model in conjunction with Sentman's diffuse model to approximate the quasi-specular component.

2.1.2 Schamberg's model for specular reflection

Schamberg's model of gas surface interaction is based on hyperthermal assumption, i.e. it does not take into account the thermal motion of the particles and uses a simple analytical representation of the incident stream. The reflection law is given by,

$$\cos\psi_r = \cos^v \psi_i. \tag{2.6}$$

where ψ_i and ψ_r are the incident and reflected flow angles respectively, and v is a parameter that decides the nature of reemission. This law is well able to explain the laboratory observations before the 1960s which were based on clean surfaces [48]. For specular reflection, $v = 1$ and for diffuse reflection, $v = \infty$. Quasi-specular reemission is represented by intermediate values of v. An analytical expression is possible only for the limiting cases of specular and diffuse reemission. The analytical expression for the case of specular reemission using the same notation used for Sentman's model is given by [19],

$$C_d = 2\frac{A}{A_{ref}}\gamma[1 + r_{rms}(2\gamma^2 - 1)], \tag{2.7}$$

where r_{rms} refers to the ratio of reemission and incident velocity given by [53],

$$r_{rms} = \frac{V_r}{V_i} = \sqrt{1 + \alpha(\frac{3RT_w}{V_i^2} - 1)}. \tag{2.8}$$

The expression given by Eq. 2.8 is different from Eq. 2.5 since Sentman's model uses most probable (mp) velocity for reemission while Schamberg's model uses root mean square (rms) velocity.

Cook's formula (Eq. 2.7) does not account for tangential drag at grazing incidences and can lead to significant deviation from the true drag coefficient when large parallel surfaces are present. Kopenwallner [53] suggested adding the drag contribution due to thermal motion at grazing incidences, given by

$$C_{d,thermal} = \frac{1}{s\sqrt{\pi}}. \tag{2.9}$$

But this drag contribution does not become zero even when the plate is facing away from the flow [25]. To account for this fact, we have made a slight modification to Schamberg's model for specular reemission, as follows,

$$C_d = 2\frac{A}{A_{ref}}\gamma[1 + r_{rms}(2\gamma^2 - 1)] + \frac{A}{A_{ref}}\frac{e^{-\gamma^2 s^2}}{s\sqrt{\pi}}. \tag{2.10}$$

The second term comes from Sentman's model and represents the drag contribution due to thermal motion. At grazing incidence, it reduces to Eq. 2.9 while it rapidly decreases to zero as γ moves away from zero. It is important to keep in mind that only the first term should be set to zero, when the plate is facing away from the flow.

2.1.3 Linear combination

In order to estimate the drag coefficients accurately, both the diffuse and specular components should be taken into account. This work uses a linear combination of both the models as suggested by Moe and Moe (2005) [77] with the diffuse part being represented by Sentman's model and the specular part being represented by Schamberg's model. The energy accommodation coefficient is assumed to be constant at a height for a given solar and geomagnetic activity level. In reality it varies with the orientation of the plate [94]. But this assumption is justified while modelling a 'cuboid-like' shape as the variations due to orientation of different plates with respect to the flow average out. The fraction assigned to each model can be calculated using the semi-empirical satellite accommodation model (SESAM) [96, 95]. The model assumes that a fraction of the surface

is covered by oxygen which exhibits diffuse reflection. Even though SESAM is used to calculate an effective accommodation coefficient, this work uses an effective drag coefficient instead with the adsorbed sites exhibiting diffuse reemmission while the clean part of the surface exhibiting specular reemmission [131]. The fraction of diffuse reemission is calculated as,

$$f = \frac{K_l P_O}{1 + K_l P_O}. \tag{2.11}$$

where K_l is the Langmuir parameter and P_O is the partial pressure of oxygen. The Langmuir parameter is a function of the incident kinetic energy which is in turn dependent on the eccentricity of the orbit. The value of the parameter is taken to be $1.44 \times 10^6 Pa^{-1}$ for this work which is derived by Walker et al.[131] for the diffuse reflection with incomplete accommodation (DRIA) model. The value was obtained by fitting the data for spherical and randomly tumbling satellites but the same value has been used in this work for other shapes and attitude profiles as well. The particular value taken here does not significantly affect the analysis since the GSIM is used simply to model the truth for the simulations or generate the initial values for estimation with real tracking data. The partial pressure of oxygen from the ideal gas equation is given by

$$P_O = n_O T k_B, \tag{2.12}$$

where n_O is the number density of oxygen and k_B is the Boltzmann constant. The drag coefficient is then calculated by assuming the accommodation coefficient of adsorbed sites to be 1 which exhibit a diffuse reflection, i.e., the accommodation coefficient for Sentman's model is taken to be 1. The accommodation coefficient for Schamberg's model is derived by using Goodman's model which is based on clean surfaces [41]. Goodman's model was constructed to explain the laboratory experiments on clean surfaces and hence works well for quasi-specular reemission [77]. The accommodation coefficient is given by,

$$\alpha_s = \frac{K_s \mu}{(1 + \mu)^2}, \tag{2.13}$$

where μ is the mass ratio between the atmospheric species and surface molecule. In this work, the mass of the surface molecule is assumed to be 65 amu while the mean molecular mass of

the incoming atmospheric flow is satellite-position dependent. K_s is the substrate coefficient, also known as the Langmuir constant, that depends on the distribution of the incident particles [71]. For a sphere, the incident particle distribution is approximately cosine and $K_s = 2.4$. For a plate perpendicular to the flow, the incident particle distribution is unidirectional and $K_s = 3.6$. For an inclined plate, the accommodation coefficient is given by,

$$\alpha_s = \frac{K_s \mu \cos\psi}{(1+\mu)^2}. \tag{2.14}$$

Denoting the drag-coefficient calculated by Sentman's model as $C_{d,diffuse}$ and Schamberg's model as $C_{d,specular}$, the drag coefficient value is given by,

$$C_d = f C_{d,diffuse} + (1-f) C_{d,specular}, \tag{2.15}$$

where $C_{d,diffuse}$ and $C_{d,specular}$ are calculated using Eqs. 2.2 and 2.10.

2.1.4 Modified Diffuse Reflection Incomplete Accommodation (DRIA) model

Walker et al. (2014) [131] developed a drag-coefficient model by linearly combining drag-coefficients based on clean surfaces and satellite surfaces completely covered by atomic oxygen, utilizing a Langmuir isotherm. They built on the work by Pilinksi et al. (2013) [96] by assuming that the fraction of the surface covered by atomic oxygen exhibits diffuse (cosine) reflection with complete accommodation while the clean part of the surface exhibits diffuse reflection with partial accommodation. They computed the Langmuir parameter for three gas-surface interaction models - diffuse reflection incomplete accommodation (DRIA), Cergignani-Lampis-Lord (CLL) and Maxwell model. The DRIA model is another name for Sentman's model given by eqs. 2.1 and 2.2. The total drag-coefficient is modeled by Walker et al. (2014) [131] as,

$$C_{d,T} = f C_{d,ads} + (1-f) C_{d,s}, \tag{2.16}$$

where $C_{d,ads}$ is the drag-coefficient for the surface covered by an adsorbate, assumed to exhibit diffuse reemission with complete accommodation ($\alpha = 1$), $C_{d,s}$ is the drag-coefficient based

on molecular beam experiments on clean surfaces, computed using Goodman's formula for energy accommodation coefficient (Eq. 2.14) and f is calculated using eq. (2.11). Therefore, $C_{d,ads} = C_d|_{(\alpha=1)}$ and $C_{d,s} = C_d|_{(\alpha=\alpha_s)}$. Note that both $C_{d,ads}$ and $C_{d,s}$ are calculated using Sentman's model, eqs. 2.1 and 2.2, depending on the satellite shape. The difference between the two is only in the accommodation coefficient used.

Chapter 3

Satellite orbit determination

This chapter reviews the different aspects of satellite orbit determination that are used in this work. The estimation algorithms are outlined in section 3.1. Sections 3.2 and 3.3 discuss the conversions between different time systems and coordinate frames. In section 3.4, modeling of the different forces acting on the satellite and their implementation in the filter are reviewed.

3.1 Estimation methods

3.1.1 Batch processor

In this estimation method, a batch of data is processed in an iterated non-linear least squares filter in order to obtain an estimate of the initial state which can then be propagated for the given duration to obtain the subsequent state estimates. A discussion of the steps that are necessary to understand the implementation of the batch algorithm are discussed next. The details of the algorithm can be found in Born et al. [124].

Solving the normal equations to obtain the initial state estimate ($\hat{\boldsymbol{x}}_0$) lies at the heart of the batch algorithm. When apriori information is available in the form of state estimate ($\bar{\boldsymbol{x}}_0$) and covariance ($\bar{\boldsymbol{P}}_0$), the normal equations are given by

$$\boldsymbol{\Lambda}\hat{\boldsymbol{x}}_0 = \boldsymbol{N}, \tag{3.1}$$

where $\boldsymbol{\Lambda}$ is the inverse of the covariance matrix and $\boldsymbol{N}$ is the normal matrix,

$$\boldsymbol{\Lambda} = \sum_{i=1}^{l} [\tilde{\boldsymbol{H}}_i \boldsymbol{\Phi}(t_i, t_0)]^T \boldsymbol{R}_i^{-1} \tilde{\boldsymbol{H}}_i \boldsymbol{\Phi}(t_i, t_0) + \bar{\boldsymbol{P}}_0^{-1}, \tag{3.2}$$

$$\boldsymbol{N} = \sum_{i=1}^{l} [\tilde{\boldsymbol{H}}_i \boldsymbol{\Phi}(t_i, t_0)]^T \boldsymbol{R}_i^{-1} \boldsymbol{y}_i + \bar{\boldsymbol{P}}_0^{-1} \bar{\boldsymbol{x}}_0, \tag{3.3}$$

where $\tilde{\boldsymbol{H}}_i$ is the measurement Jacobian, $\boldsymbol{R}_i$ is the measurement covariance matrix and $\boldsymbol{y}_i$ is the predicted measurement residual vector, each at time instant t_i, $\boldsymbol{\Phi}(t_i, t_0)$ is the state transition matrix (STM) which maps the state deviation from time t_0 to t_i and l is the total number of measurements available. Multiplying the measurement Jacobian at each time instant by the STM maps it to the initial time since we are trying to estimate the initial state vector in Eq. 3.1. The STM history can be generated by numerically integrating the following differential equation,

$$\dot{\boldsymbol{\Phi}}(t, t_0) = \boldsymbol{A}(t) \boldsymbol{\Phi}(t, t_0), \tag{3.4}$$

where $\boldsymbol{A}(t)$ is the dynamics Jacobian matrix. The initial conditions for the equation are $\boldsymbol{\Phi}(t_0, t_0) = \boldsymbol{I}_{n \times n}$, where $\boldsymbol{I}$ is the identity matrix with dimensions corresponding to the number of states (n). The inverse of $\boldsymbol{\Lambda}$ in Eq. 3.1 can be computed using Cholesky decomposition [124]. Equation 3.1 is iterated until $\hat{\boldsymbol{x}}_0$ stops changing.

The state vector estimated in the filter comprises of the position ($\boldsymbol{r}$) and velocity ($\boldsymbol{v}$) of the satellite, and any parameters being estimated ($\boldsymbol{p}$) such as the drag-coefficient. The dynamics Jacobian is then given by

$$\boldsymbol{A} = \begin{bmatrix} \frac{\partial \boldsymbol{v}}{\partial \boldsymbol{r}} & \frac{\partial \boldsymbol{v}}{\partial \boldsymbol{v}} & \frac{\partial \boldsymbol{v}}{\partial \boldsymbol{p}} \\ \frac{\partial \boldsymbol{a}}{\partial \boldsymbol{r}} & \frac{\partial \boldsymbol{a}}{\partial \boldsymbol{v}} & \frac{\partial \boldsymbol{a}}{\partial \boldsymbol{p}} \\ \frac{\partial \dot{\boldsymbol{p}}}{\partial \boldsymbol{r}} & \frac{\partial \dot{\boldsymbol{p}}}{\partial \boldsymbol{v}} & \frac{\partial \dot{\boldsymbol{p}}}{\partial \boldsymbol{p}} \end{bmatrix}. \tag{3.5}$$

Here, $\boldsymbol{a}$ is the total acceleration of the satellite and $\boldsymbol{p}$ is the vector of parameters to be estimated. With the number of parameters to be estimated as n_p, the Jacobian matrix therefore can be simplified as

$$A = \begin{bmatrix} \boldsymbol{0}_{3\times3} & \boldsymbol{I}_{3\times3} & \boldsymbol{0}_{3\times n_p} \\ \frac{\partial \boldsymbol{a}}{\partial \boldsymbol{r}} & \frac{\partial \boldsymbol{a}}{\partial \boldsymbol{v}} & \frac{\partial \boldsymbol{a}}{\partial \boldsymbol{p}} \\ \frac{\partial \dot{\boldsymbol{p}}}{\partial \boldsymbol{r}} & \frac{\partial \dot{\boldsymbol{p}}}{\partial \boldsymbol{v}} & \frac{\partial \dot{\boldsymbol{p}}}{\partial \boldsymbol{p}} \end{bmatrix}. \tag{3.6}$$

The main disadvantage with a batch filter is that process noise cannot be easily added to

account for unmodeled dynamics. A sequential filtering method such as a Kalman filter allows for that.

3.1.2 Extended Kalman filter (EKF)

In a Kalman filter, observations are processed sequentially and a correction to the reference trajectory is generated at each instant. Whereas in a conventional Kalman filter (CKF), corrections are estimated to a reference trajectory integrated offline, in an extended Kalman filter (EKF), the differential equations for the reference trajectory are reinitialized each time a new state is estimated. This reduces the linearization errors by keeping the reference trajectory from diverging too far away from the truth. At any time step, t_k, the state estimate $\hat{\boldsymbol{X}}_k$ and the covariance of the estimate $\hat{\boldsymbol{P}}_k$ can be computed from the estimates at the previous time instant ($\hat{\boldsymbol{X}}_{k-1}$, $\boldsymbol{P}_{k-1}$) as

(1) Propagate the estimated state from t_{k-1} to t_k.

$$\dot{\boldsymbol{X}}^* = \boldsymbol{F}(\boldsymbol{X}^*, t), \qquad \boldsymbol{X}^*(t_{k-1}) = \hat{\boldsymbol{X}}(t_{k-1}), \tag{3.7}$$

$$\dot{\boldsymbol{\Phi}}(t, t_{k-1}) = \boldsymbol{A}(t)\boldsymbol{\Phi}(t, t_{k-1}) \qquad \boldsymbol{\Phi}(t_{k-1}, t_{k-1}) = \boldsymbol{I}, \tag{3.8}$$

$$\bar{\boldsymbol{P}}_k = \boldsymbol{\Phi}(t_k, t_{k-1})\boldsymbol{P}_{k-1}\boldsymbol{\Phi}^T(t_k, t_{k-1}) + \boldsymbol{Q}_k, \tag{3.9}$$

where $\boldsymbol{Q}_k$ is the process noise matrix and depends on the nature of the noise being added. The addition of process noise in EKF is discussed in chapter 7.

(2) Compute predicted measurement residuals and the measurement Jacobian.

$$\boldsymbol{y}_k = \boldsymbol{Y}_k - \boldsymbol{h}(\boldsymbol{X}_k^*, t_k), \tag{3.10}$$

$$\widetilde{\boldsymbol{H}}_k = \frac{\partial \boldsymbol{h}(\boldsymbol{X}_k^*, t_k)}{\partial \boldsymbol{X}_k}, \tag{3.11}$$

(3) Update the predictions with the new measurements.

$$\boldsymbol{K}_k = \bar{\boldsymbol{P}}_k \widetilde{\boldsymbol{H}}_k^T [\widetilde{\boldsymbol{H}}_k \bar{\boldsymbol{P}}_k \widetilde{\boldsymbol{H}}_k^T + \boldsymbol{R}_k]^{-1}, \tag{3.12}$$

$$\hat{\boldsymbol{X}}_k = \boldsymbol{X}_k^* + \boldsymbol{K}_k \boldsymbol{y}_k, \tag{3.13}$$

$$\boldsymbol{P}_k = [\boldsymbol{I} - \boldsymbol{K}_k \widetilde{\boldsymbol{H}}_k] \bar{\boldsymbol{P}}_k. \tag{3.14}$$

3.2 Time systems

The processing of satellite tracking data requires conversions between different time systems. For example, GPS measurements are usually in GPS time which need to be converted to UTC such as for frame rotation and density calculation. The different time systems relevant to this work are defined below

(1) GPS Time (GPST) - A continuous time scale without leap seconds, defined by the GPS control segment and used as the basis for GPS measurements and post-processed satellite ephemerides in .sp3 format. The GPS epoch is 0^h UTC Jan 5^{th} to 6^{th} 1980.

(2) Universal time (UT) - The time standard tied to Earth's rotation. There are multiple versions of UT of which Coordinated Universal Time (UTC) and UT1 are relevant for this work. UT1 is proportional to Earth's rotation angle with respect to distant quasars and is the same everywhere on Earth. UTC is the primary time scale used for civil time-keeping on Earth. It is an atomic time scale kept within 0.9 seconds of UT1 and is derived from TAI. Time zones are defined as offsets from UTC.

(3) International Atomic Time (TAI) - A continuous reference time scale used as the basis for UTC. TAI is a statistical time derived from multiple high-precision atomic clocks in various countries.

(4) Terrestrial Time (TT) - A time system defined by the International Astronomical Union (IAU) as a basis for astronomical measurements made from the surface of Earth.

(5) Barycentric Dynamical Time (TDB) - A relativistic astronomical time scale accounting for time dilation when calculating ephemerides of celestial objects and differing from TT by less than 2 milliseconds in a periodic manner. This is the time scale used for calculating planetary ephemerides.

(6) Greenwich Mean Sidereal Time (GMST) - Hour angle of the average position of the Vernal equinox measured from the Greenwich Meridian.

(7) Earth rotation angle (ERA) - Rotation angle of the Earth measured from a non-moving origin on the celestial equator called the Celestial Intermediate Origin (CIO) instead of the equinox.

(8) Julian date (JD) - The number of fractional days since 12^h, Jan 1, 4713 BC in Universal Time.

(9) Modified Julian date (MJD) - A modified version of JD shifting the epoch to 0^h Nov. 17, 1858.

The conversions between the different time systems defined above are outlined in table 3.1 and further explanation on the time conversions is given below [118].

Table 3.1: Time frame conversions

From	**To**	**Conversion**
GPST	TAI	+19 s
TAI	UTC	-$LeapSeconds$
TAI	TT	+32.184 s
UTC	UT1	+$dut1$
TT	TDB	$+0.001658 \sin(g + 0.0167 \sin g)$
JD	MJD	-2400000.5

In order to go from TDB to TT, g can be computed by

$$g = \frac{2\pi(357.528^0 + 0.98560028^0(JD - 2451545))}{360^0}. \tag{3.15}$$

LeapSeconds are the leap seconds periodically added to UTC to keep within 0.9 ns of UT1. The difference between UT1 and UTC is given by $dut1$. The values of both *LeapSeconds* and $dut1$ are published as IERS Bulletins (`https://www.iers.org/IERS/EN/Publications/Bulletins/bulletins.html`).

ERA and GMST can be calculated as follows [91]

$$ERA = 2\pi(0.7790572732640 + 1.00273781191135448Tu), \tag{3.16}$$

where $Tu = JD - 2451545$ is the Julian date past J2000 epoch.

$$GMST = ERA + \frac{\pi}{648000}(0.014506 + 4612.156534t + 1.3915817t^2 - 0.00000044t^3 - 0.000029956t^4 - 0.000000036800t^5), \tag{3.17}$$

where $t = (JD - 2451545)/36525$ centuries in TT from J2000 epoch.

3.3 Coordinate frames

Satellite orbit determination requires the use of multiple coordinate frames at different steps of the process. For example, the attitude of the satellite is generally specified between the body frame and local orbital frame of the satellite. The observations are usually in an Earth-fixed frame while the integration of the force dynamics is in an inertial frame. There are different flavors of all these frames that are in use by different satellite operators. The main frames used in this thesis are discussed in this section.

The body-fixed frame of the satellite is a frame fixed w.r.t the satellite body, with the origin usually at the center of mass. The axes of the frame are defined w.r.t reference points on the satellite. For example, the body x-axis may point towards the front solar panel and the z-axis

may point towards the GPS antenna face while the y-axis completes the right-handed coordinate system.

A local orbital frame is attached to the satellite body, with origin at satellite center of mass, but not fixed w.r.t it. The frame rotates with the satellite orbital motion. There are multiple types of local orbital frame that can be used such as the local vertical local horizontal (LVLH) frame and the Radial-Tangential-Normal (RTN) frame. For example, the axes of LVLH frame are: Z-axis points towards $-\boldsymbol{r}$, i.e., center of the Earth, Y-axis points opposite to the orbit normal or negative of the angular momentum vector, $-\boldsymbol{h}$, and X-axis completes the right-handed coordinate system.

An Earth-centered Earth-fixed (ECEF) frame is attached to the rotating Earth with origin at the center of the Earth, i.e., a body-fixed frame for Earth. The two most common realizations of ECEF frame are the World Geodetic System (WGS-84) and the International Terrestrial Reference Frame (ITRF). They are identical to each other for all practical purposes.

An Earth-centered inertial (ECI) frame, to a close approximation, is an inertial frame with origin at the center of the Earth. The X-axis points towards the Vernal Equinox, the Y-axis is 90^0 east in the equatorial plane and the Z-axis points towards the North Pole. The frame is not strictly inertial in the sense that the equatorial plane and the Vernal Equinox are in slight motion due to precession and nutation effects. At best, a "pseudo-inertial" frame can be achieved by referring the frame to the equator and equinox at a particular epoch. The most commonly used realization of the ECI frame is the J2000 or EME2000 frame defined at the J2000 epoch, 12:00 TT on 1 January 2000 (or JD 2451545). The conversion from ITRF to J2000 frame uses the precession matrix (P), nutation matrix (N), polar motion matrix (W) and sidereal time matrix (R), with the rotation matrix given by,

$$\boldsymbol{R}_E^I = [\boldsymbol{P}(t)][\boldsymbol{N}(t)][\boldsymbol{R}(t)][\boldsymbol{W}(t)]. \tag{3.18}$$

The reader is referred to Vallado (2007) [128] for further details. In this work, the MATLAB codes by Vallado [128] are used for the frame conversions between J2000 and ITRF.

3.4 Force models

The motion of a satellite in the gravitational field of Earth is affected by different perturbing forces acting on it. The relative magnitude of the forces is dependent on the satellite altitude as well as satellite characteristics such as the area-to-mass ratio for non-conservative forces. Based on the required accuracy of the application and availability of force model parameters, individual forces can be added to the filter dynamics. The force models that are used in this work are discussed in brief below.

3.4.1 Non-spherical gravity

The perturbation force due to the non-spherical distribution of mass in a central body is most commonly modeled using a spherical harmonics formulation for the geopotential, given by [49]

$$U = \frac{GM_e}{r} \sum_{n=0}^{\infty} \sum_{m=0}^{n} \frac{R_e^n}{r^n} \bar{P}_{nm}(\sin\phi)(\bar{C}_{nm}\cos(m\lambda) + \bar{S}_{nm}\sin(m\lambda)). \tag{3.19}$$

where G is the universal gravitation constant, M_e and R_e are the mass and the mean equatorial radius of the Earth respectively, $\bar{P}_{nm}$ are the normalized associated Legendre function of degree n and order m, $\bar{C}_{nm}$ and $\bar{S}_{nm}$ are the normalized spherical harmonics coefficients, and r, ϕ and λ are the radial distance from the center of mass of the Earth, the geocentric latitude and the longitude of the satellite respectively. The acceleration due to the geopotential in ECEF frame is given by the first partial of the potential,

$$\ddot{\boldsymbol{r}}|_E = \nabla U. \tag{3.20}$$

The partial of the gravitational acceleration w.r.t the position, required for implementation in the filter, can be obtained by taking a second partial of the geopotential. Here, we use Cunningham's method [21] derived for the fully normalized spherical harmonics coefficients by Hesar (2016) [45]. The partials can be computed in the inertial frame as follows

$$\ddot{\boldsymbol{r}}|_I = \boldsymbol{R}_E^I \ddot{\boldsymbol{r}}|_E, \tag{3.21}$$

$$\left.\frac{\partial \ddot{\boldsymbol{r}}}{\partial \boldsymbol{r}}\right|_I = \boldsymbol{R}_E^I \left.\frac{\partial \ddot{\boldsymbol{r}}}{\partial \boldsymbol{r}}\right|_E (\boldsymbol{R}_E^I)^T. \tag{3.22}$$

Note that the partials w.r.t the velocity are zero since the acceleration is independent of the satellite velocity. There are various high-fidelity geopotential models available in literature that derive the spherical harmonics coefficients to different degrees and order. In this work, Earth Gravitational Model 2008 (EGM2008) [89] is mostly used unless stated otherwise. Though the model is available up to a degree and order of 2159, a much lower degree/order needs to be used for orbit determination purposes. The choice of the order of truncation can significantly affect the estimated states and needs to be chosen with care. This is explained in more detail in the next chapter.

3.4.1.1 Third-body forces

The orbital motion of an Earth orbiting satellite is affected by the gravitational field of other celestial bodies. The relative magnitude of the forces depends on the mass of the perturbing body and distance from Earth. The primary perturbing bodies for LEO satellite motion are the Sun and the Moon. The third-body acceleration acting on a satellite in an ECI frame is

$$\boldsymbol{a_{third}} = GM_j \left(\frac{\boldsymbol{s}_j - r}{|\boldsymbol{s}_j - \boldsymbol{r}|^3} - \frac{\boldsymbol{s}_j}{|\boldsymbol{s}_j|^3} \right), \tag{3.23}$$

where $j = 2, 3$, refer to the Moon and Sun with masses M_j and position vector w.r.t geocenter $\boldsymbol{s}_j$. The partial of the acceleration w.r.t the satellite position vector is as follows

$$\frac{\partial \boldsymbol{a_{third}}}{\partial \boldsymbol{r}} = -GM_j \left(\frac{1}{|\boldsymbol{r} - \boldsymbol{s}_j|^3} \boldsymbol{I}_{3\times 3} - 3(\boldsymbol{r} - \boldsymbol{s}_j) \frac{(\boldsymbol{r} - \boldsymbol{s}_j)^T}{|\boldsymbol{r} - \boldsymbol{s}_j|^5} \right). \tag{3.24}$$

3.4.2 Atmospheric drag

The acceleration due to atmospheric drag was discussed in section 1.2. Approximating the relative velocity vector due to the co-rotation of the atmosphere ($\boldsymbol{v_r} = \boldsymbol{v} - \boldsymbol{\omega} \times \boldsymbol{r}$), the partials of

the acceleration w.r.t the position and velocity are given by

$$\begin{aligned}\frac{\partial \boldsymbol{a_{drag}}}{\partial \boldsymbol{r}} =& -\frac{C_d A_{ref}}{2m}\frac{\Delta\rho}{\Delta r}\hat{\boldsymbol{r}} v_r \boldsymbol{v_r}^T + \frac{C_d A_{ref}\rho}{2m}(\hat{\boldsymbol{v}}_{\boldsymbol{r}}\boldsymbol{v_r} + v_r \boldsymbol{I}_{3x3})[\tilde{\boldsymbol{\omega}}_{\boldsymbol{e}}] \\ & -\frac{1}{2}\rho\frac{A_{ref}}{m} v_r^2 \hat{\boldsymbol{u}}\frac{\partial C_d}{\partial \boldsymbol{r}},\end{aligned} \tag{3.25}$$

$$\frac{\partial \boldsymbol{a_{drag}}}{\partial \boldsymbol{v}} = -\frac{C_d A_{ref}\rho}{2m}(\frac{\boldsymbol{v_r}\boldsymbol{v_r}^T}{v_r} + v_r \boldsymbol{I}_{3\times 3}) - \frac{1}{2}\rho\frac{A_{ref}}{m} v_r^2 \hat{\boldsymbol{u}}\frac{\partial C_d}{\partial \boldsymbol{v}}. \tag{3.26}$$

where $\frac{\Delta\rho}{\Delta r}$ = approximate change in density with altitude, taken as difference of density values every 1 km of altitude and $[\tilde{\boldsymbol{\omega}}_{\boldsymbol{e}}]$ is the skew symmetric representation of the angular velocity of Earth given by

$$[\tilde{\boldsymbol{z}}] = \begin{bmatrix} 0 & -z_3 & z_2 \\ z_3 & 0 & -z_1 \\ -z_2 & z_1 & 0 \end{bmatrix}. \tag{3.27}$$

For precise applications, the atmospheric winds might need to be taken into account in the relative velocity vector with wind models such as the the horizontal wind model (HWM) [28, 27]. The partials of the drag-coefficient w.r.t the position and velocity are zero for most applications but some of the drag-coefficient models developed in this work are dependent on the orbital states, as discussed in chapter 5. The partial of the acceleration w.r.t the higher-fidelity models of drag-coefficient are also discussed in that chapter.

3.4.3 Solar Radiation Pressure (SRP)

Solar radiation pressure (SRP) is the force exerted by the solar photons impinging on a satellite surface. The most commonly used SRP model for orbit determination is the cannonball model given by

$$\boldsymbol{a_{SRP}} = -P_s \frac{C_r A_r}{m}\left(\frac{AU}{|\boldsymbol{r_s}|}\right)^2 f_s \hat{\boldsymbol{r}}_{\boldsymbol{s}}, \tag{3.28}$$

where $P_s = 4.56\ \mu Pa$ is the solar radiation pressure at 1 AU distance, $\boldsymbol{r_s}$ is the satellite to Sun position vector, A_r is the cross-sectional of the satellite exposed to the Sun, C_r is the SRP coefficient and f_s is the shadow factor [82]. Similar to C_d, C_r accounts for the momentum exchange between

the solar photons and the satellite surface. The cannonball SRP model assumes that the satellite maintains a constant orientation w.r.t the Sun. A higher-fidelity panel model for SRP was developed for the GRACE satellites which sums up the SRP force acting on each surface as follows

$$\boldsymbol{a_{SRP}} = -P_s \frac{C_r}{m} \left(\frac{AU}{|\boldsymbol{r_s}|} \right)^2 f_s \sum_{k=1}^{N} A_k \cos\theta_k [(1-\rho_k)\hat{\boldsymbol{r}}_{\boldsymbol{s}} + 2(\frac{\delta_k}{3} + \rho_k \cos\theta_k)\hat{\boldsymbol{n}}_{\boldsymbol{k}}]. \tag{3.29}$$

where A_k are the areas of the satellite surfaces with $\hat{\boldsymbol{n}}_{\boldsymbol{k}}$ as the unit vectors in the satellite body frame, θ_k are the angles that the sun vector makes with the surface unit vectors, δ_k and ρ_k are the diffuse and specular reflectivities of the surfaces respectively. In order to use this high-fidelity model, optical properties of the surfaces need to be known. The SRP coefficient is estimated in the filter as a scaling factor to the SRP force. The partials of acceleration w.r.t the position are given by

$$\frac{\partial \boldsymbol{a_{SRP}}}{\partial \boldsymbol{r}} = P_s \frac{C_r A_r}{m} AU^2 f_s \left(\frac{1}{|\boldsymbol{r_s}|^3} \boldsymbol{I}_{3\times 3} - 3\boldsymbol{r_s} \frac{\boldsymbol{r_s}^T}{|\boldsymbol{r_s}|^5} \right) \sum_{k=1}^{N} A_k \cos\theta_k [(1-\rho_k). \tag{3.30}$$

The partial of the acceleration w.r.t the SRP coefficient is given by

$$\frac{\partial \boldsymbol{a_{SRP}}}{\partial C_r} = -\frac{P_s}{m} \left(\frac{AU}{|\boldsymbol{r_s}|} \right)^2 f_s \sum_{k=1}^{N} A_k \cos\theta_k [(1-\rho_k)\hat{\boldsymbol{r}}_{\boldsymbol{s}} + 2(\frac{\delta_k}{3} + \rho_k \cos\theta_k)\hat{\boldsymbol{n}}_{\boldsymbol{k}}]. \tag{3.31}$$

The partials can be similarly computed for the cannonball model.

3.4.4 Tidal forces

The gravitational force of the Sun, Moon and other planets acts in a differential manner on different faces of the Earth, which causes a deformation of the Earth's surface. The perturbations induced in the geopotential due to the deformations in the solid Earth are called solid Earth tides and those in the ocean surfaces are called ocean tides. It is important to clarify the three types of spherical harmonic coefficients associated with any geopotential model before proceeding—mean-tide, zero-tide and conventional tide-free. The total external geopotential in the vicinity of Earth is a sum of Earth's own gravitational potential in the absence of any other perturbing bodies (tide-free geopotential), the tidal gravitational potential of the perturbing bodies (external tidal potential) and the perturbations in the tide-free geoptential due to the deformations on Earth's surface caused by the presence of the external bodies (tide-induced geopotential).

The external tidal potential requires further explanation. For two bodies orbiting around the system barycenter, such as the Earth-Moon system, the gravitational acceleration of the Moon on Earth approximately balances out the centrifugal force at the geocenter. But at any other point on the surface of the Earth, the slight difference between the gravitational and the centrifugal acceleration gives rise to tidal accelerations. More details can be found in Wengel (1997) [134].

The external tidal potential as well as the tide-induced perturbations in the geopotential have permanent and periodic parts. When the periodic part of the external tidal potential and the tide-induced geopotential are removed from the total gravitational potential near Earth, the mean-tide potential is obtained. On removing the permanent part of the external tidal potential from the mean-tide potential, the zero-tide potential is obtained. Note that the zero-tide potential is purely the geopotential (tide-free + permanent part of the tide-induced geopotential). If the permanent part of the tide-induced geopotential is removed, a conventional tide-free geopotential is obtained. Usually for orbit propagation, either the zero-tide or the tide-free geopotential is used and the periodic parts of the tidal potential are added using the steps outlined below. Only the tidal perturbations due to the Sun and Moon are considered. Understanding the nitty-gritty of tidal perturbations can be quite complex. Therefore, an algorithmic description to compute the tidal perturbations for orbit propagation is attempted below. For further explanation, the reader is referred to the IERS document [91].

3.4.4.1 Solid Earth Tides

The solid Earth tides can be most easily added to the perturbed geopotential through additions to the spherical harmonic coefficients by using parameters called Love numbers, k_{nm}, for tides of degree n and order m in spherical harmonics. There are three types of love numbers, k^0_{nm} and $k^{\pm}_{nm}$ due to the effects of ellipticity and coriolis force due to Earth's rotation on the tidal deformations.

(1) The changes in degree 2, 3 and 4 spherical harmonic coefficients are evaluated due to the

frequency-independent nominal Love numbers k^0_{2m}, k^0_{3m} and k^+_{2m} respectively.

$$\Delta\bar{C}_{nm} - i\Delta\bar{S}_{nm} = \frac{k^0_{nm}}{2n+1}\sum_{j=2}^{3}\frac{GM_j}{GM_e}\left(\frac{R_e}{r_j}\right)^{n+1}\bar{P}_{nm}(\sin\phi_j)e^{-im\lambda_j}, \tag{3.32}$$

where i refers to the unit imaginary number, $j = 2, 3$ refer to the Sun and Moon with associated masses M_j, body-fixed geocentric latitude ϕ_j and geocentric east longitude from Greenwich λ_j, and $n = 2, 3$. The effect on degree 4 spherical harmonic coefficients can be evaluated as follows

$$\Delta\bar{C}_{4m} - i\Delta\bar{S}_{4m} = \frac{k^+_{2m}}{5}\sum_{j=2}^{3}\frac{GM_j}{GM_e}\left(\frac{R_e}{r_j}\right)^{3}\bar{P}_{2m}(\sin\phi_j)e^{-im\lambda_j}, \tag{3.33}$$

The Love numbers are tabulated in appendix C.

(2) The frequency-dependent contributions to the perturbation in spherical harmonic coefficients, $\Delta\bar{C}_{2m}$ and $\Delta\bar{S}_{2m}$, are computed next. The contribution to $\Delta\bar{C}_{20}$ are as follows

$$\Delta\bar{C}_{20} = \sum_f [A_{ip}\cos\theta_f - A_{op}\sin\theta_f]. \tag{3.34}$$

For the higher-order terms, $m = 1, 2$,

$$\Delta\bar{C}_{2m} - i\Delta\bar{S}_{2m} = \eta_m\sum_f [A_{ip} + iA_{op}]e^{i\theta_f}, \tag{3.35}$$

where $\eta_1 = -i, \eta_2 = 1$, A_{ip} and A_{op} are in-phase and out-of-phase amplitudes of the corrections for the frequency dependence of the nominal Love numbers. The argument θ_f is a function of the particular tidal frequency being considered and can be computed using integral combinations of a few basic angular arguments. There are multiple variations of these basic angular arguments, depending on the convention being used. Here, Doodson's convention is being used to compute the tidal frequencies. The Doodson arguments are given by

$\beta_1 = \tau = GMST + \pi - s$: Greenwich hour angle of the Moon plus 12 hours

$\beta_2 = s = F + \Omega$: Mean longitude of the Moon

$\beta_3 = h = s - D$: Mean longitude of the Sun

$\beta_4 = p = s - l$: Longitude of the Moon's mean perigee

$\beta_5 = N' = -\Omega$: Negative of the longitude of the Moon's mean ascending node on the ecliptic

$\beta_6 = p_s = s - D - l'$: Longitude of the Sun's mean perigee

The Doodson arguments are functions of the fundamental arguments of lunisolar nutation - mean anomaly of the Moon (l), mean anomaly of the Sun (l'), mean elonagtion of the Moon from the sun (D), Ω and $F = s - \Omega$. The computation of the fundamental arguments is outlined in appendix C.

The tidal frequencies can then be computed using their Doodson number identifiers ($\boldsymbol{n}$) multiplied with the Doodson arguments described above, i.e., $\theta_f = \boldsymbol{n}^T\boldsymbol{\beta}$. All five digits in a Doodson number after the first one, are biased by +5; therefore 5 should be subtracted from them before multiplication by the Doodson arguments. For example, a Doodson number $\boldsymbol{n} = 125,755$ would give $\theta_f = 1\beta_1 - 3\beta_2 + 0\beta_3 + 2\beta_4 + 0\beta_5 + 0\beta_6$.

If a tide-free geopotential is being used, then the solid Earth tidal perturbations on the spherical harmonic coefficients can computed by summing up the effects of steps 1 and 2 and adding them to the nominal values of the respective coefficients.

(3) If a zero-tide geopotential is being used, then the $\bar{C}_{20}$ already contains the permanent part of the tide-induced potential. Therefore, using eq. (3.32) to compute the frequency-independent tides adds the permanent part twice. This can be remedied by adding the following contribution to $\bar{C}_{20}$

$$\Delta\bar{C}_{20} = (4.4228 \times 10^{-8})(0.31460)k_{20}. \tag{3.36}$$

3.4.4.2 Ocean Tides

The perturbations due to ocean tides on the spherical harmonic coefficients can be calculated as follows

$$[\Delta\bar{C}_{nm} - i\Delta\bar{S}_{nm}](t) = \sum_{f}\sum_{+}^{-}(C^{\pm}_{f,nm} \mp iS^{\pm}_{f,nm})e^{\pm\theta_f(t)}, \tag{3.37}$$

where the geopotential harmonic amplitudes, $C^{\pm}_{f,nm}$ and $S^{\pm}_{f,nm}$, corresponding to the tide constituent f are given by ocean tide models. In this work the FES2004 ocean tide model [63] is used.

The total tidal perturbations are the sum of solid earth and ocean tides. Since the tidal perturbations are being added to the spherical harmonic coefficients, the partials of the acceleration w.r.t the position are accounted for in the partials of the geopotential with the new perturbed coefficients.

3.4.5 Relativistic correction

The post-Newtonian relativistic correction terms due to the curvature of the four-dimensional space-time is given by

$$\boldsymbol{a_r} = -\frac{GM_e}{r^2}\left(\left(4\frac{GM_e}{c^2 r} - \frac{v^2}{c^2}\right)\hat{\boldsymbol{r}} + 4\frac{v^2}{c^2}(\hat{\boldsymbol{r}}.\hat{\boldsymbol{v}})\hat{\boldsymbol{v}}\right). \tag{3.38}$$

The partials of the acceleration w.r.t the position and velocity are as follows

$$\frac{\partial \boldsymbol{a_r}}{\partial \boldsymbol{r}} = \frac{GM_e}{c^2 r^3}\left(\left(16\frac{GM_e}{r} - 3v^2\right)\hat{\boldsymbol{r}}\hat{\boldsymbol{r}}^T + 4(\hat{\boldsymbol{r}}.\boldsymbol{v})\boldsymbol{v}\hat{\boldsymbol{r}}^T - \left(4\frac{GM_e}{r} - v^2\right)\boldsymbol{I}_{3\times 3} + 4\boldsymbol{v}\boldsymbol{v}^T\right), \tag{3.39}$$

$$\frac{\partial \boldsymbol{a_r}}{\partial \boldsymbol{v}} = \frac{GM_e}{c^2 r^3}(2\boldsymbol{r}\boldsymbol{v}^T - 4\boldsymbol{v}\boldsymbol{r}^T - 4(\boldsymbol{r}.\boldsymbol{v})\boldsymbol{I}_{3\times 3}). \tag{3.40}$$

3.5 Chapter summary

In this chapter, we discussed the various aspects that are relevant for satellite orbit determination. Consistency in time and coordinate systems is very important for accurate orbit determination and prediction, therefore care must be taken in their implementation. High-fidelity modeling of the forces acting on the satellites becomes important when estimating physical parameters such as the

atmospheric density as will be discussed in chapter 7. Ignoring certain forces can corrupt the values of estimated parameters and cause them to be non-physical. This aliasing effect is analyzed in the next chapter in the context of geopotential truncation before implementing high-fidelity models of drag.

Chapter 4

Gravitational force model aliasing with non-gravitational force coefficients

The estimation of non-conservative force coefficients during orbit determination has been a long standing problem in the field of space situational awareness. The errors in the estimates of drag and SRP coefficients obtained during orbit determination have been attributed to the assumption of a constant value; therefore, various high-fidelity models have been proposed to capture the variation of these coefficients and improve the accuracy of their estimates [69, 122, 94, 72, 103]. But in many cases, errors in the estimates of these coefficients are introduced due to fundamental controllable factors that are independent of the physics of these forces. Specifically, unmodeled forces in the filter cause the estimated states and parameters, including these force coefficients, to diverge from their true values. In other words, the filter tries to compensate for the unmodeled dynamics by adjusting the estimated states and parameters [3]. The effect of introducing errors in estimated states and parameters due to the presence of unmodeled dynamics in the filter is referred to as *aliasing* [1]; not to be confused with the homonymous effect in signal processing. Therefore, even with high-fidelity estimation-based models of these coefficients, the estimates will still be inaccurate if there are other unmodeled effects in the filter. An apparently good orbit fit (minimization of residuals) is possible in such a case; however, the prediction accuracy will degrade rapidly.

This chapter quantifies the corrupting effects of unmodeled dynamics in the filter, introduced due to an arbitrary truncation of the gravitational field, on estimates of the drag and SRP coefficients in the LEO regime and demonstrates that these errors can be easily remedied. The geopotential is truncated at a degree n and order m in orbit determination models for computational

reasons. From here on, 'order' will refer to both degree and order since this work primarily deals with a 'square' gravitational field for which degree is equal to order, unless otherwise stated. The order of truncation has generally been based on the diminishing contribution of higher order terms towards orbit propagation [127, 4]. Even though the averaged effects of the higher order geopotential terms on the orbit propagation are comparatively small [105], the instantaneous acceleration due to these terms can be higher than the dominant drag and SRP forces to a significantly larger order. As a result, the ignored gravitational acceleration aliases into the estimated drag and SRP coefficients. Consequently, the effective contribution of the unmodeled geopotential to orbit prediction accuracy is much larger than anticipated purely due to propagation. Therefore, the suggested truncation orders of the geopotential [4, 127, 109] for orbit determination and prediction in LEO do not hold when the drag and SRP coefficients are being estimated. For example, Roscoe et al. [109] showed that propagation errors due to geoptential truncation almost plateau by order 30. Vallado [127] analyzed propagation errors for higher orders of truncation (up to order 70) while noting that the results would be qualitatively similar for orbit determination and propagation. While that is true if only initial states are being estimated, the prediction errors are greatly amplified when the estimated states include force-coefficients, due to aliasing effects. Barker et al. [4] recognized that solve-for parameters such as ballistic coefficient and SRP coefficient are affected by resonances at particular orders but the effect of truncation on the coefficient estimates was not quantified. The maximum order of truncation recommended by them was 30 which we show to be insufficient to obtain accurate estimates of force-coefficients. In addition, previous studies on gravitational field truncation effects on orbit determination and prediction utilized state-of-the-art geopotential models of that time. These models such as the World Geodetic System 1984 (WGS-84) global gravity model [24] were available up to much lower order (order 180 for WGS-84 global gravity model) compared to the current models such as Earth Gravitational Model 2008 (EGM2008; order 2159) [89]. Since the coefficients for the same order can be widely different for each of these models, the contribution of higher order terms towards orbit propagation needs to be re-evaluated.

The correlation of the truncated geopotential with the drag and SRP coefficients has been

hinted at [4, 84] but the current literature (within the confines of the author's knowledge) lacks a comprehensive study mapping out these correlations across LEO altitudes. As pointed out by the National Academy of Engineering [84], "*in the current orbit determination process, any errors caused by the omission of high-degree and high-order gravity terms will be non-physically absorbed into terms such as the ballistic coefficient, even though they minimize the residuals and result in state estimations that are satisfactory to current requirements.*" The same study also points out that the current special perturbations (SP) catalog, i.e. the catalog maintained by using full numerical integration to generate ephemerides for the satellites, utilizes a medium fidelity (36x36) geopotential. In this work, it is demonstrated that truncation at this order introduces significant errors in the cannonball drag and SRP coefficient estimates that ultimately leads to poor orbit prediction accuracy in LEO altitudes. The emphasis of this study is on reducing the orbit determination and prediction errors due to aliasing of drag and SRP with the gravitational force since increasing the fidelity of the gravitational field does not require any additional modeling efforts or lead to any significant increase in computational complexity. Based on this philosophy, an order 90 geopotential is suggested at 350 km and order 50 at 850 km in order to obtain prediction accuracy up to 10 m for a three-day prediction arc.

4.1 Chapter outline

This chapter analyzes the correlations between higher order gravitational forces and the non-conservative forces of SRP and atmospheric drag in the low-altitude LEO regime, 350-850 km. Before the aliasing effect in orbit determination is discussed in detail, the issue is illustrated through a simple two-dimensional kinematic example in section 4.2. In section 4.3, the simulation setup for the analysis is described. This study has been carried out using the EGM2008 global gravity model. As discussed earlier, the coefficient values can differ depending on the gravity model used. As a result, the aliasing errors will be slightly different for other models. But instead of quantifying the exact aliasing errors for each gravity model, the results are presented here for a representative model. The differences between different competing models are not large enough

to affect the aliasing errors significantly (see appendix B). Section 4.4 compares the instantaneous and average acceleration magnitudes of the forces. Understanding how the acceleration magnitudes compare to each other provides an idea of the amount of aliasing error introduced in the coefficients. In section 4.5, the aliasing error in the drag and SRP coefficients is analyzed as a function of the geopotential truncation order. This section introduces a parameter, the ratio of projected unmodeled gravitational acceleration and non-gravitational acceleration, that can be used to predict the trend of aliasing errors with truncation order.

The correlations between the forces will vary as the orbital conditions change. In particular, the gravitational field experienced by a satellite in near-polar orbit is different from a near-equatorial orbit because of the dominance of different gravitational harmonics in the two regimes. The magnitudes of drag and SRP also depend on factors such as the satellite area-to-mass ratio and solar activity level. Therefore, a sensitivity analysis is carried out to analyze changes in the aliasing error trends with these factors in section 4.6. For orbit propagation, using a non-square gravity potential can be beneficial over a square gravity field [4, 127]. This is because higher order zonal terms ($m = 0$) can have a significantly larger contribution to orbit propagation than higher order tesseral ($m < n$) and sectorial ($m = n$) terms. Section 4.7 analyzes if this holds true when drag and SRP coefficients are being estimated. In order to aid the selection of geopotential truncation order in the low-altitude LEO regime, estimation errors in the drag and SRP coefficients as well as the corresponding prediction errors are mapped out over an altitude range of 350-850 km as a function of geopotential truncation order in section 4.8. These maps can serve as tools in selecting the geopotential truncation order for orbit determination and prediction in the low-altitude LEO regime. Finally, the results of the aliasing errors obtained through simulations are corroborated using real GPS data from the Gravity Recovery and Climate Experiment (GRACE) satellite in section 5.4.

4.2 Effects of unmodeled dynamics

In this section, the effect of unmodeled dynamics on estimated parameters is demonstrated through a simple two-dimensional example. The purpose of this example is to illustrate two key points that form the basis for this study - Unmodeled dynamics in the estimator not only affect the estimated states but also any estimated parameters that in turn serve to increase the prediction errors, and unmodeled accelerations alias into estimated coefficients of forces that are acting in the same direction. Since they do not affect the covariance of the estimated states, it continues to shrink with the availability of more information to the estimator. On the other hand, the deviation of the estimated states from their true values can keep on increasing, leading to the issue of filter divergence. When the unmodeled dynamics are unknown or cannot be modeled due to computational reasons, any one of the several techniques that approximate them with the addition of process noise in one form or another can be utilized [124]. But as pointed out by McMahon and Scheeres [69], using process noise to fit the data inflates the uncertainties around the estimated states and certainly cannot compensate for prediction errors. Therefore, if there's a possibility of using a higher-fidelity model to reduce their effects on estimated states and parameters, such as in the case of the gravitational field, it is preferable over the addition of process noise. The setup

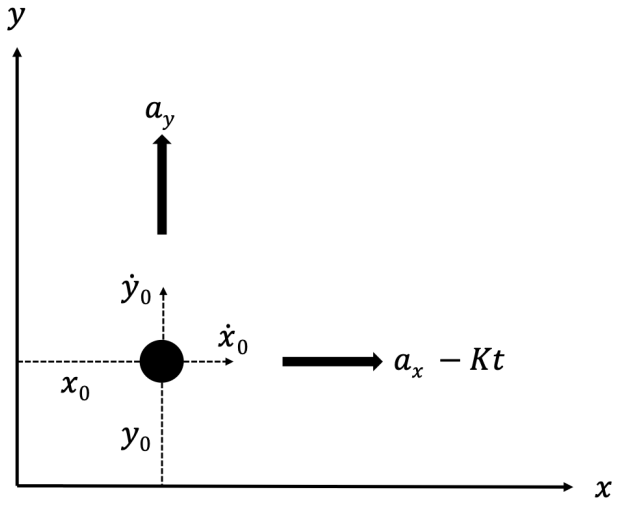

Figure 4.1: Graphical representation of kinematic example

for the example is depicted in Fig. 4.1. Two mutually perpendicular constant accelerations (a_x and a_y) are acting on the particle. The unmodeled dynamics in the estimator will be introduced through errors in these accelerations. An additional acceleration acts in the x-direction and depends linearly on time with a constant force coefficient denoted by K. The states to be estimated are the initial positions and velocities (x_0, $\dot{x}_0$, y_0, $\dot{y}_0$) and the force coefficient K. This example will demonstrate that errors in the accelerations will be absorbed by the estimates of the initial states and the estimated force coefficient. The analytical solution for the states is given by

$$\dot{x}(t) = \dot{x}_0 + a_x t - K\frac{t^2}{2}, \tag{4.1}$$

$$x(t) = x_0 + \dot{x}_0 t + a_x\frac{t^2}{2} - K\frac{t^3}{6}, \tag{4.2}$$

$$\dot{y}(t) = \dot{y}_0 + a_y t, \tag{4.3}$$

$$y(t) = y_0 + \dot{y}_0 t + a_y\frac{t^2}{2}. \tag{4.4}$$

A batch least-squares estimator [124] is used to process position measurements along x and y directions, available at $t = 0, \Delta t, 2\Delta t, ...l\Delta t$; $l > 2$ for the information matrix to be invertible. The measurement time-spacing is related to the total duration of measurements (length of data-arc, T) and number of measurements as $\Delta t = \frac{T}{l}$. The normal equations in eq. (3.1)-eq. (3.3) are used to solve for the state estimate. The measurement Jacobian ($\tilde{\boldsymbol{H}}(t_k)$) and state transition matrix ($\Phi(t_0 = 0, t_k = t)$) for this example are given by

$$\tilde{\boldsymbol{H}} = \begin{bmatrix} 1 & 0 & 0 & 0 & 0 \\ 0 & 0 & 1 & 0 & 0 \end{bmatrix}, \tag{4.5}$$

$$\Phi(0,t) = \begin{bmatrix} 1 & t & 0 & 0 & -t^3/6 \\ 0 & 1 & 0 & 0 & -t^2/2 \\ 0 & 0 & 1 & t & 0 \\ 0 & 0 & 0 & 1 & 0 \\ 0 & 0 & 0 & 0 & 0 \end{bmatrix}. \tag{4.6}$$

If the only errors in the estimator are in the initial states (δx_0, $\delta \dot{x}_0$, δy_0, $\delta \dot{y}_0$) and the force coefficient (δK), it can be shown that the state estimates are obtained within the measurement noise [69]. But if there are errors in the dynamics model, $\delta a_x = a_{x,t} - a_x$ and $\delta a_y = a_{y,t} - a_y$, estimation errors are introduced in the state estimates due to the unmodeled dynamics. In order to calculate the estimation errors using eq. 3.1, the measurement residuals in eq. 3.3 are given by

$$\boldsymbol{y}(t) = \begin{bmatrix} \delta x_0 + \delta \dot{x}_0 - \delta K t^3/6 \\ \delta y_0 + \delta \dot{y}_0 \end{bmatrix} + \begin{bmatrix} \varepsilon_x \\ \varepsilon_y \end{bmatrix} + \begin{bmatrix} \delta a_x t^2/2 \\ \delta a_y t^2/2 \end{bmatrix}. \tag{4.7}$$

The first two columns denote the residuals due to errors in the initial states and parameter being estimated, and the measurement noise respectively while the third column is the residual due to unmodeled dynamics. Assuming zero information on the initial states ($\bar{\boldsymbol{X}}_{\mathbf{0}} = \mathbf{0}$, $\bar{\boldsymbol{P}}_{\mathbf{0}}^{-1} = \mathbf{0}$), the state estimates can be calculated by substituting eqs. 4.5-4.7 in eq. (3.1) (the superscript $\hat{}$ denotes estimated states and subscript t denotes true values)

$$\begin{bmatrix} \hat{x}_0 \\ \hat{\dot{x}}_0 \\ \hat{y}_0 \\ \hat{\dot{y}}_0 \\ \hat{K} \end{bmatrix} = \begin{bmatrix} x_{0,t} \\ \dot{x}_{0,t} \\ y_{0,t} \\ \dot{y}_{0,t} \\ K_t \end{bmatrix} + \begin{bmatrix} \epsilon_x \\ \epsilon_{\dot{x}} \\ \epsilon_y \\ \epsilon_{\dot{y}} \\ \epsilon_K \end{bmatrix} + \begin{bmatrix} \frac{\delta a_x (l-2)(l-1)T^2}{6l(9l-4)} \\ -\frac{5\delta a_x (3l-2)(3l+1)T}{12(18l^2+l-4)} \\ \frac{1}{12}\delta a_y \frac{(l-1)}{l} T^2 \\ -\frac{\delta a_y T}{2} \\ \frac{35\delta a_x l^2}{(18l^2+l-4)T} \end{bmatrix}. \tag{4.8}$$

The first two columns on the right hand side indicate the sum of the true initial states and the weighted sum of measurement errors, i.e., the solution that would have been obtained in the absence of unmodeled dynamics. The third column is the error added to the solution due to the unmodeled

dynamics. Of particular significance is the estimated force coefficient $\hat{K}$, that ends up absorbing errors only in a_x. If the measurement errors are ignored, the aliasing error in the force coefficient K can be written from Eq. 4.8 as,

$$\hat{K} = K_t + \frac{35\delta a_x l^2}{(18l^2 + l - 4)T}. \tag{4.9}$$

The aliasing error in the force coefficient due to the unmodeled dynamics adversely affects predicted states. If the prediction error in $x(t)$ without unmodeled dynamics, i.e., purely due to measurement noise, is given by $\delta x(t)$ and the additional prediction error due to unmodeled dynamics is given by $\delta x_u(t)$, the overall prediction error can be computed as follows,

$$\begin{aligned}
\delta x_p(t) &= x_{p,t}(t) - \hat{x}_p(t) \\
&= \delta x(t) + \delta x_u(t) \\
&= \delta x(t) - \frac{\delta a_x (l-2)(l-1)T^2}{6l(9l-4)} + \frac{5\delta a_x (3l-2)(3l+1)T}{12(18l^2+l-4)}t + \delta a_x \frac{t^2}{2} + \frac{35\delta a_x l^2}{(18l^2+l-4)T}\frac{t^3}{6}.
\end{aligned} \tag{4.10}$$

Similarly, the error in y is given by,

$$\delta y_p(t) = \delta y(t) - \frac{1}{12}\delta a_y \frac{(l-1)}{l}T^2 + \frac{\delta a_y T}{2}t + \delta a_y \frac{t^2}{2}. \tag{4.11}$$

Eq. 4.10 clearly indicates the additional error introduced due to unmodeled dynamics. The important point to be noted here is that in the absence of aliasing error in K given by Eq. 4.9, the prediction error due to the unmodeled dynamics would have been smaller since the last term would have been zero in Eq. 4.10. It is instructive to understand the implications of this example by visualizing the prediction error due to unmodeled dynamics, both with and without aliasing error in K (Eq. 4.9). Assuming measurement noise to be zero, i.e., $\delta x(t) = 0$, and $\delta a_x = 10^{-8}$ m/s^2, $\delta a_y = 10^{-8}$ m/s^2, $l = 8640$ and $T = 86400$ s, the errors in the state estimates are given in Table 4.1. The error in the state estimates in x are smaller than in y even though the unmodeled accelerations are equal in both directions. The filter adjusts all the estimated states in order to compensate for the unmodeled dynamics. Since there are more states being estimated in the x-direction, the estimation errors are reduced in x and $\dot{x}_0$ compared to y. The prediction errors

in both the directions are plotted in Fig. 4.2. The figure clearly demonstrates the degradation in prediction due to aliasing errors. The prediction errors are higher in the presence of unmodeled dynamics when a force coefficient is being estimated.

State (error)	**Value**
x_0 (m)	1.382
$\dot{x}_0$ (m/s^2)	-1.8e-4
y_0 (m)	6.220
$\dot{y}_0$ (m/s^2)	-4.3e-4
K (m/s^3)	2.25e-13

Table 4.1: State estimation errors due to unmodeled dynamics

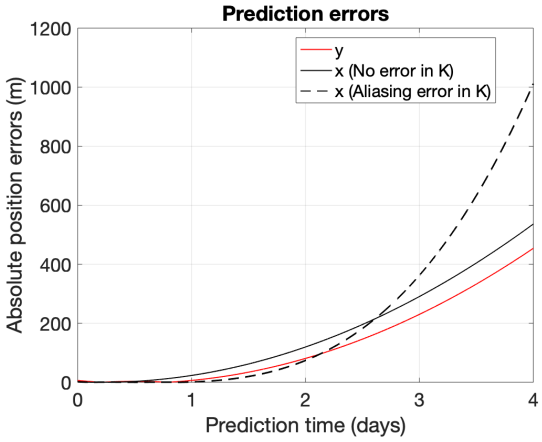

Figure 4.2: Prediction errors in x and y-directions due to unmodeled dynamics

A few important points can be noted from this analytical example. First, only the dynamics error in the x-direction (δa_x) affects the estimated force coefficient K, with no effects from δa_y. Therefore, only the dynamics errors acting in the same direction as the force coefficient affects its estimate. Second, the prediction errors due to unmodeled dynamics are larger for $x_p(t)$ compared to $y_p(t)$ due to errors introduced in the coefficient K, even if $\delta a_x = \delta a_y$. Therefore, even if the effects of δa_x on $\hat{x}_0$ and $\hat{\dot{x}}_0$ are small enough to be neglected, the prediction errors are amplified due to the introduction of additional unmodeled dynamics through $\hat{K}$ that has a cubic growth with time. Due to aliasing effects, the errors in predicted states in the presence of unmodeled dynamics are larger than expected when force coefficients are estimated. It should also be noted from eqs. 4.10-4.11 that with increasing length of the data-arc, the errors in initial positions and velocities increase while the error in the estimated force coefficient decreases. On the other hand, the estimation errors are relatively insensitive to the number of measurements in the data-arc.

From this example, an analogy can be derived for orbit determination, with a_x and a_y representing gravitational acceleration and the unmodeled errors in them similar to ignored higher orders

of the geopotential while K stands for a non-gravitational force coefficient such as drag or SRP. The example sets the context for this study by emphasizing the importance of reducing unmodeled dynamics (higher order gravitational force) in the filter, especially when force coefficients (drag and SRP coefficients) are estimated.

4.3 Simulation setup

In this section, the details of the dynamics model, measurements and filtering methodology used in the study are provided. The true and filter dynamics models in the simulations use the forces summarized in Table 4.2. In the simulations, the geopotential model is taken as EGM2008 and the atmospheric density model is taken as NRLMSISE-00 [93]. The gravitational field is truncated at order 200 for the truth because the force magnitude due to higher orders is negligible as compared to drag and SRP in the altitude regime considered (350-850 km). For example, the average acceleration magnitude of all the gravitational harmonics above order 200 is 10^{-14} m/s^2 in the drag-direction and 10^{-12} m/s^2 in the SRP-direction, compared to 10^{-7} m/s^2 for drag and 10^{-8} m/s^2 for SRP. Also many geopotential models are available up to order 180, such as GRACE-derived models [107]. JPL's DE-430 ephemerides are used for the positions of Sun and Moon [32]. The state vector being estimated in the filter consists of the satellite position, velocity, drag

True dynamics	**Filter dynamics**
200x200 Geopotential	Truncated geopotential
Cannonball atmospheric drag	Cannonball atmospheric drag, C_d is estimated
Cannonball SRP	Cannonball SRP, C_r is estimated
Third-body forces of Sun and Moon	Third-body forces of Sun and Moon

Table 4.2: Forces used in the true and filter dynamics models. EGM2008 is used for the geopotential

coefficient and radiation coefficient. The initial orbital elements are given in Table 8.1. The orbits are assumed to be circular and variation of the coefficients in orbit is ignored. This allows the analysis of errors introduced in the coefficients purely due to unmodeled gravitational force. The

area-to-mass ratio of the satellite is taken as 0.04 m^2/kg for both drag and SRP forces, unless otherwise stated.

GPS position and velocity measurements are assumed to be available every 10 s with noise standard deviations of 1.5 m and 0.5 cm/s respectively in each coordinate. A batch estimator is used to process a data arc of 1 day and the orbits are then predicted for the next three days. The initial errors and standard deviations in the position and velocity are assumed to be 10 m and 0.1 m/s in each coordinate. The initial standard deviation around the coefficients is assumed to be 0.1 while no initial error is considered.

Element	**Value**
e	0
i	90^0
Ω	0^0
u	0^0

Table 4.3: Initial orbital elements of the satellite in study

4.4 Acceleration order of magnitude analysis

In this section, a comparison of higher order gravitational field, drag and SRP acceleration magnitudes is presented. The correlations between a truncated gravitational field and non-conservative forces exist because the unmodeled geopotential has components along the direction of these non-conservative forces. The filter then tries to compensate for the dynamics error introduced due to the truncated geopotential by adjusting the free parameters; the drag and SRP coefficients. In order to compare the acceleration magnitudes, the unmodeled gravitational acceleration is projected along the relative velocity direction in eq. (1.1) and the satellite-Sun direction in fig. 7.8.

$$g_{drag}(t) = \{\boldsymbol{g}_{200\times200}(t) - \boldsymbol{g}_{m\times n}(t)\}.\hat{\boldsymbol{u}}(t), \tag{4.12}$$

$$g_{SRP}(t) = \{\boldsymbol{g}_{200\times200}(t) - \boldsymbol{g}_{m\times n}(t)\}.\hat{\boldsymbol{r}}_s(t). \tag{4.13}$$

where $\boldsymbol{g}_{200\times200}$ is assumed to be the true gravitational acceleration. Fig. 4.3 compares the amplitude spectra of g_{drag} and g_{SRP} (truncated at order 150) with those of drag (a_{drag}) and SRP accelerations (a_{SRP}), respectively, at 350 km. It can be seen that at higher frequencies, the amplitudes of projected gravitational accelerations are comparable to the drag and SRP acceleration even for a truncation order of 150. The instantaneous projected acceleration errors are then averaged over

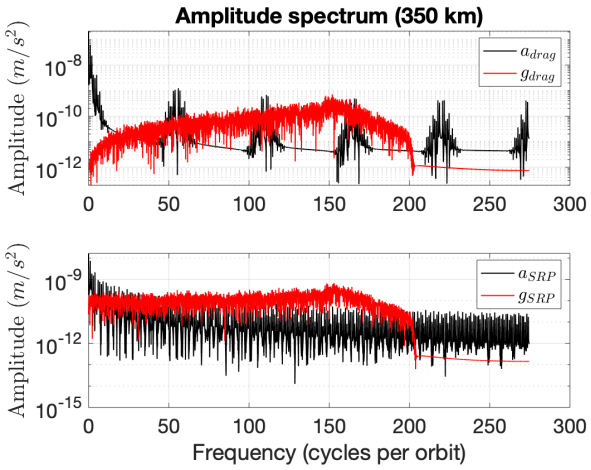

Figure 4.3: Spectra of projected unmodeled gravitational accelerations, drag and SRP accelerations at 350 km altitude

one day, i.e., the length of the estimation data-arc, to obtain the average projected gravitational acceleration errors as follows,

$$\bar{g}_{drag} = \frac{1}{T_{avg}} \int_0^{T_{avg}} g_{drag}(t)dt, \tag{4.14}$$

$$\bar{g}_{SRP} = \frac{1}{T_{avg}} \int_0^{T_{avg}} g_{SRP}(t)dt. \tag{4.15}$$

where T_{avg} denotes one day. Similarly, the drag and SRP acceleration magnitudes are averaged over a day ($\bar{a}_{drag}$ and $\bar{a}_{SRP}$). The average and root-mean-square (RMS) of the instantaneous acceleration errors are plotted in Fig. 4.4 at 350 km and 850 km as a function of truncation order. Since the drag and SRP acceleration magnitudes are independent of the geopotential truncation, they are represented as constant lines in Fig. 4.4. Note that the gravitational acceleration error curve plots the difference between the accelerations due to a 200x200 gravitational field and a gravitational

field truncated at an order specified by the x-axis projected along velocity or sun direction. It is observed that the average gravitational acceleration errors projected along the velocity and Sun directions do not monotonically decrease with the truncation order. This is consistent with the observations of Barker et al. [4] that groups of higher order tesserals can have cancelling effects at low truncation degrees in lower altitudes. At 350 km, the average drag is an order of magnitude larger than the gravitational acceleration error along velocity direction for a 10x10 field and the difference in magnitude increases for higher truncation orders. However, the RMS values of the projected gravitational error are larger than drag until order 90. Similarly, the average SRP is larger than the projected gravitational error after order 60 but the RMS value is lower even at order 100. A similar scenario but with different truncation orders is seen at 850 km. Even though the average gravitational errors become smaller than average drag and SRP at relatively low truncation orders, the instantaneous acceleration errors are comparable until a much higher truncation order. This is the primary reason for the aliasing of unmodeled gravitational accelerations into the estimated drag and SRP coefficients, discussed in the next section.

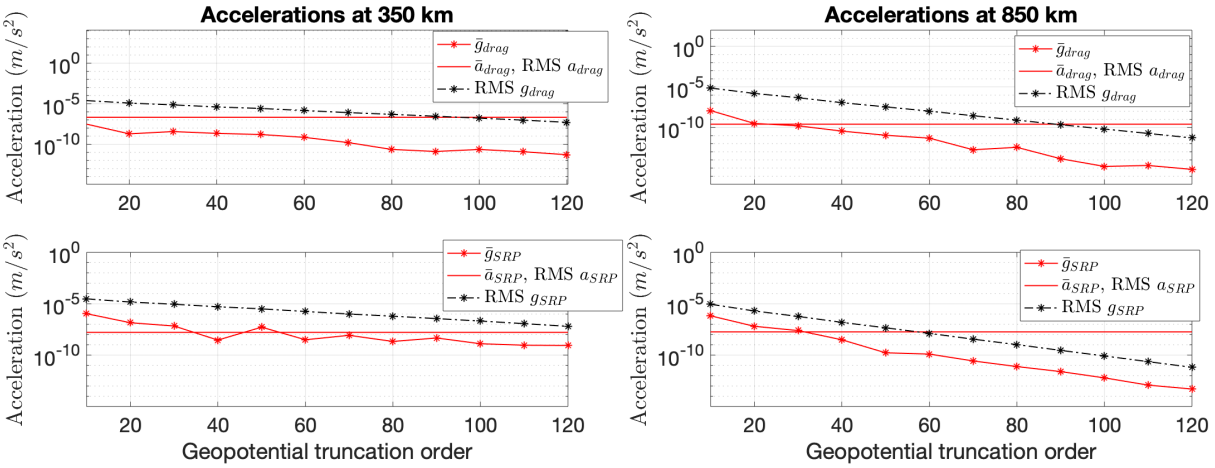

(a) (b)

Figure 4.4: Comparison of average and RMS values of gravitational acceleration errors with drag and SRP accelerations at (a) 350 km and (b) 850 km.

4.5 Coefficient estimates

In this section, the aliasing errors introduced in the coefficient estimates are analyzed as a function of geopotential truncation order and their consequence on orbit prediction is studied. The truth and filter dynamics models from section 4.3 are used to estimate the satellite states and the coefficients of drag and SRP in a batch estimator. The truncation order of the geopotential is varied in the estimator dynamics model and the difference between the true and estimated coefficients noted. The relative errors in the drag coefficient estimate ($\Delta C_d = \frac{C_d - \widehat{C}_d}{C_d}$) and the SRP coefficient estimate ($\Delta C_r = \frac{C_r - \widehat{C}_r}{C_r}$) are plotted in Fig. 4.5 (a) and (b) for altitudes 350 km and 850 km respectively. The coefficient errors exist because of unmodeled gravitational acceleration along drag and SRP directions; therefore the ratio of the average accelerations ($r_{drag} = \frac{\bar{g}_{drag}}{\bar{a}_{drag}}$ and $r_{SRP} = \frac{\bar{g}_{SRP}}{\bar{a}_{SRP}}$) are also plotted in Fig. 4.5. It can be seen that the relative error in the coefficients closely follows the trend of the acceleration ratios. At 850 km, the trends are similar until a certain order and then the coefficient errors plateau. This can be explained by the relationship between the maximum possible estimation accuracy of a force coefficient and the contribution of the force towards orbit propagation. Since the filter adjusts the estimated states based on direct or indirect measurements of the satellite position and velocity, the estimation accuracy of a force coefficient is determined by the sensitivity of the orbit propagation to it. With the orbit being more sensitive to drag at 350 km than at 850 km, the drag coefficient can be estimated to a higher relative accuracy given a high truncation order. The SRP coefficient trends can be similarly explained. The relative error in the coefficients appears quite high for low truncation orders. At 350 km, ΔC_r is much larger than ΔC_d; while at 850 km, they are similar at any given truncation order, as governed by the acceleration ratios.

For orbit determination and prediction, it is important to determine the sensitivity of the orbit propagation to errors in the force coefficients. This allows us to quantify the significance of the coefficient errors based on their effects on orbit propagation. From Fig. 4.5, it seems that the truncation order at 350 km is governed by the SRP coefficient since the relative error is much

higher for SRP than drag at any order. But it should be kept in mind that the SRP acceleration is almost an order of magnitude smaller than drag at that altitude as seen in Fig. 4.4. Therefore, a smaller relative error in drag compared to SRP might be more significant for orbit prediction. The overall effect of the errors introduced in these coefficients towards orbit propagation should determine the truncation order of the geopotential. To analyze the effect of a certain relative error on the orbit accuracy, a sensitivity analysis is performed. The drag and SRP coefficients are perturbed individually and the orbit is propagated for three days. The position error RMS value with respect to the orbital altitude is plotted in Fig. 4.6 (a) and (b) for C_d and C_r respectively. Note that when one coefficient is perturbed, the other is kept constant and that C_r is perturbed by a hundred times higher relative error than C_d. It can be seen that the effect of ΔC_d is higher than ΔC_r at all altitudes. The contribution of ΔC_r to the position error increases slowly with altitude since SRP does not change significantly in a low LEO regime while the contribution of ΔC_d drops exponentially because of atmospheric density. Fig. 4.6 can be used to determine the minimum geopotential truncation order at 350 and 850 km. For example, at 350 km, a 0.1 % error in C_d results in a position error RMS of 10 m at the end of three days as seen in Fig. 4.6 (a). From Fig. 4.5 (a), in order to reach a 0.1 % , i.e. 10^{-3} relative error, a minimum order of 90 is required. It should be noted that the errors in Fig. 4.6 are purely due to propagation with no other error than the coefficients. In an actual orbit determination scenario, the errors will be much higher since the estimated initial state will have errors and both the coefficients will be perturbed from their true values along with any other modeling errors.

4.6 Sensitivity analysis

In this section, the sensitivity of the aliasing effect to several factors is analyzed. The variation of the non-conservative forces depends on factors such as the solar activity level that change the state of the atmosphere and area-to-mass ratio (AMR) that determines the magnitude of the force acting on the satellite. Some factors such as orbital elements also govern the gravitational force acting on the satellite. The extent of correlations between the forces can change according to these

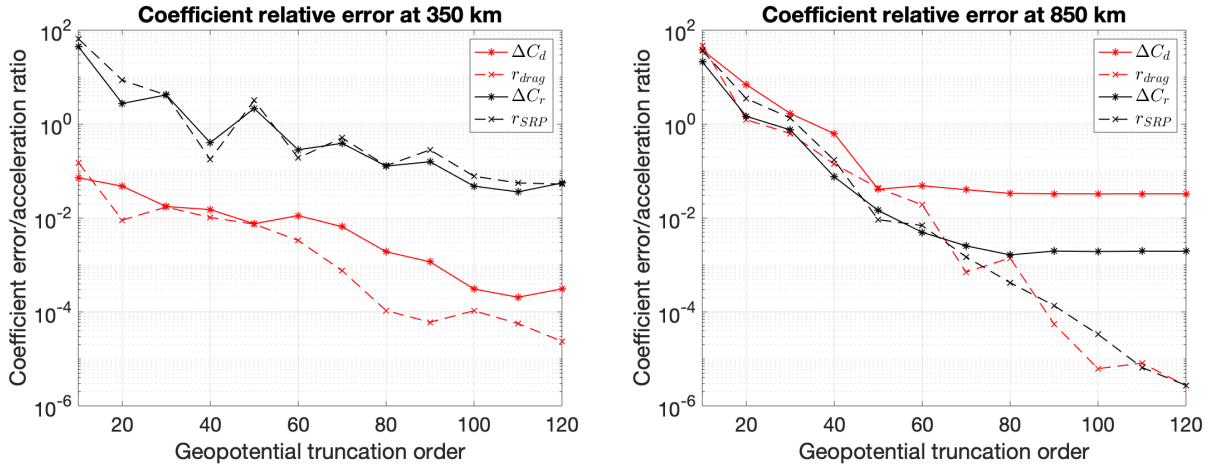

(a) (b)

Figure 4.5: Relative errors in the drag and SRP coefficient estimates as a function of the truncation order of the geopotential in the filter at (a) 350 km and (b) 850 km.

conditions. In addition, factors such as the length of the data-arc can change the aliasing errors in the estimated states and parameters even though they do not affect the forces. Therefore, it is valuable to understand how the trend of estimation error in the coefficients changes with these factors. Specifically, the change in the truncation order required to obtain a certain accuracy in the estimated coefficients due to these factors needs to analyzed. In the following discussions, the parameters are changed in both the true and filter dynamics models, i.e., there's no dynamics mismodeling other than gravitational force.

4.6.1 Orbit inclination

As seen in the previous sections, the correlations are highly dependent on the altitude of the satellite since it changes the relative magnitude of the forces. Since the drag coefficient changes with altitude and therefore, eccentricity of the orbit, a constant cannonball coefficient will not suffice for a highly eccentric orbit. It becomes non-trivial to analyze the aliasing into the drag coefficient estimate in such a case since there's no 'true' cannonball drag coefficient. The aliasing effect with high-fidelity models of the drag coefficient would be more appropriate in that case. In this study, the correlations are studied only for a circular orbit, for which orbital inclination is an

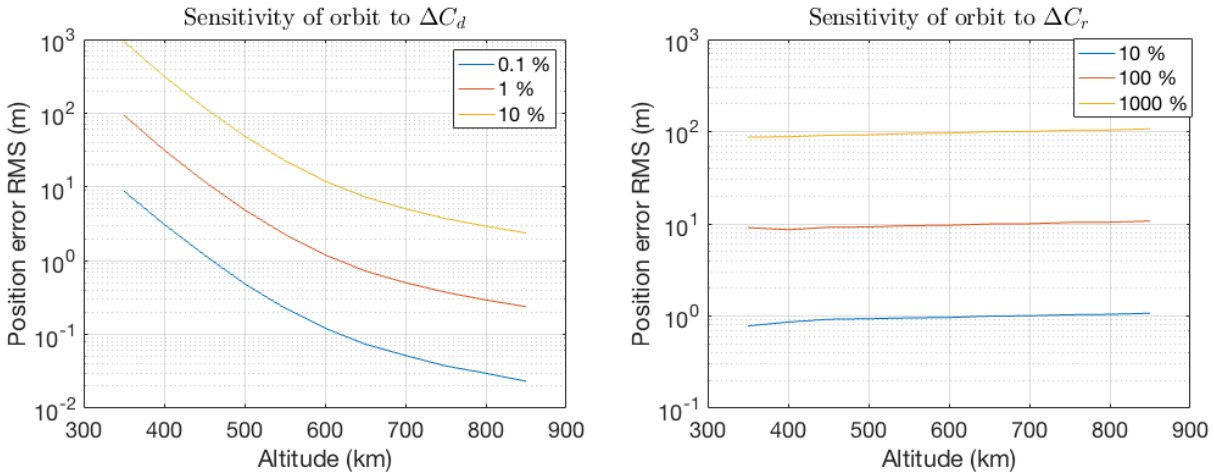

(a) (b)

Figure 4.6: The sensitivity of orbit propagation to errors in (a) drag coefficient and (b) SRP coefficient.

important governing factor that determines the nature of the forces, especially gravitational force. Until now, all the analyses have been carried out for a polar orbit. The drag and SRP coefficient estimation errors as a function of geopotential truncation order for a near-equatorial orbit with an inclination of 15^0 and a polar orbit at 350 km are plotted in Fig. 4.7 (a). Fig. 4.7 (b) plots the maximum prediction error at the end of three days, obtained by propagating the initial state estimate forward. The error trends are similar for both the inclinations but ΔC_d is smaller for the near-equatorial orbit than the polar orbit. This is because, near the equator, the altitude from the surface is smaller than at the poles for the same semi-major axis. Therefore, the drag force is larger due to the increased density leading to a decrease in the ratio of the average accelerations (r_{drag}) that governs ΔC_d as seen in section 4.5. Even though the drag coefficient has a smaller relative error for the near-equatorial orbit, the prediction errors are quite similar for both the orbits since the orbit propagation is proportionately more sensitive due to an increased drag force.

4.6.2 Solar activity level

The atmosphere is highly sensitive to the solar activity level, and atmospheric density can change by orders of magnitude in response to a change in the same. During times of high solar

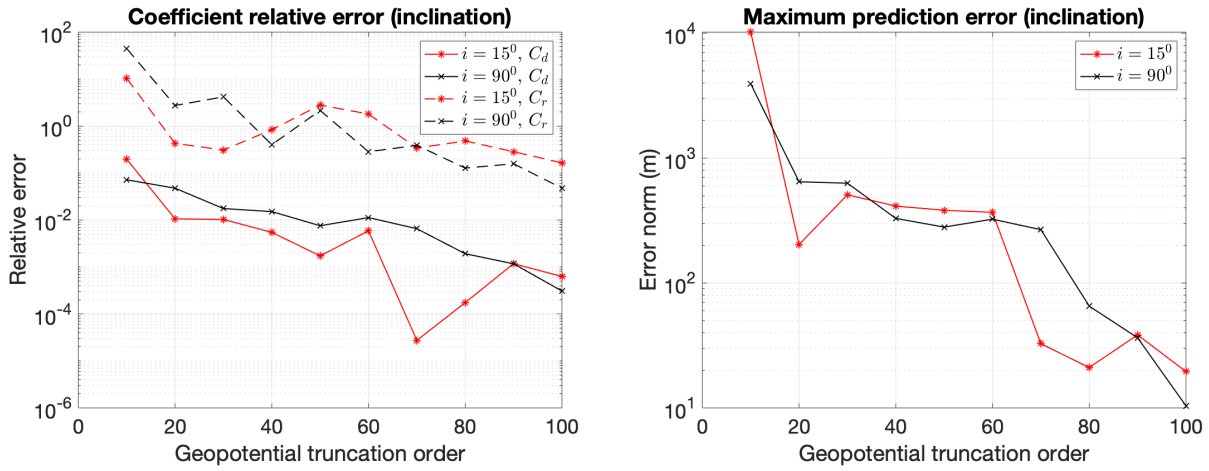

(a) (b)

Figure 4.7: (a) Relative error in the estimated coefficients; (b) Maximum error in the predicted orbits at the end of three days for two orbital inclinations at 350 km.

activity, expansion of the atmosphere leads to an increased density at all altitudes. This changes the relative magnitude of drag with respect to gravitational force, i.e. the correlation between the forces. On the other hand, SRP is relatively unaffected since the change in the total solar irradiance is only 0.1-0.2 % in a solar cycle [133]. Therefore, for different solar activity levels, the error in the drag coefficient can change by almost an order of magnitude while the radiation coefficient error remains almost the same as seen in Fig. 4.8 (a). For a higher solar activity level, the magnitude of atmospheric drag force is larger. As r_{drag} decreases, the drag coefficient relative error decreases as discussed in section 4.5. But this does not lead to a decrease in the prediction error as seen in Fig. 4.8 (b), due to an increased sensitivity of the orbit to the drag coefficient.

4.6.3 Area-to-mass ratio (AMR)

The magnitude of the non-conservative forces acting on the satellite is directly proportional to the AMR in the direction of that force. The estimation errors in the coefficients are plotted for three AMRs in Fig. 4.9. The figure also shows the maximum prediction errors at the end of three days. The relative error in the coefficients scale inversely with the AMRs since the average acceleration ratios (r_{drag} and r_{SRP}) decrease with increased AMR. But as discussed for orbit inclination and

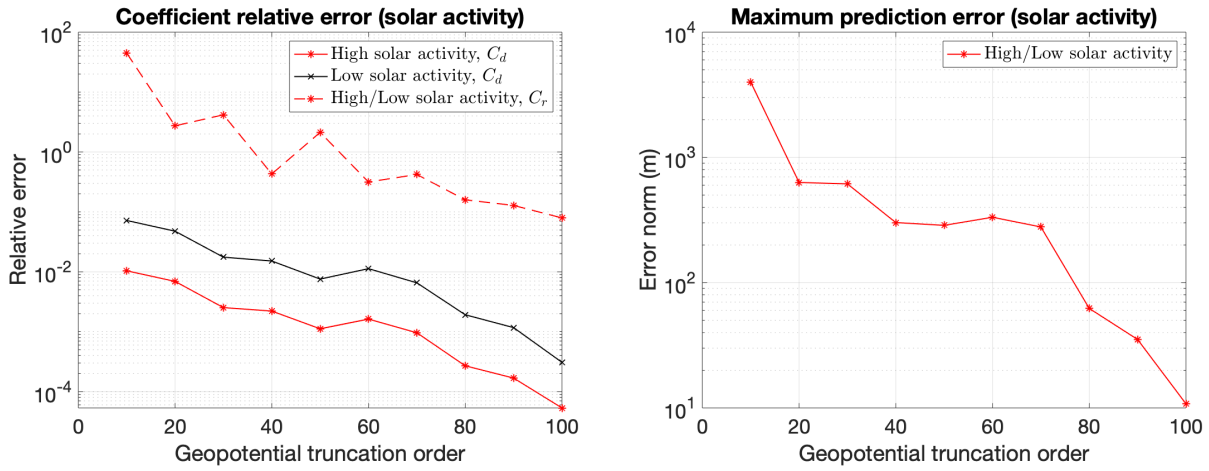

(a) (b)

Figure 4.8: (a) Relative error in the estimated coefficients; (b) Maximum error in the predicted orbits at the end of three days at 350 km during high solar activity (F10.7 = 200 s.f.u) and low solar activity (F10.7 = 65 s.f.u)

solar activity level, even though the relative error is smaller for a higher magnitude force, the sensitivity of the orbit propagation to the coefficient is larger. This can be seen in the position error plot where the error curves are similar for all the AMRs.

4.6.4 Data-arc length and number of measurements

In section 4.2, one of the points illustrated by the example was that the aliasing error in the coefficients decreases with a larger data-arc length. On the other hand, it was the opposite for the aliasing error in the initial position and velocity. In order to verify if the same holds true for unmodeled gravitational acceleration in orbit determination, several arc-lengths between 0.05 days and 10 days of measurements is processed with an order 50 gravitational model in the batch estimator. Fig. 4.10 plots the coefficient errors, the initial state errors and the maximum error at the end of three days of prediction with respect to the length of the data-arc. After an initial increase in error, the errors in the coefficients decrease with longer data-arcs until a certain point while the errors in the initial position and velocity keep increasing. The prediction error initially follows the drag coefficient error trend but gradually flattens out for longer data-arcs. Therefore,

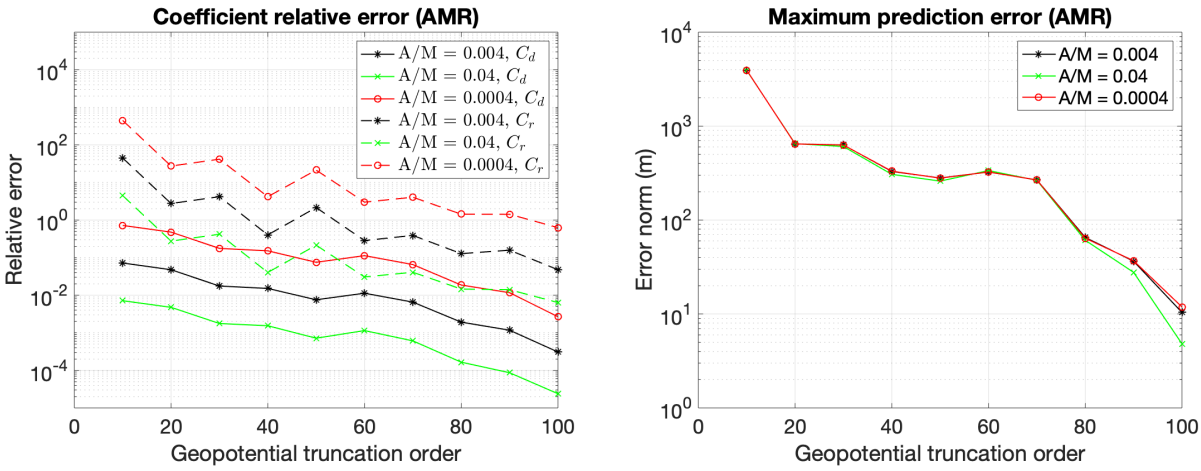

(a) (b)

Figure 4.9: (a) Relative error in the estimated coefficients; (b) Maximum error in the predicted orbits at the end of three days at 350 km for three satellite area-to-mass ratios (units: m^2/kg)

a trade-off lies between errors in the initial states and force coefficient errors when increasing the length of the data-arc in the presence of unmodeled dynamics. In section 4.2, it was also seen that the estimation errors are insensitive to the number of measurements if the length of data-arc is kept constant. In other words, increasing the number of measurements per unit time, i.e., the temporal measurement density, does not change the estimation errors. This is numerically tested by increasing the number of measurements in a 1-day data-arc in the batch estimator with an order 50 gravitational model. As seen in Fig. 4.11, the errors don't change with the number of measurements.

4.7 Non-square gravitational field

In this section, the effects of higher order tesseral terms on the coefficient relative errors are analyzed. It has been pointed out in literature that a non-square geopotential can sometimes be more beneficial for orbit propagation than a square geopotential [127, 4], i.e. higher-degree zonal terms have more contribution towards the propagation than higher order tesseral terms. In order to investigate if the same holds true for the aliasing effect with drag and SRP coefficients, geopotential model order is fixed at 40 and the degree is increased from 40 to 90 in the filter. Fig. 4.12 plots the

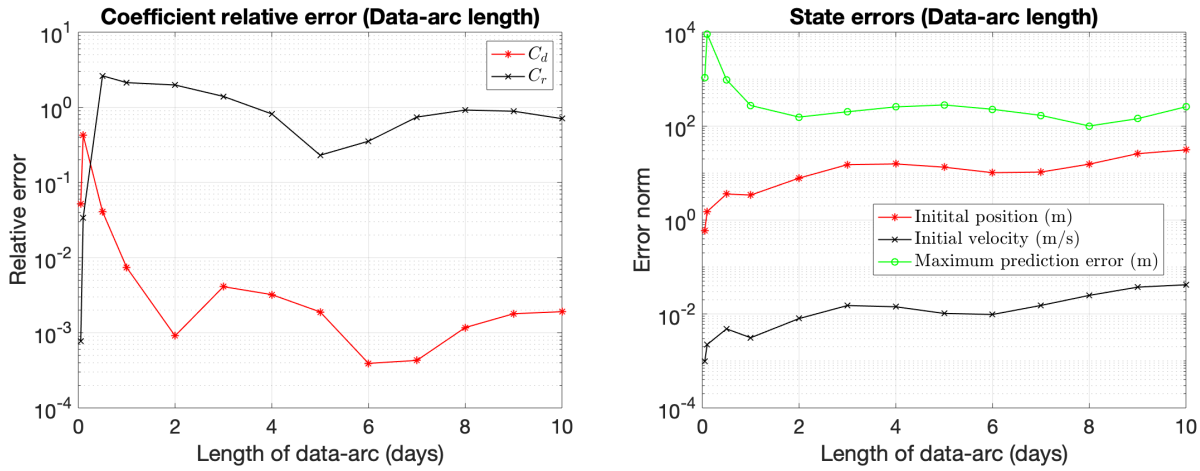

(a) (b)

Figure 4.10: (a) Relative error in the estimated coefficients; (b) Maximum error in the predicted orbits at the end of three days of prediction (right) at 350 km with respect to the length of the data-arc.

coefficient relative errors and maximum prediction error as a function of the zonal degree truncation. It can be seen that even though the maximum prediction error keeps decreasing until order 70 and then reaches a steady state, the errors in the coefficients increase slightly. Therefore, the advantage of increasing the geopotential degree is limited for a low truncation order. Next, all the zonal terms (i.e. until degree 200) are included and the tesseral terms are truncated in the filter gravitational field model. The relative errors in the estimated coefficients are plotted in Fig. 4.13 as a function of the tesseral order truncation. The relative error in the SRP coefficient becomes almost constant after order 50 but the drag coefficient error keeps decreasing. The maximum prediction error also does not seem to reach a steady state and keeps decreasing for higher tesseral orders. Therefore, a non-square field does not seem to be advantageous when drag and SRP coefficients are being estimated.

4.8 Coefficient Error Maps

In this section, the relative errors in drag and SRP coefficients are mapped out across the low-altitude LEO regime. In section 4.5, it was observed that in order to obtain a certain accuracy

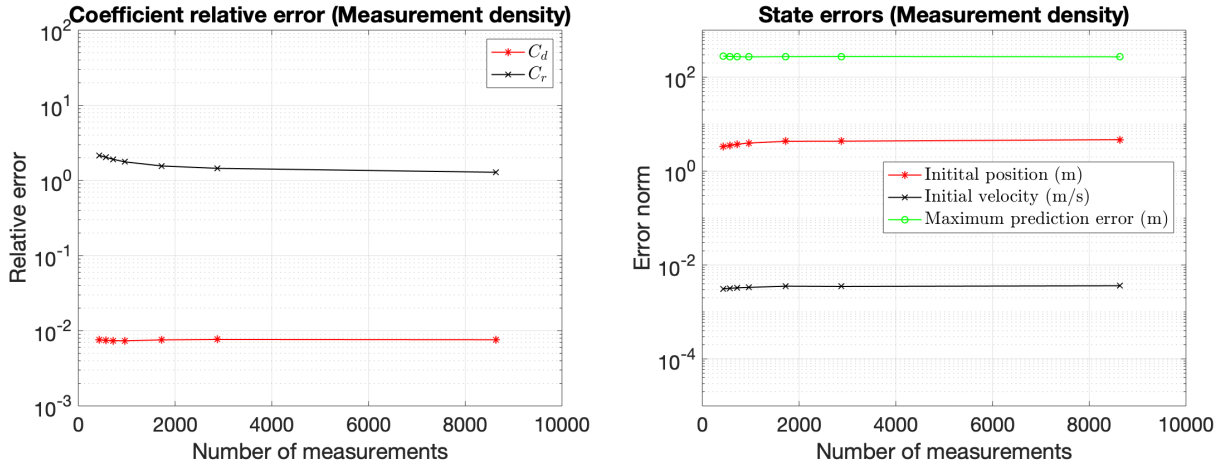

(a) (b)

Figure 4.11: (a) Relative error in the estimated coefficients; (b) Maximum error in the predicted orbits at the end of three days of prediction (right) at 350 km with respect to the temporal density of measurements.

in the coefficient estimates, the required geopotential truncation order is dependent on the satellite altitude. Based on the analyses detailed in the preceding sections, it is proposed to select the truncation order for an orbital regime based on the error introduced into the coefficients at that particular altitude and consequently their effect on orbit propagation. In order to aid the selection process, drag and radiation coefficient estimation error maps are constructed in the altitude range of 350-850 km at every 50 km with truncated gravitational field models. It should be noted that the true drag coefficient increases with altitude while the true SRP coefficient remains the same. The coefficient relative error percentages are plotted in Figs. 4.14 (a) and (b). From the drag coefficient error map, it is apparent that the relative errors are much larger at higher altitudes. But as pointed out in section 4.5, the orbit propagation is more sensitive to errors in the drag coefficient at lower altitudes. Therefore, an inaccurate drag coefficient has a more significant effect on the orbit propagation at lower altitudes. This is demonstrated by the maximum propagation error at the end of three days corresponding to the relative errors in each coefficient in Figs. 4.14 (c) and (d). It should be noted that the only error in propagation is due to an inaccurate coefficient (drag or SRP) from Fig. 4.14(a) and (b). From Figs. 4.14 (c) and (d), it is evident that even though

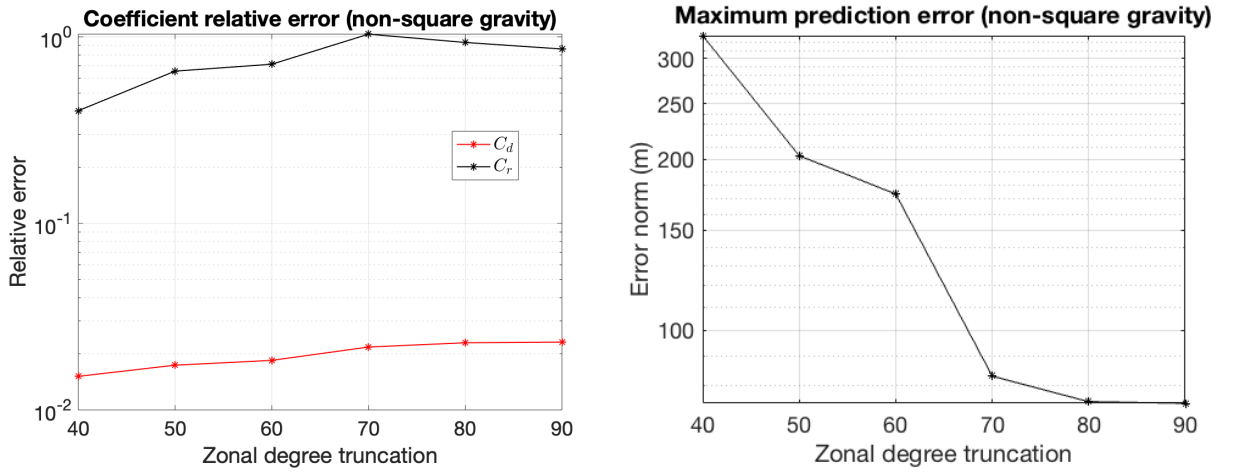

(a) (b)

Figure 4.12: (a) Relative error in the estimated coefficients; (b) Maximum error in the predicted orbits at the end of three days at 350 km with tesseral terms fixed at order 40

the relative error in the SRP coefficient is higher than in the drag coefficient at lower altitudes, the errors in orbit propagation are dominated by the latter.

Finally, it is important to look at the overall errors introduced in orbit determination and prediction due to the aliasing effects since they govern the selection of the geopotential truncation order. Fig. 4.14 (e) and (f) depict the maximum prediction error of the estimated states at the end of three days and the total RMS of orbit determination and prediction position errors. The trends are very similar to Fig. 4.14 (c) and (d), which is expected since the orbit determination and prediction errors are driven by the aliasing effects. It is evident that a larger truncation order is needed at lower altitudes compared to higher altitudes. For example, a truncation order of 80 at 350 km would yield an error magnitude similar to that obtained by a truncation order of 40 at 850 km. It should be noted that the orbit determination and prediction errors here are purely due to aliasing effects and do not account for unmodeled errors in other parameters such as density that are present in an actual orbit determination scenario. Therefore, these errors should be kept small by selecting an appropriate geopotential truncation order. The truncation order selection is suggested to be such that the maximum prediction error at the end of three days is less than 10 m for all higher orders. This translates to order 90 at 350 km and order 50 at 850 km. It should be noted that

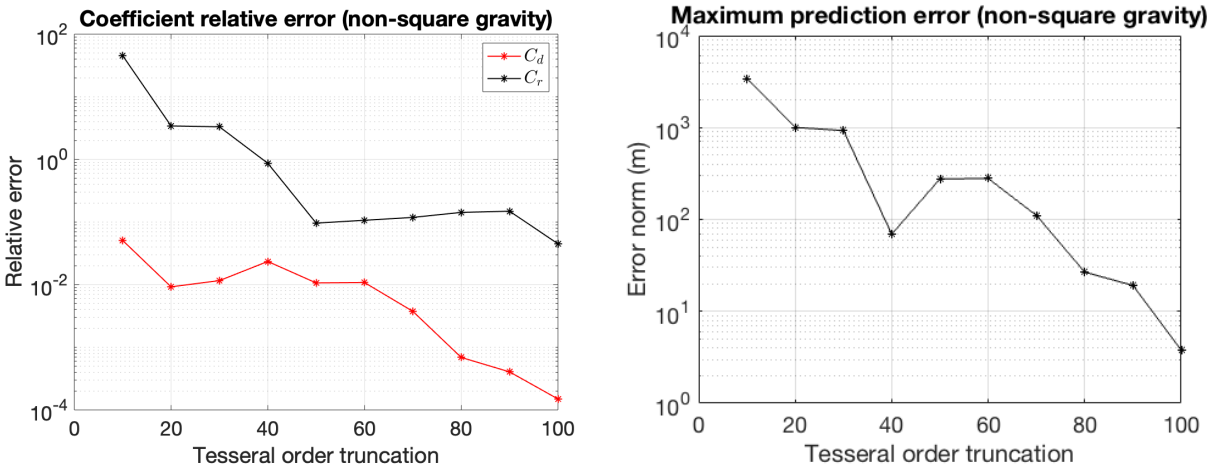

(a) (b)

Figure 4.13: (a) Relative error in the estimated coefficients; (b) Maximum error in the predicted orbits at the end of three days at 350 km with all the zonal terms included

the recommended truncation orders are smaller than the maximum meaningful expansion order of the geopotential model, defined as the order after which the truncation errors are equal or smaller than the intrinsic uncertainty of the model as governed by the standard deviation of the spherical harmonic coefficients [31]. The maps in Fig. 4.14 can be referenced for selecting geopotential truncation order across the low LEO altitude regime according to the level of accuracy needed for specific applications.

4.9 Corroboration using real data

In this section, the aliasing errors in the non-gravitational force coefficients are analyzed for real data. The analyses using simulated data in the previous sections revealed the extent of aliasing errors due to higher order gravitational accelerations. In a real orbit determination scenario, these errors will get coupled with other unmodeled dynamics such as uncertainties in atmospheric density. Moreover, the drag and SRP coefficients will vary due to changes in attitude and ambient parameters. But for the purpose of our analyses, the coefficients are estimated as constants in orbit determination.

The twin GRACE satellites are at 89^0 inclined orbits initially launched at around 485 km,

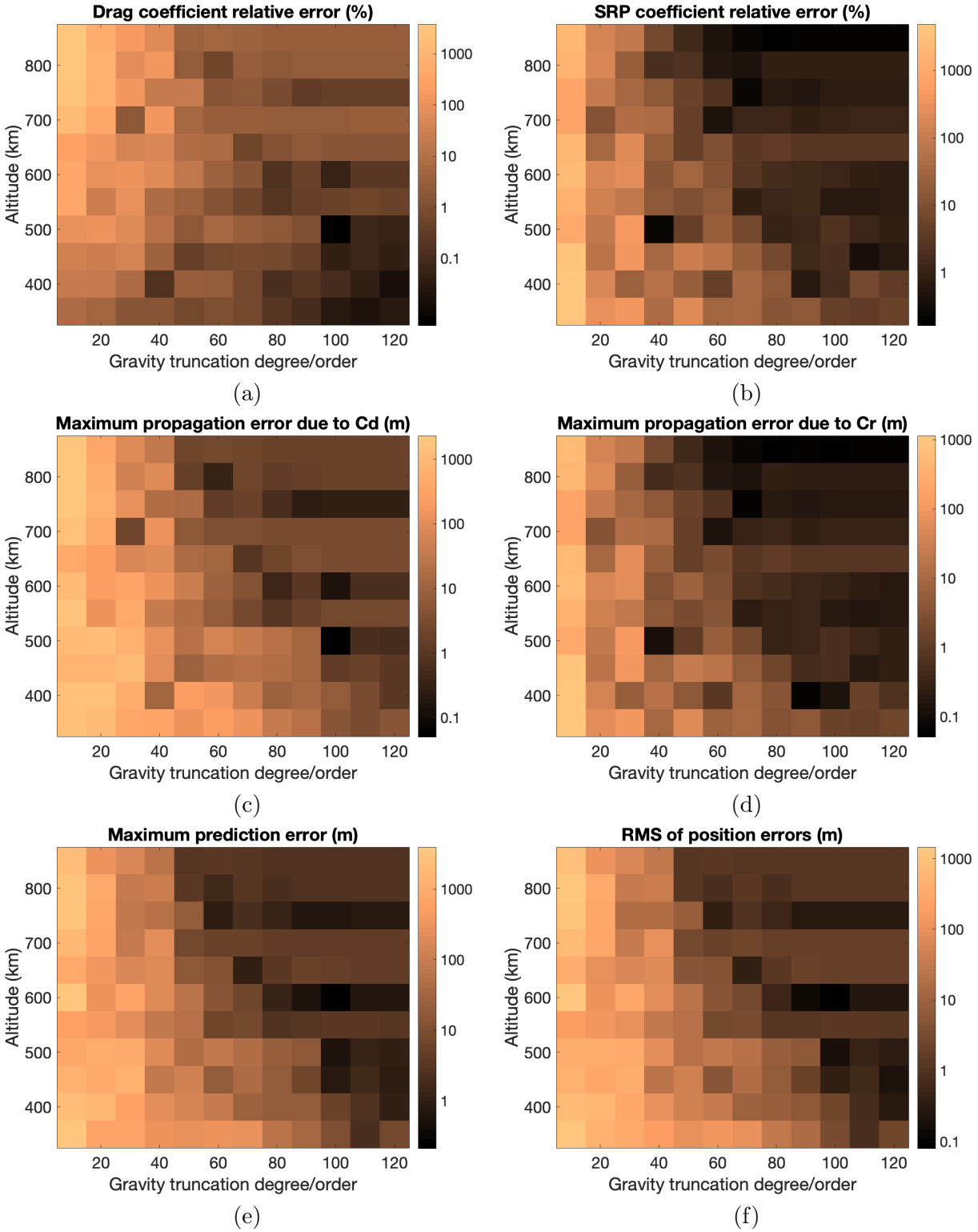

Figure 4.14: (a), (b) Error maps of coefficients; (c), (d) Error maps of errors in propagation due to individual coefficient errors; (e), (f) Total orbit prediction errors

decaying to around 300 km five years after launch. Precision orbit data (POD) or Level 1B navigation data for GRACE B satellite, available through GeoForschungsZentrum Potsdam Information System and Data Center (GFZ ISDC) (`ftp://isdcftp.gfz-potsdam.de/grace/Level-1B/JPL/INSTRUMENT/RL02/`, last access: Dec 3, 2019) are used as the truth for this work. GPS measurements are generated by adding Gaussian noise with standard deviation 1.5 m in all three position coordinates and 0.5 cm/s in all three velocity coordinates. The same forces as Table 4.2 are used to process the real data but densities and reference cross-sectional areas derived by Mehta et al. [73] are used instead of NRLMSISE-00 in order to reduce the uncertainties due to atmospheric density. A one-day data arc from March 24, 2007 is processed in the batch estimator and the orbit is predicted for the next three days. In order to compute the errors in the drag and SRP coefficients, 'true' constant values for the coefficients are needed. Since there are no 'true' cannonball drag and SRP coefficients due to their time-varying nature in orbit, the relative errors at each order of geopotential is calculated with respect to the estimates obtained with an order 200 geopotential. The coefficient estimates obtained in this manner are essentially free of aliasing errors due to gravitational field and therefore serve as a baseline for comparison purposes. However, it is also possible to obtain a cannonball estimate of the coefficients based on physics of the gas-surface and photon-surface interactions. Due to the significant efforts by researchers in accurate modeling of non-conservative forces acting on GRACE [25, 73, 15, and others], estimates of time-varying drag coefficients as well as optical properties of the satellite surfaces have been reported in literature. Mehta et al. [73, 72] have derived time-varying estimates of the drag coefficient using response surface modeling to interpolate results of Test Particle Monte Carlo (TPMC) simulations. A cannonball physics-based estimate that serves as the reference truth for calculating aliasing errors in the drag coefficient can then be obtained by averaging the time-series. The cannonball estimate of the SRP coefficient requires a bit more analysis since the actual SRP force doesn't align with the Sun-satellite direction at all times unlike the cannonball model. The SRP force for GRACE can be calculated using eq. (3.29). Using the specifications for each panel given by Cheng et al. [15], the true SRP force can be calculated at each point in the orbit. The cannonball estimate at time t can

be obtained by projecting Eq. 3.29 and Eq. 7.8 along the Sun-satellite direction and taking their ratio, as follows,

$$C_{r,t}(t) = \frac{\boldsymbol{a_{SRP,\,GRACE}}\cdot\hat{\boldsymbol{r}}_{\boldsymbol{s}}}{\boldsymbol{a_{SRP}}\cdot\hat{\boldsymbol{r}}_{\boldsymbol{s}}}. \tag{4.16}$$

Note that the scale factor C_{srp} in Eq. 3.29 is taken as 1 and the reference area in Eq. 7.8 is taken as 2.24 m^2. The time-series of the physics-based drag coefficients calculated by Mehta et al. [73] and SRP coefficient values obtained by Eq. 4.16 for March 24, 2007 along with their mean values (cannonball estimates) are plotted in Fig. 4.15.

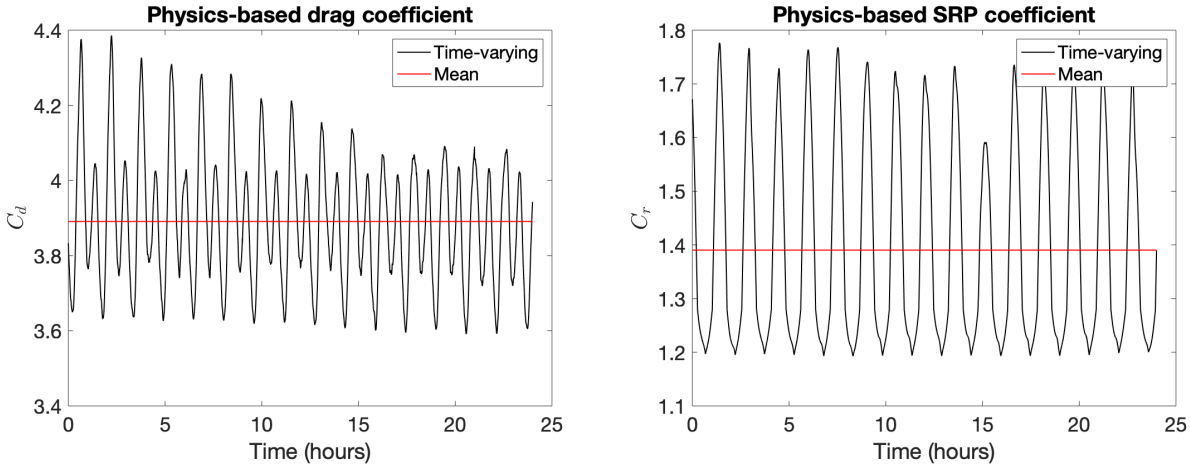

(a) (b)

Figure 4.15: Time-series of coefficients obtained by physics-based models of (a) Drag [73]; (b) SRP

The aliasing errors in the drag (ΔC_d) and SRP (ΔC_r) coefficients along with the corresponding prediction errors for GRACE are then obtained by truncating the geopotential at different orders in the estimator. Fig. 4.16 plots the error in estimated coefficients and the prediction error. Here, prediction error refers to predicted measurement residuals. The coefficient errors are calculated both with respect to the estimates obtained using an order 200 geopotential and the physics-based cannonball estimates. The errors in coefficients obtained by both the methods are consistent with each other until a certain order. Afterwards, the errors with respect to the physics-based truth plateau. This is expected since the cannonball estimates obtained by averaging the physics-based coefficients contain errors due to uncertainties in the models and the averaging process itself. On

the other hand, comparison with the estimates obtained by using order 200 geopotential as the truth essentially nullifies all other sources of error except the geopotential truncation. The results point to an important fact: at lower geopotential truncation orders, estimating the coefficients can be worse than using nominal physics-based models even with the uncertainties associated with the latter. It can be seen that the trends of the coefficient relative errors and the prediction errors are similar to Fig. 4.14, thus serving as a verification for the simulations. The prediction error plateaus to a larger value than Fig. 4.14 (e) due to the presence of other unmodeled errors such as atmospheric density that limit the prediction accuracy.

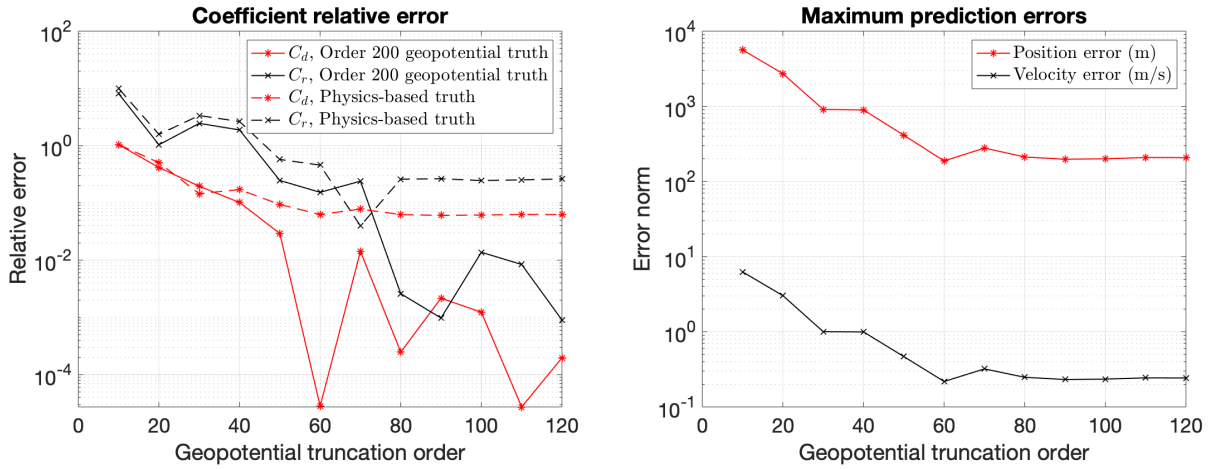

(a) (b)

Figure 4.16: (a) Relative error in the estimated coefficients; (b) Maximum error in the predicted orbits at the end of three days for GRACE

4.10 Chapter summary

In this chapter, the correlations between higher order gravitational forces and the dominant non-conservative forces in the low-altitude low Earth orbit (LEO) regime, i.e., atmospheric drag and solar radiation pressure (SRP) are analyzed. The primary issue with the current method of geopotential truncation based only on orbit propagation errors is that simply considering the contribution of the higher order harmonics towards orbit propagation is not sufficient. The unmodeled gravitational harmonics alias into the free parameters being estimated in the filter, i.e., the drag

and SRP coefficients, due to the presence of ignored gravitational force components along the drag and SRP directions. This leads to higher prediction errors than expected solely from the contribution of unmodeled gravitational force towards orbit propagation as demonstrated analytically with a simple two-dimensional example. The aliasing errors in the force-coefficients are sensitive to factors such as area-to-mass ratio, solar activity and orbit inclination but the prediction errors are relatively unaffected. With larger data-arc lengths, the errors in the estimated coefficients decrease while they increase in the estimated initial states even though the prediction error plateaus. A short data-arc is not recommended in lower altitudes where the orbit is highly sensitive to errors in the drag coefficient.

Based on the results obtained, it is recommended to account for aliasing errors in estimated non-gravitational coefficients while selecting the geopotential truncation order. Relative error maps for the drag and SRP coefficients are presented to serve as a reference while selecting the truncation order in the low-altitude LEO regime. These maps aid the selection of the order based on the amount of orbit determination and prediction error that can be tolerated due to aliasing effects. Since additional errors due to unmodeled forces and parameters such as density are present in an actual orbit determination scenario, it is suggested to reduce the errors due to aliasing effects by selecting an appropriately high truncation order based on the error maps. In order to obtain errors less than 10 m at the end of a three-day prediction arc, an order 90 geopotential should be selected at 350 km and 50 at 850 km for the ideal scenario considered here without additional sources of unmodeled dynamics and measurement errors. For an actual orbit determination scenario, the aliasing errors will be distributed among additional parameters being estimated, such as sensor biases. This may result in different truncation orders than the ones recommended, but the qualitative trends should still hold. Due to these factors, the errors will be higher at the suggested orders of truncation, as demonstrated by the GRACE data analysis. Processing of GRACE data with truncated geopotential models in the estimator serves to corroborate the extent of aliasing errors revealed through simulations. It is observed that estimating force-coefficients with a low order geopotential can potentially be worse than simply using their averaged nominal physics-based

values without estimating them, depending on the uncertainties associated with the physics-based models. Application of the high-fidelity drag-coefficient models developed in the next few chapters to real data should consider the truncation of the geopotential in the filter.

Chapter 5

Estimation-based approach to drag-coefficient modeling

In chapter 1, we discussed the problem with estimating the drag-coefficient as a constant during orbit determination as well as remaining issues with physics-based models of drag-coefficient. A model that can estimate the time-variations in the drag-coefficient from tracking data will lead to better orbit prediction and derivation of physical parameters related to the drag force.

In this chapter, Fourier-series based expansion models are proposed to develop corrections to the standard cannonball model of the drag coefficient of an arbitrary object. Fourier-series models have been used to develop improved approximations of the solar and thermal radiation coefficients [69, 68, 47, 46]. The governing principle of this approach is that any continuous periodic function can be represented by an infinite sum of sines and cosines. The main advantage of this modeling approach is that Fourier coefficients are orthogonal to each other and can be easily estimated in the filter. Moreover, accurate knowledge of gas-surface interaction parameters is not required since the Fourier coefficients estimated during the orbit determination process capture the variations in the drag coefficient governed by these parameters. In fact, the estimates of the Fourier coefficients can be used to provide insights into the variation of gas-surface interaction (GSI) parameters in orbit since each coefficient is associated with a certain frequency of variation.

Four different Fourier models are proposed based on the drag coefficient dependence on: attitude of the satellite and orbit-dependent parameters. As the orientation of the atmospheric flow vector changes w.r.t the different satellite surfaces, the drag coefficient varies. When using the cannonball model, this change in orientation is usually accounted for by taking the instantaneous

cross-sectional area of the satellite as the reference area in Eq. 1.1. But the drag coefficient is not a simple scaling of the cross-sectional area; it is a more complicated function of the orientation of the flow vector w.r.t the different satellite surfaces. We propose a spatial Fourier expansion of the drag coefficient in the body frame of the satellite with the arguments as the azimuth and elevation of the atmospheric flow vector in the body frame. This method, called the body-fixed Fourier (BFF) model, can be used only for satellites whose attitude profiles are known, as is mostly the case with functioning satellites. Though this modeling approach responds to changes in the satellite orientation, it still averages out the variation of the drag coefficient due to ambient parameters, similar to the cannonball model. The second proposed approach remedies this by carrying out a temporal Fourier expansion in the orbit frame of the satellite with the input as the argument of latitude. This approach, called the orbit-fixed Fourier (OFF) model, can capture the periodic components in the drag coefficient variation that are commensurate with the orbital period.

Next, we propose a generic model combining the body-fixed and orbit-fixed approaches called body-orbit double Fourier (BODF) model. The BODF model contains terms corresponding to variations in both orientation and periodic variations in the orbit and therefore is of higher fidelity than the individual body-fixed and orbit-fixed models at any particular order. But because of cross coupling terms between the two arguments, the number of coefficients rapidly increase for higher orders. Along with more computations associated with a higher number of coefficients to be estimated, the orbit determination accuracy can potentially deteriorate with higher orders because of over-fitting with too many free parameters in the filter. One possible fix for the problem is neglecting terms with contributions under a certain threshold but that is specific to the shape model of the satellite and the physics of drag coefficient variation. A more general simplified approach is to neglect all the cross-coupling terms, leading to a body-orbit summation (BOS) model. It should be noted that among the proposed models, only the OFF model does not require any attitude information and thus can be applied to space objects with unknown attitude profiles.

5.1 Chapter outline

The models are tested using simulation cases with different attitude profiles and orbital regimes. For each case, a reference trajectory and true measurements are generated, with drag coefficients modeled using a standard GSIM. A batch least squares estimator is then used to process the measurements with the proposed drag coefficient models incorporated in the filter. The obtained state estimates are then propagated forward to obtain the predicted orbit. Finally, the prediction performance of the proposed models is compared to the cannonball model. In all the drag models, the reference area is considered to be constant. But the performance of the models is also compared to the cannonball model when the reference area is taken to be the instantaneous cross-sectional area as discussed in the preceding paragraph. Section 5.2 details the Fourier-series models and presents a derivation of the quantities that are required to implement the models in a filter. The simulation framework and the example cases are discussed in section 5.3. The application to real tracking data from satellites is discussed in section 5.4.

5.2 Development of Fourier drag-coefficient models

In the dynamics model of an orbit determination filter, the drag-coefficient can be modeled as

$$\widetilde{C_d} = C_{d,nom}(t) + \Delta C_d, \tag{5.1}$$

where $C_{d,nom}(t)$ is a time-varying nominal model of the drag coefficient based on the physics of the problem and ΔC_d is the remaining error in the drag coefficient value that needs to be estimated in the filter. Examples of models that can provide nominal values of the drag coefficient in orbit are the flat plate model with a particular GSIM [25] and RSM [72]. In general, most satellite operators take $C_{d,nom}(t)$ to be zero and estimate ΔC_d as a constant, with a GSIM potentially providing the initial value for the estimate. We propose to expand ΔC_d as a Fourier series in terms of satellite attitude and orbital motion and estimate the Fourier coefficients in the filter. Such a method makes it possible to estimate higher-order variations in the drag coefficient error while using a

high-fidelity nominal value for the drag coefficient. If the nominal model closely represents the true drag coefficient variation and the density errors are small, the estimated Fourier coefficients will ideally go towards zero. Therefore, this approach also allows us to evaluate the accuracy of physics-based drag coefficient models.

5.2.1 Body-fixed Fourier (BFF) model

It can be seen from chapter 2 that the drag coefficient is strongly dependent on the angle between the flow unit vector and the area vector of the satellite face and hence the attitude of the satellite. If the attitude of satellite is known, as is mostly the case with functioning satellites, the drag coefficient variation with attitude can be potentially estimated during the OD process. The unit vector of the flow can be expressed in terms of an azimuthal angle (θ) and elevation angle (ϕ) in the body frame as (Fig. 5.1),

$$\hat{\mathbf{u}} = \cos\phi\cos\theta\hat{x}_b + \cos\phi\sin\theta\hat{y}_b + \sin\phi\hat{z}_b. \tag{5.2}$$

Therefore, the drag coefficient now becomes a function of θ and ϕ which allows us to expand the

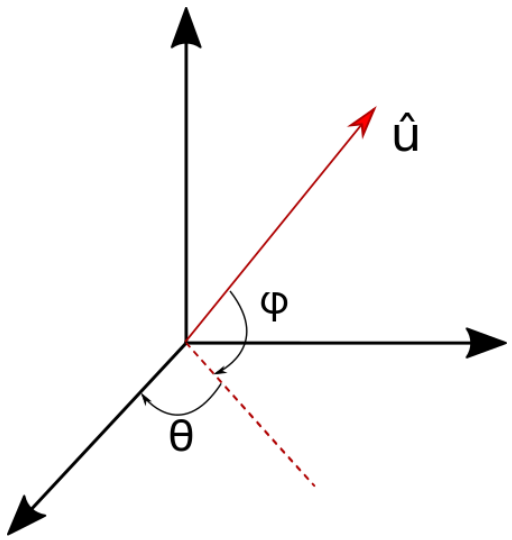

Figure 5.1: Flow unit vector in body frame

drag coefficient as a double Fourier series around θ and ϕ. The double Fourier series expansion is

given by, [98]

$$C_d = \sum_{m=0}^{\infty}\sum_{n=0}^{\infty}\lambda_{mn}(\bar{A}_{mn}\cos m\theta\cos n\phi + \bar{B}_{mn}\sin m\theta\cos n\phi + \bar{C}_{mn}\cos m\theta\sin n\phi + \bar{D}_{mn}\sin m\theta\sin n\phi). \tag{5.3}$$

The Fourier coefficients become the parameters to be estimated during the OD process instead of the drag coefficient. In order to implement the model in the filter, initial estimates (nominal values) of the coefficients and the standard deviation around them are required. The initial estimates can be calculated using the following formulae,

$$\bar{A}_{mn} = \frac{1}{\pi^2}\int_{-\pi}^{\pi}\int_{-\pi}^{\pi} C_d\cos m\theta\cos n\phi d\theta d\phi, \tag{5.4}$$

$$\bar{B}_{mn} = \frac{1}{\pi^2}\int_{-\pi}^{\pi}\int_{-\pi}^{\pi} C_d\sin m\theta\cos n\phi d\theta d\phi, \tag{5.5}$$

$$\bar{C}_{mn} = \frac{1}{\pi^2}\int_{-\pi}^{\pi}\int_{-\pi}^{\pi} C_d\cos m\theta\sin n\phi d\theta d\phi, \tag{5.6}$$

$$\bar{D}_{mn} = \frac{1}{\pi^2}\int_{-\pi}^{\pi}\int_{-\pi}^{\pi} C_d\sin m\theta\sin n\phi d\theta d\phi. \tag{5.7}$$

The value of λ_{mn} is given by,

$$\lambda_{mn} = \begin{cases} \frac{1}{4}, & m = n = 0 \\ \frac{1}{2}, & m > 0, n = 0, \text{or}, n > 0, m = 0 \\ 1, & m > 0, n > 0. \end{cases} \tag{5.8}$$

The integration can be carried out numerically in order to compute initial estimates of the coefficients. To calculate the integrals, a GSIM is selected for C_D along with a shape model for the satellite. The drag-coefficient model doesn't necessarily have to be analytical. For example, direct simulation Monte Carlo (DSMC) [5] can be used to compute the drag-coefficient for varying θ and the resultant drag-coefficient profile can be parameterized in the Fourier series. Alternatively, for

simple shapes, the satellite can be assumed to comprise of multiple flat plates and the analytical drag-coefficients of individual plates can be summed up to arrive at the total drag-coefficient for the satellite [25]. The resultant drag-coefficients of the satellite can then be integrated over the angle of variation of the velocity vector in the body frame using eqs. 5.4 - 5.8 to compute the initial estimates of the Fourier coefficients.

Once the nominal coefficients and their covariance have been computed, the coefficients for the selected order can be added to the state vector to be estimated. It is important to note that since the series is truncated at an arbitrary order, the coefficients will absorb contributions from the higher neglected orders. This is advantageous since a sufficiently low order Fourier series is able to capture the variation in drag coefficient as will be demonstrated by the results. This reduces the computational complexity of the filter. In order to estimate the Fourier coefficients, the following partial derivatives are required. The partial derivatives of the model with respect to the position and velocity are zero since the model is dependent solely on the attitude that is assumed to be given.

$$\frac{\partial C_d}{\partial \boldsymbol{r}} = 0 \tag{5.9}$$

$$\frac{\partial C_d}{\partial \boldsymbol{v}} = 0 \tag{5.10}$$

The partials of the drag coefficient, and therefore the drag force, with respect to the Fourier coefficients are given by

$$\begin{aligned} \frac{\partial \boldsymbol{a_{drag}}}{\partial A_{mn}} &= \frac{\partial \boldsymbol{a_{drag}}}{\partial C_d}\frac{\partial C_d}{\partial A_{mn}} \\ &= -\frac{1}{2}\rho\frac{A_{ref}}{m}v_r^2\hat{\boldsymbol{u}}\cos m\theta\cos n\phi \end{aligned} \tag{5.11}$$

$$\frac{\partial \boldsymbol{a_{drag}}}{\partial B_{mn}} = -\frac{1}{2}\rho\frac{A_{ref}}{m}v_r^2\hat{\boldsymbol{u}}\sin m\theta\cos n\phi \tag{5.12}$$

$$\frac{\partial \boldsymbol{a_{drag}}}{\partial C_{mn}} = -\frac{1}{2}\rho\frac{A_{ref}}{m}v_r^2\hat{\boldsymbol{u}}\cos m\theta\sin n\phi \tag{5.13}$$

$$\frac{\partial \boldsymbol{a_{drag}}}{\partial D_{mn}} = -\frac{1}{2}\rho\frac{A_{ref}}{m}v_r^2\hat{\boldsymbol{u}}\sin m\theta\sin n\phi. \tag{5.14}$$

where the factor λ_{mn} from Eq. 5.8 is absorbed into the coefficients, with $A_{mn} = \bar{A}_{mn}\lambda_{mn}$. For $m = n = 0$, the Fourier model reduces to cannonball model and only Eq. 5.11, with the cosine terms equal to 1, remains.

In many satellites, the dominant attitude variation with respect to the atmospheric flow is around a single axis and any variations around other axes can be effectively neglected for the purpose of drag coefficient computation. For example, the relative velocity vector effectively varies around the axis of angular momentum for an inertially stabilized satellite if the variation due to the co-rotating atmosphere is neglected. It is shown in subsequent sections that the drag coefficient variation due to the co-rotating atmosphere can be effectively ignored without any practical detriment to the orbit prediction accuracy. In such cases where the variation of the relative velocity vector is effectively around a single axis, the BFF model reduces to a single Fourier series around the angle of rotation (θ) as

$$C_d = \sum_{n=0}^{\infty}(\overline{\mathcal{A}}_n\cos n\theta + \overline{\mathcal{B}}_n\sin n\theta). \tag{5.15}$$

where the coefficients are given by,

$$\overline{\mathcal{A}}_n = \frac{1}{\pi}\int_0^{2\pi} C_d\cos n\theta d\theta, \tag{5.16}$$

$$\overline{\mathcal{B}}_n = \frac{1}{\pi}\int_0^{2\pi} C_d\sin n\theta d\theta, \tag{5.17}$$

for $n > 0$ and,

$$\overline{\mathcal{A}}_0 = \frac{1}{2\pi}\int_0^{2\pi} C_d d\theta, \tag{5.18}$$

and $\overline{\mathcal{B}}_0 = 0$ for $n = 0$.

It is possible to derive closed-form expressions for the body-fixed Fourier coefficients of a flat plate for the DRIA model. The velocity vector ($\hat{\boldsymbol{V}}$) is assumed to rotate around y-axis in the body frame for simplicity, with the angle of rotation to the x-axis denoted by θ. Note that a body frame can always be defined in this manner if the velocity vector is assumed to rotate around a single axis. The angle of the vector normal to an arbitrarily inclined plate ($\hat{\boldsymbol{n}}$) with y-axis in the body frame is denoted as β. The projection of the normal vector in the x-z plane ($\hat{\boldsymbol{n}}_{\boldsymbol{v}}$) makes an angle δ with the x-axis. Fig. 5.2 depicts a graphical representation of the scenario. The angle β and δ can be calculated from the known unit normal vector in the body-frame as follows

$$\cos\beta = \hat{\boldsymbol{n}}.\hat{\boldsymbol{y}} \tag{5.19}$$

$$\tan\delta = \frac{\hat{\boldsymbol{n}}.\hat{\boldsymbol{z}}}{\hat{\boldsymbol{n}}.\hat{\boldsymbol{x}}} \tag{5.20}$$

In order to carry out the Fourier expansion of the GSIM, the cosine of angle between $\hat{\boldsymbol{n}}$ and $\hat{\boldsymbol{V}}$, i.e., γ is required. Using the cosine rule in the spherical triangle formed by $\hat{\boldsymbol{n}}$, $\hat{\boldsymbol{V}}$ and $\hat{\boldsymbol{n}}_{\boldsymbol{v}}$,

$$\begin{aligned}\gamma &= \cos(\theta-\delta)\cos(\frac{\pi}{2}-\beta) + \sin(\theta-\delta)\sin(\frac{\pi}{2}-\beta)\cos\frac{\pi}{2} \\ &= \mathcal{C}\cos\psi\end{aligned} \tag{5.21}$$

where $\psi = \theta - \delta$ and $\mathcal{C} = \sin\beta$. The Fourier expansion is carried out around the angle of rotation of the velocity vector, θ. To analytically integrate Eqs. 5.16, 5.17 and 5.18 with C_d given by Eq. 2.2, a few integrals are required as evaluated in appendix A. Using these integrals, the cosine Fourier coefficients for a single plate with the DRIA model can be computed. For the i^{th}

plate inclined at an angle ψ_i to the velocity vector, the Fourier coefficients are given by-

$$\begin{aligned} a_{n,i} &= \frac{1}{2\pi}\int_0^{2\pi} C_d \cos n\psi_i d\psi_i \\ &= \frac{1}{2\pi}\int_0^{2\pi} \frac{A_i}{A_{ref}}\left[\frac{e^{-\gamma_i^2 s_i^2}}{s_i\sqrt{\pi}} + \gamma_i\{1+\mathrm{erf}(\gamma_i s_i)\}\left(1+\frac{1}{2s_i^2}\right)\right. \\ &\left. + \frac{r_i\sqrt{\pi}}{2}\gamma_i^2\{1+\mathrm{erf}(\gamma_i s_i)\} + \frac{r_i}{2s_i}\gamma_i e^{-\gamma_i^2 s_i^2}\right]\cos n\psi_i d\psi_i, \end{aligned} \tag{5.22}$$

$$a_{n,i} = \begin{cases} \frac{A_i}{2\pi A_r}\left[\frac{2\sqrt{\pi}}{s_i}e^{-\frac{s_i^2\mathcal{C}_i^2}{2}}I_0 + 2\left(1+\frac{1}{2s_i^2}\right)\right. & \\ \left.\times\sqrt{\pi}\mathcal{C}_i^2 s_i e^{-\frac{s_i^2\mathcal{C}_i^2}{2}}(I_0-I_1) + \frac{r_i\mathcal{C}_i^2\pi^{3/2}}{2}\right], & n=0, \\ \frac{A_i}{\pi A_r}\left[\left(1+\frac{1}{2s_i^2}\right)\mathcal{C}_i\pi + \frac{r_i\pi}{12}s_i\mathcal{C}_i^3 e^{-\frac{s_i^2\mathcal{C}_i^2}{2}}\right. & \\ \left.\times(9I_0-8I_1-I_2) + \frac{r_i\mathcal{C}_i\pi}{2s_i}e^{-\frac{s_i^2\mathcal{C}_i^2}{2}}(I_1+I_0)\right], & n=1, \\ \frac{A_i}{\pi A_r}\left[\frac{2\sqrt{\pi}}{s_i}e^{-\frac{s_i^2\mathcal{C}_i^2}{2}}I_1 + \left(1+\frac{1}{2s_i^2}\right)\sqrt{\pi}\mathcal{C}_i^2 s_i e^{-\frac{s_i^2\mathcal{C}_i^2}{2}}\right. & \\ \left.\times\left(\frac{3I_0-2I_1-I_2}{3}\right) + \frac{r_i\mathcal{C}_i^2\pi^{3/2}}{4}\right], & n=2, \\ \frac{A_i}{\pi A_r}\left[\frac{2\sqrt{\pi}}{s}e^{-\frac{s_i^2\mathcal{C}_i^2}{2}}I_k + \left(1+\frac{1}{2s_i^2}\right)\sqrt{\pi}\mathcal{C}_i^2 s_i e^{-\frac{s_i^2\mathcal{C}_i^2}{2}}\right. & \\ \left.\times\left(\frac{I_k-I_{k+1}}{2k+1} + \frac{I_{k-1}-I_k}{2k-1}\right)\right], & n=2k, k\in\mathbb{Z}^+-1, \\ \frac{A_i}{\pi A_r}\left[\frac{r_i\pi}{2}s_i\mathcal{C}_i^3 e^{-\frac{s_i^2\mathcal{C}_i^2}{2}}\left(\frac{I_k-I_{k+1}}{2k+1} + \frac{I_{k+1}-I_{k+2}}{2(2k+3)}\right.\right. & \\ \left.\left.+\frac{I_{k-1}-I_k}{2(2k-1)}\right) + \frac{r_i\mathcal{C}_i\pi}{2s_i}e^{-\frac{s_i^2\mathcal{C}_i^2}{2}}(I_{k+1}+I_k)\right], & n=2k+1, k\in\mathbb{Z}^+. \end{cases} \tag{5.23}$$

where I_k is the modified Bessel function of the first kind and $I_k = I_k(-\frac{s^2\mathcal{C}^2}{2})$ is implicit. The sine coefficients can be computed by replacing $\cos n\psi$ by $\sin n\psi$. All the integrals turn out to be 0.

Therefore,

$$\begin{aligned} b_{n,i} &= \frac{1}{2\pi}\int_0^{2\pi} C_d \sin n\psi_i d\psi_i \\ &= \frac{1}{2\pi}\int_0^{2\pi} \frac{A_i}{A_{ref}}\left[\frac{e^{-\gamma_i^2 s_i^2}}{s_i\sqrt{\pi}} + \gamma_i\{1+\mathrm{erf}(\gamma_i s_i)\}\left(1+\frac{1}{2s_i^2}\right)\right. \\ &\left. + \frac{r_i\sqrt{\pi}}{2}\gamma_i^2\{1+\mathrm{erf}(\gamma_i s_i)\} + \frac{r_i}{2s_i}\gamma_i e^{-\gamma_i^2 s_i^2}\right]\sin n\psi d\psi_i \\ &= 0. \end{aligned} \tag{5.24}$$

In order to compute the Fourier coefficients w.r.t θ, it should be recognized that eqs. 5.23 and 5.24 are the Fourier coefficients w.r.t ψ. Therefore,

$$\begin{aligned} C_{d,i} &= \sum_{n=0}^{\infty}(a_{n,i}\cos n\psi_i + b_{n,i}\sin n\psi_i) \\ &= \sum_{n=0}^{\infty}(a_{n,i}\cos n(\theta-\delta_i) + b_{n,i}\sin n(\theta-\delta_i)) \\ &= \sum_{n=0}^{\infty}(a_{n,i}\cos n\delta_i\cos n\theta + a_{n,i}\sin n\delta_i\sin n\theta) \\ &= \sum_{n=0}^{\infty}(\mathcal{A}_{n,i}\cos n\theta + \mathcal{B}_{n,i}\sin n\theta). \end{aligned} \tag{5.25}$$

where

$$\mathcal{A}_{n,i} = a_{n,i}\cos n\delta_i \tag{5.26}$$

and

$$\mathcal{B}_{n,i} = a_{n,i}\sin n\delta_i \tag{5.27}$$

are the Fourier coefficients of the i^{th} plate w.r.t the angle of rotation of the velocity vector. Eqs. 5.23, 5.26 and 5.27 can be used to analytically calculate the Fourier coefficients of the DRIA model for a flat plate with one side exposed to the flow. The Fourier coefficients of both the adsorbate ($C_{d,ads}$) and substrate ($C_{d,s}$) are calculated separately using Eqs. 5.23 and 5.24 that are

then combined using the orientation-independent fraction (f) using Eq. 2.16 to obtain the total Fourier coefficients for the DRIA model. Note that the closed-form expressions are possible for the substrate under the simplifying assumption that the accommodation coefficient does not depend on the inclination of flow to the plate, i.e., Eq. 2.13 is used instead of Eq. 2.14 to calculate the substrate accommodation coefficient.

In order to obtain the total drag-coefficient for the satellite, the drag-coefficients of the individual plates are summed up as follows,

$$\begin{aligned} C_d &= \sum_{i=0}^{N} C_{d,i} \\ &= \sum_{i=0}^{N} \sum_{n=0}^{\infty} (\mathcal{A}_{n,i} \cos n\theta + \mathcal{B}_{n,i} \sin n\theta) \\ &= \sum_{n=0}^{\infty} [(\sum_{i=0}^{N} \mathcal{A}_{n,i}) \cos n\theta + (\sum_{i=0}^{N} \mathcal{B}_{n,i}) \sin n\theta] \\ &= \sum_{n=0}^{\infty} [\overline{\mathcal{A}}_n \cos n\theta + \overline{\mathcal{B}}_n \sin n\theta], \end{aligned} \tag{5.28}$$

where $\overline{\mathcal{A}}_n = \sum_{i=0}^{N} \mathcal{A}_{n,i}$ and $\overline{\mathcal{B}}_n = \sum_{i=0}^{N} \mathcal{B}_{n,i}$ are the total Fourier coefficients of the satellite. In order to validate the analytical Fourier coefficients, the drag-coefficient of an inclined plate is calculated using the DRIA model as well as its BFF expansion with the analytical coefficients. The dependence of the accommodation coefficient on the angle of incidence of the flow is accounted for in the DRIA model (Eq. 2.14) while in the Fourier model, the accommodation coefficient is assumed to be independent of the angle (Eq. 2.13). As seen in Fig. 5.3, the drag-coefficients are nearly identical with the two models.

5.2.2 Orbit-fixed Fourier (OFF) model

Along with being strongly dependent on the attitude of the satellite, the drag coefficient is also a function of ambient parameters like temperature and mean molecular mass as seen in chapter 2. The ambient parameters exhibit a long-period variation along with being dependent of the location of the satellite along its orbit. Therefore, as the satellite orbits from dayside to

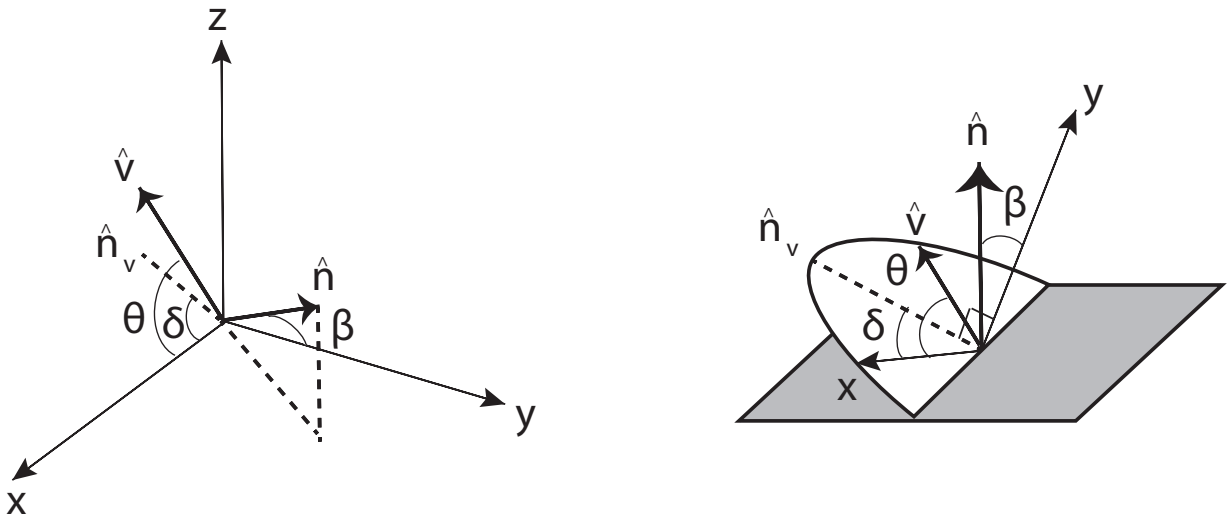

Figure 5.2: Velocity vector and normal vector of an arbitrarily inclined plate in the body frame (left); the same scenario depicted from the perspective of the plate (right)

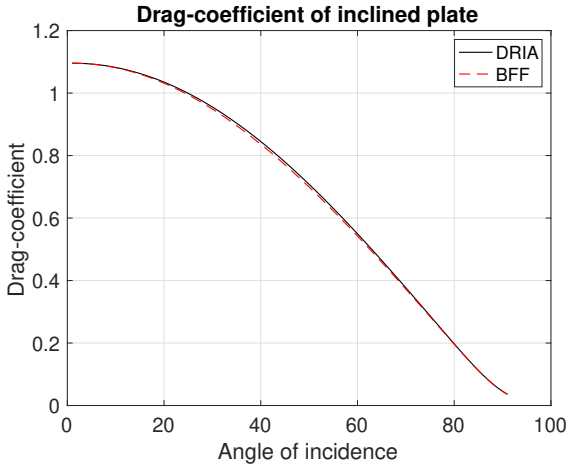

Figure 5.3: Drag-coefficient of an inclined plate using DRIA model and its BFF expansion

nightside and back, the drag coefficient exhibits a short period oscillation corresponding to the orbital motion of the satellite superposed on a long period oscillation corresponding to the rotation of atmosphere. The period of the short period oscillation is equal to the orbital period of the satellite while the period of the long period oscillation is approximately one day. There are some additional frequencies observed in the drag coefficient corresponding to the lat-long variation of the ambient parameters. The amplitude of the short period oscillations dominates over the others.

The short-period variation due to the ambient parameters is tied to the altitude variation of the satellite as it orbits around the oblate Earth. The dominant effect of the altitude variation is on the fraction of diffuse reemission. For highly eccentric orbits, the drag coefficient variation is significant due to large changes in altitude. In this case, using a body-fixed Fourier model is not advantageous since these variations are independent of the attitude of the satellite. These periodic variations can be tied to the orbit itself. The Fourier expansion of the drag coefficient around the argument of latitude of the satellite (u) in its orbit is written as,

$$C_d = \sum_{n=0}^{\infty} (\bar{A}_n \cos nu + \bar{B}_n \sin nu). \tag{5.29}$$

The nominal coefficients can be found by numerically integrating the chosen GSIM over an orbit. The order of magnitude of the standard deviation for the coefficients is taken to be the same as that of the nominal values.

The orbit-fixed model, unlike the body-fixed model, depends on the position and velocity of the satellite since the argument of latitude depends on the satellite state. Therefore, the derivative of the drag coefficient with respect to the position vector is given by

$$\frac{\partial C_d}{\partial \boldsymbol{r}} = \sum_{n=0}^{\infty} (\bar{A}_n \frac{\partial \cos nu}{\partial \boldsymbol{r}} + \bar{B}_n \frac{\partial \sin nu}{\partial \boldsymbol{r}}). \tag{5.30}$$

Similarly, the partials with respect to the velocity vector can be written. The partials of the model with respect to the position and velocity can be derived by expressing the trigonometric functions of the argument of latitude in terms of the satellite states.

$$\cos u = \hat{\boldsymbol{r}}.\hat{\boldsymbol{n}} \tag{5.31}$$

where $\hat{\boldsymbol{n}}$ denotes the unit nodal vector and $\hat{\boldsymbol{r}}$ is the unit position vector. The unit nodal vector is defined as the unit vector pointing from the center of the Earth towards the intersection point between the satellite orbit and the equator during ascension. The derivative of the expression with respect to the position vector is given by,

$$\frac{\partial \cos u}{\partial \boldsymbol{r}} = \hat{\boldsymbol{n}}^T \left(\frac{I_{3\times 3} - \hat{\boldsymbol{r}}\hat{\boldsymbol{r}}^T}{r} \right) + \hat{\boldsymbol{r}}^T \frac{\partial \hat{\boldsymbol{n}}}{\partial \boldsymbol{r}} \tag{5.32}$$

The nodal vector can be expressed in terms of the angular momentum vector ($\boldsymbol{h}$) and the unit vector along the z-axis of the J2000 frame ($\hat{\boldsymbol{z}}$) as,

$$\hat{\boldsymbol{n}} = \frac{\hat{\boldsymbol{z}} \times \boldsymbol{h}}{|\hat{\boldsymbol{z}} \times \boldsymbol{h}|} \tag{5.33}$$

where $\boldsymbol{h} = \boldsymbol{r} \times \boldsymbol{v}$. Taking the derivative of the nodal vector in terms of the position vector and substituting in Eq. 5.32

$$\frac{\partial \cos u}{\partial \boldsymbol{r}} = \hat{\boldsymbol{n}}^T \left(\frac{I_{3\times 3} - \hat{\boldsymbol{r}}\hat{\boldsymbol{r}}^T}{r} \right) + \hat{\boldsymbol{r}}^T [\tilde{\hat{\boldsymbol{z}}}][\tilde{\boldsymbol{v}}] \left(\frac{\hat{\boldsymbol{n}}\hat{\boldsymbol{n}}^T - I_{3\times 3}}{|\hat{\boldsymbol{z}} \times \boldsymbol{h}|} \right) \tag{5.34}$$

where $[\tilde{z}]$ denotes the skew-symmetric tilde matrix operator, signifying a cross-product as given by eq. (3.27). In order to avoid singularities associated with the derivative of the sine term, it is expressed as follows

$$\sin u = \frac{r_z}{r \sin i} \tag{5.35}$$

where r_z is the z-component of the position vector and i is the inclination. The derivative of the expression with respect to r can be derived as,

$$\frac{\partial \sin u}{\partial \boldsymbol{r}} = \frac{r\hat{\boldsymbol{z}}^T - r_z \hat{\boldsymbol{r}}^T}{r^2} \csc i - \frac{r_z \csc i \cot i}{r|\hat{\boldsymbol{z}} \times \boldsymbol{h}|} \hat{\boldsymbol{z}}^T [I_{3\times 3} - \hat{\boldsymbol{h}}\hat{\boldsymbol{h}}^T][\tilde{\boldsymbol{v}}] \tag{5.36}$$

where $\hat{\boldsymbol{h}}$ is the unit vector along the angular momentum. The derivatives of Eqs. 5.32 and 5.35 with respect to the velocity can be similarly derived.

$$\frac{\partial \cos u}{\partial \boldsymbol{v}} = \frac{\hat{\boldsymbol{r}}^T [\tilde{\hat{\boldsymbol{z}}}][\tilde{\hat{\boldsymbol{r}}}]}{|\hat{\boldsymbol{z}} \times \boldsymbol{h}|} (I_{3\times 3} - \hat{\boldsymbol{n}}\hat{\boldsymbol{n}}^T) \tag{5.37}$$

$$\frac{\partial \sin u}{\partial \boldsymbol{v}} = \frac{r_z \csc i \cot i}{r|\hat{\boldsymbol{z}} \times \boldsymbol{h}|} \hat{\boldsymbol{z}}^T [I_{3\times 3} - \hat{\boldsymbol{h}}\hat{\boldsymbol{h}}^T][\tilde{\boldsymbol{r}}] \tag{5.38}$$

In order to calculate the derivatives of the sines and cosines of multiple angles in Eq. 5.30, the following recursion formulae are used

$$\frac{\partial \cos nu}{\partial \boldsymbol{r}} = 2 \left(\frac{\partial \cos u}{\partial \boldsymbol{r}} \cos (n-1)u + \cos u \frac{\partial \cos (n-1)u}{\partial \boldsymbol{r}} \right) - \frac{\partial \cos (n-2)u}{\partial \boldsymbol{r}} \tag{5.39}$$

$$\frac{\partial \sin nu}{\partial \boldsymbol{r}} = 2 \left(\frac{\partial \cos u}{\partial \boldsymbol{r}} \sin (n-1)u + \cos u \frac{\partial \sin (n-1)u}{\partial \boldsymbol{r}} \right) - \frac{\partial \sin (n-2)u}{\partial \boldsymbol{r}} \tag{5.40}$$

$$\frac{\partial \cos nu}{\partial \boldsymbol{v}} = 2\left(\frac{\partial \cos u}{\partial \boldsymbol{v}}\cos(n-1)u + \cos u\frac{\partial \cos(n-1)u}{\partial \boldsymbol{v}}\right) - \frac{\partial \cos(n-2)u}{\partial \boldsymbol{v}} \tag{5.41}$$

$$\frac{\partial \sin nu}{\partial \boldsymbol{v}} = 2\left(\frac{\partial \cos u}{\partial \boldsymbol{v}}\sin(n-1)u + \cos u\frac{\partial \sin(n-1)u}{\partial \boldsymbol{v}}\right) - \frac{\partial \sin(n-2)u}{\partial \boldsymbol{v}} \tag{5.42}$$

The orbit-fixed model derived above is valid only for inclined orbits since the argument of latitude is undefined for equatorial orbits. In the latter case, the true longitude is used and the partials can be derived accordingly. The model can be essentially derived for any fast variable such as the eccentric anomaly and true anomaly.

The derivatives of the drag acceleration w.r.t the Fourier coefficients can be computed in a manner similar to Eqs. 5.11-5.14.

$$\frac{\partial \boldsymbol{a_{drag}}}{\partial \bar{A}_n} = -\frac{1}{2}\rho\frac{A_{ref}}{m}v_r^2\hat{\boldsymbol{u}}\cos nu \tag{5.43}$$

$$\frac{\partial \boldsymbol{a_{drag}}}{\partial \bar{B}_n} = -\frac{1}{2}\rho\frac{A_{ref}}{m}v_r^2\hat{\boldsymbol{u}}\sin nu \tag{5.44}$$

5.2.3 Body-Orbit Double Fourier (BODF) model

In an actual space environment, the satellite drag coefficient will generally vary due to changes in both satellite orientation as well as ambient parameters in the orbit. Additionally, there will be errors in the density model used in orbit determination with variations that are potentially periodic with the orbit. In order to capture variations due to both attitude and orbit dependent factors, a combination of the body-fixed and orbit-fixed models is desired while retaining the orthogonality of the Fourier coefficients. Now, $\overline{\mathcal{A}}_n$ and $\overline{\mathcal{B}}_n$ in eq. (5.15) are time-varying due to their dependence on ambient parameters such as molecular composition and temperature that show variations on diurnal, seasonal, annual and longer timescales. As a first approximation, we can ignore variations on these timescales since most orbit determination data-arcs are in the order of a day. But as discussed in the previous section, variations on orbital timescales can be significant for orbit determination and prediction. Therefore. re-writing Eq. 5.15 as a function of the argument of latitude

to depict the dependence of body-fixed Fourier coefficients on the orbit, we get

$$C_d = \sum_{n=0}^{\infty} (\overline{\mathcal{A}}_n(u) \cos n\theta + \overline{\mathcal{B}}_n \sin n\theta). \tag{5.45}$$

During periods of quiet geomagnetic activity, these variations will be nearly periodic with the orbit. This allowed us to carry out a Fourier expansion of the drag coefficient w.r.t the argument of latitude in the previous section. Similarly, the body-fixed Fourier coefficients can be expanded into a Fourier series w.r.t. the argument of latitude.

$$\overline{\mathcal{A}}_n(u) = \sum_{m=0}^{\infty} (\overline{\mathbb{A}}_{mn} \cos mu + \overline{\mathbb{B}}_{mn} \sin mu). \tag{5.46}$$

$$\overline{\mathcal{B}}_n(u) = \sum_{m=0}^{\infty} (\overline{\mathbb{C}}_{mn} \cos mu + \overline{\mathbb{D}}_{mn} \sin mu). \tag{5.47}$$

Substituting Eq. 8.19 and Eq. 5.47 in Eq. 5.45,

$$\begin{aligned} C_d = \sum_{m=0}^{\infty} \sum_{n=0}^{\infty} (&\overline{\mathbb{A}}_{mn} \cos mu \cos n\theta + \overline{\mathbb{B}}_{mn} \sin mu \cos n\theta \\ &+ \overline{\mathbb{C}}_{mn} \cos mu \sin n\theta + \overline{\mathbb{D}}_{mn} \sin mu \sin n\theta) \end{aligned} \tag{5.48}$$

This model, called the body-orbit double Fourier (BODF) model, can track variations in the drag coefficient due to both attitude and orbital motion. The BODF coefficients can be obtained by carrying out a Fourier expansion of the analytical BFF coefficients obtained in the previous section as follows

$$\overline{\mathbb{A}}_{mn} = \frac{1}{\pi} \int_0^{2\pi} \overline{\mathcal{A}}_n(u) \cos mu du, \tag{5.49}$$

$$\overline{\mathbb{B}}_{mn} = \frac{1}{\pi} \int_0^{2\pi} \overline{\mathcal{A}}_n(u) \sin mu du, \tag{5.50}$$

$$\overline{\mathbb{C}}_{mn} = \frac{1}{\pi} \int_0^{2\pi} \overline{\mathcal{B}}_n(u) \cos mu du, \tag{5.51}$$

$$\overline{\mathbb{D}}_{mn} = \frac{1}{\pi} \int_0^{2\pi} \overline{\mathcal{B}}_n(u) \sin mu du, \tag{5.52}$$

for $m > 0$ and,

$$\overline{\mathbb{A}}_{0n} = \frac{1}{2\pi}\int_0^{2\pi} \overline{\mathcal{A}}_n(u)du, \tag{5.53}$$

$$\overline{\mathbb{C}}_{0n} = \frac{1}{2\pi}\int_0^{2\pi} \overline{\mathcal{B}}_n(u)du, \tag{5.54}$$

and $\overline{\mathbb{B}}_{0n} = 0$, $\overline{\mathbb{D}}_{0n} = 0$ for $m = 0$. The partials of the model with respect to the position and velocity are then given by

$$\begin{aligned}\frac{\partial C_d}{\partial \boldsymbol{r}} = \sum_{m=0}^{\infty}\sum_{n=0}^{\infty}(&\bar{A}_{mn}\frac{\partial \cos mu}{\partial \boldsymbol{r}}\cos n\theta + \bar{B}_{mn}\frac{\partial \sin mu}{\partial \boldsymbol{r}}\cos n\theta \\ &+ \bar{C}_{mn}\frac{\partial \cos mu}{\partial \boldsymbol{r}}\sin n\theta + \bar{D}_{mn}\frac{\partial \sin mu}{\partial \boldsymbol{r}}\sin n\theta)\end{aligned} \tag{5.55}$$

$$\begin{aligned}\frac{\partial C_d}{\partial \boldsymbol{v}} = \sum_{m=0}^{\infty}\sum_{n=0}^{\infty}(&\bar{A}_{mn}\frac{\partial \cos mu}{\partial \boldsymbol{v}}\cos n\theta + \bar{B}_{mn}\frac{\partial \sin mu}{\partial \boldsymbol{v}}\cos n\theta \\ &+ \bar{C}_{mn}\frac{\partial \cos mu}{\partial \boldsymbol{v}}\sin n\theta + \bar{D}_{mn}\frac{\partial \sin mu}{\partial \boldsymbol{v}}\sin n\theta)\end{aligned} \tag{5.56}$$

with the partials of the trigonometric terms given by Eqs. 5.32-5.42.

5.2.4 Body-Orbit Summation (BOS) model

The number of the coefficients to be estimated in BODF model can grow very quickly for higher orders. For order 2 BODF, the coefficients to be estimated are 25 compared to 5 for order 2 orbit-fixed and single Fourier body-fixed model. In order to reduce computations associated with the model, some of the higher order terms can be neglected. A rigorous analysis of shape model of the satellite and the nature of drag coefficient variation in the orbit can reveal higher order coefficients that can be neglected for a specific satellite. A simpler generic approach is to neglect all the cross-coupling terms between the body angle and the argument of latitude. In other words, keep the order for u to be zero while considering higher orders for ϕ and vice-versa. This reduces BODF to a sum of BFF and OFF models. The resulting body-orbit summation (BOS) model is

given by

$$C_d = \bar{A}_0 + \sum_{m=1}^{\infty}(\bar{A}_m \cos mu + \bar{B}_m \sin mu) + \sum_{n=1}^{\infty}(\bar{C}_n \cos n\theta + \bar{D}_n \sin n\theta) \tag{5.57}$$

The partials of the model w.r.t position and velocity are the same as for OFF model since the body-fixed terms do not depend on position and velocity of the satellite.

5.3 Validation using synthetic data

Before the Fourier models can be implemented in an actual orbit determination process, it is necessary to test them on simulated examples. In this section, a batch estimator is used to process simulated GPS measurements sampled at every 10 s with Gaussian noise of 5 m in position and 1 mm/s in velocity. The initial estimates of the position and velocity are generated by adding an error of 10 m and 0.01 m/s respectively to the generated truth. The standard deviations are taken to be the same values. To calculate the initial estimates of the Fourier coefficients, the Sentman-Schamberg model in section 2.1.3 is integrated using the Fourier integrals.

In order to compare the prediction performance of the Fourier models against the standard cannonball model, the in-track error and the altitude error between the truth and prediction are calculated. The in-track error for the estimated and predicted trajectory is found as follows.

$$\delta I = a|u - \hat{u}| \tag{5.58}$$

where a is the nominal semi-major axis and u and $\hat{u}$ are the true and estimated/predicted argument of latitude respectively. The altitude error can be calculated as

$$\delta H = |r - \hat{r}| \tag{5.59}$$

where r and $\hat{r}$ are the norm of the true and estimated/predicted position vectors respectively. A data arc of 10 orbits is processed in the batch filter, unless otherwise stated, and the estimated initial state is propagated for 50 orbits. Therefore, the orbit prediction is done for 40 orbits. In all the results, order 0 refers to the standard cannonball model.

5.3.1 Simulation scenario 1

Th purpose of the first simulation scenario is to analyze the performances of the BFF and OFF models separately. Therefore, the drag-coefficient is assumed to vary either due to changes in attitude or changes in ambient parameters. A simplified force model is used to generate the true trajectory comprising of the two body force and atmospheric drag, therefore $\boldsymbol{a} = \boldsymbol{a_{two-body}} + \boldsymbol{a_{drag}}$. In order to isolate the effects of atmospheric drag, other perturbation forces are not included. NRLMSISE-00 is used to model the atmospheric density (ρ). There's no dynamics mismatch in the filter and only the position, velocity and Fourier coefficients are estimated. The standard deviation of the Fourier coefficients is taken as their orders of magnitude. This is done so as to constrain the magnitudes of the estimated coefficients and to prevent the filter from assigning arbitrarily large values to them. This problem is frequently encountered in gravitational field estimation [112]. The same analytical model is used to compute the truth and nominal coefficients. To calculate the nominal BFF coefficients, the ambient conditions need to be fixed at a point in time, which is taken to be the first time instant of the simulation. Since the Fourier series is being truncated at a low order for estimation, the nominal Fourier series does not capture the true drag coefficient. In addition, arbitrary errors sampled from a Gaussian distribution with zero mean and the assumed covariance are added to the nominal coefficients. The diagonal initial covariance matrix, can then be easily formulated. Even though a relatively high-order Fourier series is needed to approximate the true drag coefficient accurately (0.01 % relative error for order 20), most of the drag coefficient variation can be captured by a few Fourier coefficients during the estimation process.

In order to evaluate the Fourier models, two satellites in different orbital regimes are taken into consideration. The reported drag coefficients are normalized with a constant reference area of 0.36 m^2 for case 1 and 24 m^2 for case 2. All the cases considered are summarized in table 7.2.

Case	Attitude profile/test scenario	Drag coefficient model
1.1	Nadir pointing	Body-fixed Fourier
1.2	Random slewing	Body-fixed Fourier
1.3	Randomly tumbling	Body-fixed Fourier
2.1	Inertially stabilized	Body-fixed Fourier
2.2	Inertially stabilized with yaw maneuver	Body-fixed Fourier
2.3	Nadir pointing with ambient parameter variation	Orbit-fixed Fourier
	Density mismatch in cases 2.1 and 2.3	Body-fixed Fourier and orbit-fixed Fourier

Table 5.1: Summary of simulation cases. Note that in all the cases other than 2.3, ambient parameter variation is not considered i.e. the attitude and ambient parameter dependence of the drag coefficient are considered separately

5.3.1.1 Case 1

A cubical satellite of mass 83 kg with a simple geometry at an altitude of around 600 km is considered to analyze the performance of the body-fixed Fourier model. The initial orbital elements in order to simulate the truth are given in table 5.2.

Element	Value
a	6971 km
e	0
i	97.8^0
Ω	0^0
u	0^0

Table 5.2: Initial orbital elements of first candidate satellite to generate the reference trajectory

A simple shape model shown in fig. 5.4 is considered. The shape model is arbitrary and assumed to be cubical with dimensions 60 cm x 60 cm x 60 cm is taken, with the nadir and zenith face areas double the rest of the faces due to the presence of an antenna on the nadir face. Shadowing and multiple reflections due to the antenna have not been considered. A diagonal inertia matrix with principal values $[3, 2.5, 5]$ kg.m^2 is assigned. The satellite is assumed to be covered in Gallium Arsenide panels except the nadir face which is assumed to be made of Aluminum. The

average satellite wall temperature is taken to be 300 K [73]. The satellite wall temperature will vary along the orbit but the constant value is justified since the sensitivity of the drag coefficient to the outer wall temperature is substantially lower than the other parameters [64]. Three modes of attitude stabilization are considered.

(1) *Case 1.1 Nadir-pointing*—An nadir-pointing satellite always has its leading face (positive x in body frame) towards the flow. Therefore in a static atmosphere, the flow unit vector would be perpendicular to the satellite leading face resulting in a constant drag coefficient. The BFF model will be equivalent to the cannonball drag coefficient in this case. But since the atmosphere is co-rotating with the Earth, there is a periodic variation of the flow angle with the leading face which results in a small periodically varying component in the drag coefficient. The winds in the atmosphere contribute towards a random component in the drag coefficient variation and will be considered in the simulation scenario 2.

(2) *Case 1.2 Random periodic slewing*—It is assumed that the satellite performs random slewing within a cone periodically, for say, imaging purposes. The satellite is taken to be nominally nadir pointing while slewing within a cone of 30^0 every 10, 20 and 30 minutes. The axis of the cone points towards the center of the Earth.

(3) *Case 1.3 Randomly tumbling satellite*—In order to study the performance of the Fourier model in an extreme case, a randomly varying attitude profile is taken. In order to simulate a separatrix motion, the angular velocity along the axis of intermediate inertia is taken to be the maximum.

Due to the planes of symmetry in the satellite model, many of the Fourier coefficients turn out to be zero. In particular, all the B_{mn} coefficients are zero. D_{mn} is always zero for the GSIM considered here. For A_{mn}, only the even elevation orders and multiples of four for the azimuthal orders are non-zero. The difference between the order 20 BFF model and the GSIM is plotted in fig. 5.5.

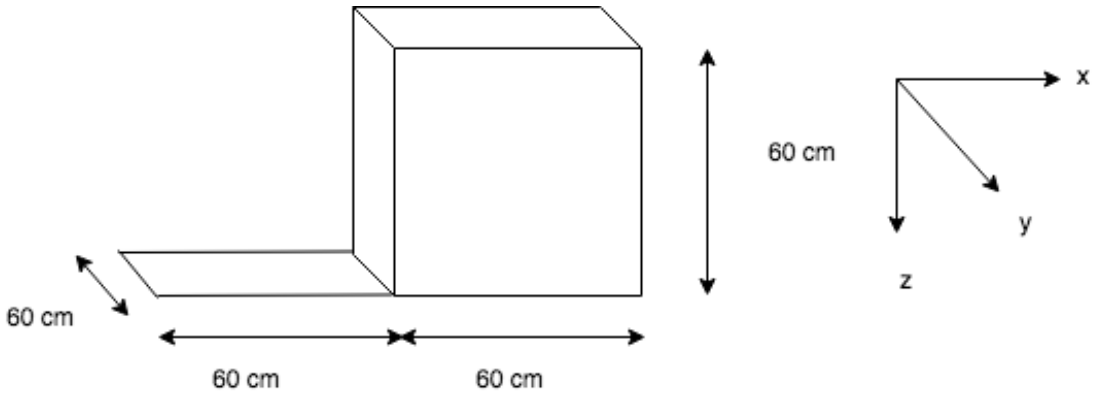

Figure 5.4: Simplified shape model of the satellite in case 1 with the defined body frame

When the satellite is nadir-pointing, there's a very small periodic oscillation in the drag coefficient. The relative velocity vector varies in the range $[-3.8^0, 3.8^0]$ in θ while in ϕ, the variation is negligible. Therefore, the double Fourier series reduces to a single series in this case. As noted before, the Fourier coefficients are zero for the azimuthal direction till order 4. Therefore, only the order 4 Fourier coefficient for θ is estimated along with the order 0 (cannonball) coefficient in the filter. The true drag coefficient, and the order 0 and order 4 drag coefficient estimates are plotted in fig. 5.6 (left). As can be seen in the figure, the drag coefficient variation is very small due to the atmospheric co-rotation. The in-track error and altitude error for the Order 0 (standard cannonball) and Order 4 BFF models are plotted in fig. 5.6 (right). Since the drag coefficient variation due to the atmospheric co-rotation is almost negligible, the improvement with Order 4 BFF model is not significant. As can be seen in fig. 5.6, the order 4 Fourier drag coefficient oscillates around the cannonball estimate and does not track the truth. The marginal improvement observed in this case is due to a better fit to the measurements that leads to an improved initial state estimate.

A periodic random slewing of the satellite within a cone of 30^0 is considered as the second attitude profile. Three different periods are considered for the variation - 10, 20 and 30 minutes in order to see if the Fourier model is able to capture variations of different frequencies. The drag coefficient variation for the 10 minute period slewing is plotted in fig. 5.7 (left). The drag coefficient changes in sudden steps since the attitude is assumed to change in steps after every

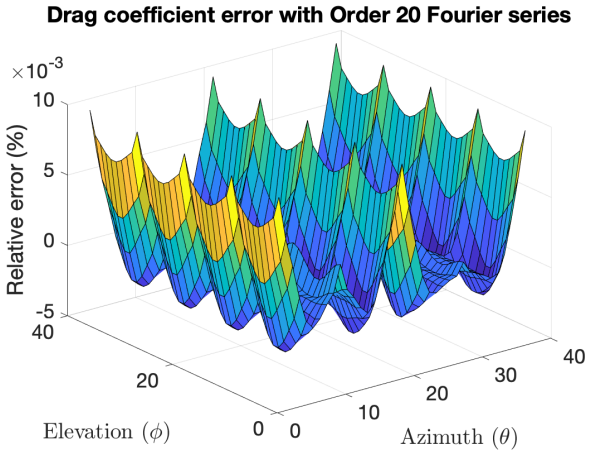

Figure 5.5: Difference in the drag coefficients between the Fourier model of order 20 and the physical model for case 1

10 minutes. Within the period of 10 minutes, the small variation in drag coefficient is due to the co-rotation of the atmosphere. In this case, the drag coefficient varies in both elevation and azimuth. There are non-zero coefficients below order 4 which capture variations in elevation. But as noted in the previous case, the coefficients below Order 4 are zero for the azimuth direction. Therefore, when a BFF model of a smaller order is used to estimate the drag coefficient, the effects of azimuth variation are absorbed in the non-zero coefficients corresponding to elevation. This results in a degradation of performance compared to the standard cannonball model. This result is quite interesting as it points out the significance of choosing the order of the Fourier model with due care. An arbitrary order Fourier model chosen without any regards to the shape model of the satellite and the attitude profile under consideration may actually degrade the performance compared to the cannonball model as shown by this case.

With an Order 4 BFF model, there's a significant improvement in the performance as shown in fig. 5.7 (right). Such a trend is seen in all the frequencies considered. The improvement in the performance with the order 4 model cannot be solely attributed to a better drag coefficient modeling since the estimated drag coefficient does not accurately track the true drag coefficient at all time instants as can be seen in fig. 5.7 (left). A better fit to the measurements which results in an improved initial state estimate complements the better drag coefficient modeling in providing

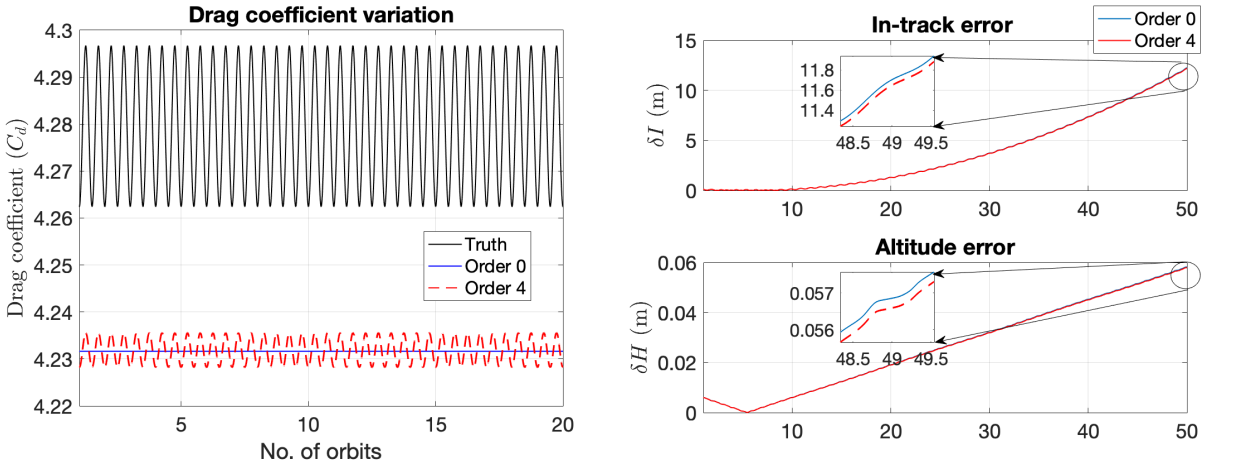

Figure 5.6: Case 1.1: True and estimated drag coefficient (left) and estimation/prediction errors (right) with order 0 (standard cannonball) and order 4 BFF model for a nadir-pointing satellite. The prediction errors are quite small since an idealized force model, with no mismatch in density or ambient parameters, has been considered

an improved prediction performance.

The third attitude profile considered for analysis is that of a randomly tumbling satellite. The initial Euler angles are taken to be 70^0 roll, 70^0 pitch and 70^0 yaw. The angular velocities along the x, y and z axes are taken to be $[0.1, 0.5, 0.1]^0/s$. An unstable separatrix motion is considered with the angular velocity taken to be maximum around the axis of intermediate inertia. The drag coefficient variation is plotted in fig. 5.8 (left). The drag coefficient seems to vary periodically due to the planes of symmetry present in the shape model of the satellite. On closer inspection, it can be seen that the drag coefficient does not exactly repeat with each oscillation.

The improvement obtained using a BFF model is negligible in this case as can be seen in fig. 5.8 (right). For a randomly tumbling satellite, the drag-coefficient variations average out and a cannonball model is sufficient for the drag-coefficient estimation.

5.3.1.2 Case 2

A satellite of mass 3850 kg with fairly complex geometry at an altitude of 407 km is considered as the second case. The orbital regime is chosen due to the significant effects of drag experienced at

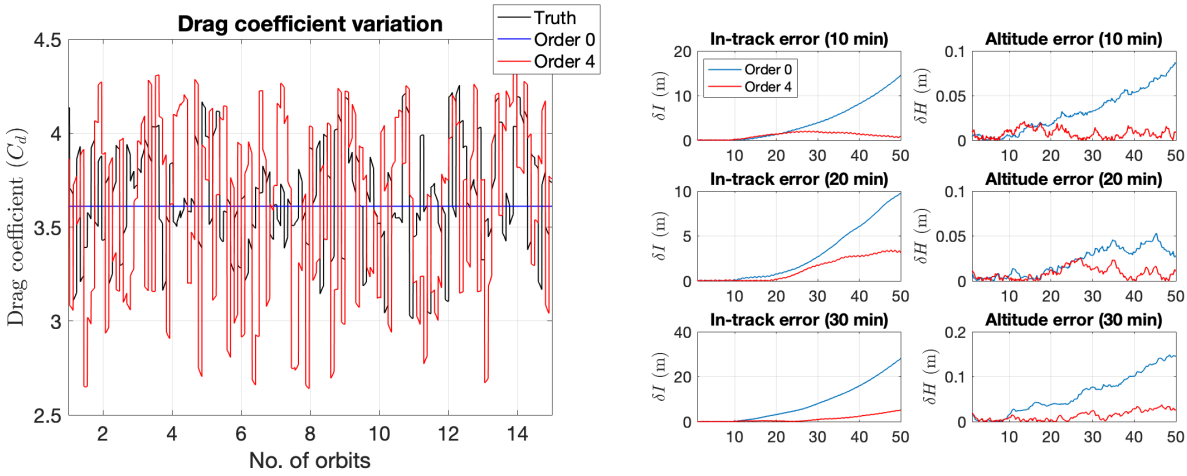

Figure 5.7: Case 1.2: True and estimated drag coefficient for a satellite slewing within a cone of 30^0 every 10 minutes (left) and estimation/prediction errors (right) with order 0 (standard cannonball) and order 4 BFF models for a satellite slewing randomly within a 30^0 cone every 10 minutes (first row), 20 minutes (second row) and 30 minutes (third row)

such a low altitude. The initial orbital elements are given in table 5.3. The model, shown in fig. 5.9,

Element	Value
a	6778 km
e	0
i	65^0
Ω	0^0
u	0^0

Table 5.3: Initial orbital elements of second candidate satellite for truth generation

is loosely based on NASA's Global Precipitation Measurement (GPM) satellite [22]. It is assumed that the satellite consists of two large solar panels with areas 16.45 m^2. In order to maximize solar power and minimize atmospheric drag, one solar panel is feathered to the flow while the other solar panel tracks the Sun. The feathered solar panel always contributes towards the tangential drag and hence it is added as a constant to the drag coefficient. The satellite bus is assumed to be fixed to the tracking solar panel and hence inertially stabilized. The dimensions of the satellite bus and solar panels are defined in fig. 5.9. Additional areas with values 1, 0.75, 1.5, 1.25 and 0.25 m^2 are added to the cuboidal faces in the +x, -x, +y, -y and +z directions to account for protrusions etc. The mean molecular mass of the satellite wall is taken to be different for each surface due to the

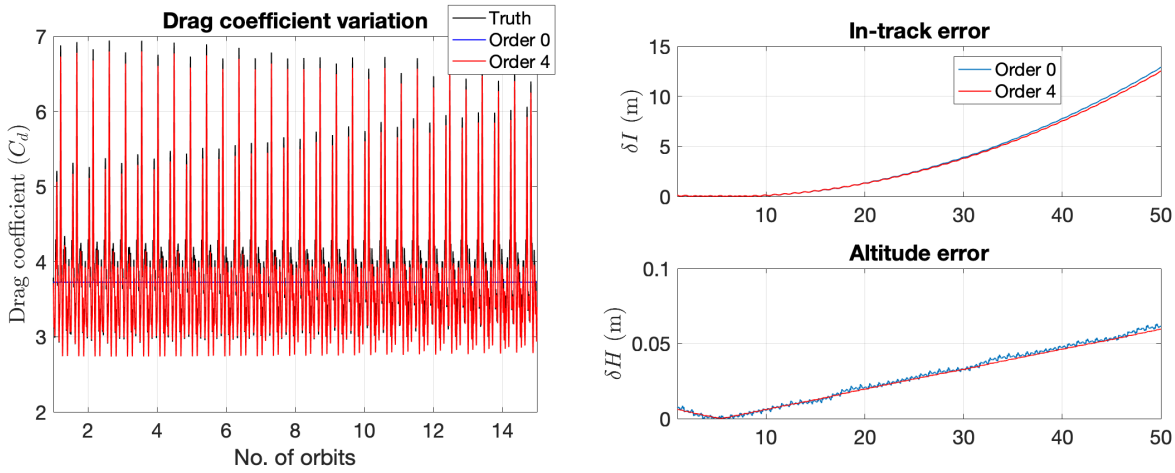

Figure 5.8: Case 1.3: True and estimated drag coefficient (left) and estimation/prediction errors (right) with order 0 (standard cannonball) and Order 4 BFF models for a randomly tumbling satellite

presence of different components on each side of the satellite. This is done in order to make the model asymmetric. Two attitude profiles are considered—

(1) *Case 2.1 Inertially stabilized*—The satellite is assumed to be inertially fixed with one solar panel always feathered to the flow. Therefore, the dominant variation of the flow direction is in the elevation angle (ϕ).

(2) *Case 2.2 Yaw maneuver*—It is assumed that the satellite performs a 180^0 yaw maneuver with a duration of half an orbit.

In all the above cases, the dependence of drag coefficient on the ambient parameters has not been considered. In addition to being a function of the satellite orientation, the drag coefficient has an almost periodic variation due to its dependence on atmospheric parameters such as molecular composition and temperature. The variation is not exactly periodic since the satellite is traversing different regions of the atmosphere in each orbit due to the co-rotation of the atmosphere with the Earth. But it serves as a close approximation during stable atmospheric conditions. During solar flares and/or geomagnetic storms, the drag coefficient may vary significantly from one orbit to the other and should be analyzed in further studies. The following case is therefore considered to test

the OFF model

(1) *Case 2.3 Ambient parameter variation* - In order to account for the ambient parameter variation, a nadir-pointing profile is considered and the atmospheric parameters used to calculate the true drag coefficient are allowed to vary throughout the orbit.

The performance of the Fourier models will be affected by any errors in the atmospheric density model used in the filter. A preliminary analysis of the performance of these models in the presence of density mismatch is presented as the last case.

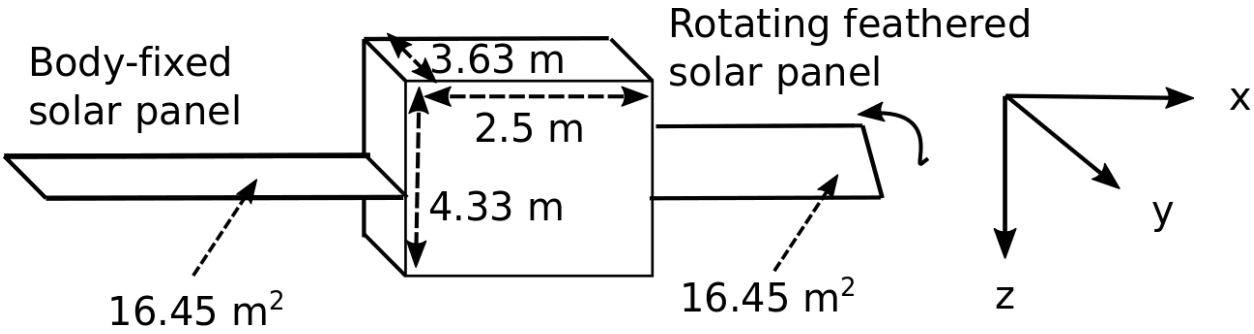

Figure 5.9: Simplified shape model of the satellite in case 2 with the defined body frame. The body z-axis points towards the Sun

Most of the Fourier coefficients for this satellite are non-zero due to the asymmetrical shape model in contrast to the previous one. For an inertially stabilized attitude profile, the drag coefficient variation is essentially in the elevation direction. There's a small variation in the azimuth direction as seen in Case 1.1 but can be ignored without any loss in accuracy. Due to the absence of planes of symmetry in this case, all the even A_{mn} coefficients for both the directions are non-zero. The drag coefficient is varies periodically as seen in fig. 5.10 (left). It is interesting to compare the performance of the higher-order BFF models with the standard cannonball model when used in conjunction with a varying cross-sectional area as is the standard in OD, i.e. A_{ref} in eq. (1.1) is taken to be the instantaneous cross-sectional area. It is evident from fig. 5.10 (right) that all higher order body-fixed models perform better than the Order 0 model, even when the varying cross-sectional area is used with the standard cannonball (represented by the cyan curve).

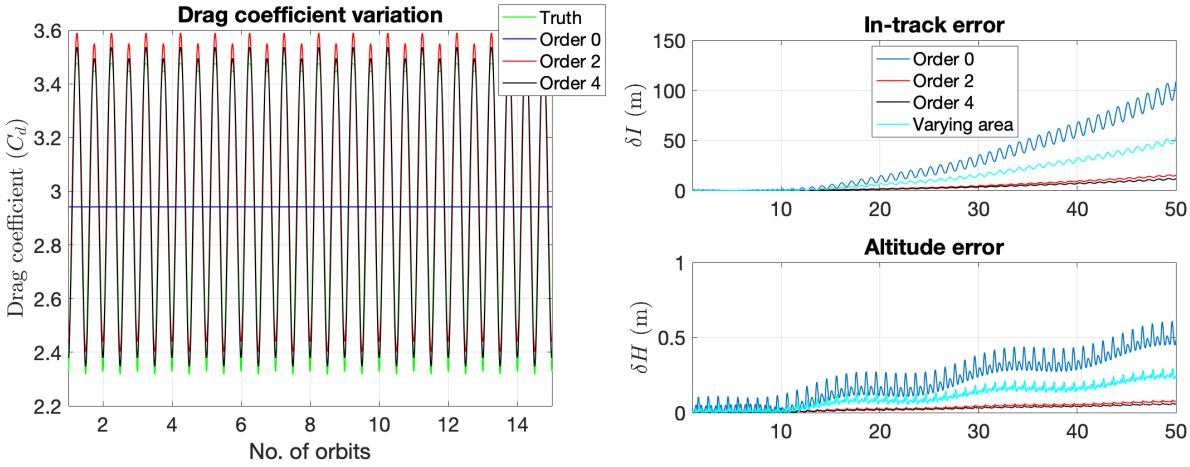

Figure 5.10: Case 2.1: True and estimated drag coefficient (left) and estimation/prediction errors (right) with order 0 (standard cannonball) and BFF models for an inertially stabilized satellite

If the satellite performs an attitude maneuver, a temporary aperiodic component is introduced in the drag coefficient. In this case, there are dominant components of the drag coefficient variation in both the azimuth and elevation directions in the body frame for the duration of the maneuver. An example of a 180^0 yaw maneuver with a duration of half an orbit is analyzed. The drag coefficient variation is shown in fig. 5.11 (left). The maneuver takes place between the second and the third orbit with a decrease in the drag coefficient during the maneuver. The BFF models track the drag coefficient and respond to the change during the yaw maneuver. With the higher order models, the secular as well as the short period errors are reduced as can be seen in fig. 5.11 (right). It is interesting to note the significant change in the performance of the cannonball drag coefficient in this case compared to the inertially stabilized attitude profile.

In all the above cases, these parameters were considered constant and the explicit dependence of the drag coefficient on the attitude was studied. In order to analyze the variation of drag coefficient solely due to ambient parameters, a nadir-pointing attitude profile with a constant-direction relative velocity vector is considered. The nominal coefficients are arbitrarily assigned to be 1 and the standard deviation around them is taken to be 10. In this case, the data for 18 orbits i.e. a complete day is processed by the filter since the mean can be captured only with a minimum of one day of data. The drag coefficient is shown in fig. 5.12 (left). It can be seen that along with a

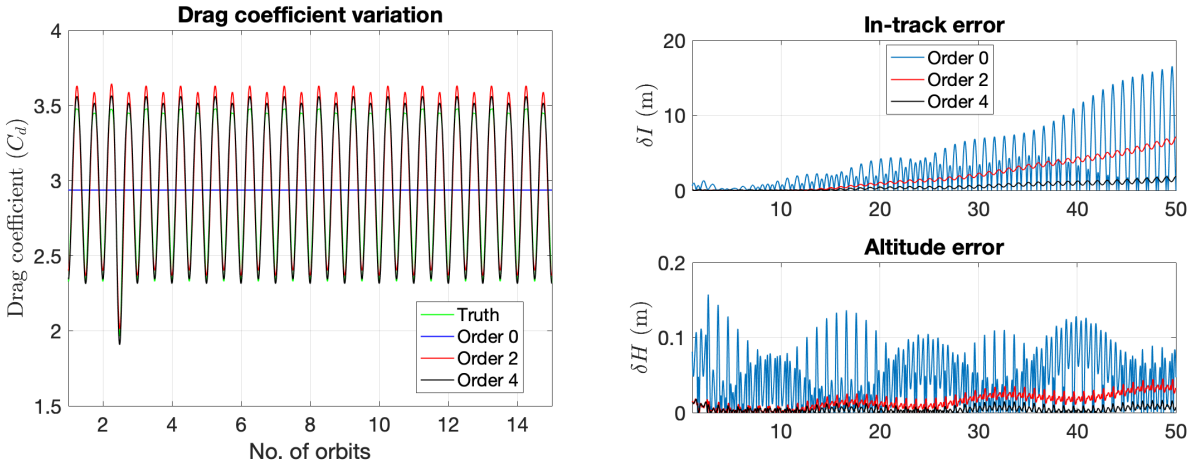

Figure 5.11: Case 2.2: True and estimated drag coefficient (left) and estimation/prediction errors (right) with order 0 (standard cannonball) and BFF models for an inertially stabilized satellite with a short duration yaw maneuver

periodicity of the drag coefficient in an orbit, there's a superposed trend with a period of around 18 orbits (1 day). This period is due to the rotation of the Earth (and atmosphere). The OFF model being dependent solely on the argument of latitude, cannot capture slowly varying periodic errors. The relatively large amplitude orbital variation of the drag coefficient is mainly due to the altitude variation as a result of Earth's oblateness. The in-track and altitude errors for the higher order Fourier models are shown in fig. 5.12 (right). The higher order models show a similar secular error as the Order 0 model but the short period oscillations in the error are reduced. The improvement for all the higher order models is nearly the same and therefore not distinguishable in the figure.

In real orbit determination scenarios, the atmospheric density model used in the filter will generally not be perfect. Since the drag force contains a product of drag coefficient and atmospheric density as seen in eq. (1.1) and the drag coefficient is the only parameter being estimated, any errors in the atmospheric density model will be absorbed in the estimate of the drag coefficient in the filter, in order to obtain the 'best' fit to the measurements [66]. In the case of a time-varying drag coefficient model such as the Fourier models with multiple parameters, the density model errors are absorbed by the parameters being estimated, i.e. the Fourier coefficients. As a result, the effective drag coefficient estimate will diverge from its true value. Due to the presence of such model errors,

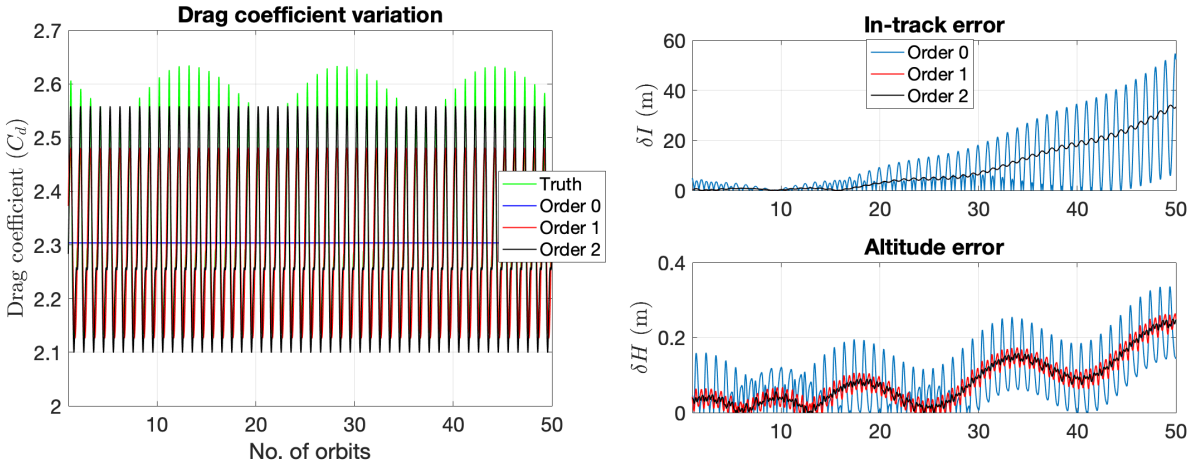

Figure 5.12: Case 2.3: True and estimated drag coefficient (left) and estimation/prediction errors (right) with order 0 (standard cannonball) and OFF models for a nadir-pointing satellite due to periodic variation of ambient parameters

the orbit prediction accuracy can be significantly degraded even though an apparently 'good' fit to the measurements is obtained. The degradation of orbit prediction accuracy will occur when density model errors are present whether a constant cannonball drag coefficient model is used in the filter or a time-varying model such as the Fourier model is used. It is important to analyze whether the prediction performance of the Fourier models degrades more than the cannonball model.

The modelled atmospheric density will have errors from various sources that can then get absorbed in the estimated Fourier coefficients. One of the primary sources of error in the different density models are inaccurate space weather parameter forecasts. The predicted $F_{10.7}$ and A_p indices that are input to NRLMSISE-00 differ from the true values. The errors in $F_{10.7}$ and A_p are generally within $\pm$ 20-40 SFU and 20 γ (10 A_p) respectively but the prediction becomes worse during solar maximum and geomagnetically active conditions [129]. Therefore, a model-plant mismatch in the atmospheric density model is introduced through the daily geomagnetic index (A_p) value. The truth is simulated with $A_p = 4$ while in the filter, $A_p = 40$ is considered. The density difference due to the mismatch is plotted in eq. (8.18). As can be seen in the figure on the right in eq. (8.18), the density error is periodic, with higher order frequencies present in the error.

The performance of the body-fixed model in the presence of density errors is tested through

case 2.1. All the parameters in the test case are kept the same except the A_p index which is taken as 40 in the filter density model for all the estimation runs discussed including the standard cannonball i.e. order 0 model. The estimated drag coefficients, shown in fig. 5.14 (left), deviate significantly from the true drag coefficient since the Fourier coefficients absorb the density errors. The estimated drag coefficient oscillates to lower values than the true drag coefficient since the density model in the filter is higher than the true density. The prediction errors of the higher-order Fourier models are still significantly smaller than the cannonball model as shown in fig. 5.14 (right). But the improvement in performance becomes less predictable in the presence of density errors since in this case the order 4 Fourier model performs worse than order 2.

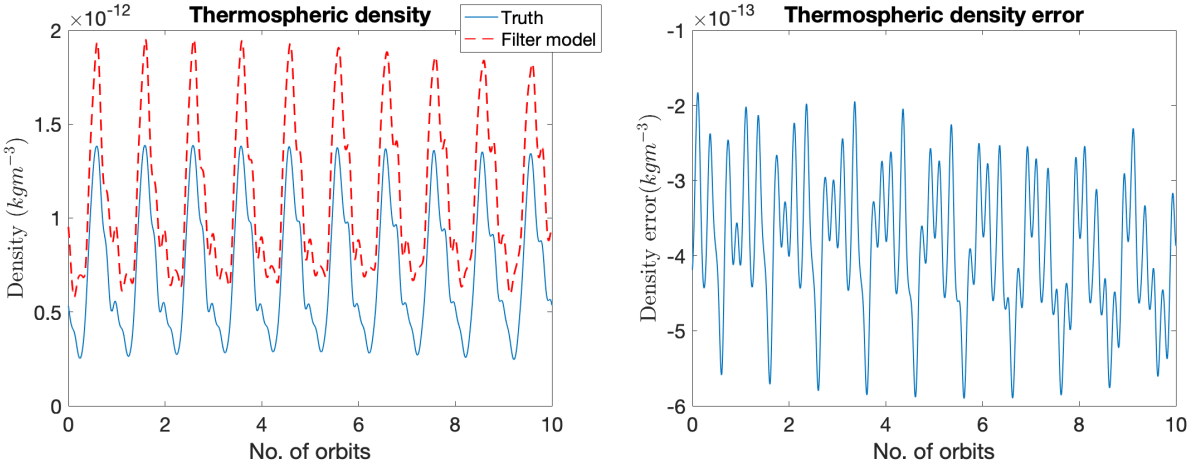

Figure 5.13: Density models in the truth and filter (left) and the difference between the densities (right)

Similarly, the performance of the OFF model is tested in the presence of density errors through case 2.3. The same density mismatch is introduced by taking $A_p = 40$ in the filter. As expected, the estimated drag coefficients do not track the true drag coefficient as shown in fig. 5.15 (left). The performance of the higher order OFF models is plotted in fig. 5.15 (right). There's a significant improvement in the prediction errors with the higher order models over the standard cannonball model, especially after order 1. The improvements with the higher order models is related to the higher order frequencies present in the density error as seen in eq. (8.18). Since the OFF model is tied to the satellite's position in its orbit, the Fourier coefficients are able to absorb

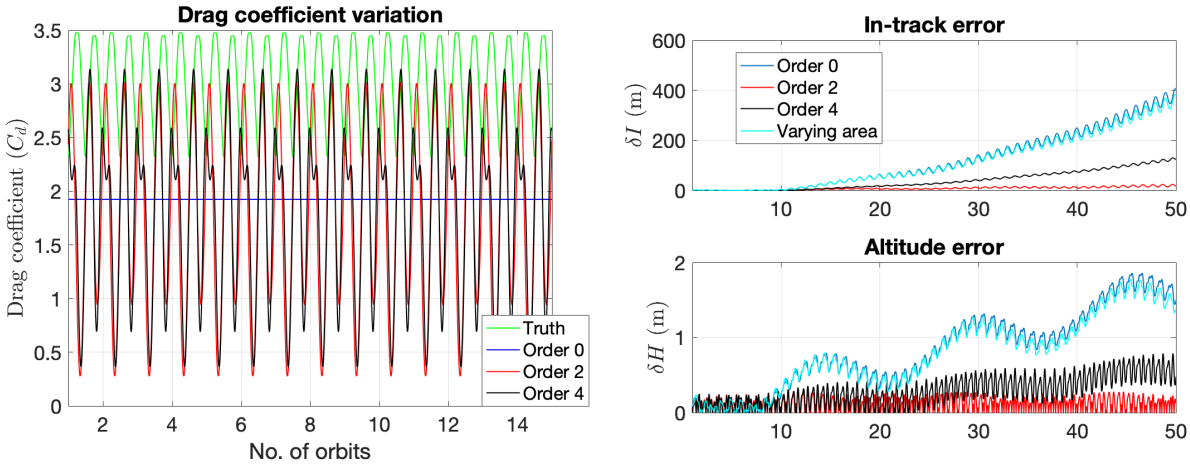

Figure 5.14: Density errors in case 2.1: True and estimated drag coefficient (left) and estimation/prediction errors (right) with order 0 (standard cannonball) and BFF models for an inertially stabilized satellite in the presence of density model errors in the filter

periodic errors in the drag force other than due to the drag coefficient variation. Specifically, the model is able to reduce estimation errors resulting due to periodic errors in the atmospheric density.

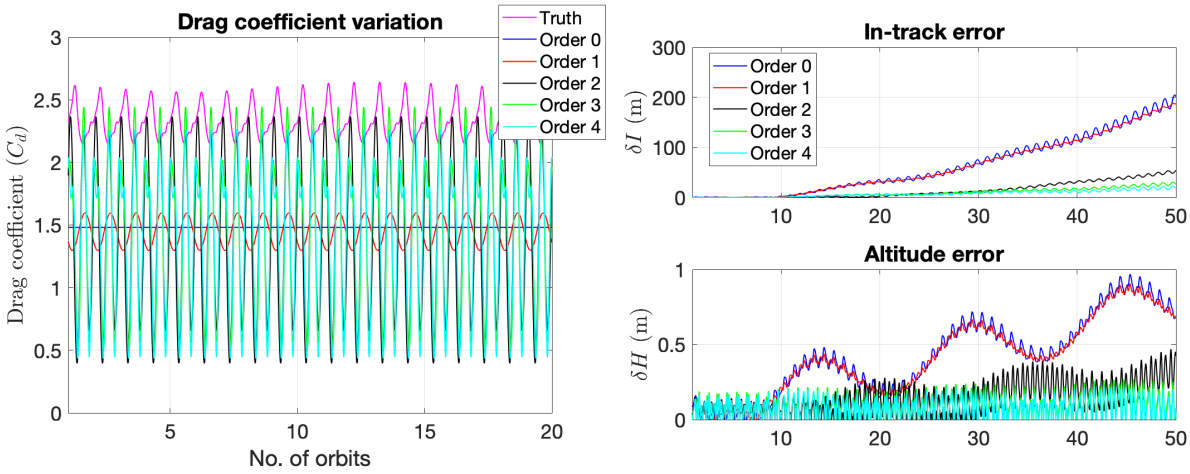

Figure 5.15: Density errors in case 2.3: True and estimated drag coefficient (left) and estimation/prediction errors (right) with order 0 (standard cannonball) and OFF models for a nadir-pointing satellite due to variation in ambient parameters in the presence of density model errors in the filter

5.3.2 Simulation scenario 2

In the second scenario, realistic orbit determination scenarios are simulated by considering perturbations due to third-body forces of Sun and Moon, Earth's gravitational harmonics and SRP. Variation in the drag-coefficient due to the coupled effects of changes in attitude and ambient parameters is simulated. The forces considered for the true trajectory and the filter model are given in table 5.4.

Table 5.4: Force models for truth and filter dynamics

Force	**Parameter**	**True dynamics**	**Filter dynamics**
Geopotential	Order and degree	10x10	10x10
Third-body forces of Sun and Moon	Ephemerides	JPL DE- 430	JPL DE-430
SRP	Model	Panel method	Cannonball, C_r is estimated
Atmospheric drag	Density model	NRLMSISE-00	NRLMSISE-00
	Drag coefficient	GSIM	Fourier model, Coefficients are estimated
	Winds	HWM-07	None
	Attitude noise	None	$\mathcal{N}(0, 0.1^0)$

A cuboidal satellite with mass 3400 kg with perigee altitude at 350 km is considered. The initial orbital elements of the satellite are given in table 5.5. A box-wing shape model for the satellite is considered, similar to case 2 in scenario 1.

In the last simulation scenario, the initial estimates of the coefficients were computed for the different models which allowed us to neglect the coefficients whose initial estimates were zero. But that assumes knowledge of the shape model and drag coefficient variation in orbit. In this scenario, no apriori knowledge of the Fourier coefficients is assumed and therefore all the coefficients up to the order considered are estimated. The coefficients are arbitrarily initialized to 1 and the standard deviations are initialized to 10. The various cases for which the Fourier models are tested are

Table 5.5: Initial orbital elements

Element	Value
Apogee altitude	550 km
Perigee altitude	350 km
Eccentricity	0.012
Inclination	65^0
Argument of perigee	40^0
Right ascension of ascending node	0^0
True anomaly	0^0
Initial epoch	$2017-05-29\ 00:00:00\ UTC$

summarized in table 5.6. It should be noted that the reference cross-sectional area in eq. (1.1) is kept constant for all the cases and drag-coefficient models. Whereas the body-dependent models such as BFF, BODF and BOS account for the varying cross-sectional area in the drag-coefficient, the cannonball and OFF models do not. Therefore, while using OFF and cannonball models, the drag equation does not account for the changing attitude. The cases considered in this scenario are summarized in table 5.6.

Table 5.6: Summary of simulated cases

Cases	**Description**
Nadir pointing	The body z-axis points towards the center of Earth
Inertially stabilized	The body z-axis tracks the Sun
Quasi-inertial stabilization	The body z-axis tracks the Sun in light and points towards the Earth center in shadow
Attitude maneuver	Quasi-inertial stabilization until end of second day and nadir pointing afterwards
Geomagnetic activity errors	Biases in the A_p indices that result in density errors in the filter model
Solar activity errors	Biases in $F_{10.7}$ indices that result in density errors in the filter model

It is valuable to see which models fit the 'true' drag coefficient the most accurately in a least-

squares sense. The Fourier models are fit to the simulated 'true' drag coefficients as a function of the body angles and/or argument of latitude (depending on the model considered) using the nonlinear least squares fit function in MATLAB. A one-day time profile of the 'true' drag coefficients for the inertially stabilized case is considered, similar to the orbit determination scenario. The root-mean-square (RMS) values of the fit are presented in table 5.7. The RMS values are progressively smaller from OFF to BODF. For BODF, there's a significant drop in the RMS value due to the larger number of fitting parameters as compared to the other models that leads to overfitting. A smaller RMS value for the fit does not imply that the performance for the model will be better in orbit determination but it does give an estimate of how well the model can approximate the true drag coefficient if the truth is available.

Table 5.7: RMS values for error between true and least-squares fit drag coefficients with different Fourier models for the inertially stabilized case. The smallest RMS value is highlighted

	OFF Order 2	**BFF Order 2**	**BOS Order 2**	**BODF Order 2**
RMS	0.234	0.225	0.211	**0.122**

1. *Nadir pointing*

The satellite is assumed to be nadir pointing. Therefore, the variation of relative velocity vector in body frame is only due to co-rotation of the atmosphere and the eccentricity of the orbit. Since the effect of the co-rotating atmosphere on drag coefficient is very small as seen in scenario 1, it can be neglected without any significant degradation in accuracy. The variation in velocity vector due to the eccentricity of the orbit is even smaller ($< 1^0$) resulting in a negligible effect on the drag coefficient. Therefore, the drag coefficient varies solely due to ambient parameters. The performance of order 2 OFF model is compared to standard cannonball (order 0) in fig. 5.16. The estimated and true drag coefficients are also plotted in the same figure.

The OFF order 2 model performs better than the standard cannonball model, resulting in a 50 % improvement in accuracy at the end of 3 days of prediction. But the errors are quite small to begin with since the only dynamics error is in the drag and SRP coefficients, and due to upper

atmospheric winds. It can be seen in fig. 5.16 that the estimated drag coefficient does not follow the true drag coefficient very well. The improvement in performance is mainly because the model provides a better orbit fit resulting in a more accurate initial state.

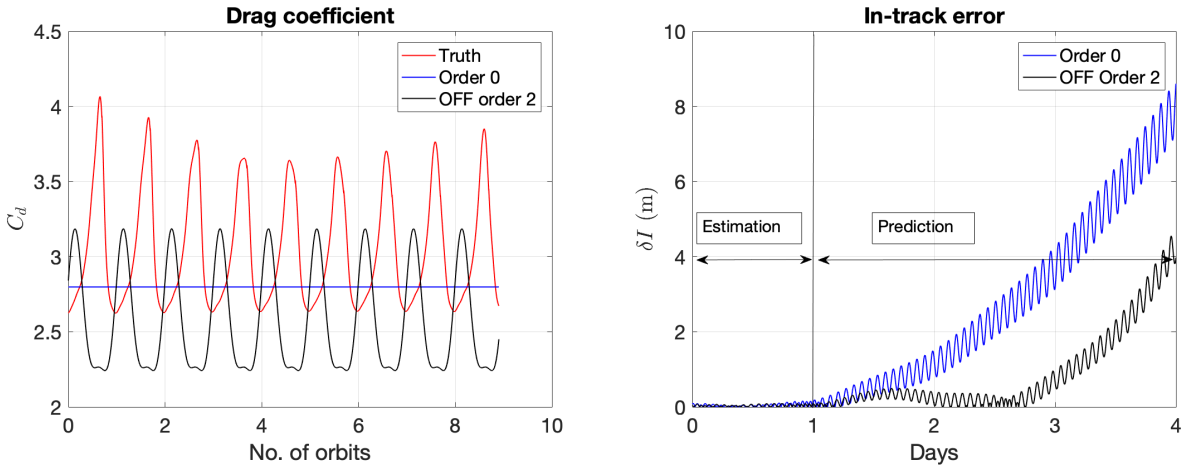

Figure 5.16: Nadir pointing: True and estimated drag coefficients (left) and in-track error (right). Order 0 refers to cannonball model.

2. *Inertially stabilized*

The satellite attitude is considered to be inertially stabilized such that the solar panels are tracking the sun. The variation of drag coefficient is due to the changing orientation with respect to the atmospheric flow and ambient parameters. The performance of BFF and OFF models are expected to be similar in this case since the rate of variation of the body angle is the same as that of argument of latitude other than a phase difference. But since the argument of latitude is tied to the orbit, its period varies with each iteration of the batch estimator as corrections are added to the initial state. In contrast, the body angle variation remains the same. Therefore, the results for BFF and OFF models are different as shown in fig. 5.17.

All the higher orders perform better than the standard cannonball model (order 0). Order 2 BODF performs the best, resulting in almost a 90 % improvement in the in-track prediction error over cannonball. In order to understand the relative performances of the models, it is useful to look at the error statistics of the estimated states for the different models. Table 5.8 lists the RMS values of the post-fit residuals in the radial-tangential-normal (RTN) frame, the norm of the initial

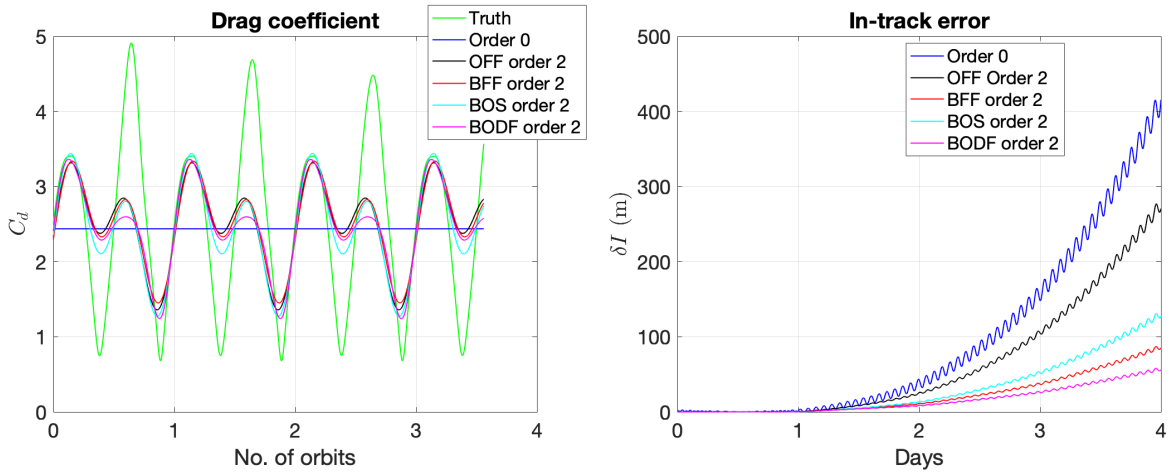

Figure 5.17: Inertially stabilized: True and estimated drag coefficients (left) and in-track error (right). Order 0 refers to cannonball model. The estimation window is until the end of the first day and the rest is prediction.

errors in the estimated states and the RMS values of the drag coefficient errors. As can be seen from table 5.8, the overall prediction errors are an interplay between improvements in orbit fit, estimated SRP coefficient and effective drag coefficient. Even though the OFF model provides the best estimates of the initial position and velocity, better estimates of the drag coefficient are obtained using the other models. It is difficult to conclude anything about the prediction performance of the

Table 5.8: RMS and norm of errors for inertially stabilized satellite. The smallest values for each parameter are highlighted

Parameter		**Error RMS/Norm**				
		Order 0	**OFF**	**BFF**	**BOS**	**BODF**
Post-fit residuals (m)	R	1.5804	1.5044	1.5041	1.5040	**1.5039**
	T	1.7929	1.5148	1.5110	1.5106	**1.5096**
	N	1.4996	1.4995	1.4995	1.4995	1.4995
Initial error	Position (m)	1.260	**0.046**	0.134	0.152	0.201
	Velocity (m)	8.994e-4	**4.804e-5**	1.347e-4	1.670e-4	2.303e-4
	C_r	1.15	0.13	0.19	**0.01**	0.03
Drag coefficient	Total	1.11	0.91	0.86	**0.84**	0.88

models through the tabulated metrics due to the presence of other unmodeled dynamics in the filter such as time-varying SRP and winds that affect the velocity magnitude. For example, even though

the error in initial estimates of the states as well as the coefficient errors are higher for BODF and BFF than BOS, the latter performs worse as seen in fig. 5.17. Therefore, in order to assess the performance of the models in an idealized scenario with no unmodeled dynamics other than drag-coefficient, the true SRP force is assumed to be known in the filter and C_r is not estimated. The winds and attitude noise are also removed from the simulated truth. The in-track errors are plotted in fig. 5.18. As seen in fig. 5.18, the prediction performance of the BFF and BODF models

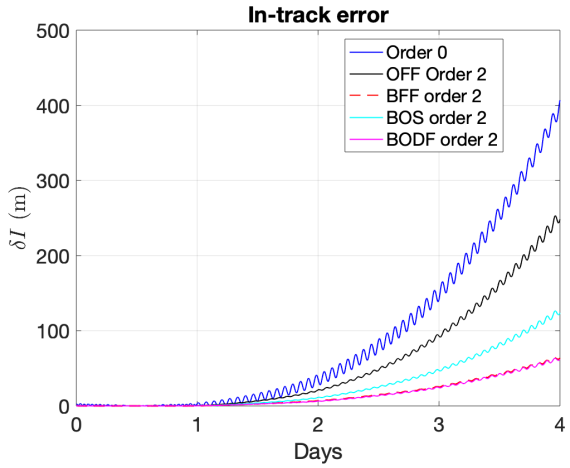

Figure 5.18: Inertially stabilized: In-track errors for the different Fourier models with no unmodeled dynamics in the filter other than drag coefficient

are similar in the absence of unmodeled dynamics other than drag coefficient. The advantage of BODF is that it provides a better fit when other force parameters are being estimated in the filter. Order 2 BOS still performs worse than BFF and BODF even though the error in the initial state estimates and the RMS of drag-coefficient error is smaller for BOS (not presented here for the sake of brevity). Why should the BOS perform worse when the overall errors in the drag acceleration are smaller for the model? The answer lies in the process of integrating the dynamics itself. Consider two time-varying arbitrary states $x(t)$ and $y(t)$ with their derivatives given by $\dot{x}(t)$ and $\dot{y}(t)$. The states at any time are given by

$$x(t) = x_0 + \int_{t_0}^{t} \dot{x}(t)dt$$

$$y(t) = y_0 + \int_{t_0}^{t} \dot{y}(t)dt \tag{5.60}$$

where x_0 and y_0 are initial states. The error between the two states can be written as

$$(x(t) - y(t)) = (x_0 - y_0) + \int_{t_0}^{t} (\dot{x}(t) - \dot{y}(t))dt \tag{5.61}$$

The error between the two states is a function of the error between the acceleration integrals. Therefore, even if the RMS of the error between the two accelerations is small, the error in the propagated states can be large if the difference between the integrals of the accelerations is significant. This provides a clue for the reason behind the prediction performance of BOS compared to BFF and BODF. The integrated drag acceleration error is essentially an integral of the drag coefficient error (ΔC_d) weighted by the density ($\rho(t)$), square of the relative velocity ($V_r(t)$) and other constant parameters. Even if the drag coefficient error is smaller for a model, the weighted sum may not be. In other words, $\int_{t_0}^{t} \Delta C_d(t)dt$ being smaller for BOS does not imply $\int_{t_0}^{t} \Delta C_d(t)\rho(t)V_r^2(t)dt$ is smaller as well. For fig. 5.18, the integral of the drag acceleration error in the relative velocity direction (compared to the true acceleration) for BOS is 3.72×10^{-4} m/s^2 compared to 1.87×10^{-4} m/s^2 for BFF and BODF. Similarly for fig. 5.17, the integrated drag acceleration error for BOS is 7.65×10^{-4} m/s compared to 7.16×10^{-4} m/s for BFF and 5.49×10^{-4} m/s for BODF.

3. *Quasi-inertial stabilization*

For many real satellites, the solar panels track the Sun when in light and become feathered to the atmosphere in shadow to reduce drag effects. A similar scenario is simulated in this case where the satellite is inertially stabilized in light and rotates gradually on entering shadow to become nadir pointing. The performance of the Fourier models is similar to the previous case as seen in fig. 5.19 though the in-track error difference between BFF and BOS is smaller.

The post-fit residuals, initial state errors, RMS of error in drag coefficient and integrated drag-acceleration error are provided in table 5.9. The BFF model provides the most accurate drag coefficient estimates while BOS provides the most accurate SRP coefficient estimates. From the discussion in the last section, order 2 BODF performs the best as it has the smallest integrated

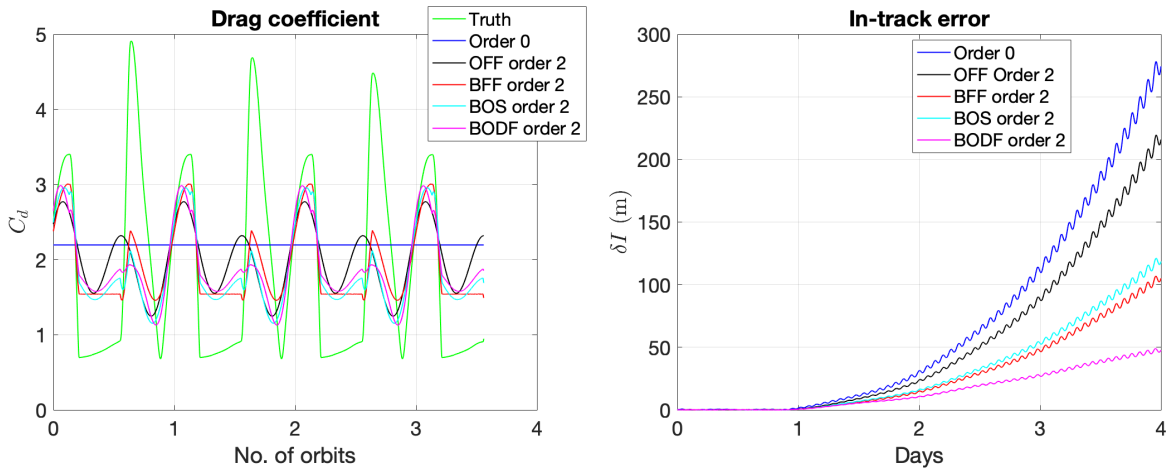

Figure 5.19: Quasi-inertial stabilization: True and estimated drag coefficients (left) and in-track error (right). Order 0 refers to cannonball model. The estimation window is until the end of the first day and the rest is prediction.

drag acceleration error value as seen in table 5.9. Order 2 BFF performs slightly better than order 2 BOS even though the integrated acceleration error is larger for the former. From eq. (5.61) the final error in the states is dependent on the initial state errors as well, which is smaller for BFF.

4. *Attitude maneuver*

Due to the large atmospheric drag effects of solar panels on a satellite orbit, they may be kept feathered to the flow for specific periods [22]. This is simulated by assuming that the satellite is quasi-inertially stabilized until the end of second day and then remains nadir pointing on entering shadow for the rest of prediction period, i.e., an attitude maneuver is assumed to take place outside the estimation interval. The estimated Fourier coefficients and therefore, the effective drag coefficients remain the same as the previous case since there's no change during the estimation interval. But the predicted drag coefficients after day 2 change for the body dependent terms as the orientation changes. The in-track errors until day 2 and for the complete prediction period are plotted in fig. 7.3 and the predicted drag coefficients after the maneuver are plotted in fig. 5.21.

All the Fourier models perform better than the cannonball but the improvement with order 2 OFF is negligible in this case. Order 2 BODF performs better than order 2 BFF until day 2 and the performance slightly degrades afterwards.

Table 5.9: RMS and norm of errors for a quasi-inertially stabilized satellite. The smallest values for each parameter are highlighted

Parameter		**RMS/Error norm**				
		Order 0	**OFF**	**BFF**	**BOS**	**BODF**
Post-fit residuals (m)	R	1.5208	1.5177	1.5181	1.5175	**1.5174**
	T	1.5505	1.5060	1.5030	1.5038	**1.5003**
	N	1.5085	1.5085	1.5085	1.5085	1.5085
Initial error	Position (m)	0.365	0.088	**0.086**	0.113	0.174
	Velocity (m/s)	5.562e-4	1.131e-4	**4.033e-5**	1.2387e-4	1.8874e-4
	C_r	1.104	0.313	0.274	**0.074**	0.114
Drag coefficient	Total	1.252	1.152	**0.890**	1.024	1.04
Integrated drag acceleration error	Integrated	1.9e-3	1.3e-3	9.74e-4	8.92e-4	**6.52e-4**

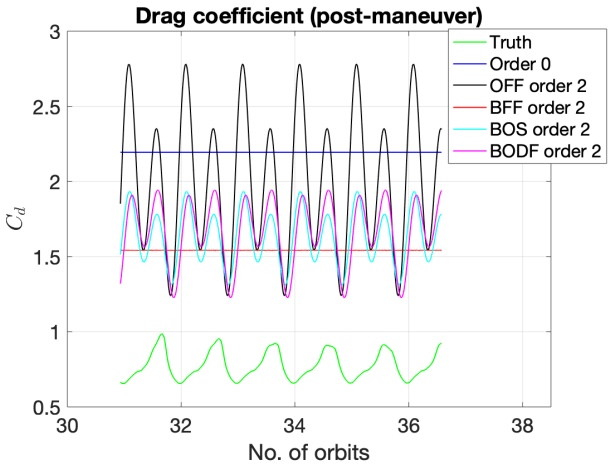

Figure 5.21: Attitude maneuver: Predicted drag coefficients post-maneuver

As can be seen from table 5.10, order 2 BFF model provides the most accurate estimates for drag coefficients pre and post-maneuver. But the integrated acceleration error is smaller for BODF pre-maneuver, which is why it performs better than BFF. After the maneuver, the integrated acceleration error is slightly larger for BODF.

The post-maneuver prediction is sensitive to the estimated Fourier coefficients and therefore, their initial covariance. For example, constraining the covariance of the zeroth order term for all the models to 1 leads to the prediction performance in Fig. 5.22. Whereas the BOS and BFF

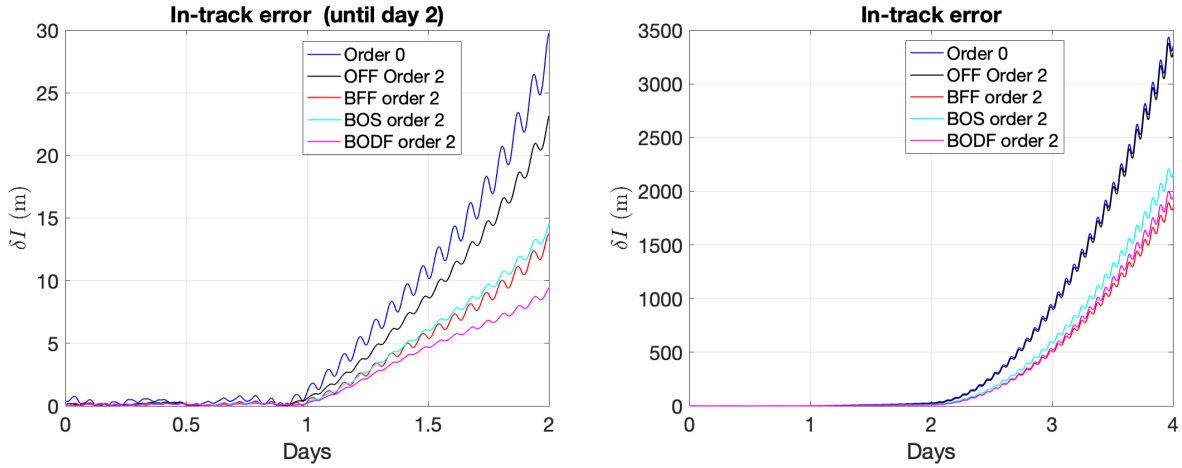

Figure 5.20: Attitude maneuver: In-track error until day 2 (left) and in-track error until day 4 (right). Order 0 refers to cannonball model. The estimation window is until the end of the first day and the rest is prediction.

Table 5.10: Drag coefficient errors (RMS) and integrated acceleration errors for the different Fourier models for a quasi-inertially stabilized satellite with an attitude maneuver

Parameter		**RMS**				
		Order 0	**OFF**	**BFF**	**BOS**	**BODF**
Drag coefficient	Pre-maneuver	1.252	1.152	0.890	1.024	1.04
	Post-maneuver	1.408	1.279	0.750	0.856	0.886
Integrated drag acceleration error	Pre-maneuver	7.15e-4	4.86e-4	3.99e-4	3.94e-4	3.57e-4
	Post-maneuver	0.0125	0.0122	0.0073	0.0081	0.0074

models degrade in performance, the BODF shows a better prediction than Fig. 7.3. The estimated Fourier coefficients are sensitive to the initial covariance in all test cases. But it is especially more significant in this case because after the attitude maneuver, the body-fixed part of the resultant drag-coefficient becomes constant at a larger error as depicted by the flatter portions of the curves in Fig. 5.19. The sensitivity of the Fourier models to the initial covariance needs to be further analyzed.

5. *Density model errors*

To simulate the effects of erroneous solar and geomagnetic activity indices in the density

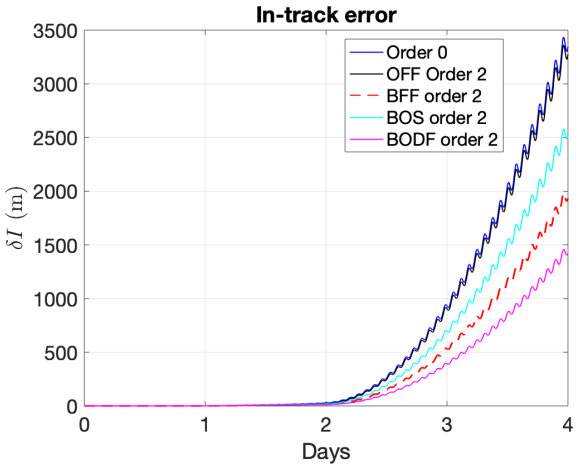

Figure 5.22: Attitude maneuver: In-track errors for the different Fourier models with a smaller covariance for the zeroth order term

models on the performance of the Fourier models, biases are introduced individually in the indices as follows.

The simulation duration is selected for a geomagnetically quiet period where the daily A_p index for the four days is 3 or 4. In the filter density model, a constant bias is added to the A_p indices for the four days of estimation and prediction. The analysis is carried out for both nadir pointing and quasi-inertially stabilized attitude profiles. The maximum predicted in-track error for both attitude profiles are plotted in Fig. 5.23.

It can be seen that all the Fourier models perform significantly better than the order 0 model. Due to the periodic nature of Fourier models, the estimated Fourier coefficients absorb periodic errors in density introduced by the A_p bias. Since the bias is introduced in both estimation and prediction intervals, the density error trends remain the same throughout. As a result, the estimated drag coefficient fits the dynamics well. But in reality, the current A_p index, i.e., the A_p index during the estimation interval, will be known more accurately than the forecasted indices for the prediction interval. Therefore, a bias is introduced in the indices, only during the prediction interval. As a result, there are no errors in the density during the orbit determination interval and the estimated drag coefficients do not respond to the A_p biases in the prediction. The performance of the models for this case is plotted in Fig. 5.24. The maximum errors in Fig. 5.24 are much higher than Fig.

5.23 due to the preceding reasons. The higher order models still perform better than order 0 but the improvement is much smaller than Fig. 5.23 since the Fourier models cannot account for errors in predicted values.

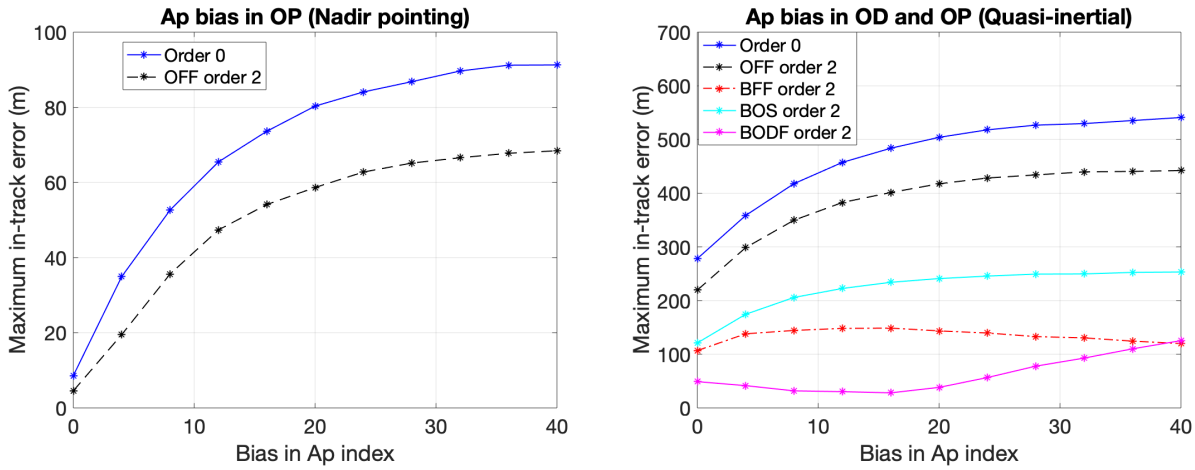

Figure 5.23: Maximum in-track prediction error as a function of bias in the A_p indices for nadir pointing (left) and quasi-inertial (right) attitude profiles. The bias is introduced in both the OD and OP intervals

The next case is selected for a period of solar minimum with the daily $F_{10.7}$ values around 63-67 SFU. A constant bias in all the forecasted indices is introduced. The performance of the different models is compared in Fig. 5.25. Since NRLSMSISE-00 uses $F_{10.7}$ index of the previous day, the bias in daily $F_{10.7}$ value affects the density model from the third day onward. But NRLMSISE-00 also uses an 81 day average of the $F_{10.7}$ index centered on the current day. Therefore, the average value is inaccurate for all the four days, with the error increasing for consecutive days of prediction as more forecasted values are used to calculate the average. All the higher order Fourier models perform better than the cannonball model.

5.4 Application to real data

In order to process real satellite measurement data with the Fourier models, a similar setup as the simulations can be used. But a higher order gravity field is needed for an actual satellite. Truncation of the gravity field at a low order and degree results in aliasing of the gravity field

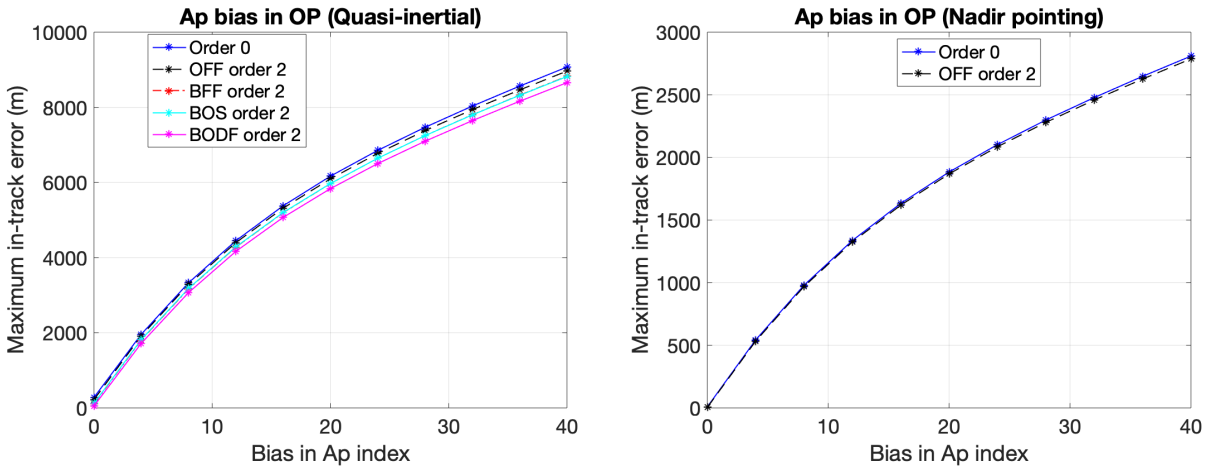

Figure 5.24: Maximum in-track prediction error as a function of bias in the A_p indices for nadir pointing (left) and quasi-inertial (right) attitude profiles. The bias is introduced only in the OP interval

with the non-gravitational force coefficients as discussed in chapter 4. Here, we simply take a 'high enough' truncation degree and order (150×150) of the gravity field in the filter model to minimize these effects. An SRP force model higher in fidelity than the simulations is used where the force is assumed to be acting along three mutually perpendicular directions known as three-constants model [69]. Therefore, the state vector to be estimated consists of position, velocity, Fourier coefficients and the three SRP constants.

5.4.1 Satellite with varying attitude

These models are applied to real data from a NASA satellite at 407 km. GPS and quaternion data are available for the satellite for two time periods: Jan 1-6, 2017 and June 29- July 6, 2017. The satellite consists of two large solar panels that track the Sun or are kept feathered to the flow to reduce drag effects. One of the solar panels is canted at an angle to the satellite body. The overall dimensions of the satellite are 5 m x 13 m x 6.5 m. The shape of the satellite is primarily cuboidal but with multiple protruding and curved surfaces. A one-day data arc is processed in the batch estimator and propagated for the rest of the available dataset. Predicted positions at the GPS epochs are then generated using the propagated orbits. The position norm of the error

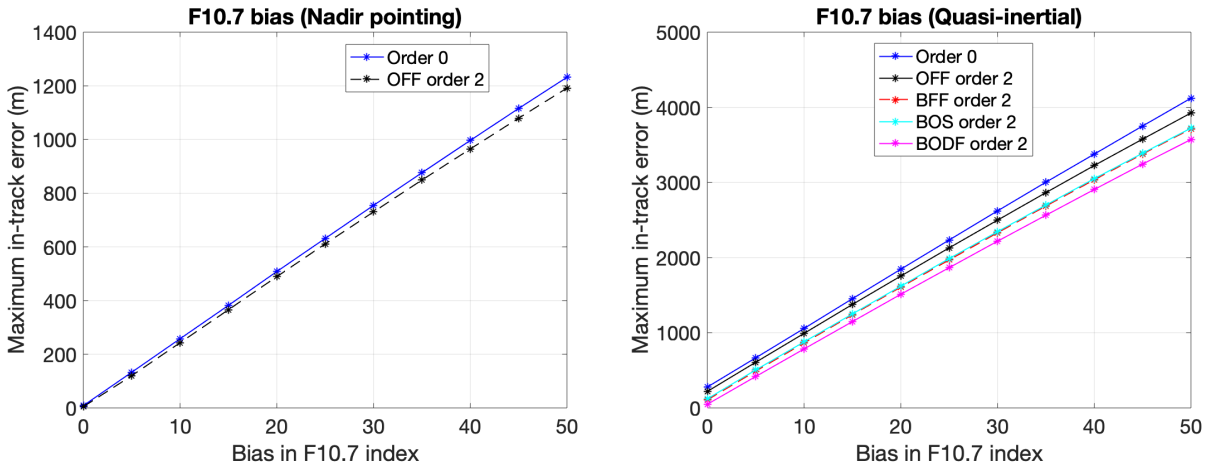

Figure 5.25: Maximum in-track prediction error as a function of bias in the $F_{10.7}$ indices for nadir pointing (left) and quasi-inertial (right) attitude profiles.

between the actual GPS measurements and predicted positions is used to compare the performance of the different Fourier models.

1. *Dataset 1: June 29- July 6, 2017*

In the first dataset, one solar panel is quasi-inertial for the first three days (two days of prediction) and then becomes feathered to the atmosphere. The other solar panel remains feathered to the atmosphere throughout. The body-dependent models are fixed to the rotating solar panel in this case. In a real orbit determination scenario, there are unmodeled dynamics through various sources such as atmospheric density and SRP. All these unmodeled dynamics are aliased in the estimates of the Fourier coefficients. In the absence of 'true' drag-coefficients and initial states, the only performance metrics are prediction errors and post-fit residuals. The prediction error at the end of the three days and nine days are plotted in fig. 5.26. All the higher order Fourier models perform better than the cannonball in this case. The BODF model reduces the prediction error by almost 50 % at the end of 9 days. The RMS values of the post-fit residuals in the RTN frame are given in table 5.11.

2. *Dataset 2: Jan 1-6, 2017*

In the second dataset, both the solar panels of the satellite are quasi-inertial, while the bus is nadir pointing. Therefore, the body dependent models are fixed to the solar panels with the

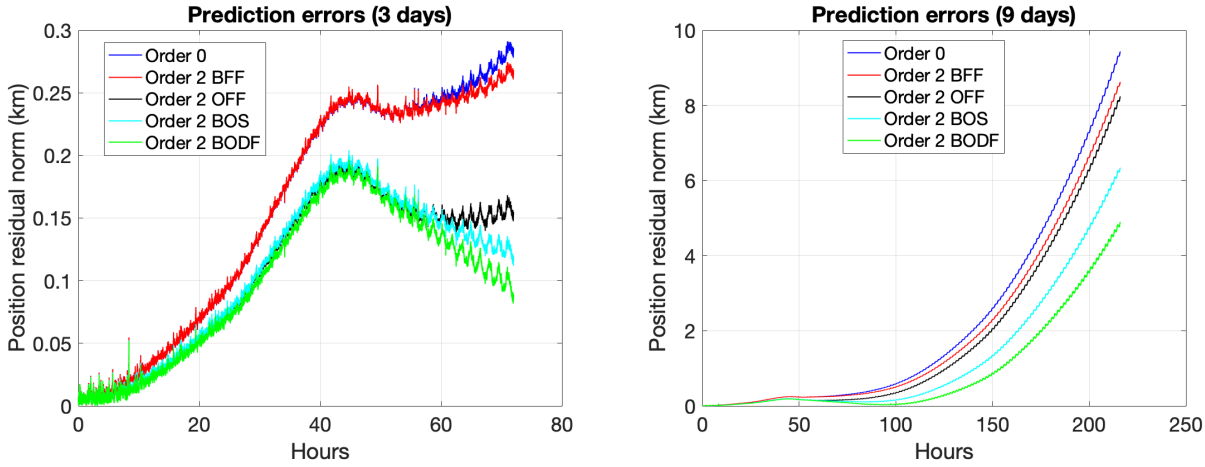

Figure 5.26: The error norm of predicted GPS positions for 3 days and 9 days; the estimation window is not shown in the figure.

Table 5.11: RMS values of post-fit residuals in RTN frame for dataset 1

Parameter		**RMS**				
		Order 0	**OFF 2**	**BFF 2**	**BOS 2**	**BODF 2**
Post-fit residuals (m)	R	5.7526	5.7259	5.7291	5.7259	**5.7248**
	T	2.8488	2.8337	2.8474	2.8340	**2.8314**
	N	2.7410	1.9962	**1.9954**	1.9961	1.9963

contribution of the bus being absorbed in the zeroth order coefficient. The prediction error at the end of the one day and five days are plotted in fig. 5.27. For this dataset, the BFF and BODF models show an improvement over cannonball model but the higher order OFF and BOS models perform worse. Inspecting the RMS values of the post-fit residuals in table 5.12, the order 2 BOS and OFF models actually provide a better fit than order 2 BFF and therefore, more accurate prediction in the initial duration after the estimation arc. But as seen in section 5.3.2, smaller post-fit residuals do not imply a better long-term prediction. The prediction performance is dependent on the integrated drag acceleration error which cannot be computed due to the absence of a 'truth'. The relative performance of each model is dependent on the metric being used to evaluate the models. Note here that the RMS values in the in-track direction are larger for dataset 2 than dataset 1 since both the solar panels are quasi-inertial in this case leading to a higher drag force.

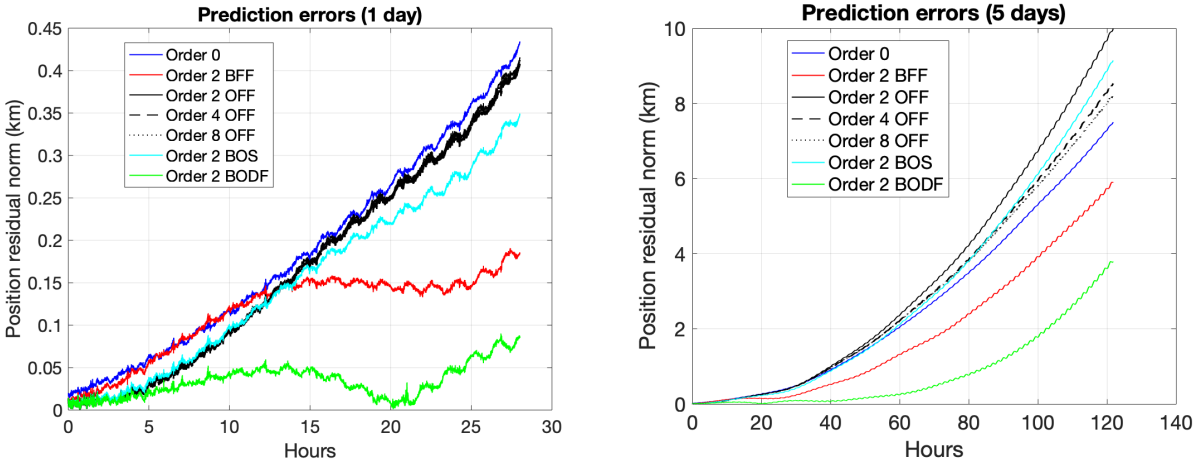

Figure 5.27: The error norm of predicted GPS positions for 3 days and 5 days; the estimation window is not shown in the figure.

5.4.2 GRACE data

POD from GRACE-B satellite in section 5.4 is processed in the batch estimator with different density models to analyze the dependence of the Fourier models' performance on density errors. The satellite maintains a stable attitude w.r.t the local velocity vector, within 5^0. And as seen for the nadir pointing case in section 5.3.1, the body-fixed models cannot capture changes in the drag-coefficient for such small attitude changes. Therefore, only the OFF model is used in this case. Four different density models/estimates as shown in fig. 5.28 are used in the filter - NRLMSISE-00, JB2008, HASDM and estimates derived by Mehta et al. [73] by using RSM modeled drag-coefficients [72]. There are significant discrepancies between the different density models that lead to differences in the orbit determination and prediction errors as seen in fig. 5.29. The nominal drag-coefficient in fig. 5.29 refers to the RSM drag-coefficients, i.e., the drag-coefficients are not estimated in this case. The performance of the higher-order OFF corrections to the RSM model depends on the density model being used - order 2 improves the prediction errors for JB2008 and HASDM but not for the others. To obtain an improvement in the prediction errors with NRLMSISE-00, an order 8 model is needed (fig. 5.29 (c)) while an order 2 model with only the cosine coefficients suffices for the Mehta et al. [73] densities (fig. 5.29(d)). It is evident that the estimated OFF coefficients

Table 5.12: RMS values of post-fit residuals in RTN frame for dataset 2

Parameter		RMS				
		Order 0	**OFF 2**	**BFF 2**	**BOS 2**	**BODF 2**
Post-fit residuals (m)	R	7.3482	5.7747	5.9454	5.7760	**5.7596**
	T	7.5628	5.1512	5.4117	5.1441	**5.1344**
	N	1.9603	1.9736	1.9916	1.9781	**1.9559**

are absorbing density model errors due to the high correlation of the model with the atmospheric density. Therefore, for a higher-fidelity density, the magnitude of Fourier corrections are smaller as seen in fig. 5.29 (b).

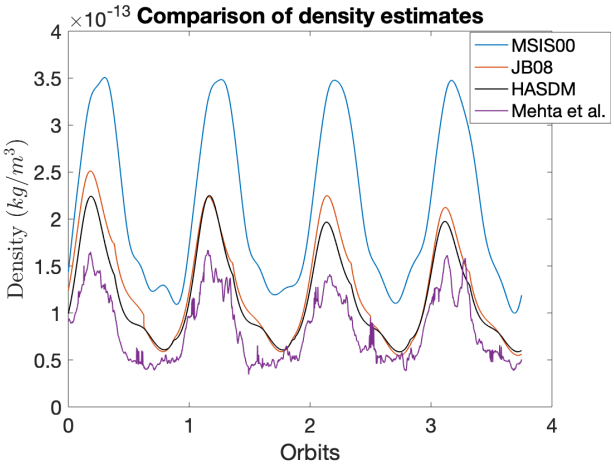

Figure 5.28: Densities used in the batch estimator to process GRACE POD

5.5 Chapter summary

In general, tracking the variations in the drag coefficient during the orbit determination process is quite difficult due to its dependence on various satellite dependent and ambient parameters. Analytical models and numerical approaches provide important insights into the physics of gas-surface interactions and are important in computing initial estimates of the drag coefficient. But these approaches can be difficult to implement in operations due to observability issues and computational load. Introduction of machine-learning techniques to the problem has resulted in significant advances for post-processing applications. But further work needs to be done before

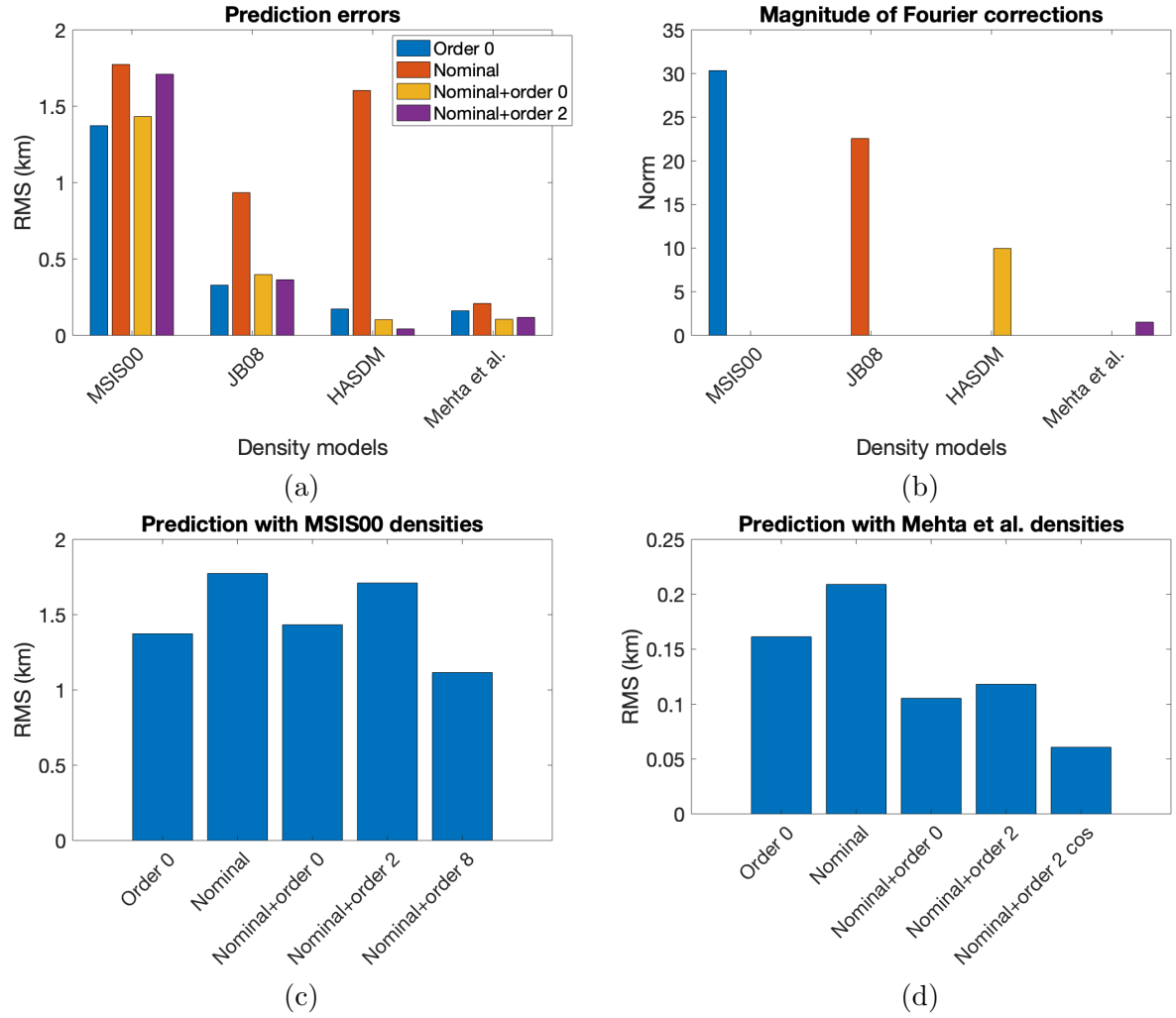

Figure 5.29: (a) Orbit prediction error with different density and drag-coefficient models; (b) Magnitude of Fourier corrections for the different density models; (c) Prediction error with NRLMSISE-00; (d) Prediction error with Mehta et al. derived densities [73]

such models can be implemented for operational use. Modeling the drag coefficient in terms of a Fourier series provides a simple way of estimating the drag coefficient due to the orthogonality of the Fourier coefficients.

Four different models are developed in this work to model the variations of the drag coefficient due to 1) attitude shifts and 2) ambient parameter variation. The first model proposed is a Fourier expansion of the drag coefficient in the body frame of the satellite. The body-fixed Fourier (BFF) model consistently improves the position errors due to the attitude dependent variation of the drag

coefficient, especially in cases where the attitude variation is significant. The order of the model needs to be chosen with care depending on the shape of the satellite in order to expect improvements in the performance. One limitation of the model is that it cannot respond to variations in the drag coefficient due to factors other than the attitude, such as ambient parameters. The second model, orbit-fixed Fourier (OFF) model, tied to the satellite's orbital position, is introduced to address this issue. In the inertially stabilized case, the BFF coefficients are close to the OFF coefficients since the attitude varies at the same rate as the true anomaly. It is evident that the body-fixed and the orbit-fixed models have advantages in different scenarios. The body-orbit double Fourier (BODF) and body-orbit summation (BOS) models are developed to combine the advantages of the BFF and OFF models to capture variations due to both attitude and orbit-dependent parameters. Whereas the BODF model uses a double Fourier expansion and contains cross-dependent terms between the body-fixed and orbit-fixed approaches, BOS is a truncation of the BODF by ignoring such terms. The OFF model is the only one among the four that can be used to estimate the drag coefficient for objects whose attitude profile is not known. But when the attitude profile is known, the other models tend to perform better than the OFF model.

The four models are evaluated on different performance metrics that can be used to select the model depending on the scenario. Whereas the orbit determination performance can be compared based on the post-fit residuals and errors in the initial states and parameters, the orbit prediction performance is tied to the integrated acceleration error. Both are correlated but one does not necessarily imply the other. Due to the presence of a larger number of terms, BODF can provide a better orbit fit in terms of post-fit residuals especially in the presence of other force parameters being estimated. BODF also tends to provide the best integrated acceleration error leading to the most accurate orbit prediction among all. The application of BODF to real data results in an improvement of almost 50 % over cannonball model in the in-track prediction error at the end of 9 days of prediction. The BFF and BOS models provide the most accurate drag-coefficients among the four. The BFF model has a similar integrated acceleration error and prediction performance to BODF when only the states and the Fourier coefficients are being estimated in the filter in

the absence of unmodeled dynamics other than drag coefficient. The BOS model provides an orbit-fit and drag coefficients matching in accuracy with BODF and BFF and even exceeding them in some cases, but tends to have a larger integrated acceleration error leading to a poorer prediction performance. OFF does not perform as well as the other models for objects with varying attitude. In terms of the number of estimated parameters for the same order and thus computational complexity, BODF contains the maximum parameters followed by BOS, and then BFF and OFF contain the same number of parameters. All the performance metrics have their own merit based on the application and can serve as guidelines while selecting among the models to estimate the drag coefficient in a filter. The best indicator for the prediction performance is the integrated acceleration but it cannot be computed for actual orbit determination scenarios. In all test cases, the model with the best prediction performance has the smallest post-fit residuals. But the same cannot be said for the intermediate performing models. Therefore, it is difficult to accurately rank the performance of all the models in real scenarios when predicting the satellite positions into the future.

Any errors in the atmospheric density model will directly affect the drag coefficient model used in the filter. A preliminary analysis of the performance of the Fourier models in the presence of simplistic density errors due to a mismatch in the geomagnetic activity between the truth and filter models demonstrates that the Fourier models still show an improved prediction performance over the standard cannonball model even though the estimated drag coefficient does not track the true drag coefficient. In fact, the orbit-fixed model can respond to periodic errors in the atmospheric density model and shows a significant advantage in the presence of density errors. The analysis of density errors presented in this work is highly simplified since in reality the density models will have more complicated time-varying errors. In particular, during times of high geomagnetic activity, the density can change in very short time scales. The prediction performance of the Fourier models with real data indicates a better performance than the cannonball model or simply using a GSIM. But the Fourier coefficients absorb errors in the density model and thus, are highly dependent on the atmospheric model being used in the filter. It is evident that a method to simultaneously estimate

the atmospheric densities is needed to obtain physically realistic values of the Fourier coefficients. We develop such a framework in chapter 7.

An important goal of this work is to use the estimated Fourier coefficients to provide better estimates of GSIM parameters and atmospheric densities. The drag-coefficient errors using the different Fourier models are relatively large even though they are improved compared to the cannonball model. In this chapter, it has been assumed that all Fourier coefficients up to the assumed order can be estimated from the given data-arc. But correlations between estimated coefficients can impact their observability and hence the estimation errors [45]. The next chapter delves into the inversion of GSIM parameters from the estimated Fourier coefficients.

Chapter 6

Inversion of gas-surface interaction model (GSIM) parameters

In the previous chapter, Fourier drag-coefficient models were developed that capture specific frequencies of the time-varying drag-coefficient in an estimation framework. It was demonstrated that supplementing the cannonball estimate (Order 0) with higher-order Fourier coefficient estimates that govern orbit-dependent and attitude-dependent frequencies can improve orbit determination and prediction significantly. A body-fixed Fourier (BFF) model was developed to capture attitude-dependence of the drag-coefficient while an orbit-fixed Fourier (OFF) model was developed for the orbit-dependence of the drag-coefficient. The overall variation of the drag-coefficient due to both attitude and orbit-related factors was modeled with body-orbit double Fourier (BODF) and body-orbit summation (BOS) methods. In this chapter, a framework is developed to invert specific GSIM parameters from the Fourier coefficients that are estimated as part of the orbit determination process. In order to derive meaningful information from the Fourier coefficient estimates, an extensive analysis of the dependence of the Fourier coefficient estimates on the information content of the tracking data-arc is required.

Observability analysis of a system forms an integral part of determining what parameters can be estimated with the given information. There are two aspects associated with the effects of parameters on a system. First, whether a parameter has a non-zero effect on the dynamics distinct from the effects of other parameters. Second, if the effects remain distinguishable when translated to the measurement space. Observability analysis deals with the latter. Observability of a system has been extensively explored in aerospace engineering systems through various observability matrix

metrics. The commonly used binary test for observability based on the rank of the observability matrix is defined for linear systems but can be extended to linearized systems such as the orbit determination problem here. There are multiple other measures of observability that can be utilized to understand the extent or 'degree' to which a parameter is observable. The degree of observability can be determined by how close the observability matrix is to singularity through measures such as condition number of the observability matrix [14, 38, 54], singular values of the observability matrix [54, 35] and the cost function of the optimization algorithm [36]. Metrics such as the correlation coefficient can be utilized to remove sets of highly correlated parameters [45] whose effects on the measurements might be indistinguishable.

Even though these measures quantify the observability of the system, they don't provide a direct method to determine which states and parameters are observable. All the metrics can be evaluated by removing combinations of parameters from the estimation set and then comparing the metric values of the different subsets to determine which parameters are poorly observable. But it can become quite cumbersome for systems with a large number of parameters. The concept of parameter identifiability [10], frequently encountered in environmental and biological systems, is useful in determining what parameter subset should be estimated. Instead of deducing observability directly, the parameters can be ranked based on sensitivity of the measurements to the parameters. Using orthogonalization methods on the measurement sensitivity matrix allows a ranking of the parameters based on the norm of the sensitivity as well as the linear dependence of the sensitivity vectors [16, 62, 61]. Another emerging approach to identifying parameters is the active subspace method but it has not been considered in this work [18].

The observability of a system is intricately tied to the uncertainties of the estimated coefficients. Adding more parameters to the estimation subset increases uncertainties of the estimated coefficients with a given data-arc according to the Information Dilution Theorem [33]. On the other hand, ignoring parameters with large distinct effects on the measurements can lead to filter divergence where the uncertainties of the estimated coefficients are small but the estimated errors are large due to aliasing effects [101]. A consider covariance analysis can reveal the parameters

that have a negligible effect on the uncertainties of the estimated coefficients [124]. In this work, different observability metrics are used in combination with parameter-ranking methods based on measurement sensitivities and consider covariance analysis to conclusively determine which Fourier coefficients need to be estimated for different cases. From the reduced estimation set of Fourier coefficients, information on the GSIM parameters is extracted.

6.1 Chapter outline

The chapter is organized as follows. Section 6.2 discusses the observability metrics that are used to determine the estimation subset of the Fourier coefficients. The framework to invert GSIM parameters from the estimated Fourier coefficients is developed in section 6.3. The application of the observability methods to synthetic data with the ultimate goal of deriving useful estimates of the GSIM parameters is discussed in section 6.4. The results as obtained in the controlled simulation environment are discussed within the broader context in section 6.5. Section 6.6 summarizes the chapter and states the key conclusions.

6.2 Observability metrics

Observability of a system is the property that determines whether the given states can be uniquely estimated for the system with the available measurements. The metrics used to evaluate the observability of the Fourier coefficients for all the models are outlined in the following sections. In order to determine the order of truncation of the Fourier models, an observable set of Fourier coefficients needs to be deduced. The next section describes the analysis tools that are used for this purpose.

6.2.1 Observability matrix

The observability matrix of a linearized time-varying system can be constructed from the measurement Jacobian and state-transition matrix (STM). A non-linear time-varying system with constant parameters and no inputs can be described as follows

$$\begin{aligned}\dot{\boldsymbol{x}}(t) &= \boldsymbol{f}(\boldsymbol{x}(t), \boldsymbol{p}),\\ \boldsymbol{y}(t) &= \boldsymbol{h}(\boldsymbol{x}(t), \boldsymbol{p}).\end{aligned} \tag{6.1}$$

where $\boldsymbol{x}(t) \in \mathbb{R}^{n_x \times 1}$ and $\boldsymbol{p} \in \mathbb{R}^{n_p \times 1}$. The state and measurement Jacobians of the linearized system are then given by

$$\begin{aligned}\boldsymbol{F}(t) &= \left[\frac{\partial \boldsymbol{f}(t)}{\partial \boldsymbol{x}(t)^T}, \frac{\partial \boldsymbol{f}(t)}{\partial \boldsymbol{p}^T}\right],\\ \tilde{\boldsymbol{H}}(t) &= \left[\frac{\partial \boldsymbol{h}(t)}{\partial \boldsymbol{x}(t)^T}, \frac{\partial \boldsymbol{h}(t)}{\partial \boldsymbol{p}^T}\right]\end{aligned} \tag{6.2}$$

All the derivatives follow the row notation. The STM allows the transformation of the linearized states from one time to another as

$$\boldsymbol{\Phi}(t, t_0) = \begin{bmatrix} \dfrac{\partial \boldsymbol{x}(t)}{\partial \boldsymbol{x}(t_0)^T} & \dfrac{\partial \boldsymbol{x}(t)}{\partial \boldsymbol{p}^T} \\ \dfrac{\partial \boldsymbol{p}}{\partial \boldsymbol{x}(t_0)^T} & \dfrac{\partial \boldsymbol{p}}{\partial \boldsymbol{p}^T} \end{bmatrix} = \begin{bmatrix} \dfrac{\partial \boldsymbol{x}(t)}{\partial \boldsymbol{x}(t_0)^T} & \dfrac{\partial \boldsymbol{x}(t)}{\partial \boldsymbol{p}^T} \\ \boldsymbol{0}_{n_p \times n_x} & \boldsymbol{I}_{n_p \times n_p} \end{bmatrix} \tag{6.3}$$

It can be computed by numerically integrating the following differential equation [124]

$$\dot{\boldsymbol{\Phi}}(t, t_0) = \boldsymbol{F}(t)\boldsymbol{\Phi}(t, t_0), \qquad \text{with} \qquad \boldsymbol{\Phi}(t_0, t_0) = \boldsymbol{I} \tag{6.4}$$

The complete measurement sensitivity matrix for the data-arc can then be computed by

$$\boldsymbol{H} = \begin{bmatrix} \tilde{\boldsymbol{H}}(t_0) \\ \tilde{\boldsymbol{H}}(t_1)\boldsymbol{\Phi}(t_1, t_0) \\ \vdots \\ \tilde{\boldsymbol{H}}(t_M)\boldsymbol{\Phi}(t_M, t_0) \end{bmatrix} \tag{6.5}$$

Finally, the observability matrix can be calculated as

$$\mathcal{O} = \boldsymbol{H}^T \boldsymbol{H} \tag{6.6}$$

Incorporating the measurement noise and multiplying out the individual matrix blocks, the stochastic observability matrix is given by [35]

$$\mathcal{O} = \sum_{k=1}^{M} \boldsymbol{\Phi}(t_k, t_0)^T \tilde{\boldsymbol{H}}(t_k)^T \boldsymbol{R}^{-1} \tilde{\boldsymbol{H}}(t_k) \boldsymbol{\Phi}(t_k, t_0) \tag{6.7}$$

Note that the stochastic observability matrix is basically the Fisher information matrix assuming no apriori information. In this work, the states to be estimated are the position and velocity coordinates of the satellite and the Fourier coefficients from GPS tracking data.

The binary test of observability is carried out by evaluating the rank of the stochastic observability matrix. If the matrix is full-ranked, all the states and parameters are observable. The amount of deficiency in rank indicates the number of unobservable parameters in the system. The numerical evaluation of rank depends on the machine precision and can lead to an incorrect result due to numerical issues. A more accurate method of evaluating the rank is to calculate the singular values. For the matrix to be full-ranked, all the singular values should be above the following threshold [35],

$$s_{\text{threshold}} = \max(s_i) \times \text{size}(\mathcal{O}) \times \text{eps} \tag{6.8}$$

where $\max(s_i)$ is the largest singular value of the observability matrix, $\text{size}(\mathcal{O})$ is the size of the observability matrix and eps is the machine precision.

6.2.2 Orthogonalization of the sensitivity matrix

The observability of a parameter for a given system with available measurements is intricately tied to the measurement sensitivity matrix as seen in Eq. 6.6. In order for the observability matrix to be full-ranked, the sensitivity matrix needs to be full column-ranked. There are two aspects that are to be considered here. First, if the effect of the parameter on the measurements is negligible, then the norm of the sensitivity vector corresponding to that parameter will be nearly zero. Second, if the effect of multiple parameters are indistinguishable, then the corresponding sensitivity vectors

are linearly dependent. In both cases, the measurement sensitivity matrix and therefore the observability matrix will be rank-deficient. The rank and singular values of the sensitivity matrix or the observability matrix provide information on the linear dependence between sensitivity vectors but they do not indicate which vectors should be removed from the matrix to improve observability. In fact, even if the linearly dependent vector subset is somehow identified, there's usually a choice on which vectors should be removed from the subset in order to make the rest linearly independent. This choice should be dictated by the norm of the individual sensitivity vectors. Measures such as collinearity index [10] in conjunction with sensitivity norms can be used to manually remove linearly dependent vectors from the sensitivity matrix. This process can be automated by employing a sequential orthogonalization method such as the Gram-Schmidt algorithm [16, 62] outlined as follows. For the given data-arc, the total sensitivity vector corresponding to parameter p_i is given by

$$\boldsymbol{s_i} = \left[\frac{d\boldsymbol{y}(t_0)^T}{dp_i}, \frac{d\boldsymbol{y}(t_1)^T}{dp_i}, \ldots, \frac{d\boldsymbol{y}(t_M)^T}{dp_i}\right]^T \tag{6.9}$$

This work is concerned only with the observability of the parameters and assumes that all the states are observable. Therefore, the required sensitivity matrix is constructed by concatenating the total sensitivity vectors corresponding to the parameters as follows

$$\mathcal{S} = \boldsymbol{W_1}[\boldsymbol{s_1}, \boldsymbol{s_2}, \ldots, \boldsymbol{s_{n_p}}]\boldsymbol{W_2} = \boldsymbol{W_1}\boldsymbol{H_p}\boldsymbol{W_2} \tag{6.10}$$

where $\boldsymbol{H_p}$ is the part of the total measurement matrix given by Eq. 6.5 corresponding to the parameters, and $\boldsymbol{W_1}$ and $\boldsymbol{W_2}$ are diagonal scaling matrices. With the sensitivity matrix constructed using Eq. 6.10, the sequential orthogonalization process can be carried out. The basic premise of the method is selecting the vector with the largest norm at the current step and subtracting the projections onto the selected vector from all other vectors. To illustrate, let $\boldsymbol{s_i}$ be the sensitivity vector with the largest norm. Then, parameter i is ranked first. Therefore, $\boldsymbol{q_1} = \dfrac{\boldsymbol{s_i}}{||\boldsymbol{s_i}||}$ is selected

as the first vector and the projection of all other vectors onto $\boldsymbol{q_1}$ is removed,

$$\tilde{\boldsymbol{s}}_{\boldsymbol{j}} = \boldsymbol{s_j} - (\boldsymbol{q_1}^T \boldsymbol{s_j})\boldsymbol{q_1}, \qquad j = \{1, 2, \ldots, M\} - \{i\} \tag{6.11}$$

Now, the process is repeated for the new set of vectors with the cardinality decreased by one. Therefore, at each step, the parameter with the largest sensitivity in the direction orthogonal to the previously selected sensitivities is selected until all the parameters have been ranked. This method can be represented in the form of QR decomposition of the sensitivity matrix with column pivoting [61] as $\mathcal{S}E = QR$, where E is the permutation matrix whose columns dictate the ranks of the parameters, the columns of Q contain the selected directions at each step and R is an upper triangular matrix with columns containing the projections of the sensitivities. A simple example with 3 parameters and 3 outputs helps illustrate the form of the matrices [62, 61]. If the selection order for the sensitivity matrix $\mathcal{S} = [\boldsymbol{s_1}, \boldsymbol{s_2}, \boldsymbol{s_3}]$ is $2, 3, 1$, then the QR decomposition is given by

$$\mathcal{S}\begin{bmatrix} 0 & 1 & 0 \\ 0 & 0 & 1 \\ 1 & 0 & 0 \end{bmatrix} = \begin{bmatrix} \boldsymbol{q_1} & \boldsymbol{q_2} & \boldsymbol{q_3} \end{bmatrix} \begin{bmatrix} \boldsymbol{q_1}^T \boldsymbol{s_2} & \boldsymbol{q_1}^T \boldsymbol{s_3} & \boldsymbol{q_1}^T \boldsymbol{s_1} \\ 0 & \boldsymbol{q_2}^T \boldsymbol{s_3} & \boldsymbol{q_2}^T \boldsymbol{s_1} \\ 0 & 0 & \boldsymbol{q_3}^T \boldsymbol{s_1} \end{bmatrix} \tag{6.12}$$

Therefore, E contains the ranks of the parameters and the diagonal elements of R contains the orthogonal fractions of the sensitivity vectors. The scaling matrices in Eq. 6.10 can change the outcome of the method significantly. If $\boldsymbol{W_1}$ is selected to contain the inverse of the measurement noise standard deviation in the diagonal and $\boldsymbol{W_2}$ is the identity matrix, then the sensitivity matrix has a direct relationship with the stochastic observability matrix. But in this case, the ranking assumes that all the nominal parameters have the same value. It is more appropriate to multiply the sensitivities with the possible variation of the parameters, i.e., $\boldsymbol{W_2}$ contains the initial standard deviations of the parameters in the diagonal. If the sensitivity to the parameters under the given uncertainty is small, then the parameter should be ranked lower even if the sensitivity due to the nominal value is relatively larger.

The QR orthogonalization method is used to assign ranks to the parameters on the basis of

norm and linear dependence between them. In order to determine till what rank the parameters should be estimated, the magnitude of the time dependent relative sensitivity vectors can be used. The relative sensitivity vector is given by

$$\boldsymbol{s_i^r}(t_k) = \boldsymbol{R}^{-1}\frac{d\boldsymbol{y}(t_k)}{dp_i}\boldsymbol{p_i} \tag{6.13}$$

The norm of the relative sensitivity vector is akin to a 'signal-to-noise ratio (SNR)' for the system. If the norm remains smaller than 1 for the given time-interval, the effect of the parameter on the measurements is smaller than the noise level and can be ignored for the data-arc. This metric can be used as a cut-off for estimating the ranked parameters.

6.2.3 Correlation coefficients

Even though the ranking of the parameters using QR orthogonalization takes into account linear dependence between them, pairwise correlations can still exist among the highly ranked parameters. This can be true for a parameter whose sensitivity is sufficiently large such that the orthogonal component to a highly correlated parameter given by Eq. 6.11 still remains higher than the other parameters. Therefore, it is worthwhile to check for pairwise correlations between the ranked parameters. The correlation coefficient between two estimated parameters is given by

$$\rho_{i,j} = \frac{\sigma_{i,j}}{\sigma_i \sigma_j} \tag{6.14}$$

where $\sigma_{i,j}$ is the covariance of the coefficients i and j with their standard-deviations given by σ_i and σ_j. For a high degree of observability, the correlation coefficients should be as close to zero as possible. A correlation coefficient of ± 1 implies a perfect correlation and the estimation problem is ill-posed. The correlation coefficients can be easily calculated from the inverse of the Fisher Information Matrix or the covariance matrix,

$$\boldsymbol{P} = (\sum_{k=1}^{M} \boldsymbol{\Phi}(t_k, t_0)^T \tilde{\boldsymbol{H}}(t_k)^T \boldsymbol{R}^{-1} \tilde{\boldsymbol{H}}(t_k) \boldsymbol{\Phi}(t_k, t_0) + \boldsymbol{P_0^{-1}})^{-1} \tag{6.15}$$

where $\boldsymbol{P_0}$ is the initial covariance. The correlation coefficient is given by

$$\rho_{i,j} = \boldsymbol{P}(i,j)/\sqrt{\boldsymbol{P}(i,i)\boldsymbol{P}(j,j)}. \tag{6.16}$$

A structured covariance analysis can be used to remove highly correlated parameters from the estimation subset [23, 87]. Here, a manual inspection of the correlation coefficients is carried out to dictate the parameters that should be estimated.

6.2.4 Consider covariance analysis

A consider covariance analysis ascertains the effect of ignored parameters on the uncertainties of the estimated parameters. Instead of ignoring the non-estimated coefficients, consider covariance analysis recognizes the associated uncertainties and possible errors and quantifies their effects by including the uncertainties in the error covariance matrix. Therefore, considered parameters are assumed to be constant in the estimator and their apriori values and uncertainties are assumed to be known [124]. If the covariance matrix of a batch estimator that ignores the non-estimated parameters is $\boldsymbol{P_x}$, then the covariance of the estimator that considers the same parameters is given by

$$\boldsymbol{P_{xx}} = \boldsymbol{P_x} + \boldsymbol{P_{xc}}\overline{\boldsymbol{P}}_{\boldsymbol{cc}}^{-1}\boldsymbol{P_{xc}^T} \tag{6.17}$$

where $\overline{\boldsymbol{P}}_{\boldsymbol{cc}}$ is the assumed covariance of the considered parameters $\boldsymbol{c}$ and $\boldsymbol{P_{xc}}$ is the covariance between the estimated states and considered parameters. In order for the non-estimated parameters to be negligible, $\boldsymbol{P_{xx}} \approx \boldsymbol{P_x}$.

6.3 GSIM parameter inversion

The estimated Fourier coefficients contain information about the GSIM parameters. In the cases where the Fourier coefficients can be analytically computed, the dependence of the Fourier coefficients on GSIM parameters is made explicit in a functional form as seen in eq. (5.23). Even in the absence of an analytical form, the dependence is evident through the integrals given by eqs.

5.16-5.18. Therefore, it is possible to invert GSIM parameters from estimates of Fourier coefficients within some uncertainty. The amount of uncertainty will depend on assumptions pertaining to the atmospheric density and other non-estimated GSIM parameters as well as the error and covariance of the estimated Fourier coefficients. Throughout this work, the atmospheric density is assumed to be accurate. Therefore, the Fourier coefficients do not absorb any other errors in the dynamics. This is, of course, not true in a realistic scenario and the errors in density model need to be accounted for. But the purpose of this chapter is to provide a framework that allows the estimation of GSIM parameters and provides a way to estimate atmospheric densities in the next chapter.

The GSIM parameters can be essentially divided into three categories - atmosphere-dependent parameters (mean molecular mass and ambient temperature), satellite-specific parameters (surface temperature) and fitting parameters (Langmuir constant). The satellite surface molecular mass, which is ideally a satellite-specific parameter, ends up as a fitting parameter in the application of most GSIMs. The uncertainties in atmosphere-dependent parameters are specific to the atmospheric model used to compute the drag-coefficient. Instead of considering uncertainties in the atmospheric model, the Fourier coefficients are considered to be specific to the atmospheric model and time epoch of the analysis, i.e., they are biased to the atmospheric model used in the filter. There's relatively little sensitivity of the drag-coefficient to the surface temperature within physically reasonable bounds, therefore uncertainties in the parameter can be ignored. The uncertainties in the surface molecular mass are ignored in this work and will be considered in the future. The largest uncertainties are associated with the fitting parameters since they are derived by analyzing data from specific satellites and are therefore inherently biased. For both DRIA and the semi-empirical satellite energy accommodation model (SESAM) [96], the largest uncertainty is in the Langmuir constant. Therefore, the Langmuir constant is inverted from the estimated Fourier coefficients assuming all other parameters are known. It should be noted that the fraction of atomic oxygen coverage is not consistently sensitive to the Langmuir constant across the atomic oxygen pressure range, as can be deduced from the nonlinearity of eq. (2.11). The sensitivity is significantly higher in lower partial pressures, hence higher altitudes.

The estimated Fourier coefficients can be used to constrain the value of the Langmuir adsorbate constant by using an iterative non-linear least-squares estimation scheme. In this method, the estimated Fourier coefficients are the measurements and the Langmuir constant is the state to be estimated. The vector of Fourier coefficients have the following functional relation to the Langmuir constant.

$$\boldsymbol{Y} = \boldsymbol{g}(X) \tag{6.18}$$

where $\boldsymbol{Y} = [\overline{\mathbb{A}}_0, \overline{\mathbb{A}}_1 ... \overline{\mathbb{A}}_n]^T$, $[\overline{\mathcal{A}}_0, \overline{\mathcal{A}}_1 ... \overline{\mathcal{A}}_n]^T$, or a combination of both, depending on the selected Fourier model, $X = K$ and $\boldsymbol{g} = [g_0, g_1 ... g_n]^T$, where g_k is the function that relates the k^{th} Fourier coefficient to the Langmuir constant. This functional form is different depending on the selected Fourier model. Therefore, the inversion method is detailed for each Fourier model separately in the following sections.

6.3.1 OFF model

The Fourier coefficient dependence on the Langmuir constant for the OFF model can be obtained as follows-

$$g_k = \frac{1}{M\pi} \int_0^{2\pi} \left[\frac{KP_o}{1+KP_o} C_d|_{(\alpha=1)} + \left(1 - \frac{KP_o}{1+KP_o}\right) C_d|_{(\alpha=\alpha_s)} \right] \cos kE dE. \tag{6.19}$$

where $M = 2$ for $k = 0$ and $M = 1, \forall k > 0$. The least-squares algorithm requires the Jacobian of the measurement matrix. Therefore, $\boldsymbol{g}$ is linearized to obtain

$$\boldsymbol{G} = \left[\frac{\partial \boldsymbol{g_1}}{\partial K}, \frac{\partial \boldsymbol{g_2}}{\partial K}, ... \frac{\partial \boldsymbol{g_n}}{\partial K} \right]^T \tag{6.20}$$

where the k^{th} partial is given by

$$\frac{\partial \boldsymbol{g_k}}{\partial K} = \frac{1}{M\pi} \int_0^{2\pi} \left[\frac{P_o}{(1+KP_o)^2} \left\{ C_d|_{(\alpha=1)} - C_d|_{(\alpha=\alpha_s)} \right\} \right] \cos kE dE \tag{6.21}$$

Therefore, the partials are Fourier expansions of the term in the square brackets. The least-squares estimate and its variance can then be found by iteratively solving the least-squares equation

$$x = (\boldsymbol{G}^T \boldsymbol{R_f}^{-1} \boldsymbol{G})^{-1} \boldsymbol{G}^T \boldsymbol{R_f}^{-1} \boldsymbol{y_f} \tag{6.22}$$

$$P = (\boldsymbol{G}^T \boldsymbol{R_f}^{-1} \boldsymbol{G})^{-1} \tag{6.23}$$

where x is the error in the estimate of the Langmuir constant at the current iteration, $\boldsymbol{y_f}$ is the measurement residual at the current iteration and $\boldsymbol{R_f}$ is the measurement noise covariance. The measurement noise covariance can be taken as the estimated covariance corresponding to the Fourier coefficients post orbit determination. The process can be repeated iteratively with the new estimate given by $K_{j+1} = K_j + x$, with j being the current iteration, until x drops below a fixed threshold.

6.3.2 BFF model

For the BFF model, the Fourier coefficients depend on the Langmuir constant from Eqs. 5.16-5.18 as follows-

$$g_k = \frac{1}{M\pi} \int_0^{2\pi} \left[\frac{KP_o}{1+KP_o} C_d|_{(\alpha=1)} + \left(1 - \frac{KP_o}{1+KP_o}\right) C_d|_{(\alpha=\alpha_s)} \right] \cos k\theta d\theta. \tag{6.24}$$

where $M = 2$ for $k = 0$ and $M = 1, \forall k > 0$. The analytical form derived in section **??** can be substituted above,

$$g_k = \left[\frac{KP_o}{1+KP_o} \overline{\mathcal{A}}_k|_{(\alpha=1)} + \left(1 - \frac{KP_o}{1+KP_o}\right) \overline{\mathcal{A}}_k|_{(\alpha=\alpha_s)} \right]. \tag{6.25}$$

Therefore, the measurement Jacobian given by Eq. 6.20 can be obtained by evaluating the partials as follows-

$$\frac{\partial \boldsymbol{g_k}}{\partial K} = \frac{P_o}{(1+KP_o)^2} \left\{ \overline{\mathcal{A}}_k(E)|_{(\alpha=1)} - \overline{\mathcal{A}}_k(E)|_{(\alpha=\alpha_s)} \right\}. \tag{6.26}$$

An estimate of the Langmuir constant and its covariance can then be obtained by Eqs. 6.22 and 6.23.

6.4 Observability analysis results

To evaluate the observability metrics and the accuracy of inverted Langmuir constant for the different Fourier models, elliptical satellite orbits are simulated. The simulation parameters are provided in Table 8.2. An ideal scenario is considered with only the two-body gravitational force and atmospheric drag acting on the satellite. A spherically symmetric exponentially decaying atmosphere is assumed in the simulations so that non-periodic variations in drag-coefficient can be neglected. The performance of the Fourier models for a realistic orbit determination scenario has been previously demonstrated with synthetic and real data [100]. The true drag-coefficient is simulated using the GSIMs described in section 2.1.4. As noted earlier, the Langmuir constant is the most uncertain parameter in the GSIM considered here. In order to compute the initial estimates of the Fourier coefficients, multiple sets of Fourier coefficients are computed for a range of Langmuir parameters. The possible range of Langmuir parameter variation is selected on the basis of the fraction obtained at 500 km. Walker et al. (2014) [131] compute the fraction to be around 0.6 at 500 km. A conservative lower limit of around 0.1 and an upper limit of 0.99 is assumed for the fraction at 500 km. This corresponds to the possible variation of Langmuir parameter in the range $[10^6, 10^8]$. A spherical satellite is considered for the OFF model to remove any variations due to attitude. Inertially stabilized symmetrical and asymmetrical cubical satellites are considered for the BFF model.

Position and velocity measurements from a GPS receiver are assumed to be available to the estimator every 10 seconds. The measurements are modeled by adding Gaussian noise with standard deviations of 1.5 m and 0.5 cm/s respectively to the simulated orbital states in the Earth-centered Earth-fixed (ECEF) frame. A nonlinear least-squares batch estimator is used to process the measurements and obtain estimates of position, velocity and the Fourier coefficients.

Table 6.1: Simulation parameters common for all the cases

Parameter		Value
Orbital elements	H_p	300 km
	H_a	500 km
	i_0	65^0
	Ω_0	60^0
	ω_0	40^0
Satellite parameters	m	500 kg
	S	10 m^2
Atmospheric parameters	$F_{10.7}$	150 s.f.u
	ρ_0	1.9417e-11 kg/m^3
	H	49.23 km

6.4.1 OFF model

For the ideal scenario considered in the simulation, all the sine coefficients are zero for the OFF model. This is because the drag-coefficient is an even function of the eccentric anomaly since the atmosphere is considered to be spherically symmetric. The variation of the drag-coefficient in the orbit for the limiting values of K are plotted in fig. 6.1 (a). For all the intermediate values of K, the drag-coefficients lie between the red and the black curves. The numerically computed Fourier coefficients are plotted as a function of K in fig. 6.1 (b). The Fourier coefficients are most sensitive to K for values smaller than around 2×10^7. The higher order Fourier coefficients become smaller as K increases since the drag-coefficient variation in orbit decreases for larger values of K. The magnitudes of the even-order Fourier coefficients and the odd-order Fourier coefficients are seen to be linear with the order in the logarithmic scale. Therefore, 'Kaula-type' rules [70], analogous to gravitational coefficient estimation, can be derived separately for the even and odd-order Fourier coefficients as follows-

$$|\bar{A}_{2k}| \sim \exp\left(a_{2k}k + b_{2k}\right), \tag{6.27}$$

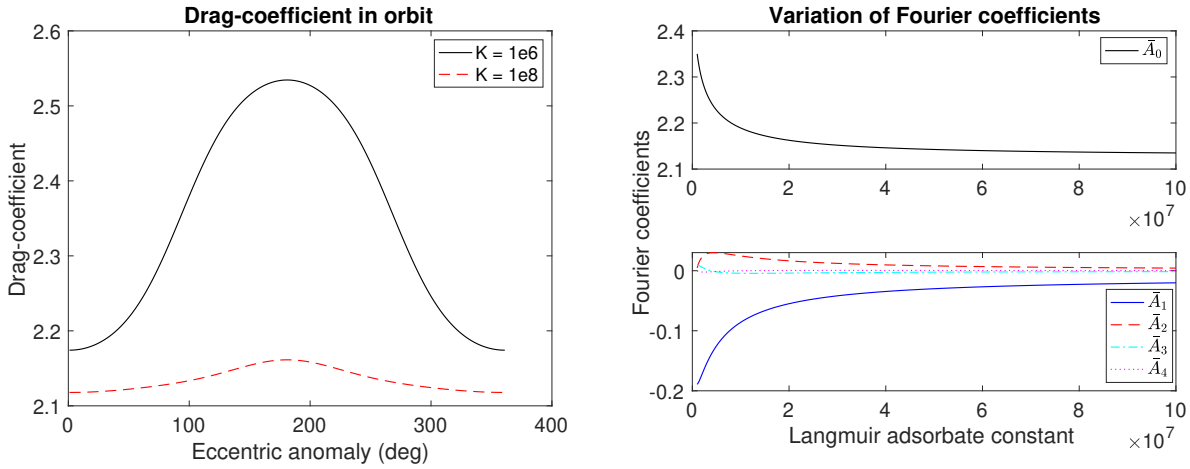

(a) (b)

Figure 6.1: (a) Variation of drag-coefficient in orbit for limiting values of the Langmuir adsorbate constant; (b) Variation of OFF coefficients as a function of Langmuir adsorbate constant

where $k \in \mathbb{Z}^+$ for even-orders, and

$$|\bar{A}_{2k+1}| \sim \exp\left(a_{2k+1}k + b_{2k+1}\right), \tag{6.28}$$

where $k \in \mathbb{Z}^{\geq}$ for odd-orders. The best-fit curves are obtained for the average of the Fourier coefficients distribution as a function of the Langmuir constant and plotted in fig. 6.2. These curve can be used to dictate the initial covariance of the Fourier coefficients in the estimator. Note that the exact curves are specific to the orbital parameters and satellite. The average value of the Fourier coefficients for each order is computed and set to the initial estimates in the batch estimator and the initial covariance is given by the 'Kaula-type' rules. In order to generate the true trajectory, the true drag-coefficients are computed by assuming $K = 10^6$.

The first step is to determine if all the Fourier coefficients are observable if no prior information is available on them. This can be determined by comparing the singular values of the stochastic observability matrix to the threshold in eq. (6.8). The two smallest singular values and the threshold are plotted in fig. 6.3. The smallest singular value is above the threshold for some initial duration but then drops below it. Therefore, all the coefficients are not fully observable with the given data-arc.

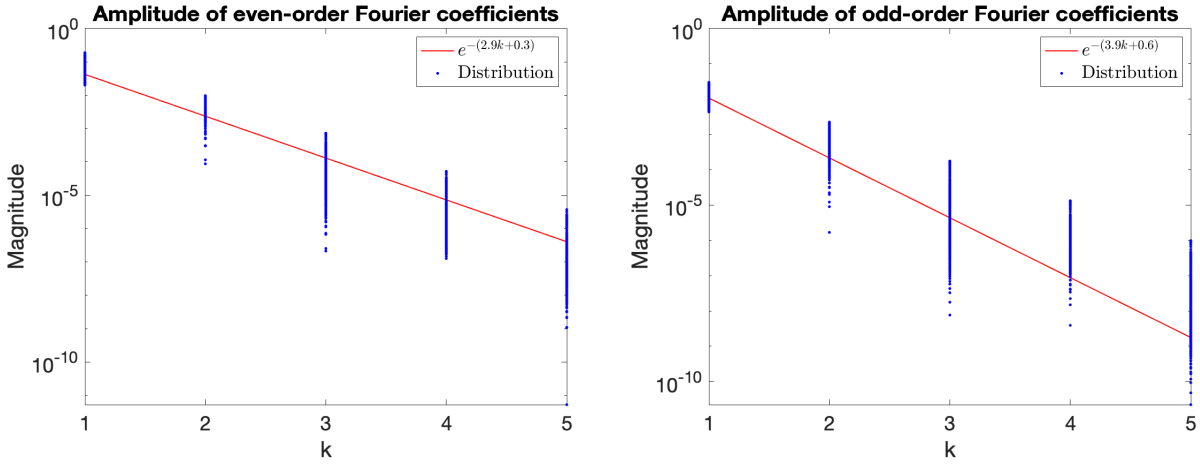

(a) (b)

Figure 6.2: (a) 'Kaula-type' rule for even-order OFF coefficients; (b) 'Kaula-type' rule for odd-order OFF coefficients

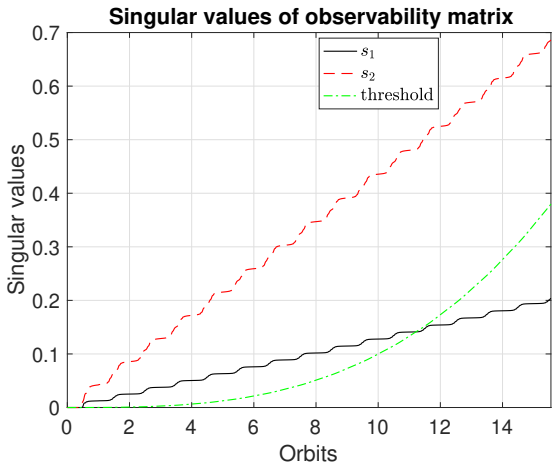

Figure 6.3: OFF model for a spherical satellite: Smallest singular values of the stochastic observability matrix

All the Fourier coefficients are ranked using the QR decomposition method in fig. 6.4. The ranking follows the order of the coefficients monotonically. It should be noted that the assigned ranks are highly dependent on the scaling matrices $\boldsymbol{W_1}$ and $\boldsymbol{W_2}$ that have been taken to be the inverse of the measurement noise standard deviations and the initial standard deviations of the Fourier coefficients. It can be seen that only the first four coefficients, until order 3, have an SNR greater than 1. Therefore, the order of coefficients to be estimated should be cut-off at 3.

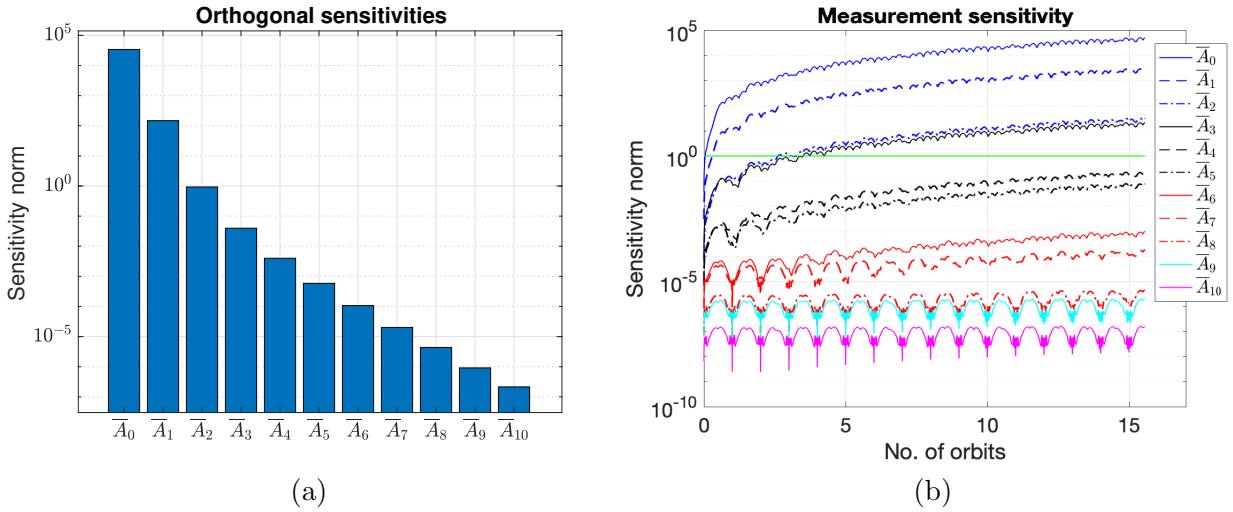

(a) (b)

Figure 6.4: OFF model for a spherical satellite: (a) Norm of the orthogonal fractions of the total normalized sensitivity vectors; (b) Norm of the time-varying relative sensitivity vectors

The effects of ignoring higher-order coefficients on the uncertainty of the estimated states are studied by a consider covariance analysis. At each truncation order of the Fourier series, all the lower-order coefficients are estimated and the higher-order coefficients are considered, i.e., they are not estimated but their uncertainty is included in the estimation error covariance matrix. The standard deviation of position, velocity and the zeroth-order coefficient are plotted in Fig. 6.5. For the position and velocity, the norm of the standard deviations across the coordinates is calculated, i.e., $\sigma = \sqrt{\sigma_x^2 + \sigma_y^2 + \sigma_z^2}$, where σ_x is the standard-deviation in the x-coordinate and so on. The solid lines represent the standard deviations obtained by a batch estimator which ignores the considered parameters and the dashed lines represent the standard deviations that includes the effect of uncertainties of the considered parameters. If the considered parameters, i.e., higher-order Fourier coefficients, have a negligible effect on the estimated states, then the two aforementioned standard deviations for the estimated states will be nearly equal. For any truncation order of the Fourier model, if the two standard-deviations of the estimated states are different, then it implies that a few of the considered parameters have a non-trivial effect on the estimated states and should be estimated. In Fig. 6.5, it can be seen that in order for the two standard deviations to be similar for position and velocity each, the Fourier coefficients need to be estimated at least up to order 1.

All higher order Fourier coefficients have a negligible effect on the estimated position and velocity. In order for the standard deviations to be consistent for order 0 coefficient, which represents the average drag-coefficient, the Fourier coefficients need to be estimated at least to order 2. It is desirable to estimate coefficients to an order higher. Therefore, the Fourier coefficients need to be estimated at least to order 3 which is consistent with the results from the QR decomposition and SNR metrics.

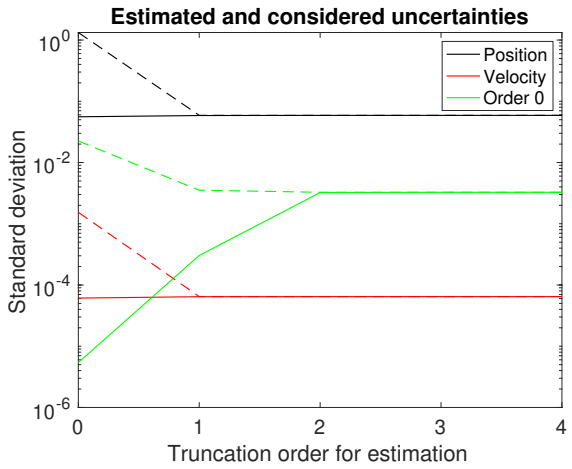

Figure 6.5: OFF model for a spherical satellite: Standard deviations assuming no errors in consider parameters (solid lines) and consider standard deviations (dashed lines) for position, velocity and zeroth-order Fourier coefficient

The standard deviations of the Fourier coefficients non-dimensionalized by their estimates are plotted in Fig. 6.6 (a). The standard-deviation ratios of $\overline{\mathbb{A}}_0$ and $\overline{\mathbb{A}}_1$ coefficients decrease below 1 after a point. On the other hand, the standard deviations of the higher order coefficients change much more slowly with more measurements. The correlation matrix for the Fourier coefficients is mapped in Fig. 6.6 (b). The coefficients until order 2 are highly correlated that results in a lower degree of observability for these coefficients. This can introduce errors in estimation if all the coefficients until order 3 are estimated. But ignoring a correlated but highly sensitive coefficient can also lead to estimation errors. If there are errors in the estimated coefficients resulting due to correlations, ignoring $\overline{\mathbb{A}}_2$ should be expected to improve the results since it has the least sensitivity among the three. In order to figure out the combination of coefficients that results in the best

estimation error, Monte Carlo simulations are carried out for the cases summarized in Table 6.2.

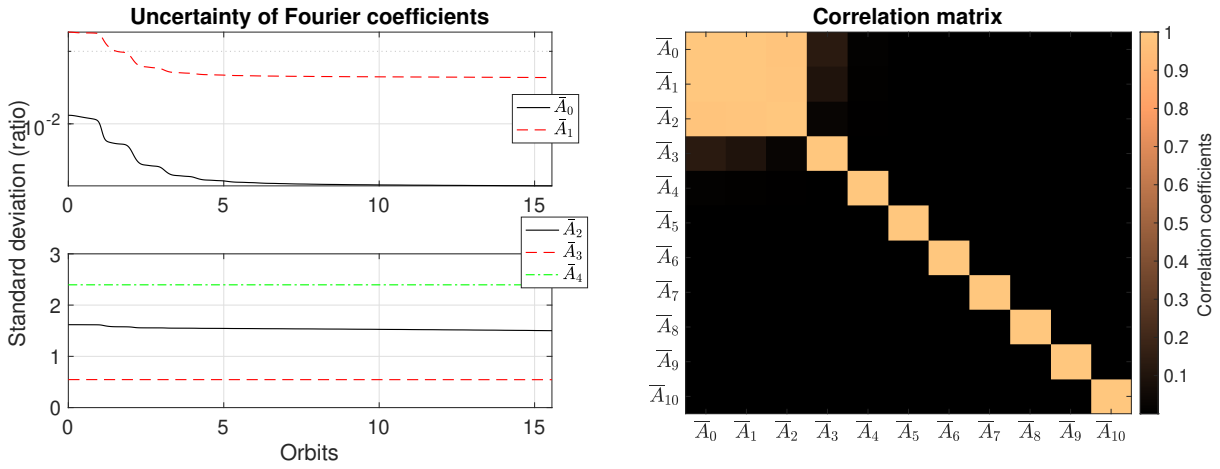

(a) (b)

Figure 6.6: OFF model for a spherical satellite: (a) Standard deviation of the Fourier coefficients; (b) Correlation matrix for the estimated Fourier coefficients

Table 6.2: OFF model for a spherical satellite: Monte Carlo simulation cases

Case	**Estimated coefficients**
1	$\overline{\mathbb{A}}_0$
2	$\overline{\mathbb{A}}_0, \overline{\mathbb{A}}_1$
3	$\overline{\mathbb{A}}_0, \overline{\mathbb{A}}_1, \overline{\mathbb{A}}_2$
4	$\overline{\mathbb{A}}_0, \overline{\mathbb{A}}_1, \overline{\mathbb{A}}_2, \overline{\mathbb{A}}_3$
5	$\overline{\mathbb{A}}_0, \overline{\mathbb{A}}_1, \overline{\mathbb{A}}_2, \overline{\mathbb{A}}_3, \overline{\mathbb{A}}_4$
6	$\overline{\mathbb{A}}_0, \overline{\mathbb{A}}_1, \overline{\mathbb{A}}_3$
7	$\overline{\mathbb{A}}_0, \overline{\mathbb{A}}_2, \overline{\mathbb{A}}_3$

For each case in Table 6.2, 200 batch estimation runs are performed. The initial state and Fourier coefficient errors are generated from the initial covariance and the measurement noise from the measurement noise covariance for each run. The drag-coefficient is calculated using the estimated Fourier coefficients and the RMS value of the drag-coefficient error is noted. The mean and standard-deviation of the error RMS is plotted for each case in Fig. 6.7. The figure compares the estimation errors for two scenarios - when the all the non-estimated coefficients are ignored in the filter dynamics versus when they are modeled and kept constant at their nominal values. Note that the errors in the nominal values of the non-estimated coefficients are generated from their

nominal covariance for each run, i.e., the modeled higher-order coefficients contain errors. The first thing that can be noticed from Fig. 6.7 is that the errors are smaller if the non-estimated coefficients are modeled in the estimator for most of the cases. The drag-coefficient errors are equally large for cases 1 and 7, i.e., not estimating $\overline{\mathbb{A}}_1$ results in an inaccurate drag-coefficient estimate. But not estimating any Fourier coefficient other than order 0 results in a large initial position error as well, as seen in Fig. 6.7 (b). If all the coefficients are modeled, then estimating coefficients after order 2 does not add further accuracy to the overall drag-coefficient whereas the order goes up to 3 if the non-estimated coefficients are ignored. A slightly more accurate drag-coefficient with a tighter error-bar is obtained for case 6 where $\overline{\mathbb{A}}_2$ is not estimated. This is consistent with the previously discussed expectation of improving the accuracy by not estimating the least-sensitive correlated coefficient. Overall, the results indicate that the all the coefficients up to order 2 should be estimated with all the higher-order coefficients being modeled.

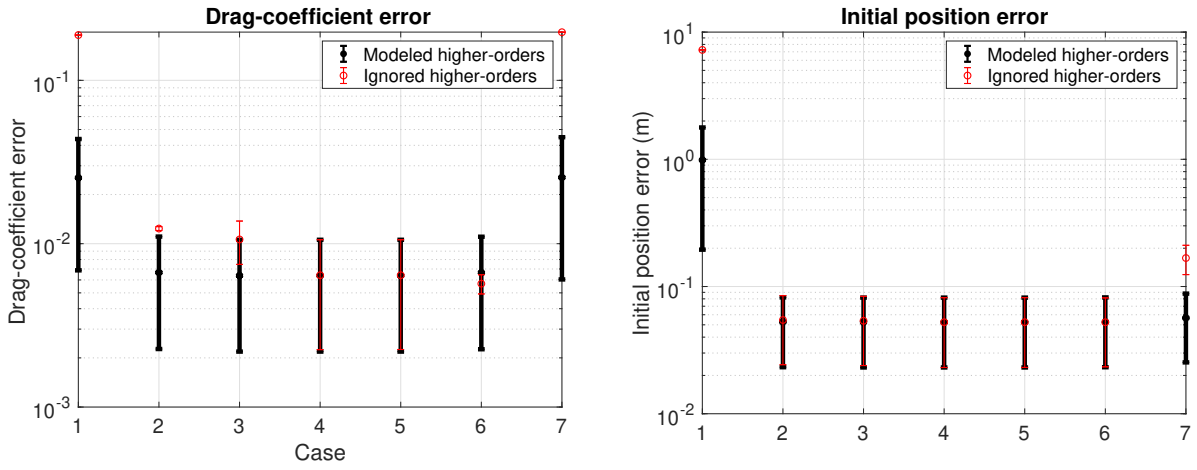

(a) (b)

Figure 6.7: OFF model for a spherical satellite: Mean and 1σ error bars for (a) Drag-coefficient error RMS values; (b) Norm of initial position error for the Monte Carlo cases

The least-squares method outlined in section 6.3 is used to estimate the Langmuir constant from the estimated Fourier coefficients for true values of $K = 10^6$ and $K = 10^8$. No prior information on the Langmuir constant is assumed to be available. With the initial estimate of the Langmuir constant assumed to be 10^7 for each case, and constraining the value of the constant to

be positive for each iteration (it is set to 0 if the estimate obtained is negative at any iteration), the final estimates and their standard deviations obtained are tabulated in 6.3. It can be seen

Table 6.3: OFF model: Estimation error and uncertainty for the Langmuir constant for two truth cases

True value	**Initial estimate**	**Final error**	**Standard deviation**
10^6	10^7	99.24	79.3
10^8	10^7	3.5×10^5	3.17×10^5

that the error in K is about 0.01% for $K = 10^6$ and 0.35% for $K = 10^8$. This is because the variation of the Fourier coefficients with K becomes much smaller for $K > 2 \times 10^6$. Therefore, the uncertainty in estimating K from the Fourier coefficients is larger in that range. If the estimated Fourier coefficients are truncated at a smaller order, i.e., a subset of the Fourier coefficients are estimated, then the accuracy with which the Langmuir constant can be estimated decreases. This occurs because the ignored higher order coefficients alias into the estimated lower order coefficients. The accuracy with which the Langmuir constant can be estimated from the Fourier coefficients at lower truncation orders are given in Table 6.4 for the $K = 10^6$ case. From order 0 to order 1, there's an improvement of two orders of magnitude and the same from order 2 to order 3. In order for the Langmuir constant to be consistent with the standard deviation, the Fourier coefficients have to be estimated at least to order 3.

Table 6.4: OFF model for a spherical satellite: Estimation error and uncertainty for the Langmuir constant for lower truncation orders of the estimated Fourier coefficients

Order	**Final error**	**Standard deviation**
0	-4.78×10^6	516.8
1	3.05×10^4	67.0
2	1.4×10^4	78.2
3	-107.5	79.7

6.4.2 BFF model

Unlike the OFF coefficients, the BFF coefficients are tied to the body frame and capture variations in the drag-coefficient due to attitude. The OFF coefficients are slowly varying if there are no variations in the attitude of the satellite and can therefore be considered constant in the orbit determination process. But the BFF coefficients will have variations in the orbit due to ambient parameters. Since the coefficients are estimated as constants in the estimator, there will be a certain degree of mismatch between the true and filter dynamics. In order to compute the initial estimates of the coefficients, the time-varying BFF coefficients are averaged over the orbit weighted by the atmospheric density.

A symmetric cubical satellite with an inertially stabilized profile is considered as the first case. All the six faces of the satellite are assumed to have the same properties such as area, surface temperature and material. Therefore the Fourier coefficients with respect to ψ ($a_{n,i}$) for all the plates are equal. It can be easily seen from Eqs. 5.26, 5.27 and 5.28 that only the fourth order cosine coefficients for the satellite, i.e., $\overline{\mathcal{A}}_{4k}, k \in \mathbb{Z}$, are non-zero. The drag-coefficient and Fourier coefficients for the limiting values of the Langmuir constant are plotted in Fig. 8.5. Note that only the zeroth order coefficient is dependent on the Langmuir constant in this case. As made evident by Eq. 5.23, only the odd-order coefficients after order 2 are dependent on the incident to reemitted velocity ratio (r_i). This is the parameter that differentiates the specular from the diffuse fraction of the GSIM. Similar to Fig. 6.1, the drag-coefficient variation is larger for a smaller Langmuir constant. Therefore, averaging errors in the Fourier coefficients will be larger for smaller values of the parameter. In the estimator, only the non-zero coefficients, i.e., multiples of order 4 coefficients are estimated. Therefore, for an order 30 Fourier model, there are only eight coefficients that need to be estimated. The truth is generated by assuming $K = 10^6$. The two smallest singular values of the stochastic observability matrix with the threshold are plotted in Fig. 6.9. It can be seen that the observability matrix is full ranked and therefore, all the coefficients are observable.

The coefficients are ranked according to the QR orthogonalization of their non-dimensionalized

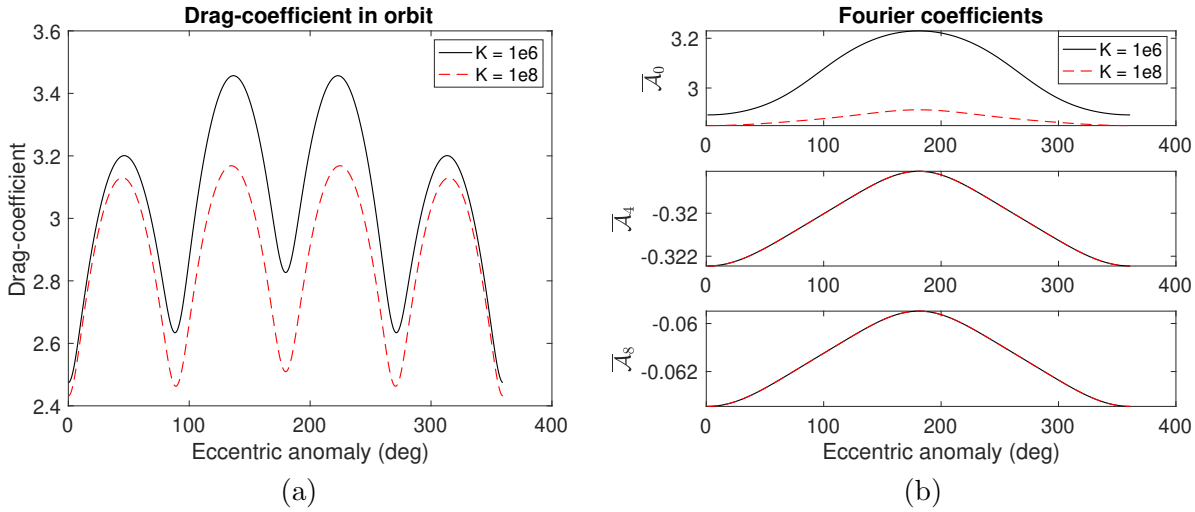

(a) (b)

Figure 6.8: (a) Variation of drag-coefficient in orbit; (b) Variation of BFF coefficients in orbit for limiting values of the Langmuir adsorbate constant

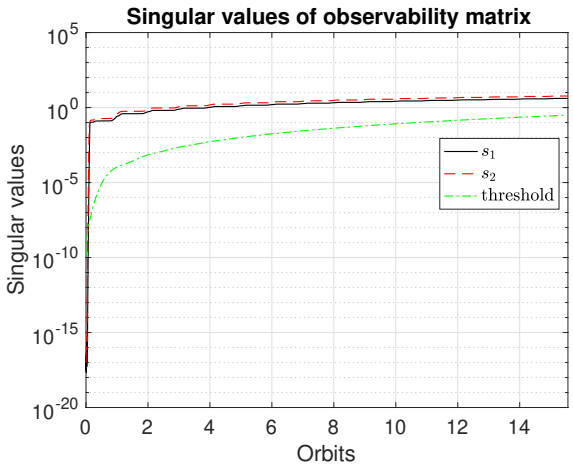

Figure 6.9: BFF model for a symmetrical satellite: Smallest singular values of the stochastic observability matrix

measurement sensitivities. As can be seen in Fig. 6.10 (a), the coefficients are ranked monotonically. The non-dimensionalized sensitivity norm or the SNR in Fig. 6.10 (b) shows that only the first and fourth order coefficients have an effect on the measurements greater than the noise. A consider covariance analysis reveals the same result as the QR decomposition and SNR metrics. From Fig. 6.11, the coefficients need to be measured at least to order 4 for the consider standard deviations (dashed lines) and standard deviations assuming no errors in considered parameters

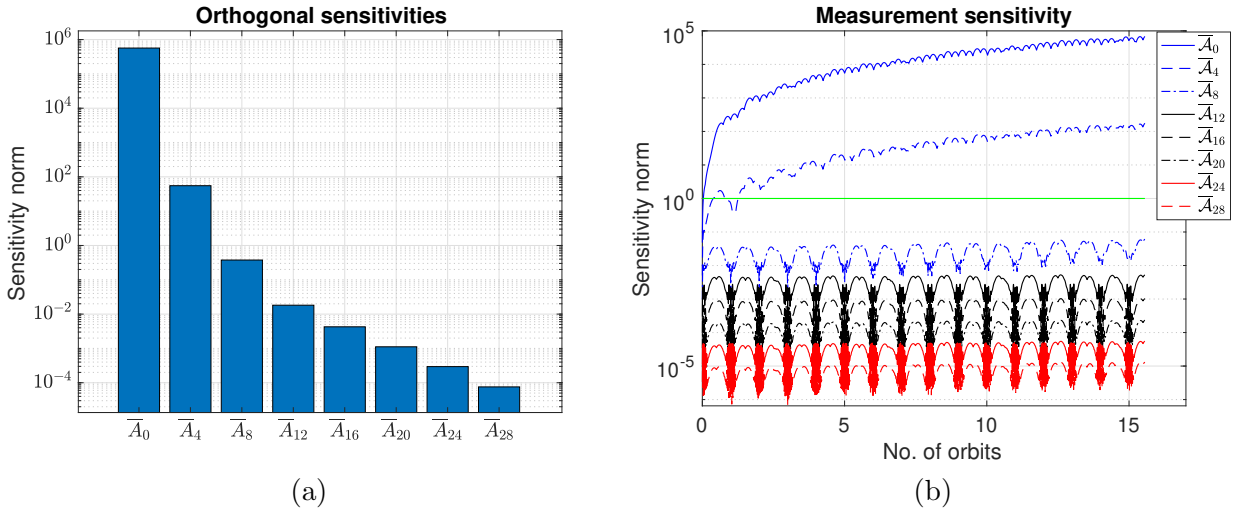

(a) (b)

Figure 6.10: BFF model for a symmetrical satellite: (a) Norm of the orthogonal fractions of the total normalized sensitivity vectors; (b) Norm of the time-varying relative sensitivity vectors

(solid lines) to be consistent.

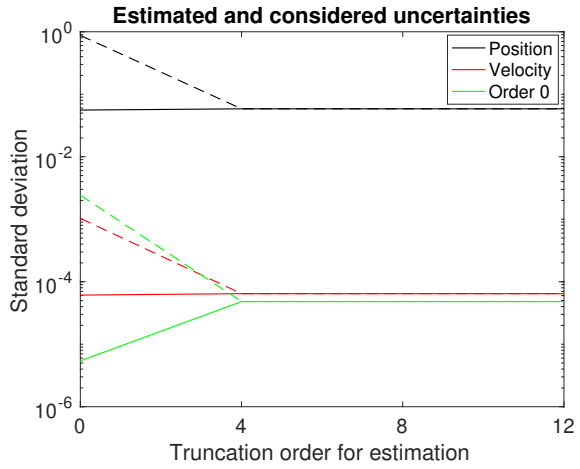

Figure 6.11: BFF model for a symmetrical satellite: Standard deviations assuming no errors in consider parameters (solid lines) and consider standard deviations (dashed lines) for position, velocity and zeroth-order Fourier coefficient

The standard deviations of the Fourier coefficients nondimensionalized by their estimated values and the correlation matrix of the BFF coefficients are plotted in Fig. 6.12. Similar to the OFF model, the uncertainty in only the first two orders decreases rapidly with more measurements. The correlation between the zeroth and fourth order coefficients is high but the rest of the coefficients

are not correlated. It is possible that estimating the zeroth and fourth order coefficients together can result in a poor estimation performance. In order to analyze the errors that are introduced in the estimates, Monte Carlo simulations similar to the OFF model are carried out for the cases summarized in Table 6.5.

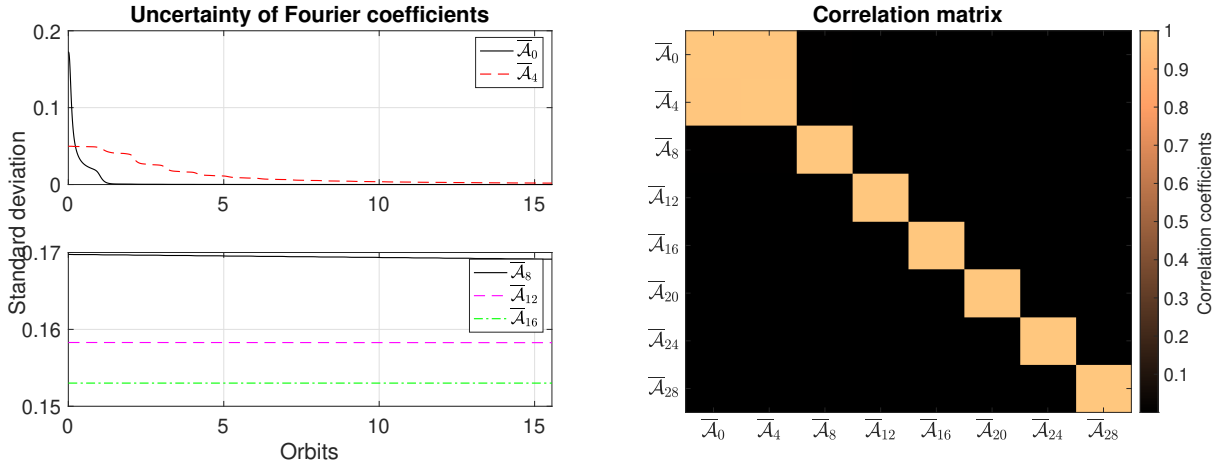

(a) (b)

Figure 6.12: BFF model for a symmetrical satellite: (a) Non-dimensionalized standard deviation of the BFF coefficients ; (b) Correlation matrix for the BFF coefficients

Table 6.5: Monte Carlo simulation cases for BFF model for a symmetrical satellite

Case	Estimated coefficients
1	$\overline{\mathbb{A}}_0$
2	$\overline{\mathbb{A}}_0, \overline{\mathbb{A}}_4$
3	$\overline{\mathbb{A}}_0, \overline{\mathbb{A}}_4, \overline{\mathbb{A}}_8$
4	$\overline{\mathbb{A}}_0, \overline{\mathbb{A}}_4, \overline{\mathbb{A}}_8, \overline{\mathbb{A}}_{12}$
5	$\overline{\mathbb{A}}_0, \overline{\mathbb{A}}_8$

The Fourier model in the estimator needs some attention. As in the OFF model case, the higher order non-estimated coefficients can either be modeled or ignored. As discussed earlier, the BFF coefficients are orbit-dependent and can be expanded into orbit-fixed coefficients given by Eqs. 8.19 and 5.47. Therefore, the modeled coefficients in the estimator should consist of the orbit-fixed part of the Fourier model as well. In other words, the complete BODF model is used in the estimator but only the BFF coefficients summarized in Table 6.5 are estimated. The 3σ of the

Fourier coefficients is taken as 50 % of their nominal values, i.e., the coefficients are assumed to have a maximum of 50 % error. The drag-coefficient error RMS, initial position error norm and the RMS of the measurement residual non-dimensionalized by the measurement noise standard deviation are plotted in Fig. 6.13. The errors are plotted for ignored and modeled non-estimated coefficients similar to the analysis for OFF model. As a reference, errors are also plotted for an ideal scenario where the modeled OFF coefficients have no errors, i.e., the true OFF coefficients are modeled in the filter. The first observation from the figures is that the errors for all cases are much higher when the non-estimated coefficients are ignored as expected. Even though the drag-coefficient errors are smaller when they are modeled, the standard deviation is larger since introducing errors in higher-order modeled coefficients increases the range of variation of the estimated coefficients. When the true OFF coefficients are modeled in the estimator, the errors as well as standard deviations are small. It is interesting to see that for both modeled and ignored non-estimated coefficients, the drag-coefficient errors are higher for case 2 than case 1, i.e., when both order 0 and 4 coefficients are estimated. But it does not necessarily mean a poorer estimation performance since both the initial position error and the non-dimensionalized measurement residuals are lower for case 2. It implies that in order to obtain a better overall orbit determination performance, the drag-coefficient accuracy needs to be compromised. If the true OFF coefficients were known, the drag-coefficient error decreases when order 4 coefficient is estimated. The non-dimensionalized measurement residuals are similar whether the modeled OFF coefficients have errors or not which shows that modeling the non-estimated coefficients provides a better orbit fit.

As seen in Fig. 8.5, only the zeroth order coefficient depends on the Langmuir constant. Even though the overall drag-coefficient error is larger when order 4 coefficient is estimated, it is more important to analyze the errors in the order 0 coefficient when inverting the Langmuir constant from estimated Fourier coefficients. The errors in the order 0 coefficient for cases 1 and 2 are given in Table 6.6. Estimating the order 4 coefficient improves the order 0 estimate when non-estimated coefficients are modeled.

The results of the Langmuir constant inversion from the estimated Fourier coefficients are

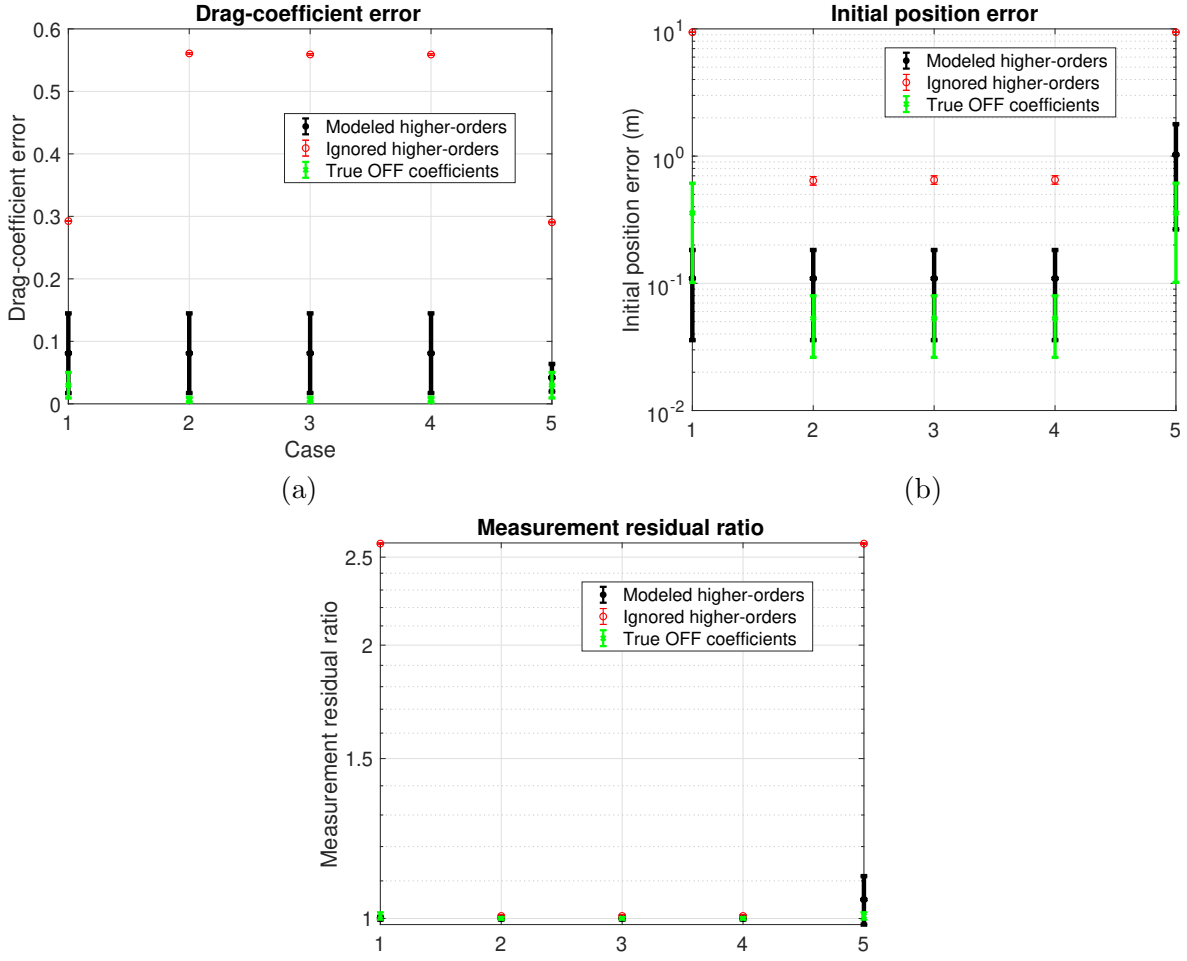

Figure 6.13: BFF model for a symmetrical satellite: Mean and 1σ error bars for (a) Drag-coefficient error RMS values; (b) Norm of initial position error; (c) Non-dimensionalized measurement residual RMS values for the Monte Carlo cases

Table 6.6: BFF model for a symmetrical satellite: Mean and standard-deviations of order 0 Fourier coefficient for cases 1 and 2

Case	Ignored	Modeled
1	$0.129 \pm 5.1 \times 10^{-6}$	-0.026 ± 0.212
2	$0.103 \pm 4.8 \times 10^{-5}$	-0.019 ± 0.150

discussed in the next section where BODF coefficients are part of the estimation subset.

For a symmetrical satellite, the accuracy with which the Langmuir constant can be determined is limited due to the absence of odd-order Fourier coefficients. It is instructive to find out if the

accuracy is increased for an asymmetrical satellite for which the odd-order coefficients are non-zero. A box-wing shape model for the satellite is considered. Two solar panels with an area of 13.5 m^2 each are fixed to the satellite bus. The dimensions of the satellite bus are taken to be 1.5x2x2.5 m^3. The body z-axis is perpendicular to the solar panels and the y-axis is parallel to solar panel axis. Additional areas of 1, 0.75, 1.5, 1, 1.5, 0.1 m^2 are added to the faces in +x, -x, +y, -y, +z and -z directions to take into account asymmetry due to shape details such as protrusions etc. The surface material properties are considered to be different for each panel [103].

The number of non-zero BFF coefficients is significantly increased for an asymmetrical satellite. A tolerance of 10^{-5} is imposed on the coefficients that introduces a maximum of around 0.02 % error on the overall drag-coefficient. This results in 27 non-zero BFF coefficients that need to be estimated for order 30. Note that the sinusoidal coefficients are non-zero for this case. Fig. 6.15 plots the smallest and the fifth smallest singular value of the stochastic observability matrix. It can be seen that the fifth smallest singular value is barely above the threshold at the end of the data-arc. Therefore, multiple coefficients are unobservable.

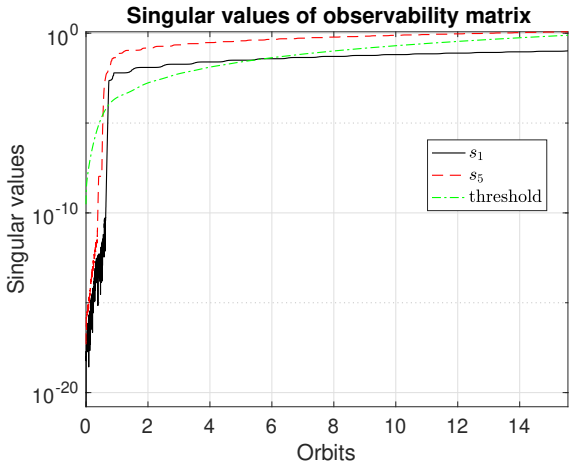

Figure 6.14: BFF model for an asymmetrical satellite: Smallest singular values of the stochastic observability matrix

Fig. 6.15 plots the QR orthogonalization based ranks for some of the BFF coefficients. The figure also plots the SNR metric of all the coefficients with SNR > 1. The metrics reveal that $\{\overline{\mathcal{A}}_0, \overline{\mathcal{A}}_2, \overline{\mathcal{B}}_1, \overline{\mathcal{A}}_4\}$ have the largest observable effects on the measurement. The rest of the

coefficients whose SNR values are larger than 1 are ranked lower than coefficients with SNRs less than 1. The non-dimensionalized standard-deviation of this subset of the BFF coefficients changes by a discernible amount over the data-arc as shown in Fig. 6.16 whereas it changes much more slowly for the other coefficients. The correlation matrix in Fig. 6.16 indicates a high correlation between the $\overline{\mathcal{A}}_4$ and $\overline{\mathcal{A}}_2$ coefficients.

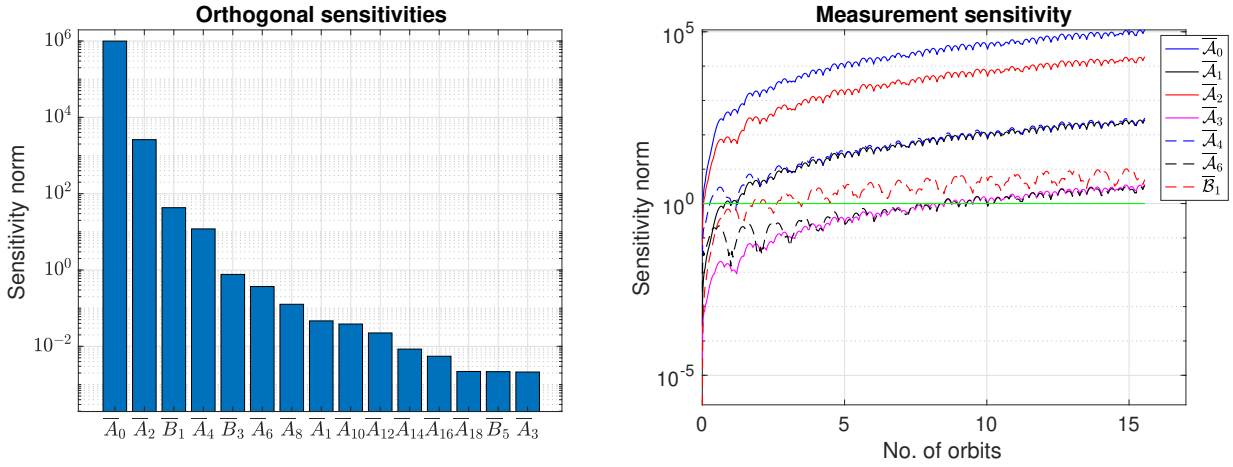

(a) (b)

Figure 6.15: BFF results for an asymmetrical satellite: (a) Norm of the orthogonal fractions of the total normalized sensitivity vectors; (b) Norm of the time-varying relative sensitivity vectors

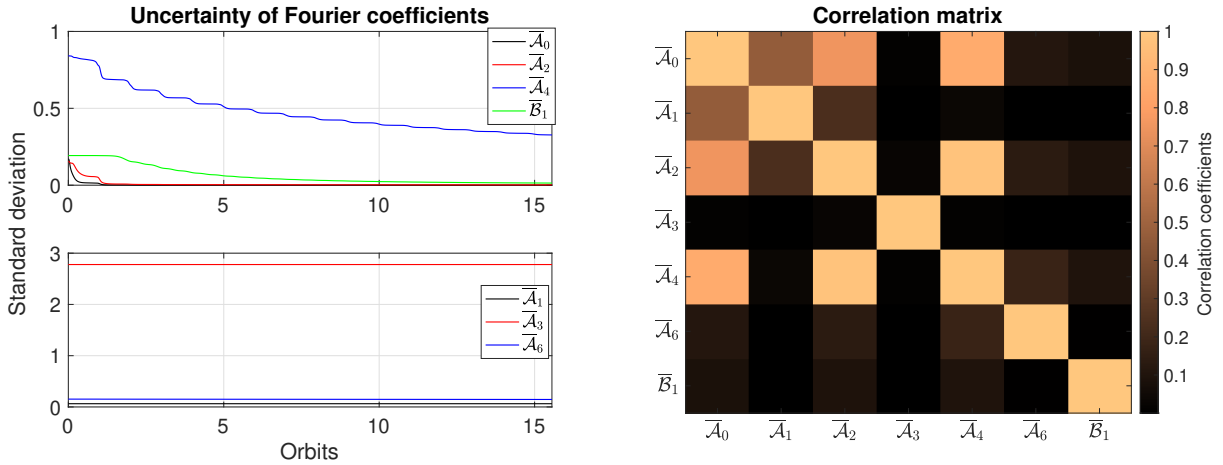

(a) (b)

Figure 6.16: (a) Non-dimensionalized standard deviation of the BFF coefficients ; (b) Correlation matrix for the BFF coefficients

Consider covariance analyses with estimation subsets given by the first six cases of Table 6.7 are carried out. The consider standard deviations and standard deviations assuming no errors in consider parameters are plotted in Fig. 6.17. The two standard deviations for the order 0 coefficient become nearly equal after case 4. Similar to the previous case, Monte Carlo simulations

Table 6.7: Monte Carlo simulation cases for BFF model for an asymmetrical satellite

Case	**Estimated coefficients**
1	$\overline{\mathcal{A}}_0$
2	$\overline{\mathcal{A}}_0, \overline{\mathcal{A}}_2$
3	$\overline{\mathcal{A}}_0, \overline{\mathcal{A}}_2, \overline{\mathcal{B}}_1$
4	$\overline{\mathcal{A}}_0, \overline{\mathcal{A}}_2, \overline{\mathcal{B}}_1, \overline{\mathcal{A}}_4$
5	$\overline{\mathcal{A}}_0, \overline{\mathcal{A}}_2, \overline{\mathcal{B}}_1, \overline{\mathcal{A}}_4, \overline{\mathcal{A}}_6$
6	$\overline{\mathcal{A}}_0, \overline{\mathcal{A}}_2, \overline{\mathcal{B}}_1, \overline{\mathcal{A}}_4, \overline{\mathcal{A}}_6, \overline{\mathcal{A}}_1$
7	$\overline{\mathcal{A}}_0, \overline{\mathcal{A}}_2, \overline{\mathcal{B}}_1, \overline{\mathcal{A}}_4, \overline{\mathcal{A}}_6, \overline{\mathcal{A}}_1, \overline{\mathcal{A}}_3$
8	$\overline{\mathcal{A}}_0, \overline{\mathcal{A}}_2, \overline{\mathcal{B}}_1, \overline{\mathcal{A}}_6, \overline{\mathcal{A}}_1, \overline{\mathcal{A}}_3$

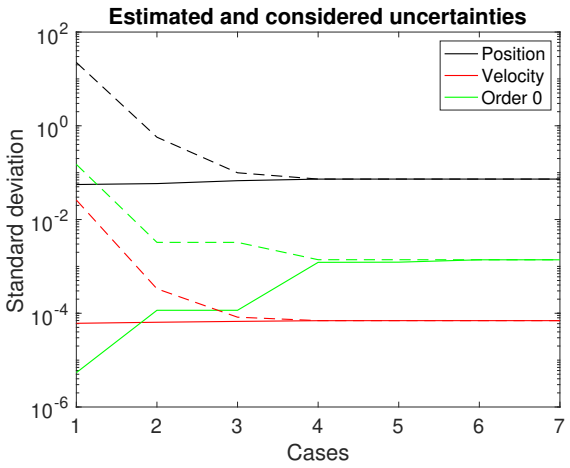

Figure 6.17: BFF model for an asymmetrical satellite: Standard deviations assuming no errors in consider parameters (solid lines) and consider standard deviations (dashed lines) for position, velocity and zeroth-order Fourier coefficient

are carried out for the cases in Table 6.7. The drag-coefficient error does not change much after case 2 but there's a very slight improvement from case 3 to case 4. The initial position error converges after case 4 and the measurement residual ratio converges after case 3. Ignoring $\overline{\mathcal{A}}_4$ due to its high correlations with $\overline{\mathcal{A}}_2$ results in a slight degradation in errors. Therefore, for this case,

$\{\overline{\mathcal{A}}_0, \overline{\mathcal{A}}_2, \overline{\mathcal{B}}_1, \overline{\mathcal{A}}_4\}$ should be estimated with all other BFF and OFF coefficients modeled.

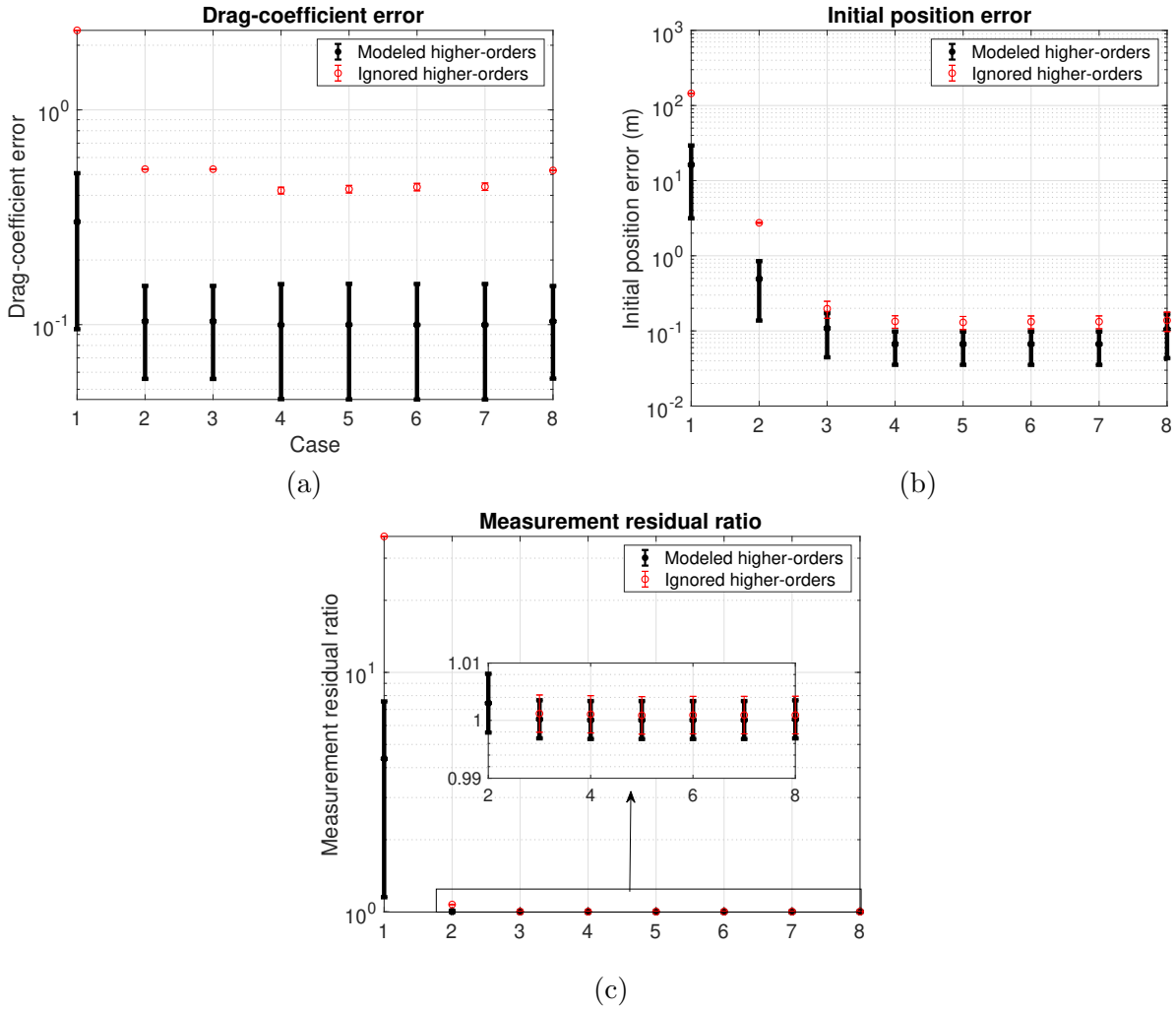

Figure 6.18: BFF model for an asymmetrical satellite: Mean and 1σ error bars for (a) Drag-coefficient error RMS values; (b) Norm of initial position error; (c) Non-dimensionalized measurement residual RMS values for asymmetrical satellite for the Monte Carlo cases

6.4.3 BODF model

In the previous section, the importance of modeling the OFF coefficients was seen from the Monte Carlo simulations where ignoring the higher order coefficients introduced much larger errors in the results. In this section, the BODF coefficients are added to the estimation subsets of the two cases of symmetrical and asymmetrical satellites considered for the BFF model.

On including the BODF coefficients, the number of coefficients with magnitude greater 10^{-5} increases to 78 for the symmetrical satellite. The observability matrix is rank-deficient as expected. Fig. 6.19 ranks the coefficients based on the QR decomposition method. The SNR metric indicates that $\overline{\mathcal{A}}_{0,0}$, $\overline{\mathcal{A}}_{0,1}$ and $\overline{\mathcal{A}}_{4,0}$ have the largest observable effects on the measurements since all other coefficients with SNR > 1 are ranked lower than coefficients with SNR < 1. The normalized standard-deviations in Fig. 6.20 support this observation. Fig. 6.20 also points out the high correlation between these three coefficients.

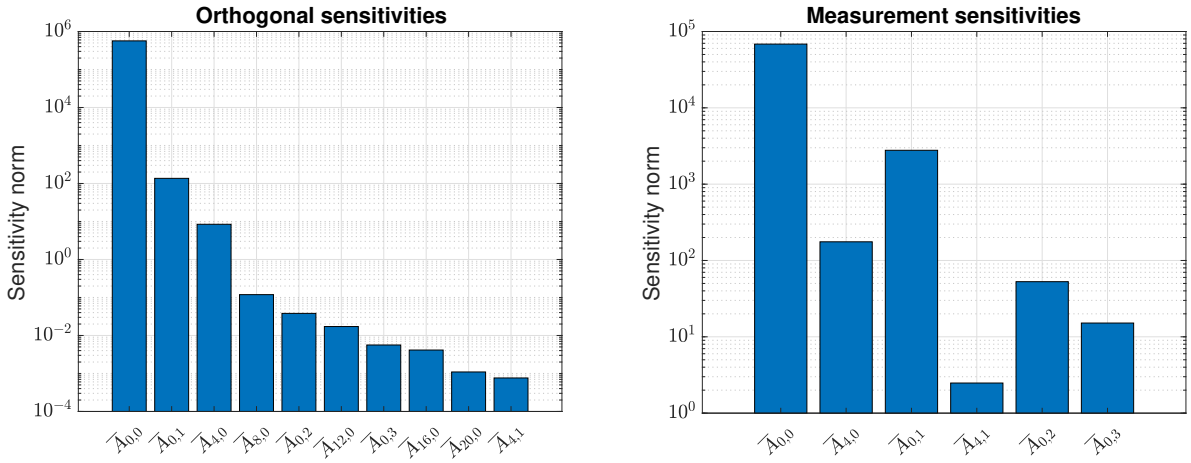

Figure 6.19: BODF results for a symmetrical satellite: (a) Norm of the orthogonal fractions of the total normalized sensitivity vectors; (b) Norm of the time-varying relative sensitivity vectors for a symmetrical cube

A consider covariance analysis is performed for the cases in Table 6.8. Fig. 6.21 shows that the consider standard-deviations and the standard-deviations assuming no errors in ignored coefficients become consistent for case 3. Monte Carlo simulations performed for all the cases validate this. It can be seen from Fig. 6.22 that the drag-coefficient error, initial position error as well as measurement residual ratio converge after case 3. Therefore, for a symmetrical satellite, estimating $\overline{\mathbb{A}}_{0,0}, \overline{\mathbb{A}}_{0,1}, \overline{\mathbb{A}}_{4,0}$ is sufficient.

The estimated Fourier coefficients are inverted to determine the Langmuir constant. The Langmuir constants are inverted from all the 200 Monte Carlo simulation run results and the mean

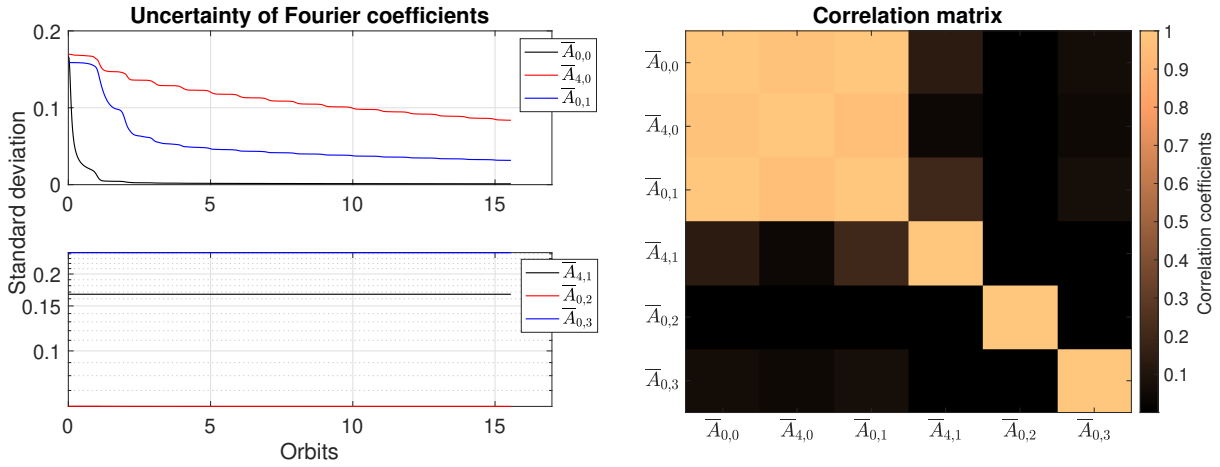

(a) (b)

Figure 6.20: BODF results for a symmetrical satellite: (a) Non-dimensionalized standard deviation of the BODF coefficients ; (b) Correlation matrix for the BODF coefficients

Table 6.8: Monte Carlo simulation cases for BODF model for a symmetrical satellite

Case	Estimated coefficients
1	$\overline{\mathbb{A}}_{0,0}$
2	$\overline{\mathbb{A}}_{0,0}, \overline{\mathbb{A}}_{0,1}$
3	$\overline{\mathbb{A}}_{0,0}, \overline{\mathbb{A}}_{0,1}, \overline{\mathbb{A}}_{4,0}$
4	$\overline{\mathbb{A}}_{0,0}, \overline{\mathbb{A}}_{0,1}, \overline{\mathbb{A}}_{4,0}, \overline{\mathbb{A}}_{4,1}$
5	$\overline{\mathbb{A}}_{0,0}, \overline{\mathbb{A}}_{0,1}, \overline{\mathbb{A}}_{4,0}, \overline{\mathbb{A}}_{4,1}, \overline{\mathbb{A}}_{0,2}$
6	$\overline{\mathbb{A}}_{0,0}, \overline{\mathbb{A}}_{0,1}, \overline{\mathbb{A}}_{4,0}, \overline{\mathbb{A}}_{4,1}, \overline{\mathbb{A}}_{0,2}, \overline{\mathbb{A}}_{0,3}$

and uncertainties are plotted in Fig. 6.23. For cases 1 and 2, the errors are much larger than the estimated uncertainty. After case 3, the errors are within the uncertainty bounds. After case 4, the uncertainty slightly increases but the estimation errors decrease. Note that only the zeroth order BFF coefficients ($\overline{\mathbb{A}}_{00}, \overline{\mathbb{A}}_{01}, \overline{\mathbb{A}}_{02}, \overline{\mathbb{A}}_{03}$) contain information on the Langmuir constant as discussed earlier. The errors decrease from case 1 to 2 because the estimated zeroth-order BODF coefficient is more accurate for case 2. The results indicate that even though it is sufficient to estimate the case 3 set in terms of orbit-determination results, the error in the inverted Langmuir constant can be further reduced by estimating the higher order coefficients, $\overline{\mathbb{A}}_{02}$ and $\overline{\mathbb{A}}_{03}$.

For the asymmetrical satellite, the number of coefficients for the BODF model is 118 on ex-

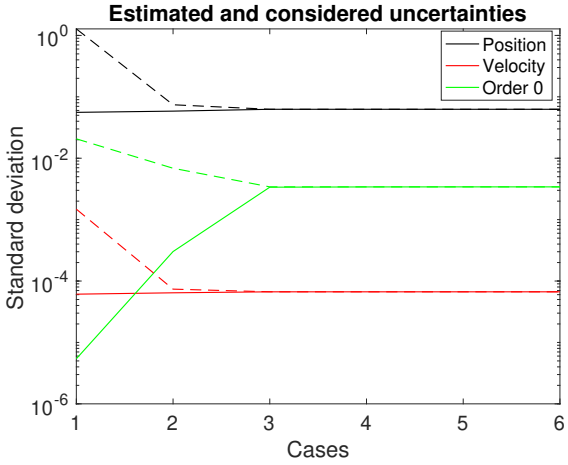

Figure 6.21: BODF results for a symmetrical satellite: Standard deviations assuming no errors in consider parameters (solid lines) and consider standard deviations (dashed lines) for position, velocity and zeroth-order Fourier coefficient

cluding coefficients with magnitudes smaller than 10^{-5}. Since the number of BFF coefficients remain the same as section 6.4.2, with the addition of BODF coefficients to the subset, the observability matrix remains rank-deficient. The non-dimensionalized sensitivity norm of all the coefficients with an SNR greater than 1 are plotted in Fig. 6.24 (b). The rank of first few coefficients are plotted in Fig. 6.24 (a). It can be seen that after $\overline{\mathbb{A}}_{0,1}$, coefficients with SNR < 1 start getting ranked higher than coefficients with SNR > 1. Therefore, it is reasonable to assume that coefficients ranked lower than $\overline{\mathbb{A}}_{0,1}$ may not need to be estimated. But some of the lower ranked coefficients with SNR $>$ 1 are still included in subsequent analysis. The non-dimensionalized standard deviations of the coefficients until $\overline{\mathbb{A}}_{0,1}$ decrease more rapidly than the rest of the coefficients as shown in Fig. 6.25 (a). The correlations between the coefficients are not very high as indicated by Fig. 6.25 (b).

A consider covariance analysis with estimation subsets given by Table 6.9 shows that it is sufficient to estimate the ranked coefficients until $\overline{\mathbb{A}}_{0,1}$. This is verified through a Monte Carlo analysis with the same cases. The results until case 4 are the same as Fig. 6.18. Fig. 6.27 shows that a significant reduction in the drag-coefficient error as well as initial position error is achieved from case 4 to case 5. The measurement residual ratio is also slightly closer to 1 for case 5.

Since the body and orbit angles vary at similar rates for an inertially stabilized satellite, it

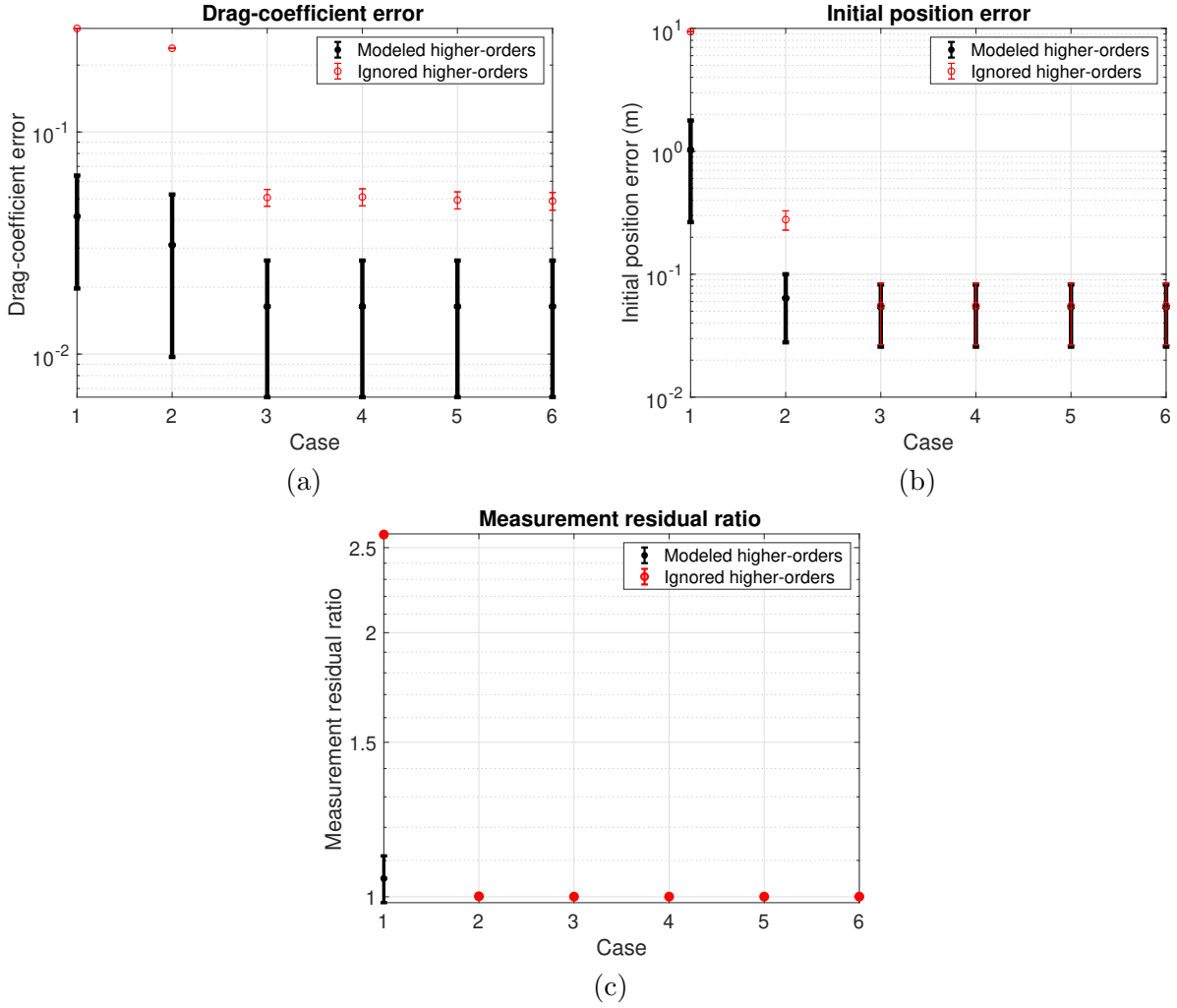

Figure 6.22: BODF results for a symmetrical satellite: Mean and 1σ error bars for (a) Drag-coefficient error RMS values; (b) Norm of initial position error; (c) Non-dimensionalized measurement residual RMS values for Monte Carlo cases

is possible that even though the drag-coefficient accuracy is improved for the BODF model, the individual Fourier coefficients might have larger errors due to aliasing effects. But the estimation errors for the coefficients in Table 6.10 prove that the Fourier coefficients have a higher accuracy when they are estimated versus when they are not. Therefore, the overall improvement in the drag-coefficient is due to the improvement in the estimation accuracy of the Fourier coefficients.

The Langmuir constant is inverted for all the Monte Carlo cases. As for the symmetrical satellite, the error decreases for more higher-order coefficients in the estimation set whereas the

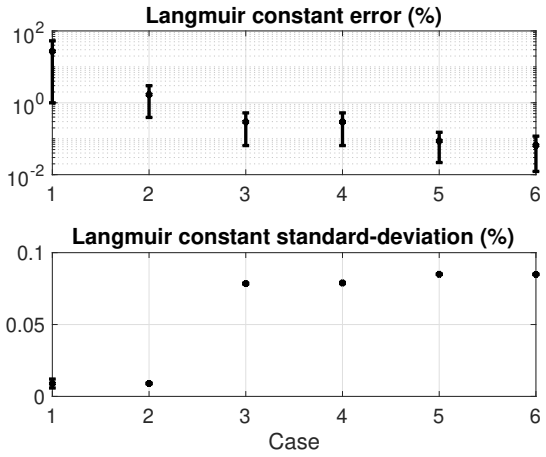

Figure 6.23: BODF results for a symmetrical satellite: Error and uncertainty of the Langmuir constant inverted from the estimated Fourier coefficients for the cases in Table 6.8

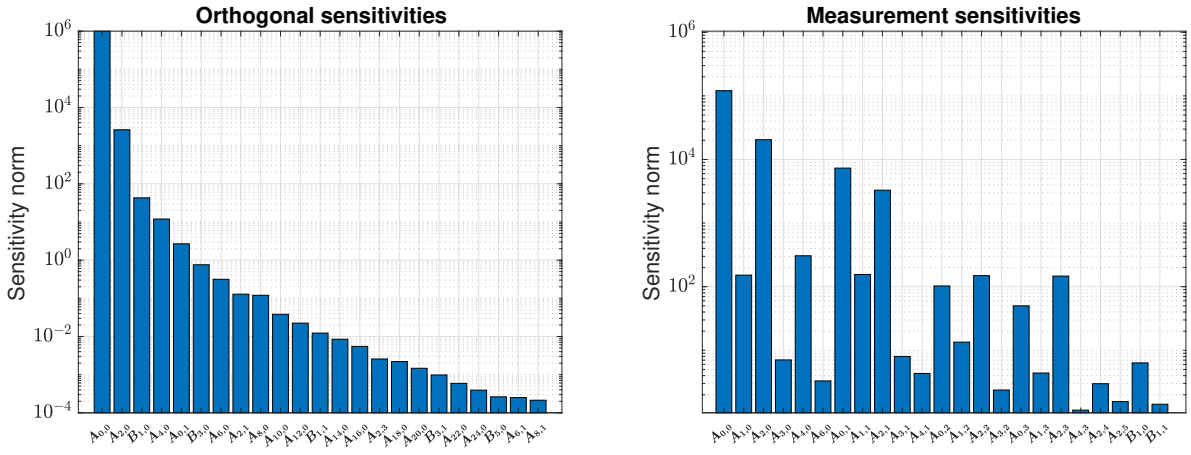

(a) (b)

Figure 6.24: BODF results for an asymmetrical satellite: (a) Norm of the orthogonal fractions of the total normalized sensitivity vectors; (b) Norm of the time-varying relative sensitivity vectors for a symmetrical cube for Monte Carlo cases

uncertainty in the inverted constant increases. The error and uncertainty converge after case 7. Even though it is sufficient to estimate the coefficients in case 5 for orbit determination, a few more higher-order coefficients should be estimated to obtain an accurate Langmuir constant.

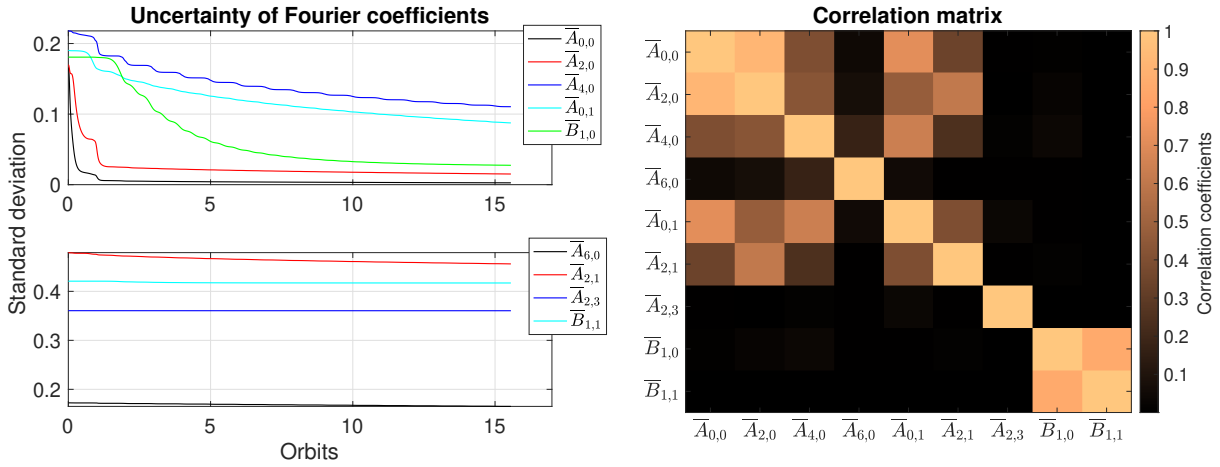

(a) (b)

Figure 6.25: BODF results for an asymmetrical satellite: (a) Non-dimensionalized standard deviation of the BODF coefficients ; (b) Correlation matrix for the BODF coefficients

Table 6.9: Monte Carlo simulation cases for BODF model for an asymmetrical satellite

Case	**Estimated coefficients**
1	$\overline{\mathbb{A}}_{0,0}$
2	$\overline{\mathbb{A}}_{1,0}, \overline{\mathbb{A}}_{2,0}$
3	$\overline{\mathbb{A}}_{0,0}, \overline{\mathbb{A}}_{2,0}, \overline{\mathbb{B}}_{1,0}$
4	$\overline{\mathbb{A}}_{0,0}, \overline{\mathbb{A}}_{2,0}, \overline{\mathbb{B}}_{1,0}, \overline{\mathbb{A}}_{4,0}$
5	$\overline{\mathbb{A}}_{0,0}, \overline{\mathbb{A}}_{2,0}, \overline{\mathbb{B}}_{1,0}, \overline{\mathbb{A}}_{4,0}, \overline{\mathbb{A}}_{0,1}$
6	$\overline{\mathbb{A}}_{0,0}, \overline{\mathbb{A}}_{2,0}, \overline{\mathbb{B}}_{1,0}, \overline{\mathbb{A}}_{4,0}, \overline{\mathbb{A}}_{0,1}, \overline{\mathbb{A}}_{6,0}$
7	$\overline{\mathbb{A}}_{0,0}, \overline{\mathbb{A}}_{2,0}, \overline{\mathbb{A}}_{1,0}, \overline{\mathbb{A}}_{4,0}, \overline{\mathbb{A}}_{0,1}, \overline{\mathbb{A}}_{6,0}, \overline{\mathbb{A}}_{2,1}$
8	$\overline{\mathbb{A}}_{0,0}, \overline{\mathbb{A}}_{2,0}, \overline{\mathbb{A}}_{1,0}, \overline{\mathbb{A}}_{4,0}, \overline{\mathbb{A}}_{0,1}, \overline{\mathbb{A}}_{6,0}, \overline{\mathbb{A}}_{2,1}, \overline{\mathbb{B}}_{1,1}$
9	$\overline{\mathbb{A}}_{0,0}, \overline{\mathbb{A}}_{2,0}, \overline{\mathbb{A}}_{1,0}, \overline{\mathbb{A}}_{4,0}, \overline{\mathbb{A}}_{0,1}, \overline{\mathbb{A}}_{6,0}, \overline{\mathbb{A}}_{2,1}, \overline{\mathbb{B}}_{1,1}, \overline{\mathbb{A}}_{2,3}$

Table 6.10: Estimation error in the BODF coefficients for an asymmetrical satellite

Coefficient	**Estimation error (Case 1)**	**Estimation error (Case 6)**
$\overline{\mathbb{A}}_{0,0}$	0.112	0.011
$\overline{\mathbb{A}}_{2,0}$	0.352	0.034
$\overline{\mathbb{B}}_{1,0}$	0.003	4.079e-4
$\overline{\mathbb{A}}_{4,0}$	0.070	0.036
$\overline{\mathbb{A}}_{0,1}$	0.063	0.027
$\overline{\mathbb{A}}_{6,0}$	0.0234	0.0228

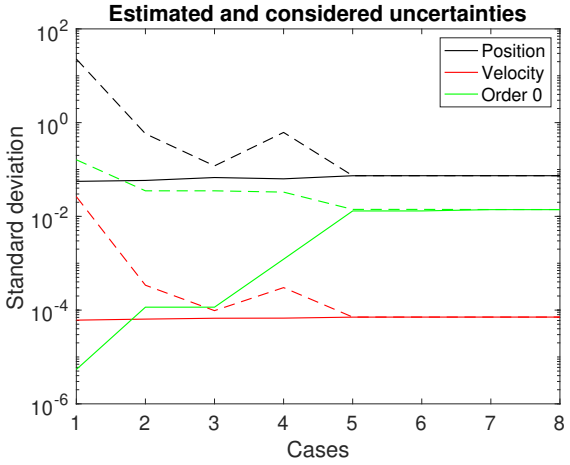

Figure 6.26: BODF results for an asymmetrical satellite: Standard deviations assuming no errors in consider parameters (solid lines) and consider standard deviations (dashed lines) for position, velocity and zeroth-order Fourier coefficient

6.5 Discussions

The observability analysis of Fourier drag-coefficient models using various metrics reveals that when a model has a large number of non-zero coefficients, only a few need to be estimated while the rest should be modeled, i.e., kept constant at their nominal values, in the orbit determination process. For the orbit-fixed Fourier (OFF) model applied to a spherical satellite, there's no attitude dependence and therefore, the OFF coefficients can be considered constant. According to the observability metrics, estimating the first three coefficients is sufficient for orbit determination. But including the order 3 coefficient improves the accuracy of the inverted Langmuir constant, which may be of future interest for improving gas surface interaction models (GSIMs). On the other hand, the body-fixed Fourier (BFF) coefficients for a satellite with a changing attitude vary in orbit. Therefore, estimating the BFF coefficients as constants leads to relatively large drag-coefficient errors even though the post-fit residuals are minimized. On including just a few body-orbit double Fourier (BODF) coefficients to the estimation set, leads to around a 50 % improvement in the drag-coefficient accuracy compared to the BFF model for both the symmetrical and asymmetrical satellites. For the symmetrical satellite, three coefficients ($\overline{\mathbb{A}}_{0,0}, \overline{\mathbb{A}}_{0,1}, \overline{\mathbb{A}}_{4,0}$) need to be estimated

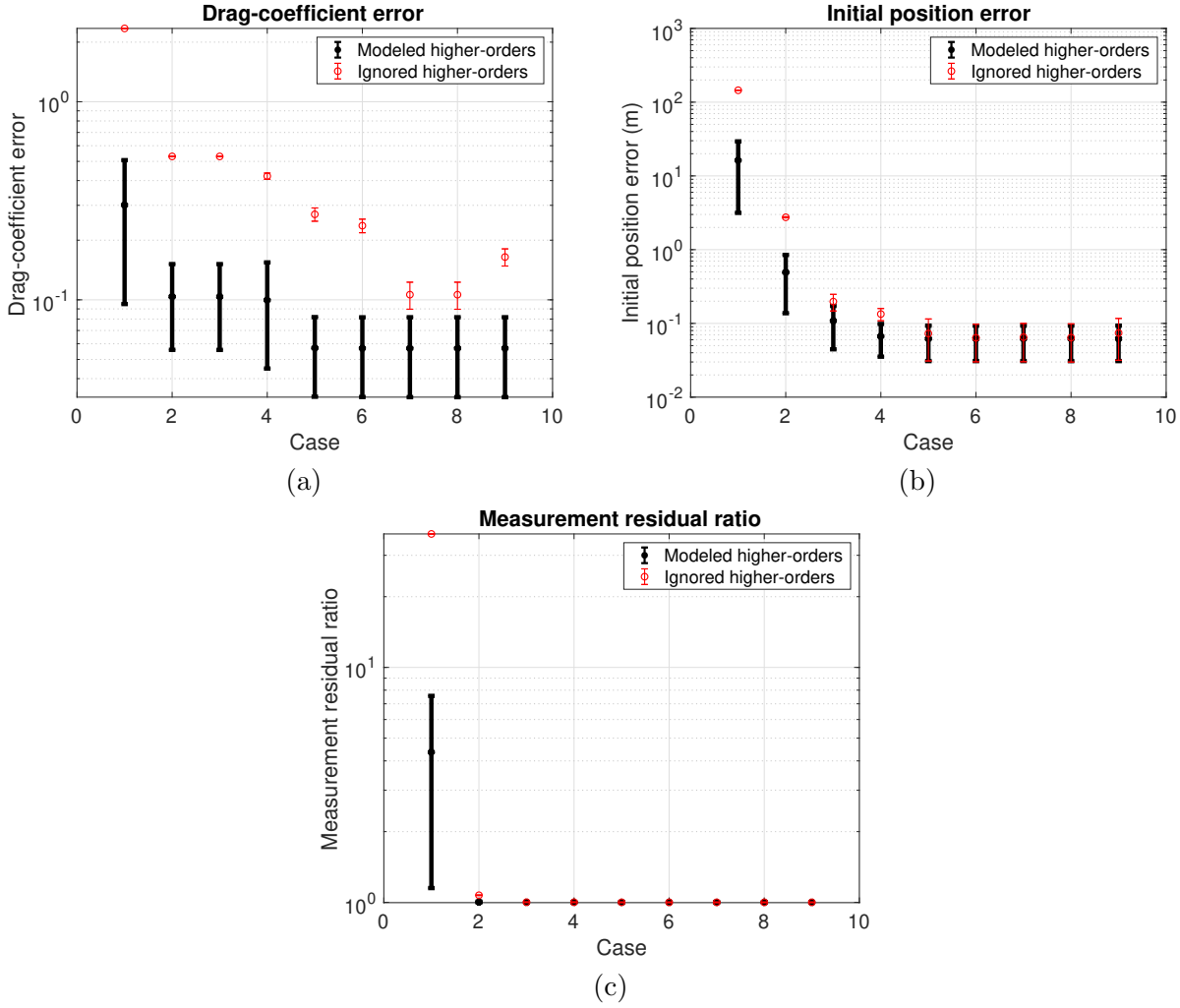

Figure 6.27: BODF results for an asymmetrical satellite: Mean and 1σ error bars for (a) Drag-coefficient error RMS values; (b) Norm of initial position error; (c) Non-dimensionalized measurement residual RMS values for asymmetrical satellite for Monte Carlo cases

while for the asymmetrical satellite, five coefficients ($\overline{\mathbb{A}}_{0,0}, \overline{\mathbb{A}}_{2,0}, \overline{\mathbb{B}}_{1,0}\overline{\mathbb{A}}_{4,0}, \overline{\mathbb{A}}_{0,1}$) need to be estimated, in terms of orbit determination accuracy. Including a few more higher-order coefficients for both the cases further improves the estimation error of the Langmuir constant. In all the cases, the accuracy of the inverted Langmuir constant is drastically improved when using higher-order Fourier coefficients as opposed to using only the zeroth-order coefficient. In order to apply the methods on real data, certain assumptions pertaining to the current analysis will need to be re-evaluated as summarized in Table 6.11.

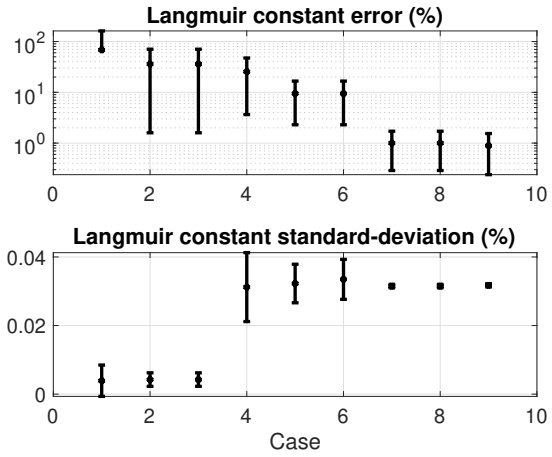

Figure 6.28: BODF results for an asymmetrical satellite: Error and uncertainty of the Langmuir constant inverted from the estimated Fourier coefficients for the cases in Table 6.9

Assumptions	**Expected impact**	**Mitigation**
Accurate density	Density errors absorbed by the estimated Fourier coefficients.	Estimate density correction simultaneously.
Single space weather condition	Observable coefficient set will change for other space weather conditions.	Carry out the analysis across varying solar and geomagnetic activities.
Error in single GSIM parameter	Errors due to other GSIM parameters will be absorbed by the estimated Langmuir constant.	1. An uncertainty analysis considering the errors in other parameters. 2. Include other GSIM parameters in the estimation.
No errors in other force parameters	Any errors in other force parameters such as solar radiation pressure will be absorbed by the Fourier coefficients.	Estimate other force parameters, especially the solar radiation pressure coefficient.

Table 6.11: Summary of assumptions made in this work, their expected impact on the results and how they can potentially be mitigated

The methods developed in this work allow the estimation of GSIM parameter sets for any given satellite. Instead of using GSIM parameters that have been determined using specific satellites for particular space weather conditions, they can be estimated for the satellite in consideration. But the estimates obtained are still biased to the atmospheric model used. Due to the correlated nature of the density and drag-coefficient, any errors in the densities will be absorbed by the estimated

drag-coefficient and vice-versa. Similarly, the Fourier coefficient estimates, and consequently the GSIM parameter estimates, will absorb errors in the density model used in the filter. This is a cyclical problem since density corrections that are calculated using orbital element changes absorb errors from fitted or physical drag-coefficients. The final goal of this research is to leverage the method developed here to obtain unbiased estimates of density and drag-coefficient. Wright and Woodburn (2004) [135] proposed a method to simultaneously estimate density and drag-coefficient during orbit-determination that was used by McLaughlin et al. (2011) [67] to arrive at CHAMP and GRACE densities. Even though their method can estimate time-variations in the density and drag-coefficient, the biases in the parameters still remain unresolved. In the next chapter, the inversion framework developed here is leveraged to simultaneously estimate the drag-coefficient and unbiased densities. Additionally, the use of other state-of-the-art GSIMs might be considered such as non-DRIA models. The inclusion of other GSIM parameters, specifically the effective satellite surface mass and quasi-specular lobe properties in the developed method might also be considered.

6.6 Chapter summary

Observability analysis using various metrics such as ranking of Fourier coefficients based on QR orthogonalization, non-dimensionalized measurement sensitivity, correlation coefficients and consider covariances was undertaken for the Fourier drag-coefficient models with the ultimate goal of inverting the Langmuir constant from the estimated Fourier coefficients. Inversion of the Langmuir constant from satellite tracking data is a step towards increasing the accuracy of current GSIMs by providing better estimates of uncertain input parameters that feed into these models. Using parameter ranking based on QR orthogonalization and the ratio of measurement sensitivity to measurement noise standard deviation facilitates the selection of estimation subset. A consider covariance analysis performed in conjunction verifies that the selected coefficients have the dominant effect on filter uncertainties. The correlations in the selected estimation set are analyzed through correlation coefficients. Finally Monte Carlo simulations are performed to validate the results. In every case, the set selected through the observability analysis leads to the best orbit-determination

fit in terms of overall drag-coefficient error, initial position error and post-fit residuals. For all the drag-coefficient models, less than six coefficients need to be estimated and rest of the coefficients modeled to obtain the best orbit-determination achievable. The estimated Fourier coefficients have been shown to improve the accuracy of the inverted Langmuir constant, obtained via a least-squares estimation method, by orders of magnitude compared to simply using the constant cannonball estimate for the same. The framework presented here can be extended to invert other GSIM parameters and to other GSIMs in general. The final aim of this research is to utilize this method to obtain unbiased atmospheric densities by simultaneously estimating density and drag-coefficient in the orbit determination process.

Chapter 7

Decorrelating density and drag-coefficient estimates

In the orbit determination process, the atmospheric density is usually modeled in the filter using semi-empirical models calibrated with satellite data and the drag-coefficient is estimated as a constant. But significant discrepancies exist between the current operational semi-empirical density models [90] such as NRLMSISE-00 [93], JB2008 [6] and DTM-2013 [8] due to the differences in calibration data as well as physics of the models. Any errors in the atmospheric density will consequently get absorbed in the estimated states and the drag-coefficient, leading to errors in predicted orbits.

In an ideal scenario, one would utilize an atmospheric density model that is calibrated real-time using tracking data from multiple satellites such as the Air Force High Accuracy Satellite Drag Model (HASDM) [117] in order to reduce errors due to atmospheric density and obtain physically consistent values of the drag coefficient. But unfortunately, HASDM is not available to users outside of the Department of Defense. The release of HASDM densities over the past twenty years as an open-source dataset by Space Environment Technologies (SET) [126] has provided the research community and non-governmental satellite operators access to the most accurate density data available for satellite tracking purposes. The HASDM densities can be used to calibrate existing semi-empirical density models or used more directly for orbit determination using a predictive framework with a chosen input parameter space [56]. This will potentially result in a significant increase in tracking accuracy and orbit predictions. But even then, more data needs to be ingested in such a framework for use across different solar cycles and during times of higher geomagnetic

activity. This is especially true since HASDM densities are available at a limited spatial and temporal resolution (3-hourly intervals, 25 km altitude level, $10^0 \times 15^0$ latitude/ longitude grid) which will not be sufficient to capture the high-frequency density variations during geomagnetic storms.

Physics-based density models are better at capturing the thermospheric response to external forcing but need to be calibrated with satellite observations of the thermosphere. Data-assimilation methods for physics-based atmospheric models have been proposed to estimate the global atmospheric density [65, 120, 121]. These methods combine the advantages of physics-based models in their ability to account for the thermospheric dynamics and provide density forecasts, and indirect measurements of the actual state of the thermosphere via data from accelerometers and satellite orbit tracking. Though their computational complexity makes it difficult for them to be used for real-time operational orbit determination, such methods can provide density estimates that can be used to calibrate semi-empirical density models. The computational complexity of physics-based models can be reduced by representing them with a smaller subset of parameters using reduced order models [74, 75]. This technique has been used to demonstrate estimation of global atmospheric density by assimilating measurements from accelerometers [76], two-line element (TLE) data [39], and radar and GPS measurements [40]. All such data-assimilation methods are demonstrating significant improvements in global atmospheric density estimates over existing semi-empirical density models. But the obtained densities are uncertain to the ballistic coefficient estimated by the filter. Moreover, real-time tracking data from multiple sources is required to provide density estimates which may prove to be a hurdle for implementation in operational use. A method that can estimate the local atmospheric density along the orbit simultaneously with the ballistic coefficient during orbit determination is needed.

The simultaneous estimation of density and drag-coefficient is complicated due to their highly correlated nature. In particular, biases in the density and drag-coefficient cannot be simultaneously observed by the filter, and will be estimated as a lumped term. Therefore, the cannonball drag-coefficient, estimated as a scale factor, not only averages out time-variations in the drag-coefficient

due to attitude and ambient parameters but also absorbs time-averaged errors in the density model. Wright et al. [135] proposed a method to simultaneously estimate the drag-coefficient and density by modeling them as exponentially correlated Gauss-Markov processes. The drag coefficient is assumed to have a much slower variation than the density which allows separation of the two. This method provides a practical way to decorrelate the two parameters and has been used by McLaughlin et al. [67] to arrive at densities derived using CHAMP POD. But the bias terms in the density and drag-coefficient still cannot be estimated simultaneously, i.e., the estimate is accurate only up to a constant bias. Moreover, time variations in the drag-coefficient due to attitude changes are not accounted for.

The goal of this chapter is to provide a framework to estimate local atmospheric densities from satellite tracking data at sub-orbital cadence with a reduction in bias contribution due to the drag-coefficient. The time-variations in the drag-coefficient induced by changes in the satellite attitude introduce frequencies in the drag force that are independent of density variations. These high-order frequencies can be estimated in the filter that can then be used to calculate the bias term by utilizing known physics of gas-surface interactions. We propose the use of Fourier series expansions to estimate the time-variations in the drag-coefficient. The estimated Fourier coefficients contain information on gas-surface interaction (GSI) parameters that govern the drag-coefficient variation and can be used to invert specific uncertain parameters, as outlined in the previous chapter. But the density was assumed to be perfectly known, and therefore, the estimated Fourier coefficients absorbed any errors present in the density. The Fourier model for the drag-coefficient still might lead to improvements in short-term orbit predictions if the estimated Fourier coefficients are able to emulate the combined variations in the drag-coefficient and density error as shown in chapter 5. But the Fourier coefficients themselves will not represent a true time series of drag-coefficient. Therefore, the inverted GSI parameters will be physically inconsistent. But if the density error is modeled as a Gauss-Markov process, the higher-order Fourier coefficients (except the bias term) can be estimated simultaneously with the density corrections. The Fourier coefficients are then used to invert uncertain GSI parameters. With a better constraint on the GSI model, a more

accurate bias term can be calculated. Therefore, with high-frequency tracking measurements such as GPS data, accurate local atmospheric densities along the orbit at a sub-orbital cadence can be obtained. An improvement in the estimated densities and drag-coefficients with the proposed method is demonstrated using synthetic data across different altitudes and space weather conditions. A preliminary validation of the method is presented using precision orbit determination (POD) from the Spire satellites.

7.1 Modeling density using a Gauss-Markov process

The dynamical model used in the estimation method can have structural errors as well as errors in governing parameters. Whereas some parameters can be estimated within the filtering framework, structural errors are more difficult to compensate for and can lead to filter divergence, where the estimation error exceeds the covariance bounds. A common way to take them into account in the filter is to model them as stochastic processes. The dynamics equation with noise can be written as [124]

$$\dot{\boldsymbol{x}}(t) = \boldsymbol{A}(t)\boldsymbol{x}(t) + \boldsymbol{B}(t)\boldsymbol{u}(t). \tag{7.1}$$

The noise vector, $\boldsymbol{u}(t)$ is generally added to a subset of the states and is therefore of a smaller dimension than the state vector. In State Noise Compensation (SNC), white noise with a known covariance is used to compensate for the dynamics errors. Though SNC can prevent filter divergence by expanding the covariance bounds, it cannot provide an estimate of the dynamics error. The use of Gauss-Markov processes in the filter known as Dynamic Model Compensation (DMC) allows the possibility of estimating the dynamics errors. A Gauss-Markov process is a correlated Gaussian noise such that the probability density function at the current time (t_n) depends only on the probability density at the previous time instant (t_{n-1}). A zeroth-order Gauss Markov process (GMP0) is equivalent to SNC. The first-order Gauss Markov process (GMP1) is given by the

first-order differential equation known as Langevin equation,

$$\dot{\eta}(t) = -\lambda\eta(t) + u(t), \tag{7.2}$$

where $E(u) = 0$ and $E[u(t)u(t+\tau) = Q\delta(\tau)]$. The GMP state, $\eta(t)$, is augmented with the state vector and estimated in the filter. The time constant or correlation time $(1/\lambda)$ is a tuning parameter and needs to be calibrated. The first order Gauss-Markov process has been shown to be more accurate in compensating for errors in force models during orbit determination than simply adding white noise [17].

For dynamics errors with periodic components, a second-order Gauss-Markov process (GMP2) can prove to be more beneficial. The advantage of using a GMP2 over GMP1 has been demonstrated for gravity error compensation and the possibility of modeling other orbit-dependent errors such as atmospheric drag and solar radiation pressure using GMP2 was suggested [55]. In particular, using GMP2 to model the atmospheric density was suggested by Nievinski et al. [85] due to the oscillatory nature of the parameter. In the following, a framework to model errors in atmospheric density using a GMP2 is developed. The second order Gauss-Markov process can be represented in the state-space form as

$$\begin{bmatrix} \dot{x}_1 \\ \dot{x}_2 \end{bmatrix} = \begin{bmatrix} 0 & 1 \\ -\omega_n^2 & -2\zeta\omega_n \end{bmatrix} \begin{bmatrix} x_1 \\ x_2 \end{bmatrix} + \begin{bmatrix} 0 \\ c_1 \end{bmatrix} w(t), \tag{7.3}$$

where $E(w) = 0$ and $E[w(t)w(t+\tau) = q\delta(\tau)]$. The natural frequency of the process (ω_n), the damping factor (ζ) and the strength of the white noise (c_1 with $q = 1$) are tuning parameters that need to be calibrated. The calibration process can be performed by fitting the covariance of sample data for the modeled state to the autocovariance function of the GMP2. For example, in the case of density estimation, the sample data can be obtained from satellite missions GRACE and CHAMP or datasets such as the SET HASDM database [126]. The autocovariance function is

given by [55]

$$\psi_{nn}(\tau) = \frac{qc^2}{4\omega_n^3\zeta}\exp\left(-\zeta\omega_n|\tau|\right)(\cos\beta|\tau| + \frac{\zeta\omega_n}{\beta}\sin\beta|\tau|), \tag{7.4}$$

where $\beta = \omega_n\sqrt{1-\zeta^2}$. The covariance of the data samples can be fit to Eq. 7.4 with c, ζ and ω_n as the fitting parameters. The fitting process is detailed in Leonard et al. [55]. The fitting process doesn't always converge on the correct tuning parameters and some trial and error is usually required, since significant differences between density models can be observed depending on the ambient conditions. An adaptive DMC to correct for the tuning parameters using tracking data can potentially provide a better solution [116] and will be considered in future work.

In the filter, x_1 and x_2 are both estimated and the correction to the modeled density is given by x_1. In addition to modeling the density correction using a GMP2, a GMP0 correction to the density with noise standard deviation c_2 is estimated as well. The next section details the implementation of the algorithm in the filter.

7.1.1 Filter implementation

In this section, the implementation of the DMC algorithm in an extended Kalman filter (EKF) is outlined. The framework is presented for GMP2 but GMP1 can be similarly implemented in the filter. The augmented state vector to be estimated is composed of the satellite position ($\boldsymbol{r}$) and velocity ($\dot{\boldsymbol{r}}$), parameters ($\boldsymbol{p}$) such as the Fourier drag-coefficients and the GMP states for density correction,

$$\boldsymbol{X} = \begin{bmatrix} \boldsymbol{r}^T & \dot{\boldsymbol{r}}^T & \boldsymbol{p}^T & x_1 & x_2 & x_3 \end{bmatrix}^T, \tag{7.5}$$

where x_3 is the GMP0 correction and $\boldsymbol{p} \in \mathbb{R}^{m\times 1}$. The time derivative of the state vector is then given by

$$\dot{\boldsymbol{X}} = \begin{bmatrix} \dot{\boldsymbol{r}}^T & \ddot{\boldsymbol{r}}^T & \dot{\boldsymbol{p}}^T & x_2 & -\omega_n^2 x_1 - 2\zeta\omega_n x_2 & 0 \end{bmatrix}^T. \tag{7.6}$$

The density in the filter (ρ) at any time instant is given by

$$\rho = \rho_{mod}(1 + x_1 + x_3), \tag{7.7}$$

where ρ_{mod} is the nominal density from an atmospheric model such as NRLMSISE-00 or JB2008 being used in the filter. Note that the corrections are normalized by the nominal density for numerical stability. The dynamics Jacobian is then given by

$$\boldsymbol{A}(t) = \begin{bmatrix} \mathbf{0}_{3\times3} & \boldsymbol{I}_{3\times3} & 0_{3\times m} & 0 & 0 & 0 \\ \frac{\partial \ddot{\boldsymbol{r}}}{\partial \boldsymbol{r}} & \frac{\partial \ddot{\boldsymbol{r}}}{\partial \dot{\boldsymbol{r}}} & \frac{\partial \ddot{\boldsymbol{r}}}{\partial \boldsymbol{p}} & \frac{\partial \ddot{\boldsymbol{r}}}{\partial x_1} & 0 & \frac{\partial \ddot{\boldsymbol{r}}}{\partial x_3} \\ \frac{\partial \dot{\boldsymbol{p}}}{\partial \boldsymbol{r}} & \frac{\partial \dot{\boldsymbol{p}}}{\partial \dot{\boldsymbol{r}}} & \frac{\partial \dot{\boldsymbol{p}}}{\partial \boldsymbol{p}} & 0 & 0 & 0 \\ \mathbf{0}_{1\times3} & \mathbf{0}_{1\times3} & \mathbf{0}_{1\times m} & 0 & 1 & 0 \\ \mathbf{0}_{1\times3} & \mathbf{0}_{1\times3} & \mathbf{0}_{1\times m} & -\omega_n^2 & -2\zeta\omega_n & 0 \\ \mathbf{0}_{1\times3} & \mathbf{0}_{1\times3} & \mathbf{0}_{1\times m} & 0 & 0 & 0 \end{bmatrix}. \tag{7.8}$$

The partial of the acceleration with respect to the DMC parameters can be calculated by taking the derivative of the drag acceleration. The partial can be calculated by using eqs. 1.1 and 7.7,

$$\frac{\partial \ddot{\boldsymbol{r}}}{\partial x_1} = \frac{\partial \ddot{\boldsymbol{r}}}{\partial x_3} = -\frac{1}{2}\rho_{mod} C_d \frac{A_{ref}}{m} v_r^2 \hat{\boldsymbol{u}}, \tag{7.9}$$

The process noise matrix $\boldsymbol{Q}_{k+1}$ can be obtained by integrating the following equation

$$\boldsymbol{Q}_{k+1} = \int_{t_k}^{t_{k+1}} \boldsymbol{\phi}(t, t_k) \boldsymbol{B_a} \boldsymbol{Q_a} \boldsymbol{B_a}^T \boldsymbol{\phi}(t, t_k)^T dt. \tag{7.10}$$

Here $\boldsymbol{Q_a} = \boldsymbol{I}_{3\times3}$ and

$$\boldsymbol{B_a} = \begin{bmatrix} \mathbf{0}_{(6+m)\times2} \\ \text{diag}(\boldsymbol{c}) \end{bmatrix}, \tag{7.11}$$

where $\boldsymbol{c} = [c_1, c_2]$. Note that the measurement matrix does not depend on the DMC states.

Since noise is added to the states, a smoothing algorithm is implemented to reduce the error in the estimated states.

7.1.2 Iterated EKF with smoothing

One simple approach to obtain higher accuracy states in post-processing is improving the past estimates by using the current filtered states and measurements. The smoothing problem is that of finding an optimal estimate at time t_k given measurements till time t_j where $j > k$. Here we follow the fixed-interval smoothing approach [37], i.e., using the complete data-arc to smooth back to the past estimates. In order to implement this smoothing algorithm, the time histories of the state transition matrix, the process noise matrix and the correction factor required to account for the non-linearity of the EKF, need to be saved while forward filtering. The smoothing matrix is given by

$$\boldsymbol{S}_k = \boldsymbol{P}_k^+ \boldsymbol{\phi}_{k+1,k}^T \boldsymbol{P}_{k+1}^-. \tag{7.12}$$

The smoothed state ($\boldsymbol{X}_k^s$) and state covariance ($\boldsymbol{P}_k^s$) at the k^{th} instant given the smoothed state at time instant $k+1$ is given by,

$$\boldsymbol{X}_k^s = \hat{\boldsymbol{X}}_k + \boldsymbol{S}_k(\boldsymbol{X}_{k+1}^s - \boldsymbol{\phi}_{k+1,k}\hat{\boldsymbol{X}}_k - \boldsymbol{b}_{k+1}), \tag{7.13}$$

$$\boldsymbol{P}_k^s = \boldsymbol{P}_k^+ + \boldsymbol{S}_k(\boldsymbol{P}_{k+1}^s - \boldsymbol{P}_{k+1}^-)\boldsymbol{S}_k^T, \tag{7.14}$$

where $\hat{\boldsymbol{X}}_k$ is the state estimate at the k^{th} instant. The smoothing algorithm is initialized with $\boldsymbol{X}_N^s = \hat{\boldsymbol{X}}_N$ and $\boldsymbol{P}_N^s = \boldsymbol{P}_N^+$, where N is the number of measurements in the given data-arc. The correction factor ($\boldsymbol{b}_{k+1}$)) is computed by integrating the following differential equation from t_k to t_{k+1}.

$$\dot{\boldsymbol{b}}(t) = \boldsymbol{A}(t)\boldsymbol{b}(t) + \dot{\boldsymbol{X}}(t) - \boldsymbol{A}(t)\boldsymbol{X}^*(t), \tag{7.15}$$

with $\boldsymbol{b}(t_k) = \mathbf{0}$, $\boldsymbol{X}^*(t)$ refers to the propagated state estimate and $\dot{\boldsymbol{X}}(t)$ is given by eq. 7.6. The states are smoothed back to the first time instant and the EKF with smoothing is run again with the new initial state estimate. The filter is iterated until the initial state correction drops below a certain threshold.

7.2 Simultaneous estimation of density and drag-coefficient

During orbit determination, the drag-coefficient is usually estimated as part of the state vector since it is not accurately known apriori and its value can change in orbit. If the drag-coefficient was constant, it would not be simultaneously observable with the density bias since the filter would not be able to distinguish between two constant terms that exist in a product. Any correction to one term can be easily compensated for by the other term. Therefore, with an inaccurate constant drag-coefficient in the filter, the density can be estimated only up to a bias using the algorithm in the previous section. But for a satellite with attitude variations, the drag-coefficient will be time-varying as discussed in section 5.2.1. Using the BFF model outlined in that section, the time-varying components of the drag-coefficient can be estimated simultaneously with the density. The bias term (zeroth order Fourier coefficient, $\overline{\mathcal{A}}_0$) still cannot be estimated due to the observability problem, but the higher order Fourier coefficients can be estimated simultaneously with the density corrections due to the attached time-varying attitude terms. The bias in the drag-coefficient is primarily absorbed by the estimated density bias correction, modeled by the GMP0. The estimated Fourier coefficients will also be affected but to a lesser extent since they govern higher-order frequencies in the drag-coefficient variation that cannot be captured by the zeroth-order term. In order to calculate the drag-coefficient bias term, the functional relationship between the GSIM parameters and the Fourier coefficients represented by the integrals in Eqs. 5.16-5.17 can be utilized. A few GSIM parameters with the largest uncertainties can be inverted from the estimated Fourier coefficients, as outlined in the previous chapter. Then these inverted GSIM parameters can be used to calculate the zeroth-order term using Eq. 5.18. The filter is re-initialized with the new value of the zeroth-order term, with estimates and covariances of the

states from the previous iteration. A more accurate drag-coefficient bias term in the filter dynamics leads to a reduction in the density bias. The simultaneous estimation algorithm (Fig. 7.1) can be summarized as follows-

(1) Initial values of the Fourier coefficients are obtained using the filter density model and GSIM parameter estimates.

(2) The Kalman filter-smoother is initialized using these Fourier coefficients. In the filter, the zeroth-order Fourier coefficient or the bias term is kept constant while the higher-order Fourier coefficients are estimated simultaneously with the satellite position and velocity, density DMC states and any other parameters being estimated.

(3) The least-squares method outlined above is used to invert chosen GSIM parameters with the highest uncertainties from the estimated Fourier coefficients. The inverted values of the GSIM parameters are used to re-calculate the zeroth-order Fourier coefficient using Eq. 5.18.

(4) The Kalman filter-smoother is reinitialized with the new drag-coefficient bias term. All the other states are reinitialized with the estimated values and covariances from the first iteration, with the covariances slightly inflated. An improved estimate of the drag-coefficient bias leads to a more accurate density estimation.

7.3 Validation using simulated data

The proposed algorithm is validated in this section using controlled simulation scenarios before applying on real data. The performance of the method is tested on different altitude regimes, space weather conditions and filter model errors to understand its limitations. The true trajectory for all the cases is generated with a 10×10 geopotential (EGM-2008), a cannonball SRP model and atmospheric drag with time-varying drag-coefficient modeled using the modified DRIA model,

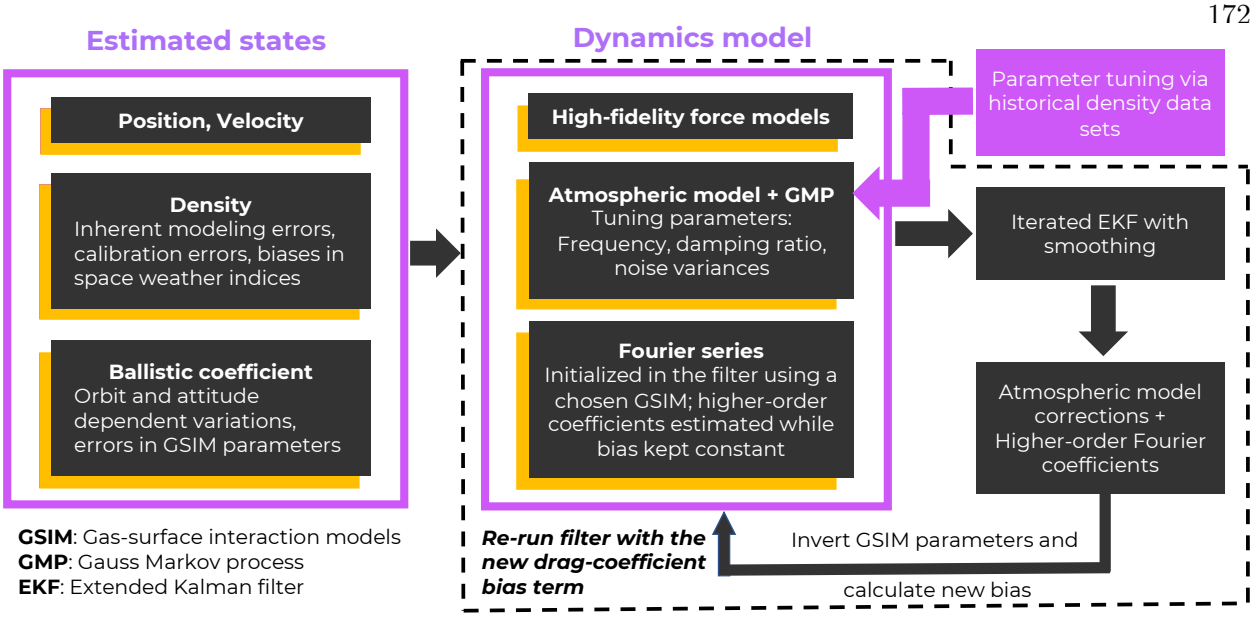

Figure 7.1: Summary of the algorithm

unless otherwise stated. Here, the fractional coverage parameter is assumed to be at a steady state value since the orbits considered are nearly circular.

The densities from the SET HASDM database are used for the true density during periods of nominally low to moderate geomagnetic activity. In order to implement the densities in orbit determination, a gridded linear interpolation of the logarithm of the densities is performed over latitude, longitude, altitude and time. The satellite is modeled on Spire [121] using a box-wing shape. The attitude profile is such that it tracks the Sun in light and assumes the minimal drag configuration in eclipse.

The performance of semi-empirical density models degrades during geomagnetic storms [9]. With the limited temporal resolution of the HASDM dataset, it cannot accurately capture the time variations in density over short time-scales. Therefore, in order to simulate the density variations during a geomagnetic storm, densities derived from the accelerometer measurements on-board CHAMP by Mehta et al. [73] using their Response Surface Model (RSM) drag-coefficients are used. In order to be consistent with the densities, orbital elements of CHAMP for the given time epoch are used to simulate the true trajectory. The simulated cases are summarized in Table

7.1. The symbols in the table stand for —r_{ads} is the velocity ratio for the surface covered by atomic oxygen which is a function of the energy accommodation coefficient α and the satellite wall temperature T_w, M is the mean molar mass of the ambient gases and T is the ambient temperature.

Table 7.1: Summary of simulated cases. The dashes indicate that the parameters are the same as the previous column.

Case	**1**	**2**	**3**
Epoch	Mar 23 2007	-	Oct 29 2003
Daily F10.7	72.5	-	279.1
Daily Ap	10	-	204
Apogee/Perigee altitude (km)	360/370	510/520	385/398
True density	HASDM	-	RSM CHAMP
Nominal filter density	NRLMSIS00	-	HASDM
True C_d GSIM parameters	$f = 0.7$	$f = 0.5$	$f = 0.65$, $T_w = 450$ K, JB2008 for M and T
Filter C_d GSIM parameters	$f = 0.98$	$f = 0.98$	$f = 0.98$, $T_w = 300K$, NRLMSISE-00 for M and T
Inverted GSIM parameters	f	-	r_{ads}

The estimated drag-coefficients and densities for the different cases are plotted in Fig. 7.2. For all the cases, the tuning parameters used are —$\omega_n = 0.0011$, $\zeta = 0.5$, $c_1 = 10^{-8}$ and $c_2 = 10^{-5}$. The natural frequency is taken as the orbit angular frequency while the rest of the parameters are chosen arbitrarily. It is apparent that there's a significant discrepancy between the true and nominal filter densities. NRLMSISE-00 consistently overpredicts the densities compared to HASDM for the first two cases during times of low geomagnetic activity while HASDM densities are larger than the CHAMP densities during the period of the 2003 Halloween storms. Part of the difference can be attributed to the interpolation of the HASDM densities. For the first two cases, the estimated drag-coefficients and densities after the second iteration track the truth quite well. The density and drag-coefficient biases are reduced in the second iteration, as a better constraint on the fractional coverage parameter is obtained from the Fourier coefficient estimates.

The third case simulates a scenario where it is not obvious which GSIM parameters are the most uncertain and should be inverted. The actual error is in the fractional coverage parameter and wall temperature but the velocity ratio is inverted from the Fourier coefficients, i.e., if two different GSIM parameters are able to model a given variation in the drag-coefficient. Though the estimated densities track the truth (CHAMP) better than the nominal filter density (HASDM), the bias due to the drag-coefficient is not greatly reduced as can be seen from the estimated drag-coefficient plot. The estimated densities are also not able to track the high-frequency variations visible in the truth. This is primarily because the tuning parameters are not well calibrated to model the higher-frequency variations during the geomagnetic storm. If the damping ratio is reduced and noise standard deviations increased ($\zeta = 0.09$, $c_1 = 10^{-4}$, $c_2 = 10^{-2}$), the estimated densities are able to track the temporal variations better. But in this case, the Fourier coefficients diverge from the truth, which subsequently increases the bias in the estimated densities. This happens because the Fourier coefficient uncertainties are smaller than the noise introduced in the filter; therefore, the corrections introduced are larger than the initial uncertainties. As seen in Fig. 7.3, it is better not to estimate the Fourier coefficients in this case. The estimated densities still contain the bias due to the drag-coefficient; it is just more difficult to estimate the bias due to the larger noise in the filter.

There's a possible solution around the problem —modify the tuning parameters between the first and the second iterations. If low noise levels are used in the first iteration, more accurate estimates of the Fourier coefficients can be obtained though the densities do not track the time-variations well. After a better constraint on the bias is obtained from the Fourier coefficient estimates, larger noise levels are introduced in the second iteration and the Fourier coefficients are no longer estimated. The estimated densities with this modified method accurately track the truth as seen in Fig. 7.3. It can be concluded from this example that the tuning parameters, especially the noise levels should be selected based on the space weather activity. The mean and RMS values of the drag coefficient and density error percentages, $(truth - estimate)/truth$, are given in Table 7.2. In all the simulated cases, the errors in drag-coefficient and density improve compared to

initial estimates after the second iteration of the algorithm. The improvement in density with the modified algorithm for case 3 is significant.

Table 7.2: Mean and RMS values of estimated drag-coefficient and density errors (%). The dashes indicate that the values are the same as the previous column.

Case		**1**		**2**		**3**		**3 (Modified)**	
		Mean	RMS	Mean	RMS	Mean	RMS	Mean	RMS
Drag-coefficient error	Initial	5.2	5.3	10.1	10.4	6.8	7	-	-
	Iteration 1	11.6	13.9	9.3	9.4	13.2	15.6	-	-
	Iteration 2	2.5	2.7	0.7	1.2	6.4	6.8	3.6	3.7
Density error	Initial	31	38.9	52.2	63	32.4	46	-	-
	Iteration 1	13	17.4	24.4	56.7	22	32.7	-	-
	Iteration 2	8.5	12.7	19.3	51.3	16.9	25.3	7.4	10.3

7.4 Application to real data

7.4.1 Dataset

The algorithm is tested on POD for Spire satellites. The PODs were obtained (and made available to us) by processing GNSS pseudorange and carrier phase measurements using the RTOrb software in a Kalman filtering framework. The software considers non-spherical gravity up to degree and order 120, third-body perturbations from Sun and Moon, atmospheric drag with MSISe-90 as the density model and solar radiation pressure (SRP) with a cylindrical shadow model. Cannonball drag-coefficient and SRP coefficient are estimated within each arc. The PODs obtained by RTOrb have a precision of several centimeters in position and sub-mm/s in velocity and are mostly available with a cadence of 1 s in data-arcs of 40-60 minutes. The attitude information of the satellites is in the form of quaternions between the body and the orbit frame. The quaternions are not uniformly available and can vary between a sample time of 10 s to 1000 s. For our application, the quaternions are needed as frequently as possible since the Spire satellites make frequent attitude maneuvers between an observing mode with the GNSS antennas aligned along-track and a power mode where the solar flux on the solar panels is maximized. Therefore, only a small subset of the

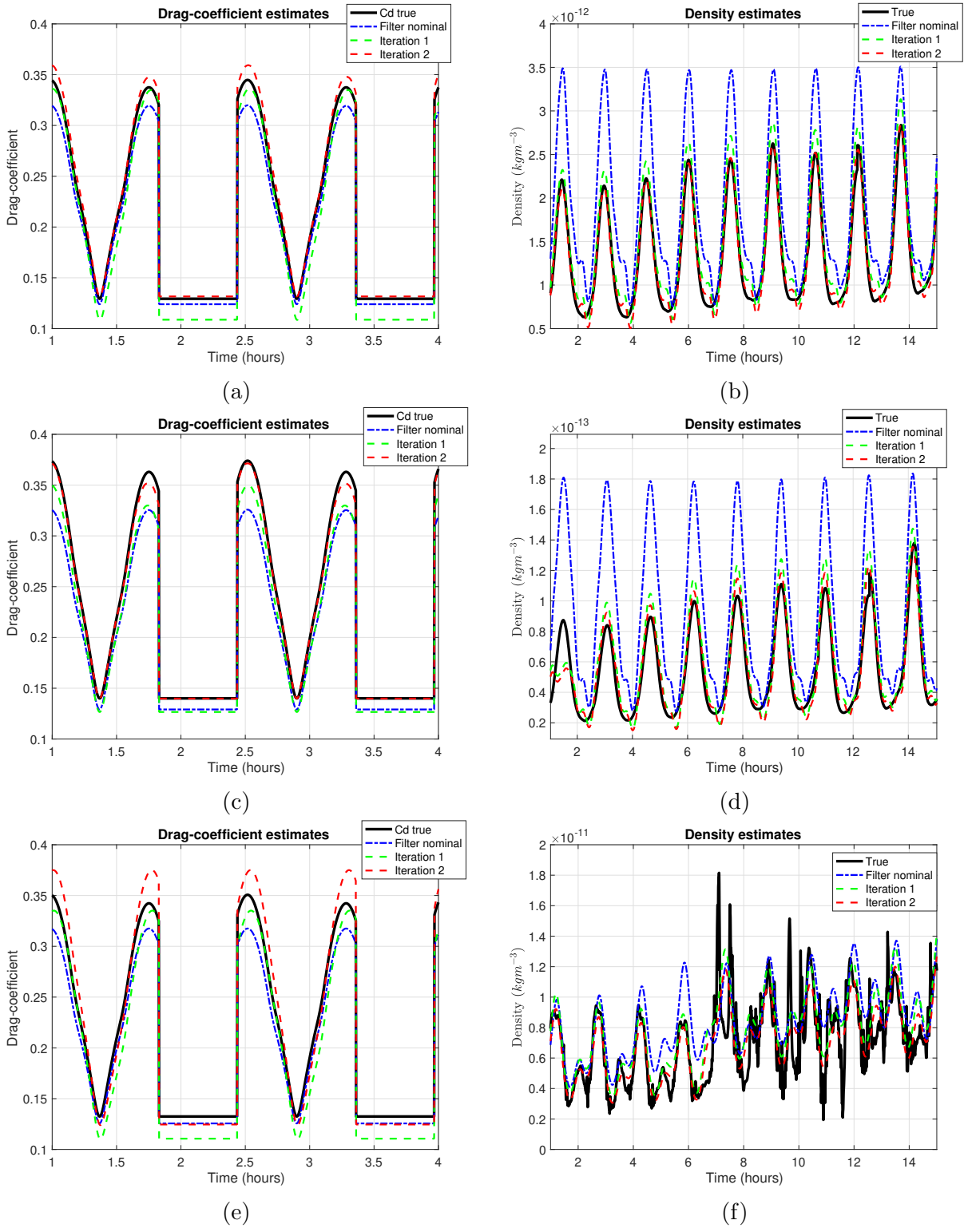

Figure 7.2: Drag coefficients and densities for (a), (b): Case 1, (c), (d): Case 2 and (e), (f): Case 3

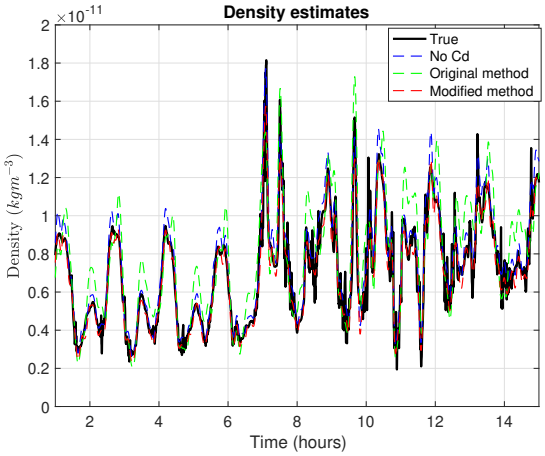

Figure 7.3: Comparison of case 3 estimated densities with Fourier coefficients not estimated in the filter and higher noise levels for the GMP, original method with higher noise levels for the GMP, modified method with different noise levels between the two iterations

data can be used for our applications. The POD and attitude data from Nov. 7, 2018 for satellite ID 83 is used in this work. The quaternions are interpolated to 1 s intervals using Spherical Linear IntERPolation (SLERP) [115]. As can be seen in Fig. 7.4, the velocity vector varies significantly and frequently in the x-y plane of the body frame. The variation out of the x-y plane is negligible.

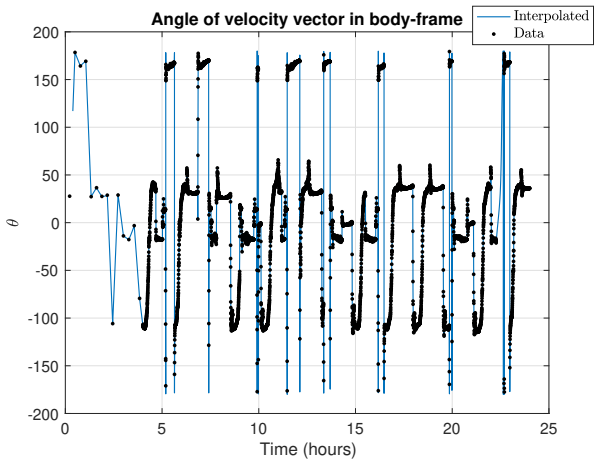

Figure 7.4: Angle of velocity vector with body-x axis

7.4.2 Force model

A high-fidelity force model is required to propagate the Spire satellite orbits to be able to isolate the orbit determination residuals solely due to errors in atmospheric drag. The forces considered in the dynamics model are given in Table 7.3. The initial state from the POD for a given day is propagated with the different forces to analyze the relative contribution of each force to the orbital states. The POD is assumed to be the "truth" to compare the propagated orbit to.

Table 7.3: Forces considered in propagation

Force	**Parameters**
Non-spherical gravity	EGM-2008 80X80
Third-body forces from Sun and Moon	DE-430 Ephemerides
Atmospheric drag	Density model - NRLMSISE-00, JB2008, SET HASDM densities Drag-coefficient- Cannonball, Panel (DRIA)
Solid Earth and Ocean tides	IERS 2010 Models [91]
Solar radiation pressure (SRP)	Cannonball, Panel
Relativistic correction	Post-Newtonian correction [82]

The norm of the propagated position errors (w.r.t the POD) is plotted in the upper tile of Fig. 7.5 (a) for the major perturbing forces with different density models for drag in the propagator. A cannonball drag coefficient is used by averaging the predicted output from the DRIA model with input parameter values of $f = 1$ and $\alpha = 0.93$ [121] which results in a value of 0.23. The only other forces considered are non-spherical gravity (80x80) and third-body forces. HASDM performs a little better than JB2008 and both are significantly better than NRLMSISE-00, as expected. In the lower tile of Fig. 7.5 (a), the higher-fidelity forces are added one-by-one to the force model with HASDM as the density model. The addition of solid Earth tides and ocean tides leads to around 30 m improvement in the position at the end of the day and SRP improves it further by 25-30 m. Both the forces are non-negligible when trying to isolate orbit errors due to variations in

the drag-coefficient. Adding the relativistic corrections leads to a small improvement of around 2 m and changing the gravity field to order 120 improves the error by less than a m which is barely discernible as shown in Fig. 7.5 (b).

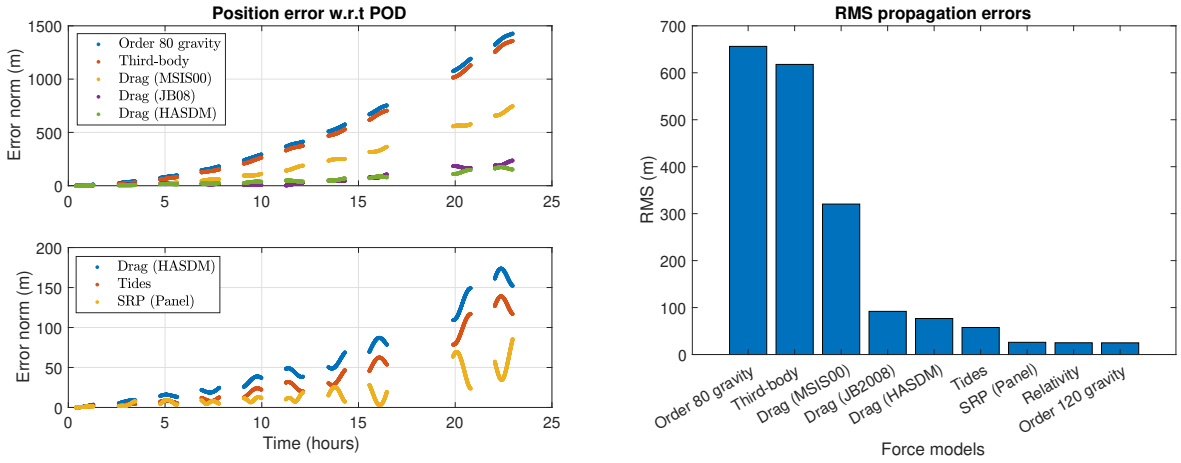

(a) (b)

Figure 7.5: Propagation errors w.r.t POD: (a) Position errors with different forces added to the force model, (b) RMS of propagation errors with addition of each high-fidelity force to the dynamics.

In Fig. 7.5, the drag-coefficient is considered to be constant in the force model. But as seen in Fig. 7.4, the relative velocity vector varies significantly in the body frame of the satellite. The propagation error with the drag-coefficient modeled using DRIA with different values of f and α are compared in Fig. 7.6. From Fig. 7.6 (a), it would seem that drag-coefficient with $f = 0$ and $\alpha = 0.93$ would provide the most accurate drag-coefficient as the propagation errors are the smallest with these parameters and HASDM as the density model. But the propagation errors depend on the product of the density and drag-coefficient and it's quite possible that this particular drag-coefficient model is able to compensate for the lack of spatial and temporal resolution of HASDM densities to result in better propagation errors even though the drag-coefficient itself is less accurate. This can be seen from Fig. 7.6 (b) where the propagation error trends are quite different with NRLMSISE-00 as the density model and the same drag-coefficient values. The density and drag-coefficient values from the different models are plotted in Fig. 7.7. Note that the drag-coefficients are calculated with NRLMSISE-00 as the density model for the input ambient parameters to the DRIA model.

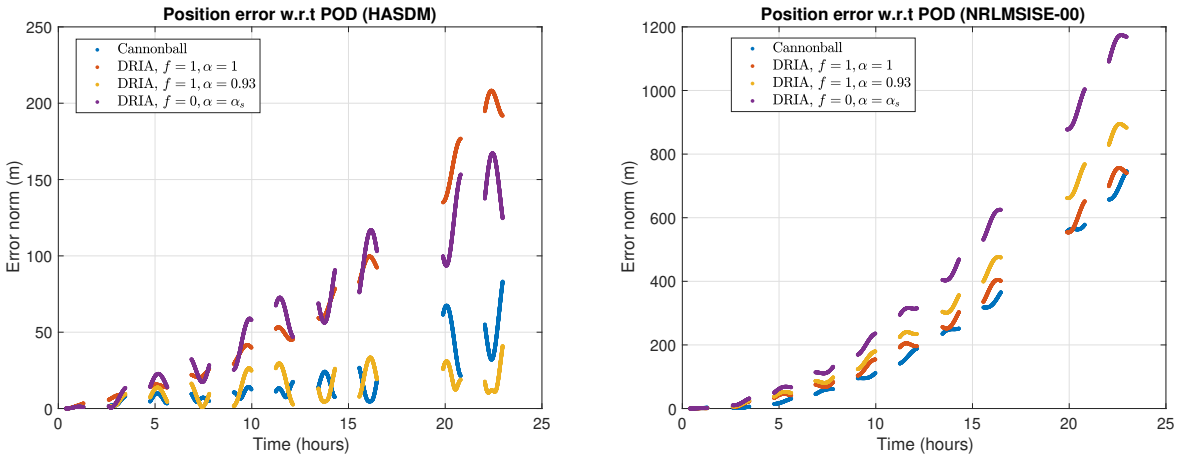

(a) (b)

Figure 7.6: Propagation errors w.r.t POD with all forces and different drag-coefficient models with: (a) HASDM as the density model, (b) NRLMSISE-00 as the density model

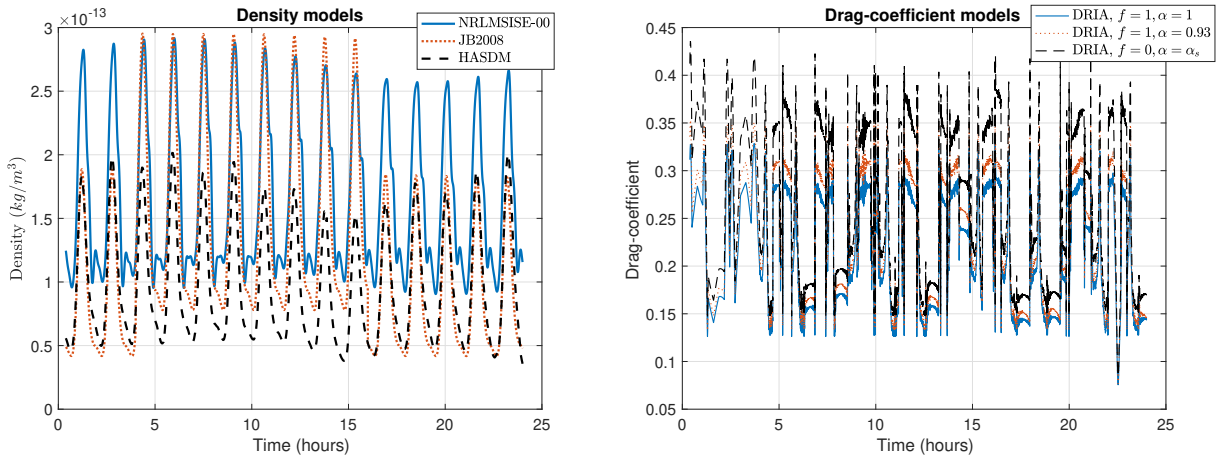

(a) (b)

Figure 7.7: (a) Density values from different models, (b) Drag-coefficient values from different models

In the propagation, the SRP force model is assumed to be known accurately. The available satellite properties used in the panel SRP method are assumed to be accurate in the force model with $C_r = 1$. But it is instructive to compare the orbit determination residuals for a cannonball model and the given panel model with C_r being estimated in both cases to analyze if the given panel model is indeed closer to the truth. Therefore, the POD are processed in a batch filter with all the

high-fidelity force models included in the dynamics and run for the two SRP models. The initial position and velocity, cannonball drag-coefficient and SRP coefficient are estimated with HASDM as the density model.

The position and velocity measurement residuals, plotted in Fig. 7.8, are smaller for the panel model. This can be further verified from Table 7.4 where the correction to the initial state (which is taken to be the initial POD state) is smaller for the panel model. It is encouraging to note that for either model, the estimated drag-coefficient value is pretty much the same, i.e., the SRP errors don't alias into the estimated drag-coefficient [101]. The panel model with $C_r = 0.41$ is considered in the force model for the density inversion method.

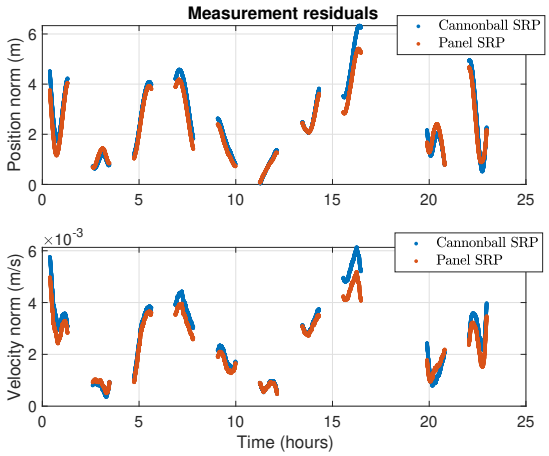

Figure 7.8: Measurement residuals from batch processing of POD with two different SRP models

Table 7.4: Initial and final estimates from the batch estimator for the two SRP models

Parameter	Initial	Final	
		Cannonball SRP	Panel SRP
Norm of position error w.r.t POD (m)	0	4.522	3.766
Norm of velocity error w.r.t POD (m/s)	0	5.8e-3	5.0e-3
SRP coefficient	1	0.95	0.41
Drag-coefficient	0.23	0.262	0.259

The initial estimates of the Fourier coefficients are calculated using the analytical expressions

for DRIA derived in the previous chapter. The standard deviations are calculated by considering the extremities of the range of variation of the GSIM input parameters. The fraction of surface covered by atomic oxygen (f) is assumed to vary from 0 to 1 and the accommodation coefficient of the covered surface is varied from 0 to 1. It is important to note here that the drag-coefficient and consequently, the BFF coefficients depend on ambient parameters that vary in the orbit. Ideally, a second Fourier series expansion in the orbit frame would be carried out to capture the periodic variations of the BFF coefficients as derived in chapter chapter 5. But the orbit-fixed coefficients are highly correlated with density variations since both are dependent on similar sets of parameters which makes it difficult for them to be estimated simultaneously. Therefore, only the BFF coefficients are estimated in the filter as constants. The initial estimates of the body-fixed coefficients are calculated by averaging the GSIM in the orbit. The initial values are also dependent on the density model used to provide the GSIM parameter inputs such as the mean molecular mass. The Fourier coefficients are calculated using both NRLMSISE-00 and JB2008 for the input parameters to compare the dependence of the drag-coefficient on the density model. The effective initial drag-coefficient is calculated from the Fourier coefficients using eq. 5.15. The relative error introduced in the drag-coefficient due to averaging of the Fourier series expansion ($(C_{d,T} - C_{d,f})/C_{d,T}$, where $C_{d,T}$ is the modified DRIA model and $C_{d,f}$ is the orbit-averaged BFF drag-coefficient) is plotted in Fig. 7.9 (a) for extremal values of the GSIM parameters with NRLMSISE-00 as the density model. The relative error of the drag-coefficients calculated using JB2008 as the density model w.r.t the drag-coefficients calculated using NRLMSISE-00 as the density model is plotted in Fig. 7.9 (b). Both the averaging error and density model-dependent error are within 2 % when the accommodation coefficient is constant. But if the fractional coverage parameter is assumed to be zero and the accommodation coefficient is modeled using Goodman's formula, and therefore dependent on the density model, the relative errors are larger since now an additional parameter in the GSIM is tied to the density model.

The iterated EKF-smoother is run with the POD as measurements and NRLMSISE-00 as the density model. The state vector consists of the position, velocity, SRP coefficient, the density

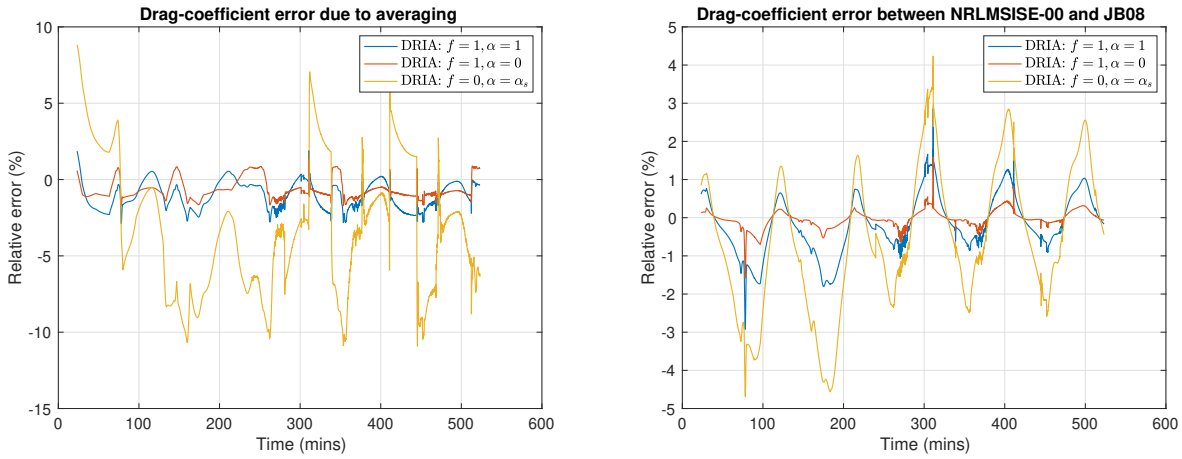

(a) (b)

Figure 7.9: (a) Averaging error in the drag-coefficient, (b) Density model-dependent error in the drag-coefficient

GMP2 states and the Fourier drag-coefficients. Only the first and second order Fourier coefficients are estimated while rest of the coefficients till order 30 are kept constant in the filter. The tuning parameters for the GMP2 are found by fitting the autocovariance function in Eq. 7.4 to the error between NRLMSISE-00 and HASDM and then modified further by trial and error. The smoothed post-fit residuals after one iteration of the algorithm are less than a m in position as seen in Fig. 7.10 (a). But the estimated densities in Fig. 7.10 (b) are non-physical. The Fourier drag-coefficients are non-physical as well. The estimates are clearly absorbing other periodic unmodeled dynamics errors in the orbit due to the periodic nature of GMP2 modeling.

Therefore, the density correction model is changed to a GMP1 instead with the time constant taken as the orbital period. This improves the density estimates as well as the Fourier coefficient estimates. The proposed method outlined in 7.2 is used to estimate the states with the velocity ratio (r_{ads}) inverted from the Fourier coefficient estimates. The post-fit residuals and the estimated densities from the two iterations are plotted in Fig. 7.11. The figure also shows the density corrections when JB2008 is used as the nominal density model. It can be immediately noted that the estimated densities after each iteration move closer to HASDM, i.e., the algorithm is able to estimate the density bias. The error statistics for the density errors w.r.t HASDM, similar to Table

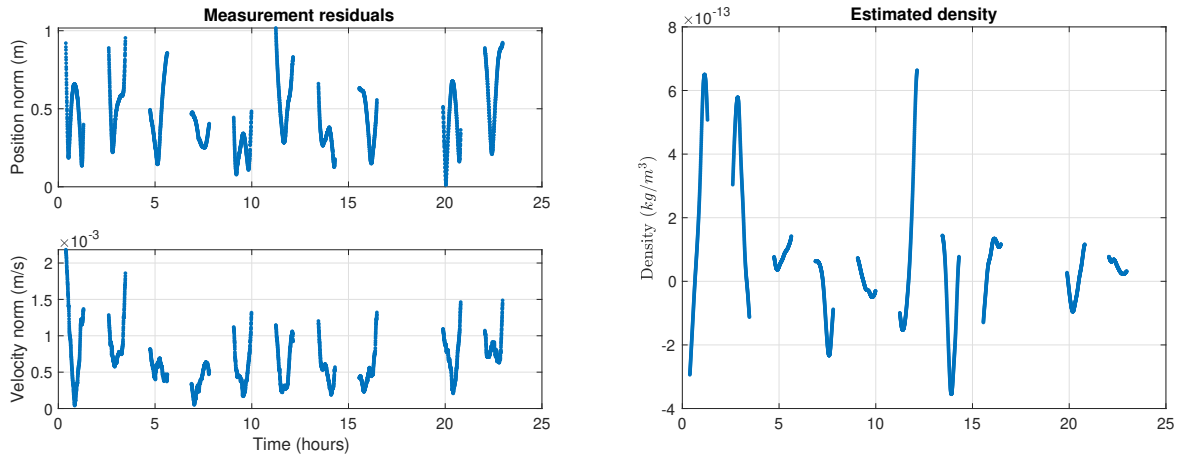

(a) (b)

Figure 7.10: (a) Smoothed post-fit residuals, (b) Estimated densities from the iterated EKF-smoother

7.1, are given in Table 7.5. There's an improvement of about 26 % after the first iteration and 29 % after the second iteration in the density bias with NRLMSISE-00 as the density model. With JB2008 as the nominal density model, the percentage improvement increases to 44 % and 49 % after two iterations respectively. It should be noted that the JB2008 densities are closer to the HASDM densities to begin with. Although the estimated densities after both iterations are closer to the HASDM densities, the post-fit residuals are worse than Fig. 7.10. Even between the iterations, whereas the estimated density is closer to HASDM after the second iteration, the post-fit residuals are worse. This hints that there are remaining unmodeled dynamics that are getting absorbed in the estimated densities and Fourier drag-coefficients. But even with remaining unmodeled errors, improved estimates of the density are still obtained, demonstrating the applicability of the method in real scenarios.

7.5 Chapter summary

In this chapter, an algorithm to simultaneously estimate the density and drag-coefficient was developed. A Gauss Markov process was utilized to model the density correction in the filter. For a satellite with a constant drag-coefficient, the density and drag-coefficient bias cannot be estimated

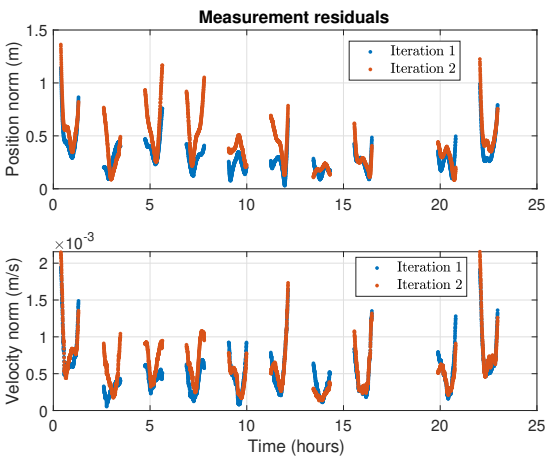

(a)

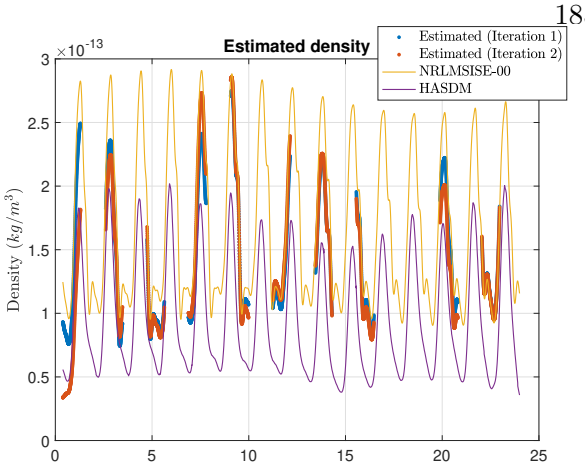

(b)

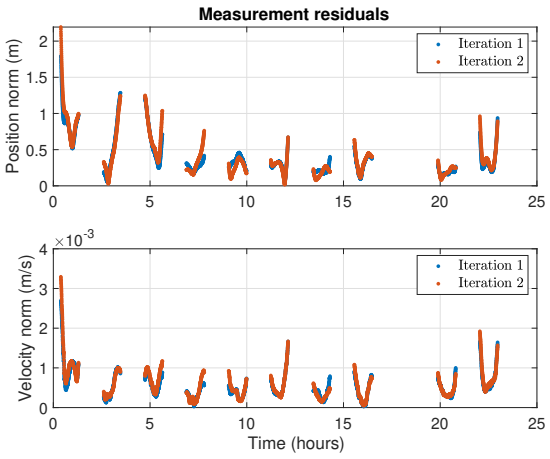

(a)

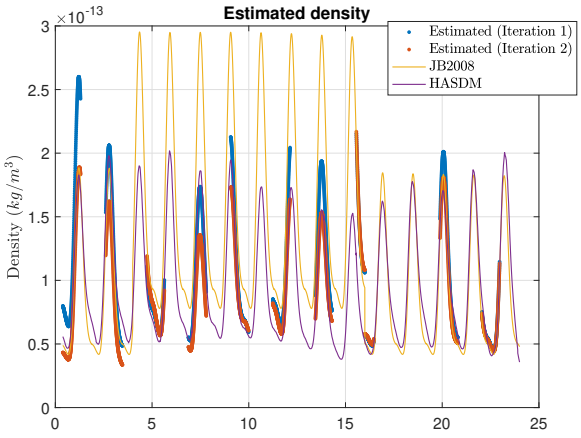

(b)

Figure 7.11: (a) Smoothed post-fit residuals and (b) Estimated densities from the iterated EKF-smoother with NRLMSISE-00 as the nominal density model; (c) Smoothed post-fit residuals and (d) Estimated densities from the iterated EKF-smoother with JB2008 as the nominal density model

Table 7.5: Mean and RMS values of estimated density errors w.r.t HASDM densities. Iteration 0 refers to the initial errors of the nominal density model.

Iteration		**NRLMSISE-00**	**JB2008**
0	Mean	89.4	36.6
	RMS	95.5	45.5
1	Mean	65.8	20.3
	RMS	75.1	27.8
2	Mean	63.3	18.5
	RMS	73.7	26.9

simultaneously. But time-variations in the drag-coefficient due to a changing satellite attitude allows the possibility of decorrelating the two. For a satellite with varying attitude, the time-variations in the drag-coefficient are modeled using a body-fixed Fourier expansion. The higher-order Fourier coefficients can be estimated simultaneously with the density corrections since the attitude-induced drag-coefficient signal is independent of the density variations. A few uncertain GSIM parameters are inverted from the estimated Fourier coefficients in a least-squares methodology utilizing the functional relationship between them, and thereby providing a better constraint on the GSIM. The bias term is then re-calculated using the new GSIM parameter estimates and the filter-smoother is run again. Through simulations, the improvement in estimating the density and drag-coefficient with this algorithm was demonstrated for both geomagnetically quiet and active conditions, different altitudes and errors in GSIM parameters. The bias in the drag coefficient and density was reduced by more than 70 % in some cases. The algorithm was validated using POD from Spire satellites. Even though the density correction modeled using a second-order GMP didn't converge on the truth, using a first order GMP allowed an improved estimate of the density. The NRLMSISE-00 density bias and error RMS w.r.t to HASDM are reduced by 26 % after the first iteration and 29 % after the second iteration whereas with JB2008 as the density model, the errors are reduced by 44 % and 49 % respectively. The poor density estimate with a GMP2 suggests unmodeled periodic dynamics remaining in the filter which need to be further analyzed. Remaining errors such as Earth albedo and infrared radiation pressure need to be modeled. Additionally, more dense data is needed to improve the estimates. The method developed in this work can provide accurate local atmospheric density estimates at a sub-orbital cadence and can therefore, be used as a data-source in data-assimilation methods for density models.

Chapter 8

King-Hele theory for periodic orbit and attitude variations

The motion of satellites in an atmosphere is governed by parameters with complex time-dependent profiles such as the atmospheric density and the drag-coefficient. A prediction of the satellite states, the position and velocity or the orbital elements, can be most accurately obtained by numerical integration of the equations of motion. But numerical integration is a computationally expensive process and does not prove feasible for analysis of long-term evolution of the orbital elements. A time profile of the semi-major axis and eccentricity evolution is required to obtain an estimate of the satellite lifetime which is indispensable for mission design and maneuver planning. Therefore, a closed-form analytical solution of the change in semi-major axis and eccentricity, i.e., orbit contraction, is essential. Fortunately, a closed-form solution is possible under some simplifying assumptions regarding the atmosphere and was outlined by King-Hele (1964) [51] in his comprehensive treatise on the subject. Assuming an exponentially decaying atmosphere with constant density surfaces at any altitude, expressions for changes in semi-major axis and eccentricity, averaged over an orbital period, were derived for both spherically symmetrical and oblate atmospheres. The integration of the Lagrange planetary equations led to separate series formulations for three eccentricity regimes - circular, low eccentricity ($e < 0.2$) and high eccentricity ($e > 0.2$).

Several improvements to the original King-Hele formulation have been developed in the literature. Whereas King-Hele developed separate formulations for low and high eccentricity regimes with an empirical boundary condition of $e = 0.2$ using heuristic methods for integration, Vinh et al. (1979) [130] provided a rigorous analytic solution using Poincaré's method for small parameters

[97]. The singularities arising in classical orbital elements for nearly circular orbits were removed by Sharma (1991) [114] by formulating the theory in non-singular elements. One of the weakest assumptions in the original King-Hele formulation is the stationary and exponentially decaying nature of the atmospheric density. The effect of diurnal and latitudinal variation of atmospheric density on the orbital elements have been addressed by various authors [51]. The assumption of a fixed scale height for the exponentially decaying density can introduce large errors as the distance from the perigee increases. King-Hele (1964) [51] tried to address this approximation by assuming a linear variation of scale height. More recently, significant advances were made in incorporating a generic atmospheric model in the theory by fitting multiple exponentially decaying partial atmospheres to the model [34]. Frey et al. (2019) [34] were also able to arrive at a variable boundary condition for the eccentricity regime that was fixed by King-Hele at 0.2.

8.1 Proposed improvement to the original King-Hele theory

In the original King-Hele theory and all the modifications thereafter, the drag-coefficient has been considered constant. This is partly because it is not possible to incorporate complex physics-based drag-coefficients models in their original form in the King-Hele theory and obtain a closed-form solution. But a parameterization of these models in terms of a high-frequency orbital element such as true anomaly or eccentric anomaly can allow the drag coefficient to vary in the King-Hele theory. In this work, the original King-Hele theory for a spherically symmetric atmosphere is expanded upon by allowing the drag-coefficient to vary in time using the Fourier drag-coefficient models. This extended King-Hele theory will not only be useful in improving lifetime estimates of the satellite but also improve derivation of atmospheric densities from satellite decay data using general perturbation methods since the drag-coefficient is assumed to be constant in such studies [92]. The extended theory also reveals the value of the constant drag-coefficient that should be used in the original King-Hele formulation to obtain an accurate approximation to numerical results. Additionally, it can be combined with the other improvements outlined previously to obtain a generalized analytical theory of satellite orbits in the presence of atmospheric drag. The inclusion

of drag-coefficient variation in the perturbation equations is an added layer of complexity that improves the approximation to the true variation of the orbits.

8.2 Chapter outline

The analytical change in the semi-major axis, eccentricity and argument of perigee over an orbital period with the proposed extension is derived in detail while noting that the other orbital elements remain constant under the given assumptions. It should be noted that the OFF model developed in 5 was expanded in terms of the argument of latitude while noting that it can be derived for any fast variable in orbit. Here, the OFF expansion is done in terms of the eccentric anomaly,

$$C_D = \sum_{n=0}^{\infty} (\overline{\mathbb{A}}_n \cos nE + \overline{\mathbb{B}}_n \sin nE). \tag{8.1}$$

The transformation of the time variation of the drag-coefficient to eccentric anomaly simplifies the integration of the Lagrange planetary equations as will be seen in section 8.3. In section 8.4, the orbit-fixed Fourier (OFF) model is applied to the King-Hele theory and the orbital element changes are derived for both low eccentricity and high eccentricity regimes. The drag-coefficient is assumed to vary solely due to ambient parameters and the orientation w.r.t the atmosphere is assumed to be constant. Section 8.5 carries out the procedure for the body-fixed Fourier (BFF) model for a nadir-pointing and an inertially stabilized satellite where the drag-coefficient is assumed to vary solely due to changes in orientation of velocity vector in the body-frame. But the drag-coefficient in an actual scenario varies due to both the factors. An approximate method to capture the dependence of the drag-coefficient on both the factors is provided. In section 8.6, it is demonstrated that the higher-order Fourier coefficients do not contribute to the change in orbital elements for a circular orbit under the assumptions of the King-Hele theory. The theory is validated using simulated satellite trajectories in section 8.7. Finally, section 8.8 discusses and summarizes the developed theory.

8.3 Lagrange planetary equations for air drag

In this section, the Lagrange planetary equations for the classical orbital elements in terms of the eccentric anomaly are repeated using King-Hele's notation. The magnitude of the drag force acting tangential to the orbit is given by

$$f_T = -\frac{1}{2}\rho \mathrm{v}^2 \delta. \tag{8.2}$$

The variation in velocity direction due to the rotating atmosphere is neglected since the angle between the absolute velocity vector and relative velocity vector never exceeds $\approx 4^\circ$ [103] but the magnitude is accounted for in the drag-parameter that is assumed to be constant,

$$\delta = \frac{FSC_d}{m_s}.$$

F is the wind-factor that accounts for the relative speed w.r.t the atmosphere, given by

$$F = (1 - \frac{r_{p0} w}{\mathrm{v}_{p0}} \cos i_0)^2.$$

The atmosphere in this theory is assumed to be symmetric and exponentially decaying with a constant scale-height,

$$\rho = \rho_{p0} \exp\{(r_{p0} - r)/H\}. \tag{8.3}$$

A closed-form analytical theory is possible for a higher-fidelity density model accounting for oblateness of the atmosphere, day-night and solar activity variations, meridional winds and varying scale-height [52, 34]. But the modified theory is developed for the simplest case in this work and can be extended to incorporate other refinements.

Following King-Hele (1964) [51], the theory is derived for the semi-major axis (a), the focal-length ($x = ae$) and the argument of periapsis (ω) of the satellite orbit. The orientation of the orbital plane is affected by atmospheric rotation leading to time-variations in the inclination, right-ascension of ascending node and argument of perigee. Whereas the inclination and right-ascension vary solely due to atmospheric forces perpendicular to the orbit plane, the argument of periapsis depends on the forces in the orbital plane. In this work, the forces perpendicular to the velocity

direction are neglected. Therefore, the variation of inclination and right-ascension is considered to be zero. The Lagrange planetary equations for semi-major axis and eccentricity expressed in the tangential (T) and orbit inward normal in the orbit plane (N) directions are as follows-

$$\dot{a} = \frac{2a^2 \mathrm{v}}{\mu} f_T, \tag{8.4}$$

$$\dot{e} = \frac{1}{\mathrm{v}} \left\{ 2f_T(e + \cos\theta) - f_N \frac{r}{a} \sin\theta \right\}. \tag{8.5}$$

For the argument of perigee, the derivation deviates a little from King-Hele, since the normal forces due to atmospheric rotation are neglected here. The Lagrange Planetary equation for argument of perigee expressed in the radial (r)-transverse (t) direction is given by King-Hele [51]

$$\dot{\omega} + \dot{\Omega}\cos i = \frac{1}{\mathrm{e}} \sqrt{\frac{p}{\mu}} \left\{ -f_r \cos\theta + f_t \left(1 + \frac{r}{p} \right) \sin\theta \right\}. \tag{8.6}$$

The forces in the radial-transverse direction can be expressed in the tangential-inward normal directions as [51]

$$f_r = \frac{1}{\mathrm{v}} \sqrt{\frac{\mu}{p}} \{ f_T e \sin\theta - f_N (1 + e\cos\theta) \}$$

$$f_t = \frac{1}{\mathrm{v}} \sqrt{\frac{\mu}{p}} \{ f_T (1 + e\cos\theta) + f_N e \sin\theta \} \tag{8.7}$$

Substituting Eq. 8.7 in 8.6 and simplifying,

$$\begin{aligned} \dot{\omega} = & \frac{1}{\mathrm{v}e} \left[f_T \left\{ \sin\theta + \frac{r}{p}(1 + e\cos\theta)\sin\theta \right\} \right. \\ & \left. + f_N \left\{ e + \cos\theta + \frac{r}{p} e \sin^2\theta \right\} \right] \end{aligned} \tag{8.8}$$

The rate of right-ascension is neglected here, as discussed before. Considering only the drag force, Eqs. 8.4, 8.5 and 8.8 can be re-written as,

$$\dot{a} = -\frac{a^2 \rho \delta \mathrm{v}^3}{\mu}, \tag{8.9}$$

$$\dot{e} = -\rho \delta \mathrm{v} (e + \cos\theta). \tag{8.10}$$

$$\dot{\omega} = \frac{-\rho \mathrm{v} \delta}{2e} \left[\sin\theta + \frac{r}{p}(1 + e\cos\theta)\sin\theta \right] \tag{8.11}$$

It is desirable to transform the time variable into eccentric anomaly as that simplifies the integration of these equations. After transforming the time variable to eccentric anomaly, the final form of the Lagrange planetary equations is [51]

$$\frac{da}{dE} = -a^2 \rho \delta \frac{(1 + e\cos E)^{3/2}}{(1 - e\cos E)^{1/2}}, \tag{8.12}$$

$$\frac{dx}{dE} = -a^2 \rho \delta \left(\frac{1 + e\cos E}{1 - e\cos E} \right)^{1/2} (\cos E + e), \tag{8.13}$$

$$\frac{d\omega}{dE} = -\frac{a\rho\delta}{e}\sqrt{1 - e^2} \left(\frac{1 + e\cos E}{1 - e\cos E} \right)^{1/2} \sin E. \tag{8.14}$$

In the original formulation [51], the equations are integrated over an orbital period by assuming δ to be constant. This is modified by allowing the drag-coefficient to vary in orbit as a function of the eccentric anomaly, i.e., $\delta = \delta' C_d(E)$. The modified integrated equations are given by,

$$\Delta a = -a^2 \delta' \int_0^{2\pi} \frac{(1 + e\cos E)^{3/2}}{(1 - e\cos E)^{1/2}} C_d(E) \rho dE, \tag{8.15}$$

$$\Delta x = -a^2 \delta' \int_0^{2\pi} \left(\frac{1 + e\cos E}{1 - e\cos E} \right)^{1/2} (\cos E + e) C_d(E) \rho dE. \tag{8.16}$$

$$\Delta \omega = -\frac{a\delta'}{e}\sqrt{1 - e^2} \int_0^{2\pi} \left(\frac{1 + e\cos E}{1 - e\cos E} \right)^{1/2} \sin E C_d(E) \rho dE. \tag{8.17}$$

The density transformed to eccentric anomaly is given by,

$$\rho = \rho_{p0} \exp\{\beta(a_0 - a - x_0) + \beta x \cos E\}. \tag{8.18}$$

Substituting Eq. 8.18 in Eqs. 8.15-8.17,

$$\begin{aligned} \Delta a = &- \delta' a^2 \rho_{p0} \exp\{\beta(a_0 - a - x_0)\} \int_0^{2\pi} \left[\frac{(1 + e\cos E)^{3/2}}{(1 - e\cos E)^{1/2}} \right. \\ &\left. \times C_d(E) \exp(\beta x \cos E) \right] dE \end{aligned} \tag{8.19}$$

$$\begin{aligned}\Delta x = &- \delta' a^2 \rho_{p0} \exp \beta(a_0 - a - x_0)\} \int_0^{2\pi} \left[\left(\frac{1 + e\cos E}{1 - e\cos E} \right)^{1/2} \right. \\ &\left. \times (\cos E + e) C_d(E) \exp\left(\beta x \cos E\right) \right] dE \end{aligned} \tag{8.20}$$

$$\begin{aligned}\Delta\omega = &- \frac{\delta' a}{e} \sqrt{1 - e^2} \rho_{p0} \exp \beta(a_0 - a - x_0)\} \\ &\times \int_0^{2\pi} \left[\left(\frac{1 + e\cos E}{1 - e\cos E} \right)^{1/2} \sin E C_d(E) \exp\left(\beta x \cos E\right) \right] dE \end{aligned} \tag{8.21}$$

To integrate these equations, the integrand (without the time-varying drag-coefficient) is expressed as a power series expansion in e and truncated at the third order by King-Hele. A similar approach is followed here after expressing the drag-coefficient as an analytical function in eccentric anomaly using the Fourier models of chapter 5. An important point to note here is that the R.H.S of Eq. 8.14 is an odd function unlike Eqs. 8.12 and 8.13. Therefore, when it is integrated from 0 to 2π, Eq. 8.14 should integrate to zero for a spherically symmetric, non-rotating atmosphere as noted by King-Hele (1964) [51]. But since the drag-coefficient is considered time-varying here, the argument of perigee variation can integrate to a non-zero value as will be demonstrated in subsequent sections.

8.4 Re-deriving the King-Hele theory using OFF model

The dependence of the drag-coefficient on eccentric anomaly in the OFF model is introduced through input ambient parameters to the chosen drag-coefficient model such as the partial pressure of oxygen and mean molecular mass that vary in the orbit. For an exponentially decaying spherically symmetric atmosphere, they are dependent only on the altitude and therefore symmetric about $E = 0, \pi$. Therefore $C_d(E)$ is an even function of eccentric anomaly and therefore the sine coefficients reduce to

$$\overline{\mathbb{B}}_n = 0.$$

Note that this is, in general, not true for an arbitrary atmosphere. Since there is no odd component to the drag-coefficient, the integrand in Eq. 8.21 is odd and therefore, the argument of perigee

change is zero over an orbit. The following sections provide details of the derivation for low and high eccentricities with the OFF drag-coefficient model. Note that the derivations are independent of the gas-surface interaction model considered.

8.4.1 Low eccentricity regime, $e < 0.2$

For low eccentricities, Eqs. 8.19 and 8.20 can be integrated by expanding the integrands as power series in e. The power series for the integrand in Eq. 8.19 truncated at order 3 is given by,

$$\frac{(1+e\cos E)^{3/2}}{(1-e\cos E)^{1/2}} = 1 + 2e\cos E + \frac{3}{2}e^2\cos^2 E + e^3\cos^3 E + \mathbb{O}(e^4) \tag{8.22}$$

Substituting for OFF C_d and 8.22 in Eq. 8.19 and rearranging,

$$\begin{aligned}\Delta a = &-\delta' a^2 \rho_{p0} \exp\{\beta(a_0 - a - x_0)\} \int_0^{2\pi} \left[\sum_{n=0}^{\infty} (\overline{\mathbb{A}}_n \cos nE \right. \\ &\left. \times (1 + 2e\cos E + \frac{3}{2}e^2\cos^2 E + e^3\cos^3 E) \exp(\beta x \cos E)\right] dE\end{aligned} \tag{8.23}$$

The following multiple angle formulae are used to integrate the equation,

$$\cos^2 E = \frac{1+\cos 2E}{2} \tag{8.24}$$

$$\cos^3 E = \frac{3\cos E + \cos 3E}{4} \tag{8.25}$$

Substituting Eqs. 8.24 and 8.25 in Eq. 8.23,

$$\begin{aligned}\Delta a = &D_c \int_0^{2\pi} \left[\sum_{n=0}^{\infty} \overline{\mathbb{A}}_n \cos nE (1 + 2e\cos E + \frac{3}{4}e^2(1+\cos 2E) \right. \\ &\left. + e^3 \frac{3\cos E + \cos 3E}{4}) \exp(\beta x \cos E)\right] dE\end{aligned} \tag{8.26}$$

where $D_c = -\delta' a^2 \rho_{p0} \exp\{\beta(a_0 - a - x_0)\}$. Using the following cosine product formula in Eq. 8.26,

$$\cos A \cos B = \frac{\cos(A+B) + \cos(A-B)}{2}$$

$$\begin{aligned}\Delta a =& D_c \int_0^{2\pi} \Bigg[\sum_{n=0}^{\infty} \overline{\mathbb{A}}_n \{\cos nE + e(\cos(n+1)E + \cos(n-1)E) \\ &+ \frac{3}{4}e^2 \left(\cos nE + \frac{\cos(n+2)E + \cos(n-2)E}{2}\right) \\ &+ \frac{e^3}{4}\left(\frac{3}{2}(\cos(n+1)E + \cos(n-1)E)\right. \\ &\left. + \frac{\cos(n+3)E + \cos(n-3)E}{2}\right)\} \exp(\beta x \cos E)\Bigg] dE\end{aligned} \tag{8.27}$$

Now, the integral can be expressed as a sum of modified Bessel functions of the first kind with imaginary argument,

$$I_n(z) = \frac{1}{2\pi}\int_0^{2\pi} \cos nx \exp(z\cos x) \tag{8.28}$$

Therefore, Eq. 8.27 is written as,

$$\begin{aligned}\Delta a =& 2\pi D_c \Bigg[\sum_{n=0}^{\infty} \overline{\mathbb{A}}_n \{I_n + e(I_{n+1} + I_{n-1}) + \frac{3}{4}e^2(I_n + \frac{I_{n+2} + I_{n-2}}{2}) \\ &+ \frac{e^3}{4}(\frac{3}{2}(I_{n+1} + I_{n-1}) + \frac{I_{n+3} + I_{n-3}}{2})\}\Bigg]\end{aligned} \tag{8.29}$$

where $I_n = I_n(\beta x)$ is implicit. The derivation of Δx follows similar steps. The integrand in Eq. 8.20 can be expanded as a power series in e. Truncating the power series at the third order and substituting OFF C_d, Eq. 8.20 can be written as

$$\begin{aligned}\Delta x =& D_c \int_0^{2\pi} \Bigg[\sum_{n=0}^{\infty} (\overline{\mathbb{A}}_n \cos nE)\{\cos E + \frac{1}{2}e(3 + \cos 2E) \\ &+ \frac{1}{8}e^2(11\cos E + \cos 3E) + \frac{1}{16}e^3(7 + 8\cos 2E + \cos 4E) \\ &+ \mathbb{O}(e^4)\} \exp(\beta x \cos E) dE\Big]\end{aligned} \tag{8.30}$$

Carrying out the trigonometric simplifications outlined in Eqs. 8.23-8.29, the final form of Eq. 8.30 is

$$\begin{aligned}\Delta x =& 2\pi D_c \Bigg[\sum_{n=0}^{\infty} \overline{\mathbb{A}}_n \left\{\frac{1}{2}(I_{n+1} + I_{n-1}) + \frac{1}{4}e\{6I_n + (I_{n+2} + I_{n-2})\}\right. \\ &+ \frac{1}{16}e^2\{11(I_{n+1} + I_{n-1}) + (I_{n+3} + I_{n-3})\} \\ &\left. + \frac{1}{32}e^3\{14I_n + 8(I_{n+2} + I_{n-2}) + (I_{n+4} + I_{n-4})\}\right\}\Bigg]\end{aligned} \tag{8.31}$$

Eqs. 8.29 and 8.31 calculate the change in semi-major axis and focal-length over an orbital period for the modified King-Hele theory. Note that for $n = 0$, the equations reduce to the original forms derived by King-Hele as follows since $I_n = I_{-n}$,

$$\Delta a = 2\pi D_c \overline{\mathbb{A}}_0 [I_0 + 2eI_1 + \frac{3}{4}e^2(I_0 + I_2) + \frac{1}{4}e^3(3I_1 + I_3)] \tag{8.32}$$

$$\begin{aligned} \Delta x = 2\pi D_c \overline{\mathbb{A}}_0 [I_1 + \frac{1}{2}e(3I_0 + I_2) + \frac{1}{8}e^2(11I_1 + I_3) \\ + \frac{1}{16}e^3(7I_0 + 8I_2 + I_4)] \end{aligned} \tag{8.33}$$

For the original formulation, the drag-coefficient is assumed to be constant, denoted by $\overline{\mathbb{A}}_0$ in Eqs. 8.32 and 8.33. The constant drag-coefficient can be assumed to be the zeroth-order order Fourier coefficient ($\overline{\mathbb{A}}_0$), the drag-coefficient evaluated at perigee or a weighted average of the orbital drag-coefficient variation. The value that will approximate the results of the Fourier theory given by Eqs. 8.15 and 8.16 can be calculated by equating the original King-Hele Δa and Δe to the Fourier theory given by Eqs. 8.19 and 8.20 as follows,

$$\begin{aligned} C_{d0} \int_0^{2\pi} \frac{(1 + e\cos E)^{3/2}}{(1 - e\cos E)^{1/2}} \rho dE = \int_0^{2\pi} \frac{(1 + e\cos E)^{3/2}}{(1 - e\cos E)^{1/2}} \\ \times C_d(E)\rho dE \end{aligned} \tag{8.34}$$

$$\begin{aligned} C_{d0} \int_0^{2\pi} \left(\frac{1 + e\cos E}{1 - e\cos E}\right)^{1/2} (\cos E + e)\rho dE = \\ \int_0^{2\pi} \left(\frac{1 + e\cos E}{1 - e\cos E}\right)^{1/2} (\cos E + e) C_d(E)\rho dE \end{aligned} \tag{8.35}$$

A drag-coefficient that approximates both Eqs. 8.34 and 8.35 can be calculated by considering only the density and the Fourier drag-coefficient inside the integral. This results in a weighted average of the Fourier drag-coefficient as follows-

$$C_{d0} = \frac{\int_0^{2\pi} \rho C_d(E) dE}{\int_0^{2\pi} \rho dE} \tag{8.36}$$

Using Eqs. 8.18 and 8.28, an analytical form of the constant drag-coefficient can be found as

$$C_{d0} = \frac{\sum_{n=0}^{\infty} \overline{\mathbb{A}}_n I_n}{I_0} \tag{8.37}$$

8.4.2 High eccentricity regime, $0.2 \leq e < 1$

For large values of eccentricity, expanding the integrands in Eqs. 8.19 and 8.20 as a power series in e is not appropriate. King-Hele (1964) [51] introduced the auxiliary variable λ to integrate Eqs. 8.19 and 8.20 and carried out the following transformation of variables,

$$\cos E = 1 - \lambda^2/z \tag{8.38}$$

such that,

$$dE = \sqrt{\frac{2}{z(1-\lambda^2/2z)}}d\lambda \tag{8.39}$$

where $z = \beta x = \frac{ae}{H}$, where z goes to infinity as e approaches 1. Replacing the integrals in Eqs. 8.19 and 8.20 from 0 to 2π by twice the integrals from 0 to π and substituting Eqs. 8.38 and 8.39,

$$\begin{aligned}\Delta a =& 2\exp(z)\sqrt{2/z}D_c \int_0^{\sqrt{2z}} \frac{(1+e-e\lambda^2/z)^{3/2}}{(1-e+e\lambda^2/z)^{1/2}} \exp(-\lambda^2) \\ &\times \sqrt{\frac{1}{(1-\lambda^2/(2z))}} C_d(\lambda) d\lambda\end{aligned} \tag{8.40}$$

$$\begin{aligned}\Delta x =& 2\exp(z)\sqrt{2/z}D_c \int_0^{\sqrt{2z}} (e+1-\lambda^2/z) \left(\frac{1+e-e\lambda^2/z}{1-e+e\lambda^2/z}\right)^{1/2} \\ &\times \exp(-\lambda^2)\sqrt{\frac{1}{(1-\lambda^2/(2z))}} C_d(\lambda) d\lambda\end{aligned} \tag{8.41}$$

The drag-coefficient in Eq. 8.1 needs to be first expressed in the new variable before substituting in Eqs. 8.40 and 8.41. The following formulae for multiple angles are used for that purpose,

$$\cos nE = \sum_{k=0}^{\lfloor n/2 \rfloor} (-1)^k \binom{n}{2k} \sin^{2k} E \cos^{n-2k} E \tag{8.42}$$

$$\sin nE = \sum_{k=0}^{\lfloor (n-1)/2 \rfloor} (-1)^k \binom{n}{2k+1} \sin^{2k+1} E \cos^{n-2k-1} E \tag{8.43}$$

where $\lfloor n/2 \rfloor$ denotes the floor function and $\binom{n}{2k}$ denotes the binomial coefficient. Therefore, Eq. 8.1 can be expressed as

$$C_d(\lambda) = \sum_{n=0}^{\infty} \overline{\mathbb{A}}_n \left[\sum_{k=0}^{\lfloor n/2 \rfloor} (-1)^k \binom{n}{2k} \left\{ \frac{\lambda^2}{z}(2 - \frac{\lambda^2}{z}) \right\}^k \left(1 - \frac{\lambda^2}{z}\right)^{n-2k} \right] \tag{8.44}$$

since $\overline{\mathbb{B}}_n = 0$ as noted before. Substituting Eq. 8.44 in Eq. 8.40 and carrying out a power series expansion in λ^2/z,

$$\begin{aligned}\Delta a =& 2\exp(z)\sqrt{2/z}D_c\frac{(1+e)^{3/2}}{(1-e)^{1/2}}\int_0^{\sqrt{2z}}\sum_{n=0}^{\infty}\sum_{k=0}^{\lfloor n/2\rfloor}\overline{\mathbb{A}}_n(-1)^k\binom{n}{2k}\\ &\times 2^k\Big[(\lambda^2/z)^k + K_1(\lambda^2/z)^{k+1} + K_2(\lambda^2/z)^{k+2}\\ &+\mathbb{O}((\lambda^2/z)^{k+3})\Big]\exp(-\lambda^2)d\lambda\end{aligned} \tag{8.45}$$

where K_1 and K_2 are functions of the summation indices n and k, and the eccentricity e and are given by

$$K_1 = \frac{1}{4(1-e^2)}[(-4n+6k+1) - 8e + (4n-6k+3)e^2] \tag{8.46}$$

$$\begin{aligned}K_2 =& \frac{1}{32(1-e^2)^2}[(4n-6k)(4n-6k-6) + (4k+3) + 16(4n-6k\\ &-1)e + \{(4n-6k)(-8n+12k+4) - (8k-50)\}e^2 - 16(4n\\ &-6k-1)e^3 + \{(4n-6k)(4n-6k+2) + (4k-5)\}e^4]\end{aligned} \tag{8.47}$$

Approximating the upper limit of the integral as ∞ since the integrand becomes very small as λ becomes large and $\sqrt{2z} > 6$ [51], the integrals can be expressed as a sum of Gamma functions that are given by

$$\int_0^{\infty}\lambda^k\exp(-\lambda^2)d\lambda = \frac{1}{2}\Gamma\left(\frac{k+1}{2}\right) \tag{8.48}$$

Therefore, the final form of Eq. 8.45 is given by

$$\begin{aligned}\Delta a =& D_c'\sum_{n=0}^{\infty}\sum_{k=0}^{\lfloor n/2\rfloor}\overline{\mathbb{A}}_n(-1)^k\binom{n}{2k}(\frac{2}{z})^k\left[\Gamma\left(\frac{2k+1}{2}\right)\right.\\ &\left.+\frac{K_1}{z}\Gamma\left(\frac{2k+3}{2}\right) + \frac{K_2}{z^2}\Gamma\left(\frac{2k+5}{2}\right)\right]\end{aligned} \tag{8.49}$$

where $D_c' = \exp(z)\sqrt{2/z}\dfrac{(1+e)^{3/2}}{(1-e)^{1/2}}D_c$. Similarly, the equation for Δx can be derived by substituting Eq. 8.44 in Eq. 8.41 and carrying out a power series expansion,

$$\begin{aligned}\Delta x =& 2\exp(z)\sqrt{2/z}D_c\frac{(1+e)^{3/2}}{(1-e)^{1/2}}\int_0^{\sqrt{2z}}\sum_{n=0}^{\infty}\sum_{k=0}^{\lfloor n/2\rfloor}\overline{\mathbb{A}}_n(-1)^k\binom{n}{2k}\\ &\times 2^k\Big[(\lambda^2/z)^k + M_1(\lambda^2/z)^{k+1} + M_2(\lambda^2/z)^{k+2}\\ &+\mathcal{O}((\lambda^2/z)^{k+3})\Big]\exp(-\lambda^2)d\lambda\end{aligned} \tag{8.50}$$

where M_1 and M_2 are functions of the summation indices n and k, and the eccentricity e and are given by

$$M_1 = \frac{1}{4(1-e^2)}[(-4n+6k-3)+(4n-6k-1)e^2] \tag{8.51}$$

$$\begin{aligned}M_2 =& \frac{1}{32(1-e^2)^2}[(4n-6k)(4n-6k+2)+(4k-5)+32e\\ &-2\{(4n-6k)(4n-6k-2)+(4k+7)\}e^2+32e^3\\ &+\{(4n-6k)(4n-6k-6)+(4k+3)\}e^4]\end{aligned} \tag{8.52}$$

The final form of Eq. 8.50 in terms of Gamma functions is as follows

$$\begin{aligned}\Delta x =& D_c'\sum_{n=0}^{\infty}\sum_{k=0}^{\lfloor n/2\rfloor}\overline{\mathbb{A}}_n(-1)^k\binom{n}{2k}(\frac{2}{z})^k\left[\Gamma\left(\frac{2k+1}{2}\right)\right.\\ &\left.+\frac{M_1}{z}\Gamma\left(\frac{2k+3}{2}\right)+\frac{M_2}{z^2}\Gamma\left(\frac{2k+5}{2}\right)\right].\end{aligned} \tag{8.53}$$

For $n=0$, the equations reduce to the original King-Hele formulation,

$$\Delta a = D_c' A_0\sqrt{\pi}\left[1+\frac{K_1}{2z}+\frac{3K_2}{4z^2}\right], \tag{8.54}$$

where

$$K_1 = \frac{1}{4(1-e^2)}[1-8e+3e^2],$$

$$K_2 = \frac{1}{32(1-e^2)^2}[3-16e+50e^2+16e^3-5e^4],$$

and,

$$\Delta x = D_c'\sqrt{\pi}A_0\left[1+\frac{M_1}{2z}+\frac{3M_2}{4z^2}\right], \tag{8.55}$$

where

$$M_1 = -\frac{1}{4(1-e^2)}[3+e^2],$$

$$M_2 = \frac{1}{32(1-e^2)^2}[-5+32e-14e^2+32e^3+3e^4].$$

The density-averaged constant drag-coefficient derived for the low eccentricity regime can be used for high-eccentricity regime as well.

8.5 Re-deriving the King-Hele theory using BFF model

In this section, the theory is developed for two attitude profiles for which ϕ can be expressed as a function of the eccentric anomaly. Unlike the OFF model, $\overline{\mathcal{B}}_n$ is not generally zero for BFF since the drag-coefficient may not be symmetric about $\phi = 0, \pi$. If the satellite shape is symmetric about $\phi = 0, \pi$, then $\overline{\mathcal{B}}_n = 0$.

8.5.1 Nadir-pointing profile

For a nadir-pointing profile, the angle between the velocity vector and the body axis is equal to the flight path angle that can be expressed in terms of the eccentric anomaly as

$$\cos\theta = \sqrt{\frac{1-e^2}{1-e^2\cos^2 E}} \tag{8.56}$$

$$\sin\theta = \frac{e\sin E}{\sqrt{1-e^2\cos^2 E}} \tag{8.57}$$

Using Eqs. 8.42, 8.43, 8.56 and 8.57 in Eq. 5.15,

$$\begin{aligned} C_d(E) = \sum_{n=0}^{\infty}\Bigg[\overline{\mathcal{A}}_n\Bigg\{\sum_{k=0}^{\lfloor\frac{n}{2}\rfloor}(-1)^k\binom{n}{2k}\left(\frac{e\sin E}{\sqrt{1-e^2\cos^2 E}}\right)^{2k} \\ \times\left(\sqrt{\frac{1-e^2}{1-e^2\cos^2 E}}\right)^{n-2k}\Bigg\} + \overline{\mathcal{B}}_n\Bigg\{\sum_{k=0}^{\lfloor\frac{n-1}{2}\rfloor}(-1)^k\binom{n}{2k+1} \\ \times\left(\frac{e\sin E}{\sqrt{1-e^2\cos^2 E}}\right)^{2k+1}\left(\sqrt{\frac{1-e^2}{1-e^2\cos^2 E}}\right)^{n-2k-1}\Bigg\}\Bigg] \end{aligned} \tag{8.58}$$

Low eccentricity regime

Substituting Eq. 8.58 in Eq. 8.19 and noting that the integrand corresponding to $\overline{\mathcal{B}}_n$ is an odd function, the equation reduces to

$$\begin{aligned}\Delta a = D_c \int_0^{2\pi} \sum_{n=0}^{\infty} \sum_{k=0}^{\lfloor \frac{n}{2} \rfloor} \overline{\mathcal{A}}_n (-1)^k \binom{n}{2k} \left(\frac{e \sin E}{\sqrt{1 - e^2 \cos^2 E}} \right)^{2k} \\ \times \left(\sqrt{\frac{1 - e^2}{1 - e^2 \cos^2 E}} \right)^{n-2k} \frac{(1 + e \cos E)^{3/2}}{(1 - e \cos E)^{1/2}} \exp(\beta x \cos E) dE\end{aligned} \tag{8.59}$$

Expanding the integrand as a power series in e,

$$\begin{aligned}\Delta a = D_c \int_0^{2\pi} \sum_{n=0}^{\infty} \sum_{k=0}^{\lfloor \frac{n}{2} \rfloor} \overline{\mathcal{A}}_n (-1)^k \binom{n}{2k} [1 + 2 \cos E e + \{k - \frac{n}{2} \\ + \frac{1}{2}(n+3) \cos^2 E\} e^2 + \cos E \{2k - n + (n+1) \cos^2 E\} e^3] \\ \times (e \sin E)^{2k} \exp(\beta x \cos E) dE\end{aligned} \tag{8.60}$$

Truncating the series at $\mathcal{O}(e^3)$, k can only be 0 and 1. Therefore, Eq. 8.60 can be written as,

$$\begin{aligned}\Delta a = D_c \int_0^{2\pi} \left[\sum_{n=0}^{\infty} \overline{\mathcal{A}}_n \{1 + 2 \cos E e + \{-\frac{n}{2} + \frac{1}{2}(n+3) \cos^2 E\} e^2 \right. \\ + \cos E \{-n + (n+1) \cos^2 E\} e^3 \} + \sum_{n=2}^{\infty} -\overline{\mathcal{A}}_n \binom{n}{2} \{\sin^2 E e^2 \\ \left. + 2 \sin^2 E \cos E e^3 \} \right] \exp(\beta x \cos E) dE\end{aligned} \tag{8.61}$$

The trigonometric powers can be written as

$$\sin^2 E = \frac{1 - \cos 2E}{2} \tag{8.62}$$

$$\sin^2 E \cos E = \cos E - \frac{1}{4}(3 \cos E + \cos 3E) \tag{8.63}$$

Using Eqs. 8.24, 8.25, 8.28, 8.62 and 8.63, Eq. 8.61 is given by,

$$\begin{aligned}\Delta a = 2\pi D_c \sum_{n=0}^{\infty} \overline{\mathcal{A}}_n \left[I_0 + 2 I_1 e + \left\{ \left(\frac{n+3}{4} \right) (I_0 + I_2) - \frac{n}{2} I_0 \right\} e^2 \right. \\ + \left\{ \left(\frac{n+1}{4} \right) (3 I_1 + I_3) - n I_1 \right\} e^3 \Big] - \sum_{n=2}^{\infty} \overline{\mathcal{A}}_n \binom{n}{2} \left[\frac{(I_0 - I_2)}{2} e^2 \right. \\ \left. + \frac{(I_1 - I_3)}{2} e^3 \right]\end{aligned} \tag{8.64}$$

A similar procedure can be followed to derive Δx. Substituting Eq. 8.58 in Eq. 8.20,

$$\begin{aligned}\Delta x = D_c \int_0^{2\pi} \left(\frac{(1+e\cos E)}{1-e\cos E}\right)^{1/2} (\cos E + e)\exp\{\beta x \cos E\} \\ \times \sum_{n=0}^{\infty} \overline{\mathcal{A}}_n \left[\sum_{k=0}^{\lfloor \frac{n}{2} \rfloor} (-1)^k \binom{n}{2k} \left(\frac{e\sin E}{\sqrt{1-e^2\cos^2 E}}\right)^{2k}\right. \\ \left. \times \left(\sqrt{\frac{1-e^2}{1-e^2\cos^2 E}}\right)^{n-2k}\right] dE\end{aligned} \tag{8.65}$$

Expanding the integrand as a power series in e,

$$\begin{aligned}\Delta x = D_c \int_0^{2\pi} \sum_{n=0}^{\infty} \sum_{k=0}^{\lfloor \frac{n}{2} \rfloor} \overline{\mathcal{A}}_n (-1)^k \binom{n}{2k} [\cos E + \left(\frac{3+\cos 2E}{2}\right) e \\ + \frac{1}{4}\cos E\{5+4k-n+(n+1)\cos 2E\}e^2 + \frac{1}{8}(3+\cos 2E)\{1+4k \\ - n + (n+1)\cos 2E\}e^3](e\sin E)^{2k}\exp(\beta x \cos E) dE\end{aligned} \tag{8.66}$$

Truncating the series at $\mathcal{O}(e^3)$, k can only be 0 and 1. Therefore, Eq. 8.60 can be written as,

$$\begin{aligned}\Delta x = D_c \int_0^{2\pi} \left[\sum_{n=0}^{\infty} \overline{\mathcal{A}}_n [\cos E + \frac{3+\cos 2E}{2} e + \frac{1}{4}\{(5-n)\cos E \right. \\ + \frac{(n+1)}{2}(\cos 3E + \cos E)\}e^2 + \frac{1}{8}[3\{(1-n)+(n+1)\cos 2E\} \\ + \{(1-n)\cos 2E + (n+1)\frac{(1+\cos 4E)}{2}\}e^3]]\exp(\beta x \cos E) \\ + \sum_{n=2}^{\infty} -\overline{\mathcal{A}}_n \binom{n}{2} [\frac{(\cos E + \cos 3E)}{4} e^2 - (\cos 2E + \frac{1}{4}\cos 4E \\ \left. - \frac{5}{4})\frac{e^3}{2}]\exp(\beta x \cos E)\right] dE\end{aligned} \tag{8.67}$$

Integrating the equation,

$$\begin{aligned}\Delta x = 2\pi D_c \left[\sum_{n=0}^{\infty} \overline{\mathcal{A}}_n [I_1 + \frac{3I_0 + I_2}{2} e + \frac{1}{4}\{(5-n)I_1 + \frac{(n+1)}{2} \right. \\ \times (I_3 + I_1)\}e^2 + \frac{1}{8}[3\{(1-n)I_0 + (n+1)I_2\} + \{(1-n)I_2 \\ + (n+1)\frac{(I_0+I_4)}{2}\}e^3]] + \sum_{n=2}^{\infty} -\overline{\mathcal{A}}_n \binom{n}{2} [\frac{(I_1+I_3)}{4} e^2 \\ \left. - (I_2 + \frac{1}{4}I_4 - \frac{5}{4}I_0)\frac{e^3}{2}]\right]\end{aligned} \tag{8.68}$$

For a satellite with an arbitrary shape, $\Delta\omega \neq 0$ since $\overline{\mathcal{B}}_n \neq 0$. To derive $\Delta\omega$, it should be noted that the even part of the drag-coefficient will integrate out to zero unlike Δa and Δx.

Therefore, Eq. 8.21 can be written as,

$$\begin{aligned}\Delta\omega = D_w \int_0^{2\pi} \Bigg[\left(\frac{(1+e\cos E)}{1-e\cos E}\right)^{1/2} \sin E \exp\left(\beta x \cos E\right) \sum_{n=0}^{\infty} \overline{\mathcal{B}}_n \\ \times \Bigg\{ \sum_{k=0}^{\lfloor \frac{n-1}{2} \rfloor} (-1)^k \binom{n}{2k+1} \left(\frac{e\sin E}{\sqrt{1-e^2\cos^2 E}}\right)^{2k+1} \\ \times \left(\sqrt{\frac{1-e^2}{1-e^2\cos^2 E}}\right)^{n-2k-1} \Bigg\} \Bigg] dE\end{aligned} \tag{8.69}$$

where $D_w = -\dfrac{\delta' a}{e}\sqrt{1-e^2}\rho_{p0}\exp\left\{\beta(a_0 - a - x_0)\right\}$. On expanding the integrand as a power series in e and truncating at order 3,

$$\begin{aligned}\Delta\omega =& 2\pi D_w \sum_{n=0}^{\infty} n\overline{\mathcal{B}}_n \left[\frac{I_0 - I_2}{2}e + \frac{I_1 - I_3}{4}e^2 + \frac{1}{4}\{(n+1)\right. \\ & \left. \times \frac{2I_1 - I_4 - 1}{4} - (n-3)\frac{I_0 - I_2}{2}\}e^3\right]\end{aligned} \tag{8.70}$$

For $n = 0$, Eqs. 8.64 and 8.68 reduce to the original King-Hele formulation given by Eqs. 8.32 and 8.33 while Eq. 8.70 reduces to zero. The average drag-coefficient that best approximates the higher order Fourier theory given by Eqs. 8.64 and 8.68 can be calculated using Eq. 8.36 as follows,

$$\begin{aligned}C_{d0} &= \frac{\int_0^{2\pi} \rho C_d(E) dE}{\int_0^{2\pi} \rho dE} \\ &= \frac{1}{\int_0^{2\pi} \exp(\beta x \cos E) dE} \left[\int_0^{2\pi} \exp(\beta x \cos E) \sum_{n=0}^{\infty} \sum_{k=0}^{\lfloor \frac{n}{2} \rfloor} \overline{\mathcal{A}}_n \right. \\ &\left. \times (-1)^k \binom{n}{2k} \left(\frac{e\sin E}{\sqrt{1-e^2\cos^2 E}}\right)^{2k} \left(\sqrt{\frac{1-e^2}{1-e^2\cos^2 E}}\right)^{n-2k} dE\right] \\ &= \frac{1}{I_0}\left[\sum_{n=0}^{\infty} \overline{\mathcal{A}}_n \{I_0 + \frac{n}{4}(I_2 - I_0)e^2\} + \sum_{n=2}^{\infty} \frac{\overline{\mathcal{A}}_n}{2}\binom{n}{2}(I_2 - I_0)e^2\right]\end{aligned} \tag{8.71}$$

High eccentricity regime, $0.2 \leq e < 1$

Similar to the OFF model in high eccentricity regime, the eccentric anomaly is transformed to the auxiliary variable λ. The flight path angle in the new variable is given by

$$\sin\phi = e\sqrt{\frac{1-(1-\lambda^2/z)^2}{1-e^2(1-\lambda^2/z)^2}} \tag{8.72}$$

$$\cos\phi = \sqrt{\frac{1-e^2}{1-e^2(1-\lambda^2/z)^2}} \tag{8.73}$$

The drag-coefficient in the transformed variable is given by

$$\begin{aligned} C_d(\lambda) = \sum_{n=0}^{\infty} \Bigg[\overline{\mathcal{A}}_n \Bigg\{ \sum_{k=0}^{\lfloor \frac{n}{2} \rfloor} (-1)^k \binom{n}{2k} \left(e\sqrt{\frac{1-(1-\lambda^2/z)^2}{1-e^2(1-\lambda^2/z)^2}} \right)^{2k} \\ \times \left(\sqrt{\frac{1-e^2}{1-e^2(1-\lambda^2/z)^2}} \right)^{n-2k} \Bigg\} + \overline{\mathcal{B}}_n \Bigg\{ \sum_{k=0}^{\lfloor \frac{n-1}{2} \rfloor} (-1)^k \binom{n}{2k+1} \\ \times \left(e\sqrt{\frac{1-(1-\lambda^2/z)^2}{1-e^2(1-\lambda^2/z)^2}} \right)^{2k+1} \left(\sqrt{\frac{1-e^2}{1-e^2(1-\lambda^2/z)^2}} \right)^{n-2k-1} \Bigg\} \Bigg] \end{aligned} \tag{8.74}$$

Substitute Eq. 8.74 in Eq. 8.40 and carrying out a power series expansion in λ^2/z,

$$\begin{aligned} \Delta a =& 2\exp(z)\sqrt{2/z} D_c \frac{(1+e)^{3/2}}{(1-e)^{1/2}} \int_0^{\sqrt{2z}} \sum_{n=0}^{\infty} \sum_{k=0}^{\lfloor n/2 \rfloor} \overline{\mathcal{A}}_n (-1)^k \binom{n}{2k} \\ & \times \left(\frac{2e^2}{1-e^2} \right)^k \Big[(\lambda^2/z)^k + P_1(\lambda^2/z)^{k+1} + P_2(\lambda^2/z)^{k+2} \\ & + \mathcal{O}((\lambda^2/z)^{k+3}) \Big] \exp(-\lambda^2) d\lambda \end{aligned} \tag{8.75}$$

where P_1 and P_2 are functions of the summation indices n and k, and the eccentricity e and are given by

$$P_1 = -\frac{1}{4(1-e^2)} [(2k-1) + 8e + (4n-2k-3)e^2] \tag{8.76}$$

$$\begin{aligned} P_2 =& \frac{1}{32(1-e^2)^2} [(4k^2 - 8k + 3) + 16(2k-1)e + (8n - 8k^2 \\ & + 16kn + 50)e^2 + 16(4n - 2k + 1)e^3 + \{(4(n-k)(n-k-2) \\ & + 4nk - 5\}e^4] \end{aligned} \tag{8.77}$$

Using Eq. 8.48,

$$\begin{aligned} \Delta a =& D_c' \sum_{n=0}^{\infty} \sum_{k=0}^{\lfloor n/2 \rfloor} \overline{\mathcal{A}}_n (-1)^k \binom{n}{2k} \left(\frac{2e^2}{z(1-e^2)} \right)^k \Bigg[\Gamma\left(\frac{2k+1}{2} \right) \\ & + \frac{P_1}{z} \Gamma\left(\frac{2k+3}{2} \right) + \frac{P_2}{z^2} \Gamma\left(\frac{2k+5}{2} \right) \Bigg] \end{aligned} \tag{8.78}$$

To derive Δx, substitute Eq. 8.74 in Eq. 8.41 and expand as a power series in λ^2/z to obtain,

$$\begin{aligned}\Delta x =& 2\exp(z)\sqrt{2/z}D_c\frac{(1+e)^{3/2}}{(1-e)^{1/2}}\int_0^{\sqrt{2z}}\sum_{n=0}^{\infty}\sum_{k=0}^{\lfloor n/2\rfloor}\overline{\mathcal{A}}_n(-1)^k\binom{n}{2k}\\ &\times\left(\frac{2e^2}{1-e^2}\right)^k\Big[(\lambda^2/z)^k+Q_1(\lambda^2/z)^{k+1}+Q_2(\lambda^2/z)^{k+2}\\ &+\mathcal{O}((\lambda^2/z)^{k+3})\Big]\exp(-\lambda^2)d\lambda\end{aligned}\tag{8.79}$$

where Q_1 and Q_2 given by

$$Q_1=-\frac{1}{4(1-e^2)}[(2k+3)+(4n-2k+1)e^2]\tag{8.80}$$

$$\begin{aligned}Q_2 =&\frac{1}{32(1-e^2)^2}[(4k^2+8k-5)+32e-2(4k^2-20n-8kn\\ &+7)e^2+32e^3+\{4(2n-k)(2n-k+2)+8n+3\}e^4]\end{aligned}\tag{8.81}$$

Using Eq. 8.48,

$$\begin{aligned}\Delta x =&D_c'\sum_{n=0}^{\infty}\sum_{k=0}^{\lfloor n/2\rfloor}\overline{\mathcal{A}}_n(-1)^k\binom{n}{2k}\left(\frac{2e^2}{z(1-e^2)}\right)^k\left[\Gamma\left(\frac{2k+1}{2}\right)\right.\\ &\left.+\frac{Q_1}{z}\Gamma\left(\frac{2k+3}{2}\right)+\frac{Q_2}{z^2}\Gamma\left(\frac{2k+5}{2}\right)\right]\end{aligned}\tag{8.82}$$

The change in argument of perigee can be similarly derived. Eq. 8.21 in the transformed variable can be written as

$$\Delta\omega=\frac{4}{z}\exp(z)D_w\int_0^{\sqrt{2z}}\left(\frac{1+e-e\lambda^2/z}{1-e+e\lambda^2/z}\right)^{1/2}\lambda\exp(-\lambda^2)C_d(\lambda)d\lambda\tag{8.83}$$

On substituting Eq. 8.74 and carrying out a power series expansion, the equation simplifies to the following form

$$\begin{aligned}\Delta\omega =&4\exp(z)D_w\sqrt{\frac{1+e}{1-e}}\int_0^{\sqrt{2z}}\sum_{n=0}^{\infty}\sum_{k=0}^{\lfloor\frac{n-1}{2}\rfloor}\overline{\mathcal{B}}_n(-1)^k\binom{n}{2k+1}\\ &\times\left(\frac{2e^2}{1-e^2}\right)^{\frac{2k+1}{2}}\left[(\lambda^2/z)^{\frac{2k+3}{2}}+W_n(\lambda^2/z)^{\frac{2k+5}{2}}\right]d\lambda\end{aligned}\tag{8.84}$$

where

$$W_n = -\frac{1}{4(1-e^2)}[(2k+1)+4e+(4n-2k-1)e^2] \tag{8.85}$$

The integrated change is given by

$$\begin{aligned}\Delta\omega =& 2\exp(z)D_w\sqrt{\frac{1+e}{1-e}}\sum_{n=0}^{\infty}\sum_{k=0}^{\lfloor\frac{n-1}{2}\rfloor}\overline{\mathcal{B}}_n(-1)^k\binom{n}{2k+1}\\ &\times\left(\frac{2e^2}{z(1-e^2)}\right)^{\frac{2k+1}{2}}\left[\frac{1}{z}\Gamma(k+2)+\frac{W_n}{z^2}\Gamma(k+3)\right]\end{aligned} \tag{8.86}$$

The constant drag-coefficient to be used with the original King-Hele formulation has to be re-derived for the high eccentricity regime in this case since Eq. 8.71 consists of a series truncation in e. The drag-coefficient in the auxiliary variable is given by

$$\begin{aligned}C_{d0} =& \frac{\exp z}{\pi\sqrt{2z}I_0}\left[\sum_{n=0}^{\infty}\sum_{k=0}^{\lfloor\frac{n}{2}\rfloor}\overline{\mathcal{A}}_n(-1)^k\binom{n}{2k}\left(\frac{2e^2}{z(1-e^2)}\right)^k\right.\\ &\left.\times\left\{\Gamma\left(\frac{2k+1}{2}\right)+\frac{C_{N1}}{z}\Gamma\left(\frac{2k+3}{2}\right)+\frac{C_{N2}}{z^2}\Gamma\left(\frac{2k+5}{2}\right)\right\}\right]\end{aligned} \tag{8.87}$$

where

$$C_{N1} = -\frac{1}{4(1-e^2)}[(2k-1)+(4n-2k+1)e^2], \tag{8.88}$$

$$\begin{aligned}C_{N2} =& \frac{1}{32(1-e^2)^2}[(4k^2-8k+3)(1-e^2)^2+8ne^2(3e^2-2ke^2\\ &+2k+1+2ne^2)].\end{aligned} \tag{8.89}$$

8.5.2 Inertially stabilized attitude

For an inertially stabilized satellite, the angle between the velocity vector and the body axis can be computed from the velocity components in the perifocal frame. The sine and cosine of the angle is given by

$$\begin{aligned}\sin\theta &= \frac{\mathrm{v}_P}{\sqrt{\mathrm{v}_P^2+\mathrm{v}_Q^2}}\\ &= \frac{\sin\theta}{\sqrt{1+e^2+2e\cos\theta}} = \frac{\sin E}{\sqrt{1-e^2\cos^2 E}}\end{aligned} \tag{8.90}$$

$$\begin{aligned}\cos\theta &= \frac{\mathrm{v}_Q}{\sqrt{\mathrm{v}_P^2+\mathrm{v}_Q^2}} \\ &= \frac{e+\cos\theta}{\sqrt{1+e^2+2e\cos\theta}} = \frac{\sqrt{1-e^2}\cos E}{\sqrt{1-e^2\cos^2 E}}\end{aligned} \tag{8.91}$$

Substituting Eqs. 8.90 and 8.91 in Eq. 5.15 and using Eqs. 8.43 and 8.42,

$$\begin{aligned}C_d(E) = \sum_{n=0}^{\infty}\Bigg[\overline{\mathcal{A}}_n\Bigg\{\sum_{k=0}^{\lfloor\frac{n}{2}\rfloor}(-1)^k\binom{n}{2k}\left(\frac{\sin E}{\sqrt{1-e^2\cos^2 E}}\right)^{2k} \\ \times\left(\frac{\sqrt{1-e^2}\cos E}{\sqrt{1-e^2\cos^2 E}}\right)^{n-2k}\Bigg\} + \overline{\mathcal{B}}_n\Bigg\{\sum_{k=0}^{\lfloor\frac{n-1}{2}\rfloor}(-1)^k\binom{n}{2k+1} \\ \times\left(\frac{\sin E}{\sqrt{1-e^2\cos^2 E}}\right)^{2k+1}\left(\frac{\sqrt{1-e^2}\cos E}{\sqrt{1-e^2\cos^2 E}}\right)^{n-2k-1}\Bigg\}\Bigg]\end{aligned} \tag{8.92}$$

Low eccentricity regime, $e < 0.2$

Following the same procedure as the nadir pointing profile, only the $\overline{\mathcal{A}}_n$ terms are considered substituting Eq. 8.92 in Eq. 8.19 since the $\overline{\mathcal{B}}_n$ terms integrate to zero,

$$\begin{aligned}\Delta a = D_c\int_0^{2\pi}\sum_{n=0}^{\infty}\sum_{k=0}^{\lfloor\frac{n}{2}\rfloor}\overline{\mathcal{A}}_n(-1)^k\binom{n}{2k}\left(\frac{\sin E}{\sqrt{1-e^2\cos^2 E}}\right)^{2k} \\ \times\left(\frac{\sqrt{1-e^2}\cos E}{\sqrt{1-e^2\cos^2 E}}\right)^{n-2k}\frac{(1+e\cos E)^{3/2}}{(1-e\cos E)^{1/2}}\exp(\beta x\cos E)dE\end{aligned} \tag{8.93}$$

Expanding as a power series in e and truncating at order 3,

$$\begin{aligned}\Delta a = D_c\int_0^{2\pi}\sum_{n=0}^{\infty}\sum_{k=0}^{\lfloor\frac{n}{2}\rfloor}\overline{\mathcal{A}}_n(-1)^k\binom{n}{2k}[1+2\cos E e+\{k-\frac{n}{2} \\ +\frac{1}{2}(n+3)\cos^2 E\}e^2+\cos E\{2k-n+(n+1)\cos^2 E\}e^3] \\ \times\sin^{2k}E\cos^{n-2k}E\exp\{\beta x\cos E\}dE\end{aligned} \tag{8.94}$$

Unlike the nadir pointing profile case, the series cannot be truncated in k as there's no e^k in the expression. The trigonometric powers have to be expressed in multiple angles to integrate the equation. The following identities are used to express an arbitrary trigonometric power in multiple angles,

$$\sin^{2k}E = \frac{1}{2^{2k}}\binom{2k}{k} + \frac{(-1)^k}{2^{2k-1}}\sum_{j=0}^{k-1}(-1)^j\binom{2k}{j}\cos[2(k-j)E] \tag{8.95}$$

$$\cos^k E =$$

$$\begin{cases} \dfrac{1}{2^k}\binom{k}{k/2} + \dfrac{1}{2^{k-1}}\displaystyle\sum_{i=0}^{k/2-1}\binom{k}{i}\cos\left[k-2i\right]E, & k \in 2q, q \in \mathbb{Z}^{\geq} \\ \dfrac{1}{2^{k-1}}\displaystyle\sum_{i=0}^{(k-1)/2}\binom{k}{i}\cos\left[k-2i\right]E, & k \in 2q+1, q \in \mathbb{Z}^{\geq}. \end{cases} \tag{8.96}$$

To simplify the algebra, introduce the following notation.

$${}^{p}a = \begin{cases} \dfrac{1}{2^p}\binom{p}{p/2}, & p \in 2q, q \in \mathbb{Z}^{\geq}, \\ 0, & p \in 2q+1, q \in \mathbb{Z}^{\geq}, \end{cases} \tag{8.97}$$

$${}^{p}_{j}\mathcal{S}_1 = \begin{cases} \dfrac{(-1)^{p/2}}{2^{p-1}}\displaystyle\sum_{j=0}^{p/2-1}(-1)^j\binom{p}{j}, & p \in 2q, q \in \mathbb{Z}^{+}, \\ 0, & p \in \{0, 2q+1\}, q \in \mathbb{Z}^{\geq}, \end{cases} \tag{8.98}$$

$${}^{p}_{i}\mathcal{S}_2 = \begin{cases} \dfrac{1}{2^{p-1}}\displaystyle\sum_{i=0}^{p/2-1}\binom{p}{i}, & p \in 2q, q \in \mathbb{Z}^{+}, \\ 0, & p \in \{0, 2q+1\}, q \in \mathbb{Z}^{\geq}, \end{cases} \tag{8.99}$$

$${}^{p}_{i}\mathcal{S}_3 = \begin{cases} \dfrac{1}{2^{p-1}}\displaystyle\sum_{i=0}^{(p-1)/2}\binom{p}{i}, & p \in 2q+1, q \in \mathbb{Z}^{\geq}, \\ 0, & p \in 2q, q \in \mathbb{Z}^{\geq}, \end{cases} \tag{8.100}$$

Eqs. 8.95 and 8.96 can be represented using the notations in 8.100 as

$$\sin^{2k} E = {}^{2k}a + {}^{2k}_{j}\mathcal{S}_1 \cos\left[2(k-j)E\right] \tag{8.101}$$

$$\cos^k E = \begin{cases} {}^{k}a + {}^{k}_{i}\mathcal{S}_2 \cos\left[k-2i\right]E, & k \in 2q, q \in \mathbb{Z}^{\geq}, \\ {}^{k}_{i}\mathcal{S}_3 \cos\left[k-2i\right]E, & k \in 2q+1, q \in \mathbb{Z}^{\geq}. \end{cases} \tag{8.102}$$

The following integrals are computed to integrate Eq. 8.94.

$$
\begin{aligned}
h_{n,k}(l) &= \int_0^{2\pi} \sin^{2k} E \cos^{n-2k+l} E \exp\{\beta x \cos E\} dE \\
&= \int_0^{2\pi} ({}^{2k}a + {}^{2k}_{j}\mathcal{S}_1 \cos[2(k-j)E])({}^{n+l-2k}a \\
&+ {}^{n+l-2k}_{i}\mathcal{S}_2 \cos[(n+l-2k-2i)E]) \exp(\beta x \cos E) dE \\
&= 2\pi[({}^{2k}a)({}^{n+l-2k}a) I_0 + ({}^{2k}a)({}^{n+l-2k}_{i}\mathcal{S}_2) I_{n+l-2k-2i} \\
&+ ({}^{n+l-2k}a)({}^{2k}_{j}\mathcal{S}_1) I_{2(k-j)} + \frac{({}^{2k}_{j}\mathcal{S}_1)({}^{n+l-2k}_{i}\mathcal{S}_2)}{2} \\
&\times (I_{n+l-2i-2j} + I_{n+l-4k-2i+2j})], \\
&\qquad \text{if } (n+l) \in 2q, q \in \mathbb{Z}^{\geq},
\end{aligned}
\tag{8.103}
$$

$$
\begin{aligned}
g_{n,k}(l) &= \int_0^{2\pi} \sin^{2k} E \cos^{n-2k+l} E \exp\{\beta x \cos E\} dE \\
&= \int_0^{2\pi} ({}^{2k}a + {}^{2k}_{j}\mathcal{S}_1 \cos[2(k-j)E])({}^{n+l-2k}_{i}\mathcal{S}_3 \\
&\times \cos[(n+l-2k-2i)E]) \times \exp(\beta x \cos E) dE \\
&= 2\pi[({}^{2k}a)({}^{n+l-2k}_{i}\mathcal{S}_3) I_{n+l-2k-2i} + \frac{({}^{2k}_{j}\mathcal{S}_1)({}^{n+l-2k}_{i}\mathcal{S}_3)}{2} \\
&\times (I_{n+l-2i-2j} + I_{n+l-4k-2i+2j})], \\
&\qquad \text{if } (n+l) \in 2q+1, q \in \mathbb{Z}^{\geq}.
\end{aligned}
\tag{8.104}
$$

Using Eqs. 8.103 and 8.104 to integrate Eq. 8.94,

$$
\begin{aligned}
\Delta a = D_c[&\sum_{\substack{l=0 \\ n \in 2l}}^{\infty} \sum_{k=0}^{\lfloor \frac{n}{2} \rfloor} A_n (-1)^k \binom{n}{2k} [h_{n,k}(0) + 2g_{n,k}(1)e + \{(k - \frac{n}{2}) \\
&\times h_{n,k}(0) + \frac{1}{2}(n+3) h_{n,k}(2)\} e^2 + \{(2k-n) g_{n,k}(1) + (n+1) \\
&\times g_{n,k}(3)\} e^3] + \sum_{\substack{l=0 \\ n \in 2l+1}}^{\infty} \sum_{k=0}^{\lfloor \frac{n}{2} \rfloor} A_n (-1)^k \binom{n}{2k} [g_{n,k}(0) + 2h_{n,k}(1)e \\
&+ \{(k - \frac{n}{2}) g_{n,k}(0) + \frac{1}{2}(n+3) g_{n,k}(2)\} e^2 + \{(2k-n) h_{n,k}(1) \\
&+ (n+1) h_{n,k}(3)\} e^3]]
\end{aligned}
\tag{8.105}
$$

The derivation of Δx follows a similar procedure. Substituting Eq. 8.92 in Eq. 8.20 and considering only $\overline{\mathcal{A}}_n$ terms,

$$\begin{aligned}\Delta x = D_c \int_0^{2\pi} \sum_{n=0}^{\infty} \sum_{k=0}^{\lfloor \frac{n}{2} \rfloor} \overline{\mathcal{A}}_n (-1)^k \binom{n}{2k} [\cos E + (1+\cos^2 E)e \\ + \frac{1}{2}\{(2+2k-n)\cos E + (n+1)\cos^3 E\}e^2 + \frac{1}{2}\{(2k-n) \\ + (2k+1)\cos^2 E + (n+1)\cos^4 E\}e^3] \sin^{2k} E \cos^{n-2k} E \\ \times \exp(\beta x \cos E) dE\end{aligned} \tag{8.106}$$

Using Eqs. 8.103 and 8.104 to integrate Eq. 8.106,

$$\begin{aligned}\Delta x = D_c \Bigg[\sum_{\substack{l=0 \\ n \in 2l}}^{\infty} \sum_{k=0}^{\lfloor \frac{n}{2} \rfloor} \overline{\mathcal{A}}_n (-1)^k \binom{n}{2k} [g_{n,k}(1) + (h_{n,k}(0) \\ + h_{n,k}(2))e + \frac{1}{2}\{(2+2k-n)g_{n,k}(1) + (n+1)g_{n,k}(3)\}e^2 \\ + \frac{1}{2}\{(2k-n)h_{n,k}(0) + (2k+1)h_{n,k}(2) + (n+1)h_{n,k}(4)\}e^3] \\ + \sum_{\substack{l=0 \\ n \in 2l+1}}^{\infty} \sum_{k=0}^{\lfloor \frac{n}{2} \rfloor} \overline{\mathcal{A}}_n (-1)^k \binom{n}{2k} [h_{n,k}(1) + (g_{n,k}(0) + g_{n,k}(2))e \\ + \frac{1}{2}\{(2+2k-n)h_{n,k}(1) + (n+1)h_{n,k}(3)\}e^2 + \frac{1}{2}\{(2k-n) \\ \times g_{n,k}(0) + (2k+1)g_{n,k}(2) + (n+1)g_{n,k}(4)\}e^3] \Bigg]\end{aligned} \tag{8.107}$$

The change in argument of perigee can be derived similarly as,

$$\begin{aligned}\Delta\omega = D_w \int_0^{2\pi} \sum_{n=0}^{\infty} \sum_{k=0}^{\lfloor \frac{n-1}{2} \rfloor} \overline{\mathcal{B}}_n (-1)^k \binom{n}{2k+1} [1 + \cos E e \\ + \frac{1}{2}\{(n+1)\cos^2 E - (n-2k-1)\}e^2 + \frac{1}{2}\cos E\{(n+1)\cos^2 E \\ - (n-2k-1)\}e^3] \sin^{2k+2} E \cos^{n-2k-1} E \exp(\beta x \cos E) dE\end{aligned} \tag{8.108}$$

Integrating the equation, the final form is given by

$$\begin{aligned}\Delta\omega = D_w \Bigg[& \sum_{\substack{l=0 \\ n\in 2l}}^{\infty} \sum_{k=0}^{\lfloor \frac{n-1}{2} \rfloor} \overline{\mathcal{B}}_n (-1)^k \binom{n}{2k+1} [g_{n,k+1}(1) + h_{n,k+1}(2)e \\ & + \frac{1}{2}\{(n+1)g_{n,k+1}(3) - (n-2k-1)g_{n,k+1}(1)\}e^2 + \frac{1}{2}\{(n+1) \\ & \times h_{n,k+1}(3) - (n-2k-1)g_{n,k+1}(1)\}e^3] + \sum_{\substack{l=0 \\ n\in 2l+1}}^{\infty} \sum_{k=0}^{\lfloor \frac{n-1}{2} \rfloor} \overline{\mathcal{B}}_n (-1)^k \\ & \times \binom{n}{2k+1} [h_{n,k+1}(1) + g_{n,k+1}(2)e + \frac{1}{2}\{(n+1)h_{n,k+1}(3) \\ & - (n-2k-1)h_{n,k+1}(1)\}e^2 + \frac{1}{2}\{(n+1)g_{n,k+1}(3) - (n-2k-1) \\ & \times h_{n,k+1}(1)\}e^3]\Bigg]\end{aligned} \tag{8.109}$$

For $n = 0$, the equations for semi-major axis and focal-length reduce to the original King-Hele formulation given by Eqs. 8.32 and 8.33 while the argument of perigee change reduces to zero. The average drag-coefficient that best approximates the higher order Fourier theory given by Eqs. 8.105 and 8.107 can be calculated using Eq. 8.36 as follows

$$\begin{aligned} C_{d0} &= \frac{\int_0^{2\pi} \rho C_d(E) dE}{\int_0^{2\pi} \rho dE} \\ &= \frac{1}{I_0} \Bigg[\sum_{\substack{l=0 \\ n\in 2l}}^{\infty} \sum_{k=0}^{\lfloor \frac{n}{2} \rfloor} \overline{\mathcal{A}}_n (-1)^k \binom{n}{2k} [h_{n,k}(0) + \{(k - \frac{n}{2})h_{n,k}(0) \\ &\quad + \frac{n}{2} h_{n,k}(2)\}e^2] + \sum_{\substack{l=0 \\ n\in 2l+1}}^{\infty} \sum_{k=0}^{\lfloor \frac{n}{2} \rfloor} \overline{\mathcal{A}}_n (-1)^k \binom{n}{2k} [g_{n,k}(0) \\ &\quad + \{(k - \frac{n}{2})g_{n,k}(0) + \frac{n}{2} g_{n,k}(2)\}e^2]\Bigg] \end{aligned} \tag{8.110}$$

High eccentricity regime, $0.2 \leq e < 1$

Similar to the nadir pointing case, the body angle in the transformed variable is given by

$$\sin\phi = \sqrt{\frac{1 - (1 - \lambda^2/z)^2}{1 - e^2(1 - \lambda^2/z)^2}} \tag{8.111}$$

$$\cos\phi = \sqrt{\frac{1 - e^2}{1 - e^2(1 - \lambda^2/z)^2}}(1 - \lambda^2/z) \tag{8.112}$$

The drag-coefficient in the transformed variable is given by

$$\begin{aligned} C_d(\lambda) = \sum_{n=0}^{\infty} \Bigg[\overline{\mathcal{A}}_n \Bigg\{ \sum_{k=0}^{\lfloor \frac{n}{2} \rfloor} (-1)^k \binom{n}{2k} \left(\sqrt{\frac{1-(1-\lambda^2/z)^2}{1-e^2(1-\lambda^2/z)^2}} \right)^{2k} \\ \times \left(\sqrt{\frac{1-e^2}{1-e^2(1-\lambda^2/z)^2}} (1-\lambda^2/z) \right)^{n-2k} \Bigg\} + \overline{\mathcal{B}}_n \Bigg\{ \sum_{k=0}^{\lfloor \frac{n-1}{2} \rfloor} (-1)^k \\ \times \binom{n}{2k+1} \left(\sqrt{\frac{1-(1-\lambda^2/z)^2}{1-e^2(1-\lambda^2/z)^2}} \right)^{2k+1} \\ \times \left(\sqrt{\frac{1-e^2}{1-e^2(1-\lambda^2/z)^2}} (1-\lambda^2/z) \right)^{n-2k-1} \Bigg\} \Bigg] . \end{aligned} \tag{8.113}$$

Substitute Eq. 8.113 in Eq. 8.40 and carrying out a power series expansion in λ^2/z,

$$\begin{aligned} \Delta a =& 2 \exp(z) \sqrt{2/z} D_c \frac{(1+e)^{3/2}}{(1-e)^{1/2}} \int_0^{\sqrt{2z}} \sum_{n=0}^{\infty} \sum_{k=0}^{\lfloor n/2 \rfloor} \overline{\mathcal{A}}_n (-1)^k \\ & \times \binom{n}{2k} \left(\frac{2}{1-e^2} \right)^k \Big[(\lambda^2/z)^k + L_1 (\lambda^2/z)^{k+1} + L_2 (\lambda^2/z)^{k+2} \\ & + \mathcal{O}((\lambda^2/z)^{k+3}) \Big] \exp(-\lambda^2) d\lambda, \end{aligned} \tag{8.114}$$

where L_1 and L_2 are functions of the summation indices n and k, and the eccentricity e and are given by

$$L_1 = \frac{1}{4(1-e^2)} [(6k - 4n + 1) - 8e + (3 - 6k)e^2], \tag{8.115}$$

$$\begin{aligned} L_2 =& \frac{1}{32(1-e^2)^2} [\{4(2n-3k)^2 + 40k - 24n + 3\} + 16(4n \\ & - 6k - 1)e - (72k^2 + 32k - 24n - 48kn - 50)e^2 + 16(6k \\ & + 1)e^3 + ((2k-1)(18k+5)e^4]. \end{aligned} \tag{8.116}$$

Using Eq. 8.48,

$$\begin{aligned} \Delta a =& D_c' \sum_{n=0}^{\infty} \sum_{k=0}^{\lfloor n/2 \rfloor} \overline{\mathcal{A}}_n (-1)^k \binom{n}{2k} \left(\frac{2}{z(1-e^2)} \right)^k \left[\Gamma\left(\frac{2k+1}{2} \right) \right. \\ & \left. + \frac{L_1}{z} \Gamma\left(\frac{2k+3}{2} \right) + \frac{L_2}{z^2} \Gamma\left(\frac{2k+5}{2} \right) \right]. \end{aligned} \tag{8.117}$$

To derive Δx, substitute Eq. 8.113 in Eq. 8.41 and expand as a power series in λ^2/z to obtain,

$$\begin{aligned}\Delta x =& 2\exp(z)\sqrt{2/z}D_c\frac{(1+e)^{3/2}}{(1-e)^{1/2}}\int_0^{\sqrt{2z}}\sum_{n=0}^{\infty}\sum_{k=0}^{\lfloor n/2\rfloor}\overline{\mathcal{A}}_n(-1)^k\binom{n}{2k}\\ &\times\left(\frac{2}{1-e^2}\right)^k\Big[(\lambda^2/z)^k+N_1(\lambda^2/z)^{k+1}+N_2(\lambda^2/z)^{k+2}\\ &+\mathcal{O}((\lambda^2/z)^{k+3})\Big]\exp(-\lambda^2)d\lambda,\end{aligned}\tag{8.118}$$

where N_1 and N_2 given by

$$N_1=-\frac{1}{4(1-e^2)}[(4n-6k+3)+(6k+1)e^2],\tag{8.119}$$

$$\begin{aligned}N_2=&\frac{1}{32(1-e^2)^2}[\{4(2n-3k)^2+8(n-k)-5\}+32e-2(36k^2\\ &+16k-28n-24kn+7)e^2+32e^3+(36k^2+40k+3)e^4].\end{aligned}\tag{8.120}$$

Using Eq. 8.48,

$$\begin{aligned}\Delta x =&D_c'\sum_{n=0}^{\infty}\sum_{k=0}^{\lfloor n/2\rfloor}\overline{\mathcal{A}}_n(-1)^k\binom{n}{2k}\left(\frac{2}{z(1-e^2)}\right)^k\left[\Gamma\left(\frac{2k+1}{2}\right)\right.\\ &\left.+\frac{N_1}{z}\Gamma\left(\frac{2k+3}{2}\right)+\frac{N_2}{z^2}\Gamma\left(\frac{2k+5}{2}\right)\right].\end{aligned}\tag{8.121}$$

The change in argument of perigee can be similarly derived by retaining the $\overline{\mathcal{B}}_n$ terms,

$$\begin{aligned}\Delta\omega =&4\exp(z)D_w\sqrt{\frac{1+e}{1-e}}\int_0^{\sqrt{2z}}\sum_{n=0}^{\infty}\sum_{k=0}^{\lfloor\frac{n-1}{2}\rfloor}\overline{\mathcal{B}}_n(-1)^k\binom{n}{2k+1}\\ &\times\left(\frac{2}{1-e^2}\right)^{\frac{2k+1}{2}}\left[(\lambda^2/z)^{\frac{2k+3}{2}}+W_I(\lambda^2/z)^{\frac{2k+5}{2}}\right]d\lambda\end{aligned}\tag{8.122}$$

where

$$W_I=-\frac{1}{4(1-e^2)}[(4n-6k-3)+4e+(6k+3)e^2]\tag{8.123}$$

The integrated change is given by

$$\begin{aligned}\Delta\omega =&2\exp(z)D_w\sqrt{\frac{1+e}{1-e}}\sum_{n=0}^{\infty}\sum_{k=0}^{\lfloor\frac{n-1}{2}\rfloor}\overline{\mathcal{B}}_n(-1)^k\binom{n}{2k+1}\\ &\times\left(\frac{2}{z(1-e^2)}\right)^{\frac{2k+1}{2}}\left[\frac{1}{z}\Gamma(k+2)+\frac{W_I}{z^2}\Gamma(k+3)\right]\end{aligned}\tag{8.124}$$

The density-averaged drag-coefficient can be derived as follows

$$C_{d0} = \frac{\exp z}{\pi\sqrt{2z}I_0}\left[\sum_{n=0}^{\infty}\sum_{k=0}^{\lfloor\frac{n}{2}\rfloor}\overline{\mathcal{A}}_n(-1)^k\binom{n}{2k}\left(\frac{2}{z(1-e^2)}\right)^k \times\left\{\Gamma\left(\frac{2k+1}{2}\right)+\frac{C_{I1}}{z}\Gamma\left(\frac{2k+3}{2}\right)+\frac{C_{I2}}{z}\Gamma\left(\frac{2k+5}{2}\right)\right\}\right] \tag{8.125}$$

where

$$C_{I1} = -\frac{1}{4(1-e^2)}[(2n-2k-1)+(2n+2k+1)e^2], \tag{8.126}$$

$$\begin{aligned} C_{I2} =& \frac{1}{32(1-e^2)^2}[(4k^2+16k+3)(1-e^2)^2+4n(3e^4+2ke^4 \\ &+8e^2-2k-3)+(1+e^2)^2n^2]. \end{aligned} \tag{8.127}$$

8.5.3 Body-Orbit double Fourier (BODF) model

In developing the theory for the BFF model, the Fourier coefficients were assumed to be constant in the orbit. But since the drag-coefficient is a function of ambient parameters, the body-fixed Fourier coefficients are periodic functions of the eccentric anomaly. This allows the body-fixed Fourier coefficients to be expressed as Fourier series expansions around the eccentric anomaly.

$$\overline{\mathcal{A}}_n(E) = \sum_{m=0}^{\infty}(\overline{\mathbb{A}}_{mn}\cos mE + \overline{\mathbb{B}}_{mn}\sin mE), \tag{8.128}$$

$$\overline{\mathcal{B}}_n(E) = \sum_{m=0}^{\infty}(\overline{\mathbb{C}}_{mn}\cos mE + \overline{\mathbb{D}}_{mn}\sin mE). \tag{8.129}$$

Therefore, the body-orbit double Fourier (BODF) model expressed in terms of eccentric anomaly is,

$$\begin{aligned} C_D = \sum_{m=0}^{\infty}\sum_{n=0}^{\infty}(&\overline{\mathbb{A}}_{mn}\cos mE\cos n\phi + \overline{\mathbb{B}}_{mn}\sin mE\cos n\phi \\ &+\overline{\mathbb{C}}_{mn}\cos mE\sin n\phi + \overline{\mathbb{D}}_{mn}\sin mE\sin n\phi). \end{aligned} \tag{8.130}$$

Since the sinusoidal orbit terms are zero under the assumptions of the theory, the drag coefficient can be simplified to

$$C_D = \sum_{m=0}^{\infty}\sum_{n=0}^{\infty}(\overline{\mathbb{A}}_{mn}\cos mE\cos n\phi + \overline{\mathbb{C}}_{mn}\cos mE\sin n\phi). \tag{8.131}$$

Instead of re-deriving the analytical change for the nadir-pointing and inertially stabilized cases, an approximation is made for the drag-coefficient. The orbit-fixed terms are averaged over the orbit weighted by the density to obtain more accurate body-fixed Fourier coefficients. Therefore, the body-fixed Fourier coefficients can be written as

$$\begin{aligned}\overline{\mathcal{A}}_{n0} &= \frac{\int_0^{2\pi}\rho\overline{\mathcal{A}}_n(E)dE}{\int_0^{2\pi}\rho dE}\\ &= \frac{\int_0^{2\pi}\rho\sum_{m=0}^{\infty}\overline{\mathbb{A}}_{mn}\cos mEdE}{\int_0^{2\pi}\rho dE}\\ &= \frac{\sum_{m=0}^{\infty}\overline{\mathbb{A}}_{mn}I_m}{I_0}.\end{aligned} \tag{8.132}$$

$$\begin{aligned}\overline{\mathcal{B}}_{n0} &= \frac{\int_0^{2\pi}\rho\overline{\mathcal{B}}_n(E)dE}{\int_0^{2\pi}\rho dE}\\ &= \frac{\int_0^{2\pi}\rho\sum_{m=0}^{\infty}\overline{\mathbb{C}}_{mn}\cos mEdE}{\int_0^{2\pi}\rho dE}\\ &= \frac{\sum_{m=0}^{\infty}\overline{\mathbb{C}}_{mn}I_m}{I_0}.\end{aligned} \tag{8.133}$$

The body-fixed Fourier coefficients calculated using Eqs. 8.132 and 8.133 can be used in the theory developed in Section 8.5 for a more accurate computation of the change in the orbital elements.

8.6 Circular orbits

Under the assumptions of this work, the drag-coefficient variation due to ambient parameters is zero at a constant altitude. Therefore, only the zeroth order coefficient remains in the OFF model. The drag-coefficient can still vary due to attitude and therefore, the higher order BFF coefficients are still non-zero. For the nadir pointing profile, $\phi = 0$ and the C_d remains constant. But for the inertially stabilized profile, $\phi = E$. Therefore, the change in semi-major axis can be

written from Eq. 8.15 as

$$\begin{aligned}\Delta a &= -a^2\delta' \int_0^{2\pi} \frac{(1+e\cos E)^{3/2}}{(1-e\cos E)^{1/2}} \sum_{n=0}^{\infty} (\overline{\mathcal{A}}_n \cos nE + \overline{\mathcal{B}}_n \sin nE) \\ &\quad \times \rho dE \\ &= -2\pi a^2 \delta' \rho \overline{\mathcal{A}}_0.\end{aligned} \tag{8.134}$$

since density is constant for a circular orbit. Therefore, the higher-order Fourier coefficients do not contribute to the change in orbital elements for an inertially stabilized profile in a circular orbit.

8.7 Validation results

The theory developed in Sections 8.4 and 8.5 is validated through comparisons with numerical integration of simulated satellite trajectories. The satellite orbits are simulated under the assumptions of the King-Hele theory. Only the two-body and atmospheric drag forces are considered in the dynamics. A spherically symmetric and exponentially decaying atmosphere is assumed with a constant scale height. For the OFF model, a spherical satellite is considered such that there are no variations in the attitude. For the BFF model, non-spherical satellites are considered with the only variations considered in the drag-coefficient being due to attitude, unless stated otherwise. The drag-coefficients are modeled using the diffuse reflection incomplete accommodation (DRIA) model that linearly combines drag-coefficients based on clean surfaces and satellite surfaces completely covered by atomic oxygen [131]. Note that the model is not valid for altitudes greater than 500 km. Since the variation of drag-coefficient is not well understood for higher altitudes, the DRIA model is used for all altitudes. With future developments in drag-coefficient modeling for higher altitudes, a different model can be used in the current framework with no changes to the developed theory. All ambient parameters are modeled using NRLMSISE-00 [93] as the atmospheric model. The qualitative results are independent of the specific attributes of the atmosphere and the satellite surface; therefore, the details have been left out. The errors between the analytically and numerically computed changes in semi-major axis and focal length are compared for the Fourier theory and the original King-Hele theory with three constant drag-coefficients - the zeroth-order

Fourier coefficient, the drag-coefficient evaluated at perigee and the derived density-averaged drag-coefficient, summarized in Table 8.1. The orbital elements and satellite parameters in Table 8.2 remain constant for all the cases.

Table 8.1: Nomenclature for the graphical results

Case	**Description**
Fourier C_d	Full Fourier theory developed here
KH: Averaged C_d	Original King-Hele formulation with derived density-averaged C_d
KH: Perigee C_d	Original King-Hele formulation with C_d evaluated at perigee
KH: Order 0 C_d	Original King-Hele formulation with zeroth order Fourier coefficient

Table 8.2: Simulation parameters common for all the cases

Parameter		Value
Orbital elements	i_0	65°
	Ω_0	60°
	ω_0	40°
Satellite parameters	m	500 kg
	S	10 m^2

8.7.1 Test cases for OFF model

A spherical satellite with perigee at 300 km and apogee at 500 km and 7000 km for low and high eccentricity regimes respectively is considered for the OFF theory. The density parameters at the perigee for both cases are $\rho_{p0} = 1.9417e-11$ kg/m^3 and $H = 49.23$ km corresponding to a mean solar activity level ($F_{10.7} = 150$ s.f.u). The drag coefficient for the low and high eccentricity cases along with the Fourier coefficients are plotted in Fig. 8.1. The Fourier series approximates the drag-coefficient at lower eccentricities more accurately than at higher eccentricities and the Fourier coefficients decrease more rapidly for higher orders in the former. In the high eccentricity case, the drag-coefficient from $E = 40°$ to $E = 320°$ does not affect the orbit since the altitude

within that range is greater than 1000 km. For order 10, the number of coefficients evaluate to 11 for the OFF model.

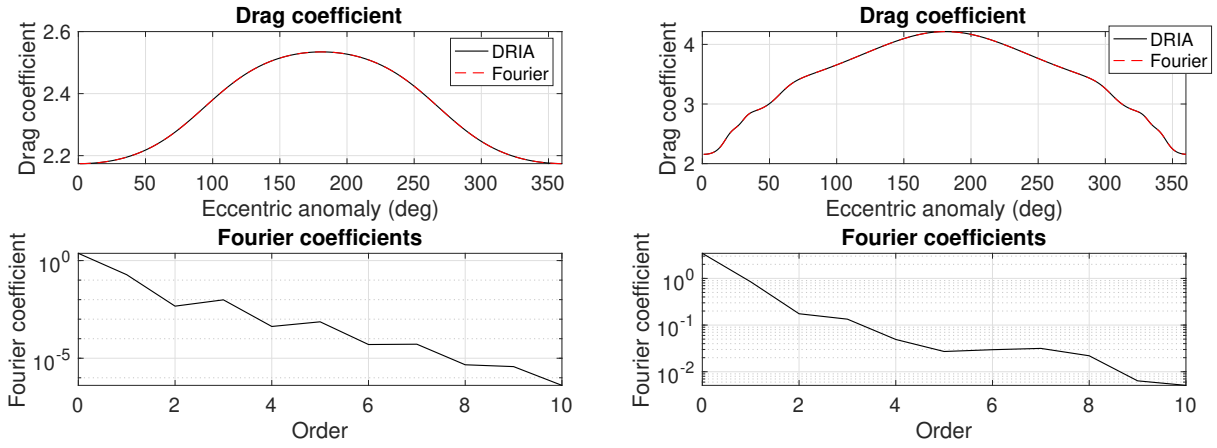

Figure 8.1: Diffuse reflection incomplete accommodation (DRIA) modeled drag-coefficient and Fourier coefficients for the OFF model in the (a) low eccentricity regime; (b) high eccentricity regime.

Time-profiles of the errors in the analytically computed change in semi-major axis and focal-length compared to the numerical results are plotted in Fig. 8.2 for low and high eccentricities. The figures depict errors for the Fourier theory as well as the original King-Hele theory with three constant drag-coefficients. The error for the order 0 drag-coefficient is plotted separately as it is much larger than the other errors. It can be seen that the results of the full Fourier theory and the derived average drag-coefficient are similar though the full Fourier theory gives a more accurate focal-length change in the low eccentricity regime. They both perform an order of magnitude better than the perigee C_d.

The relative errors in the analytical semi-major axis and focal-length over a single orbital period are computed for a grid of perigee and apogee heights with a constraint of $0.01 < e < 0.15$ in the low eccentricity regime and $0.25 < e < 0.75$ in the high eccentricity regime to avoid truncation errors. The errors are plotted in Fig. 8.3 and 8.4 for low and high eccentricity regimes respectively. The performances of the full Fourier theory and the original King-Hele formulation with the derived

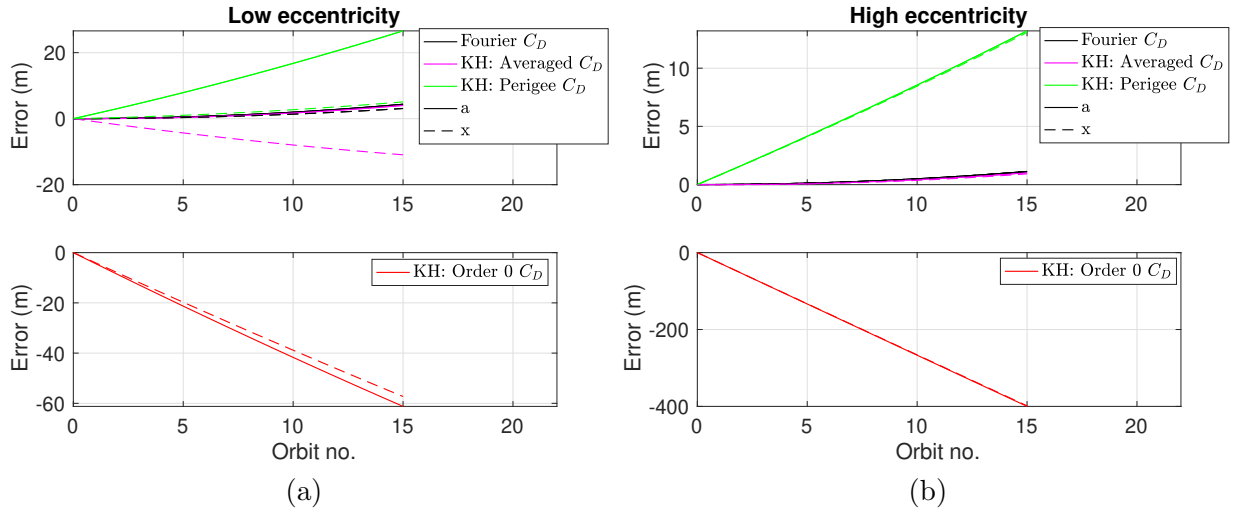

Figure 8.2: Error between analytical and numerical changes in semi-major axis and focal length for the the OFF model and the original King-Hele (KH) theory with three constant drag-coefficients (density-averaged, perigee and order 0 Fourier) in (a) low eccentricity regime and (b) high eccentricity regime

average C_d are similar to each other except for focal-length for low eccentricity regime. The relative errors are largest for high perigees and apogees since the change in the orbital elements over an orbital period is very small at such high altitudes. The relative errors for perigee C_d and order 0 C_d are worse throughout the grid.

8.7.2 Test cases for the BFF model

To validate the BFF model, a symmetric cubical satellite with equal properties for all the six surfaces is considered with the perigee and apogee altitudes same as the previous case. The drag coefficients for the nadir-pointing and inertially stabilized cases are plotted in Fig. 8.5. The variation in the drag-coefficient for the nadir-pointing case is very small for the low eccentricity regime since the flight-path angle is very small. On the other hand, the drag-coefficients for the inertial case are similar for both eccentricity regimes since ϕ undergoes a complete rotation. For a symmetric cubical satellite, only the cosine Fourier coefficients with orders that are multiples of four are non-zero. All the sine Fourier coefficients are zero due to symmetry. For the order 20 BFF model, the number of coefficients are 6 in this case.

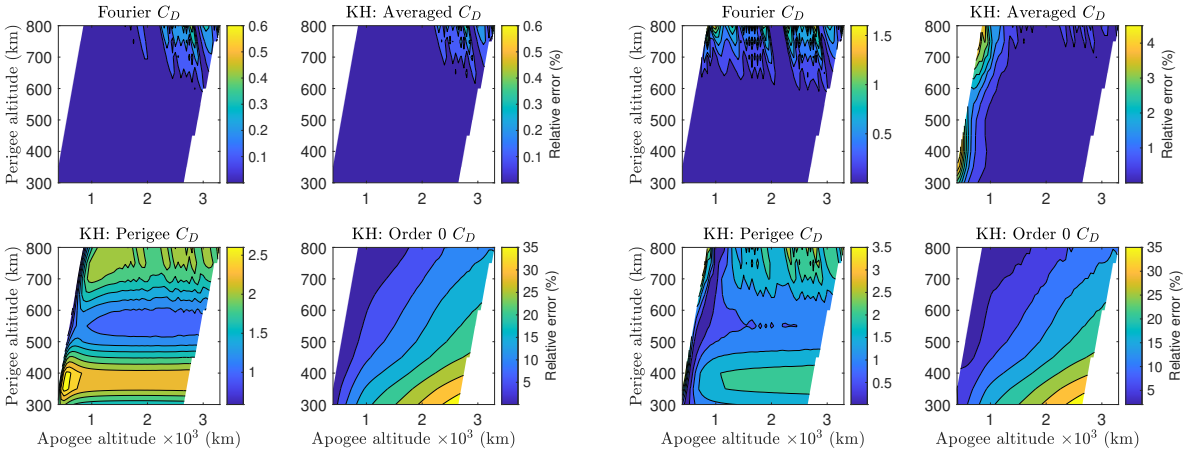

(a) (b)

Figure 8.3: Relative error in analytically computed change in (a) semi-major axis and (b) focal length compared to numerical results for OFF model and original King-Hele (KH) theory with three constant drag-coefficients (density-averaged, perigee and order 0 Fourier) in low eccentricity regime

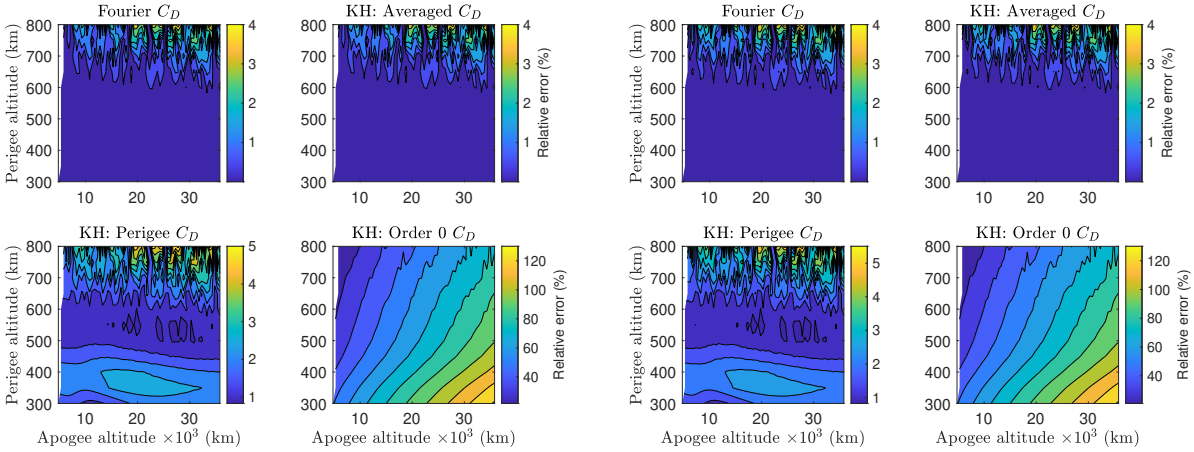

(a) (b)

Figure 8.4: Relative error in analytically computed change in (a) semi-major axis and (b) focal length compared to numerical results for OFF model and original King-Hele (KH) theory with three constant drag-coefficients (density-averaged, perigee and order 0 Fourier) in high eccentricity regime

The errors between the Fourier theory and the numerical results are compared with the original formulation with the three constant drag-coefficients in Fig. 8.6 for low and high eccentricities. The averaged C_d and the full Fourier theory have similar errors in the both the eccentricity regimes.

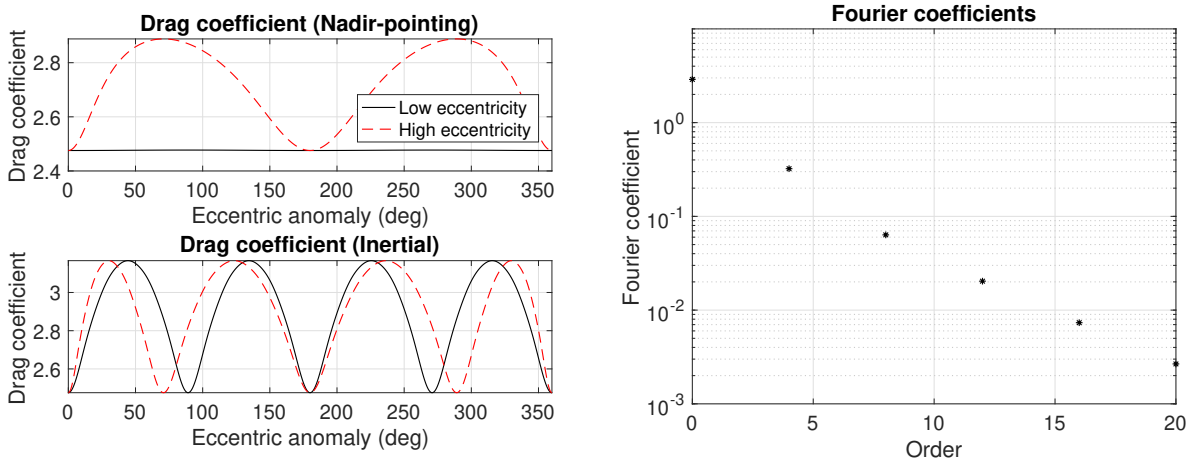

(a) (b)

Figure 8.5: Diffuse reflection incomplete accommodation (DRIA) modeled drag-coefficients for the BFF model in the nadir pointing and inertially stabilized cases; (b) Fourier coefficients for the BFF model.

This is also demonstrated by relative errors over a grid of perigee and apogee altitudes in Figs. 8.7 and 8.8. It should be noted that the variation of drag-coefficients is very small for a nadir-pointing profile as seen in Fig. 8.5. In the high eccentricity regime, most of the variation is in higher altitudes, which has a negligible contribution to the orbit. Therefore, the averaged and full King-Hele theory are expected to perform similarly.

For the inertially stabilized case, the averaged C_d performs better than the full Fourier theory for the particular perigee and apogee heights considered as shown in Fig. 8.9. Over a grid of perigee and apogee altitudes, the full Fourier theory has a larger variation of relative errors in Figs. 8.10 and 8.11. But overall, it performs better than the averaged drag-coefficient; the errors for the full theory are smaller for 65.7 % cases of the grid for semi-major axis and 77 % cases for focal-length in the low eccentricity regime.

To test the theory for the argument of perigee change, an asymmetrical satellite is considered with non-zero $\overline{\mathcal{B}}_n$. The satellite is considered to be of half-trapezoidal shape with one face inclined at 45°. All the six surfaces are considered to have different material properties such that the satellite is asymmetric in the body frame. An order 30 BFF model is considered in this case with

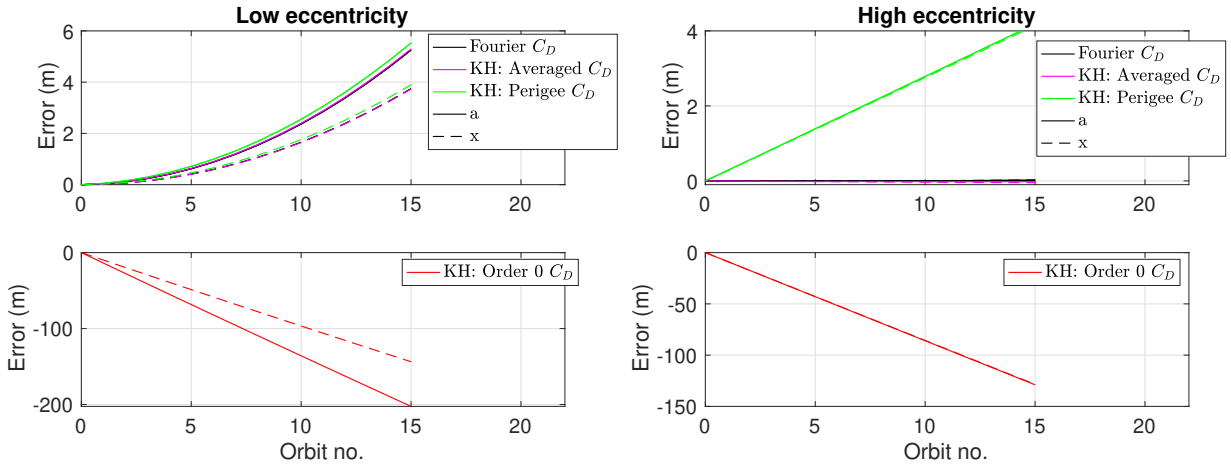

Figure 8.6: Error between analytical and numerical changes in semi-major axis and focal length for the the BFF model and the original King-Hele (KH) theory with three constant drag-coefficients (density-averaged, perigee and order 0 Fourier) in (a) low eccentricity regime and (b) high eccentricity regime for a nadir-pointing satellite

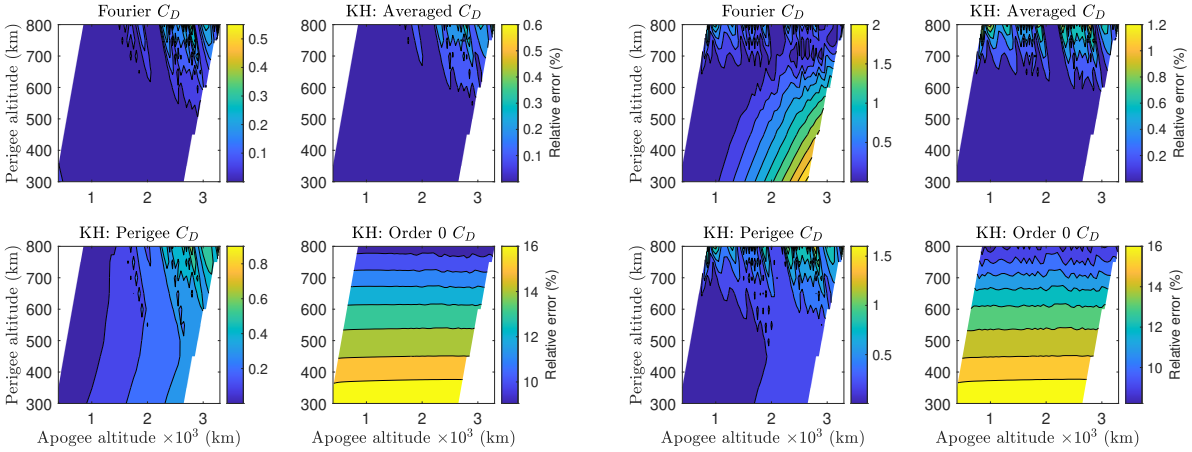

Figure 8.7: Relative error in analytically computed change in (a) semi-major axis and (b) focal length compared to numerical results for BFF model and original King-Hele (KH) theory with three constant drag-coefficients (density-averaged, perigee and order 0 Fourier) in low eccentricity regime for a nadir pointing profile

54 non-zero coefficients. It should be noted that the magnitude of the coefficients decrease rapidly with higher-orders and therefore many of the 54 coefficients can be ignored for most applications. The semi-major axis, focal-length and argument of perigee errors for low eccentricity regime are

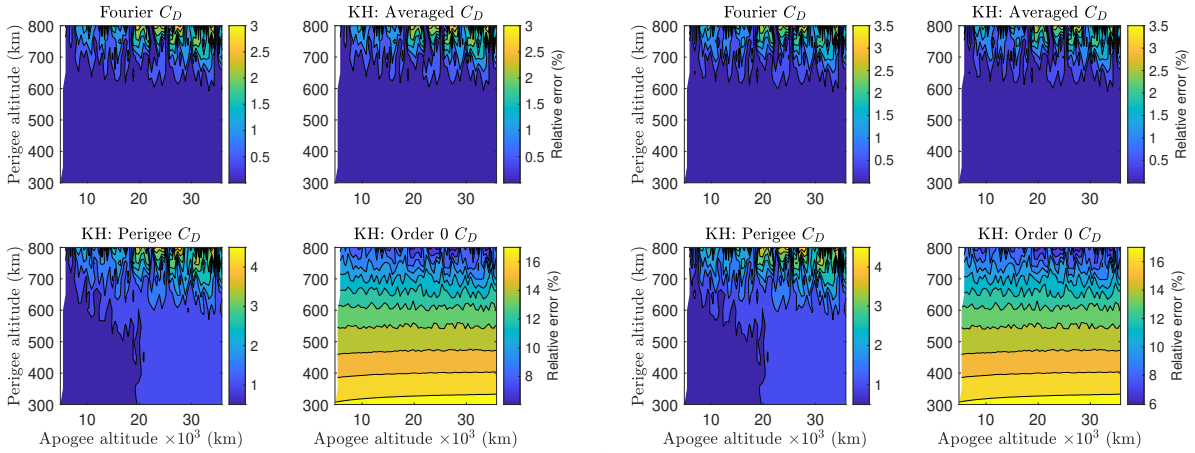

(a) (b)

Figure 8.8: Relative error in analytically computed change in (a) semi-major axis and (b) focal length compared to numerical results for BFF model and original King-Hele (KH) theory with three constant drag-coefficients (density-averaged, perigee and order 0 Fourier) in high eccentricity regime for a nadir-pointing profile

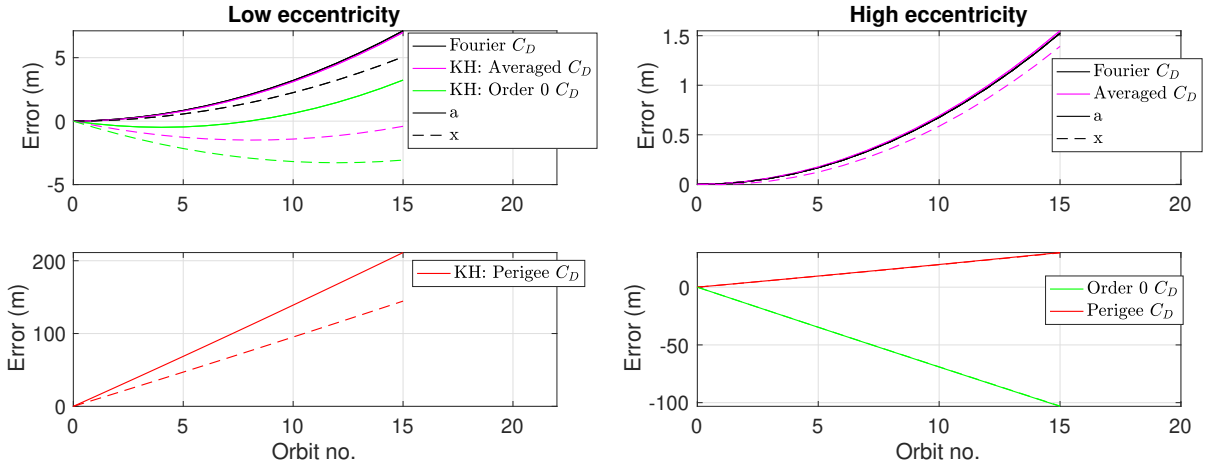

(a) (b)

Figure 8.9: Error between analytical and numerical changes in semi-major axis and focal length for the the BFF model and the original King-Hele (KH) theory with three constant drag-coefficients (density-averaged, perigee and order 0 Fourier) in (a) low eccentricity regime and (b) high eccentricity regime for an inertially stabilized satellite

plotted in Fig. 8.12. The full Fourier theory performs better than the averaged drag-coefficient for 95 % of the cases for semi-major axis but for 41 % of the cases for focal-length. For a constant drag-coefficient, the argument of perigee change is zero. Therefore, 100 % relative errors are obtained

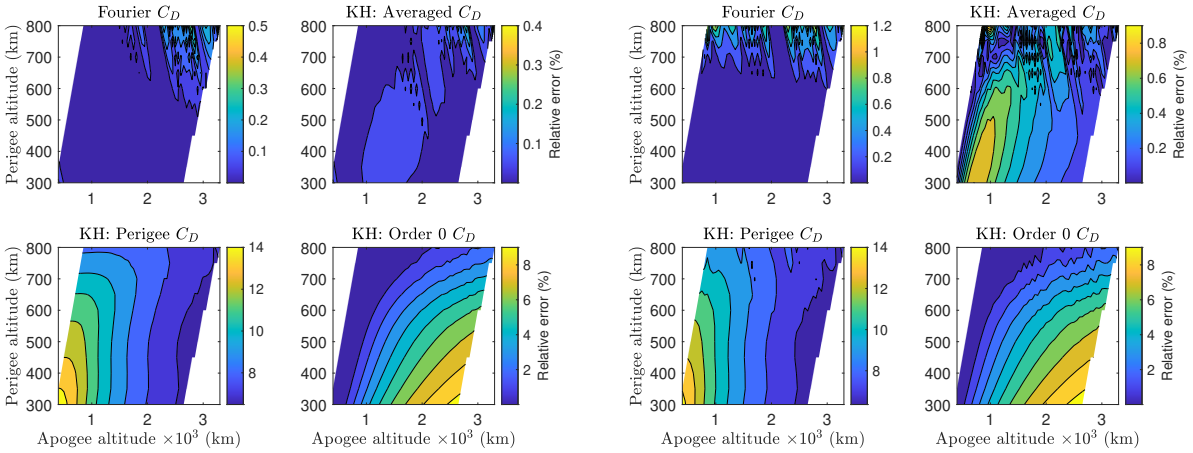

(a) (b)

Figure 8.10: Relative error in analytically computed change in (a) semi-major axis and (b) focal length compared to numerical results for BFF model and original King-Hele (KH) theory with three constant drag-coefficients (density-averaged, perigee and order 0 Fourier) in low eccentricity regime for an inertially stabilized profile

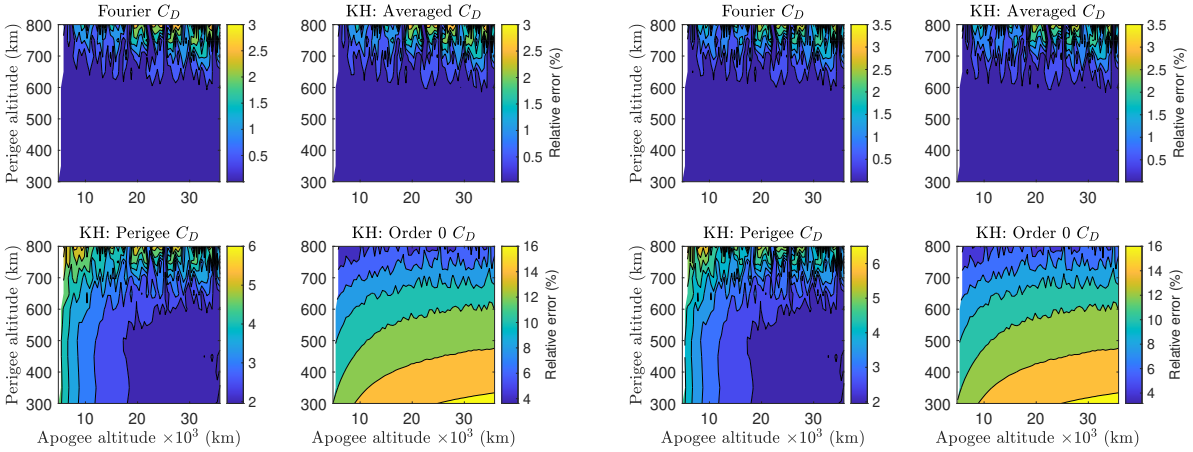

(a) (b)

Figure 8.11: Relative error in analytically computed change in (a) semi-major axis and (b) focal length compared to numerical results for BFF model in and original King-Hele (KH) theory with three constant drag-coefficients (density-averaged, perigee and order 0 Fourier) in high eccentricity regime for an inertially stabilized profile

with the original King-Hele formulation. With the full Fourier theory, the errors are less than 100 % for around 61 % of the cases. The results are not shown for high-eccentricity regime because the change in argument of perigee over an orbit is negligible.

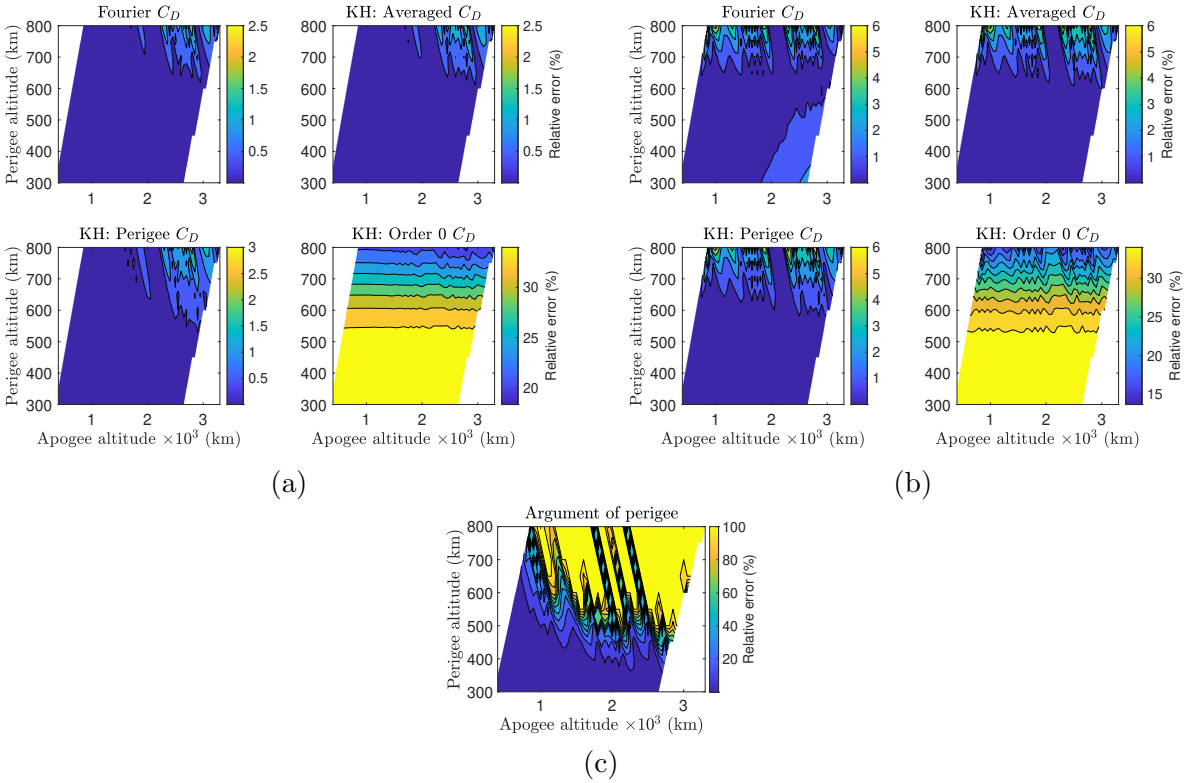

Figure 8.12: Relative error in analytically computed change in (a) semi-major axis, (b) focal length and (c) argument of perigee compared to numerical results for BFF model in and original King-Hele (KH) theory with three constant drag-coefficients (density-averaged, perigee and order 0 Fourier) in low eccentricity regime for a nadir-pointing asymmetrical satellite

The inertially stabilized case is more interesting since the argument of perigee change is larger in this case due to larger variations in the drag-coefficient. The errors in the orbital elements are plotted in Fig. 8.13. It is evident that the full Fourier theory performs better than the averaged drag-coefficient for all the orbital elements. Similar to the nadir-pointing case, the argument of perigee variation is negligible in the high-eccentricity regime and therefore, the results have not been shown here.

8.7.3 Test cases for the BODF model

The asymmetrical satellite introduced for the BFF model is utilized to validate the BODF model. Each of the 54 non-zero BFF coefficients are expanded in the orbit frame to order 10

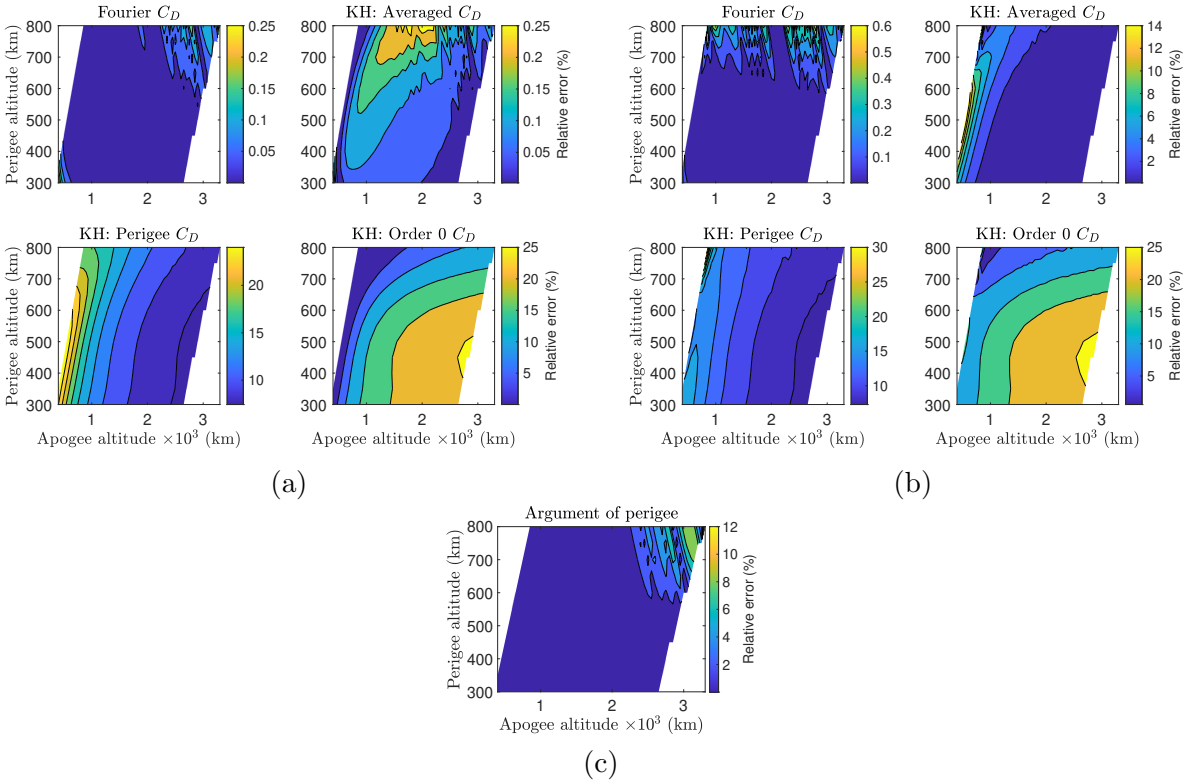

Figure 8.13: Relative error in analytically computed change in (a) semi-major axis, (b) focal length and (c) argument of perigee compared to numerical results for BFF model in and original King-Hele (KH) theory with three constant drag-coefficients (density-averaged, perigee and order 0 Fourier) in low eccentricity regime for an inertially stabilized asymmetrical satellite

and then averaged. Therefore, the number of coefficients used in the derived theory remain 54. The results of BODF are compared with BFF for which the Fourier coefficients are evaluated at perigee. Figs. 8.14 and 8.15 plot the relative errors for the BODF model compared to BFF model and constant drag-coefficients for low and high eccentricity regimes. The argument of perigee errors are calculated only for the BODF model. It can be seen that in both cases, BODF has the highest accuracy in maximum areas of the grid, followed by the averaged drag-coefficient except for focal length in low eccentricity regime. Simply averaging the BFF coefficients weighted by density over the orbit can improve the prediction performance over a constant set of BFF coefficients evaluated at perigee.

The simulation results for BFF, OFF and BODF models clearly demonstrate that capturing

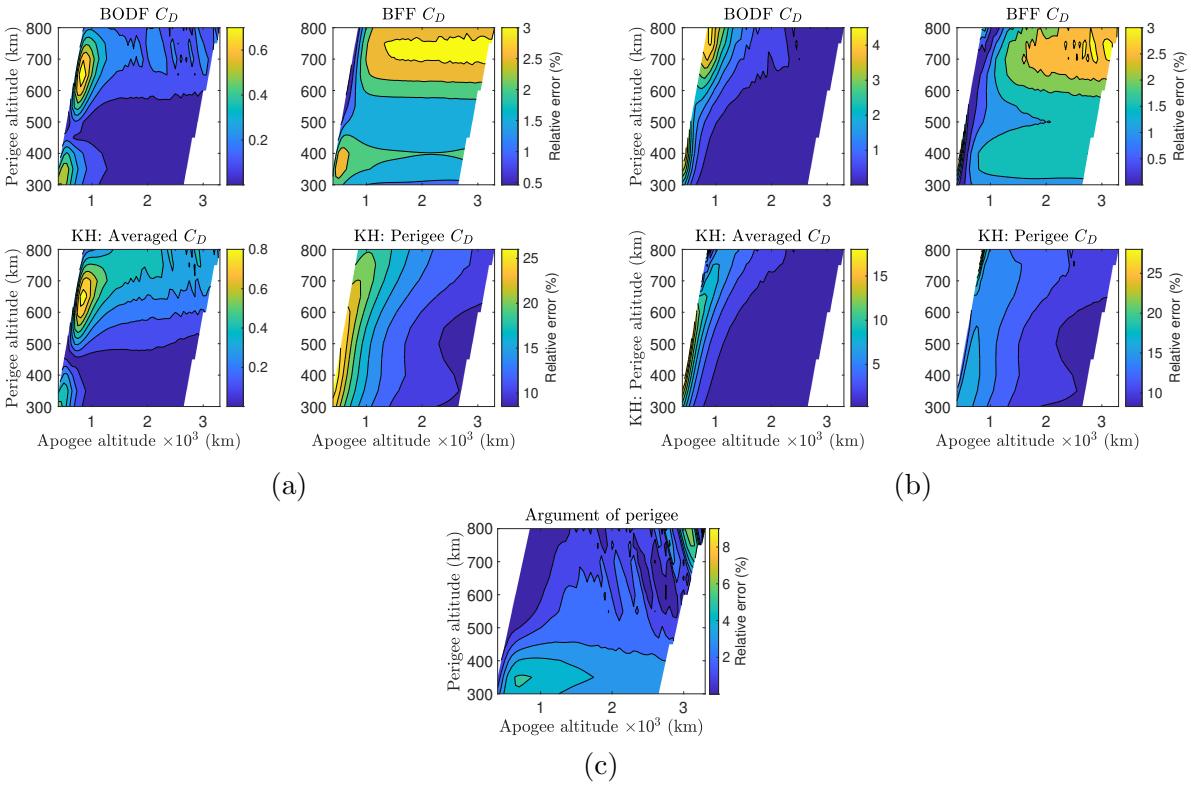

Figure 8.14: Relative error in analytically computed change in (a) semi-major axis, (b) focal length and (c) argument of perigee compared to numerical results for BODF model, BFF model with coefficients evaluated at perigee and and original King-Hele (KH) theory with two constant drag-coefficients (density-averaged and perigee) in low eccentricity regime for an inertially stabilized profile

the periodic variation of the drag-coefficient in orbit can lead to improvements in predicting the evolution of the orbital elements. For many of the cases, the density-averaged drag-coefficient derived from the full Fourier theory is as accurate as the full Fourier theory. Therefore, if using the original King-Hele theory, the density-averaged drag-coefficients derived in Eqs. 8.37, 8.71 and 8.110 should be used depending on the case. Most of the differences observed between the full Fourier theory and the averaged drag-coefficient are due to the possible loss of fidelity during the drag-coefficient averaging process. If the averaging was carried out using Eq. 8.35, the results for the focal length would have been very close to the full Fourier theory for all cases. Similarly, if the averaging had been carried out using Eq. 8.34, the results for semi-major axis would have been similar to the full Fourier theory. Instead, the averaging is carried out using Eq. 8.36, i.e.,

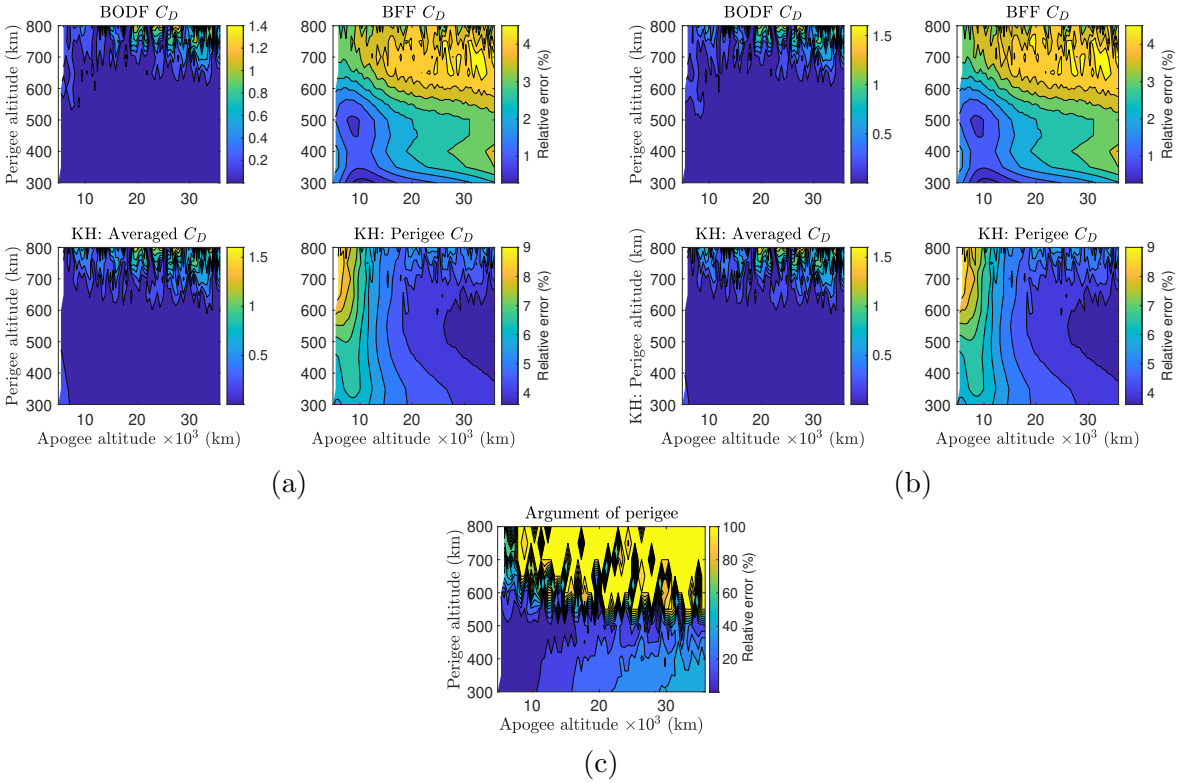

Figure 8.15: Relative error in analytically computed change in (a) semi-major axis, (b) focal length and and (c) argument of perigee compared to numerical results for BODF model, BFF model with coefficients evaluated at perigee and and original King-Hele (KH) theory with two constant drag-coefficients (density-averaged and perigee) in high eccentricity regime for an inertially stabilized profile

considering only the density in the analytical formula, which makes the most physical sense and is the middle ground approach between the above two.

It should be noted that for periodic attitude profiles, such as the cases considered here, the drag-coefficient variation due to both ambient parameters and attitude can be captured using OFF model. But the theory developed here considers the BFF model separately since the BFF coefficients are physically different from OFF coefficients and are fixed to the body-frame. Therefore, they don't have to be evaluated for different orbital parameters unlike the OFF coefficients.

8.8 Chapter summary

This chapter addresses the problem with a constant drag-coefficient in the King-Hele theory and derives a modified theory with a time-varying drag-coefficient. Under the assumptions of the original King-Hele formulation for a symmetric exponentially decaying atmosphere with a constant scale height, the drag-coefficient dependence on ambient parameters is periodic and can be expressed as a Fourier series in the orbit-fixed frame. Similarly, the variation of the drag-coefficient with orientation of the velocity vector in the body frame can be captured using a Fourier series expansion in the body-frame. Using these two models, the King-Hele theory is extended to include the variation of drag-coefficient in the averaging equations. An approximate framework is provided to capture the dependence of the drag-coefficient on both body and orbit dependent factors. In the original King-Hele theory and subsequent modifications, the constant drag-coefficient that should be used is not explicitly stated since the variation of drag-coefficient is not considered. This paper provides an analytical formula for the constant drag-coefficient that approximates the full Fourier theory most accurately. The developed theory predicts secular changes in the argument of perigee for an asymmetrical satellite with periodic attitude variations whereas the original King-Hele formulation states the change to be zero under the assumptions of the theory. The simulation results for the body-fixed Fourier (BFF), orbit-fixed Fourier (OFF) and body-orbit double Fourier (BODF) models demonstrate that the predictions of orbital element evolution can be improved by allowing the drag-coefficient to vary in the averaging integrals. The improvements can be orders of magnitude depending on the constant drag-coefficient being used. This development can lead to improvements in estimation of orbital lifetimes and derivation of densities from orbit decay data. The theory developed for OFF model can be used for satellites with no variations in attitude or whose attitude profiles are unknown. The BFF model with the Fourier coefficients averaged in the orbit can be used for a general case with a known attitude profile.

Chapter 9

Conclusions and future work

In this dissertation, we developed a new approach to modeling the atmospheric drag effects on the orbit of a LEO satellite. The drag force is the largest source of uncertainty in the orbit determination and prediction of LEO satellites, primarily due to modeling errors in the drag parameters - density and drag-coefficient. The drag-coefficient is most commonly estimated as a constant in the orbit determination, which not only averages out the time-variations in the parameter but also absorbs errors in the density model. Physical models of the drag-coefficient allow a time-varying representation of the drag-coefficient, rooted in the physics of gas-surface interactions but unfortunately suffer from a gap in knowledge of the input parameters that feed into them. Therefore, any atmospheric densities that are derived from satellite tracking data will absorb biases in the drag-coefficients used in the inversion process. These orbit-derived densities then feed into the calibration of climatological models, that are used in the investigations of Earth's atmospheric evolution. The densities also play an important role in calibrating semi-empirical atmospheric models that are used in operational orbit determination. Therefore, errors in the drag-coefficient feed into the density which further affects drag-coefficient estimates. This work proposes a method to break out of this circular problem by utilizing the time-variations in the drag-coefficient induced by attitude and orbital motion. We develop Fourier series expansion-based models to estimate the higher-order frequencies in the drag-coefficient that are functions of ambient parameters and satellite-dependent factors. This allows the complex physics of the gas-surface interactions to be condensed into the observable Fourier coefficients that can be corrected during orbit determination

using satellite tracking data.

This work is focused on improving the state-of-the-art of the atmospheric drag model for orbit determination and prediction among other applications. In addition to the dynamical errors introduced due to uncertainties in non-conservative force parameters, arbitrary truncation of the geopotential without a careful consideration of the resulting aliasing effects into parameter estimates can be detrimental to orbit prediction accuracy. Aliasing effects can mask any improvements in modeling of non-conservative forces by rendering the estimates of force parameters non-physical in the orbit determination process. The contribution of this work is in quantifying the aliasing effects on the drag-coefficient and the solar radiation pressure coefficient across orbital altitudes and studying their sensitivity to various factors such as space weather activity, orbital inclination and length of data-arc. The aliasing effects are analyzed using real POD from GRACE satellite and it is observed that estimating non-gravitational coefficients with a low order geopotential can be worse than simply using nominal modeled values.

The primary contribution of this work is the development of the estimation-based drag-coefficient models by carrying out Fourier series expansions of nominally chosen GSIMs in the body and orbit frames of the satellite. The estimated Fourier coefficients provide a more accurate representation of the drag-coefficient by capturing higher-order time variations in the drag-coefficient. The most obvious application of this development is in improving orbit determination and prediction of satellites. We demonstrate improved orbit predictions over the standard constant drag-coefficient estimate by around 50 % with real data.

The Fourier coefficients can be used to provide insights into the physics of the gas-surface interactions since they contain information on the GSIM parameters. The coefficients of each order have an explicit functional relationship with different GSIM parameters as represented by the Fourier integrals. This work derives analytical closed-form solutions of the body-fixed Fourier coefficients for the Diffuse Reflection Incomplete Accommodation (DRIA) model. This allows a way to calculate the subset of the Fourier coefficients that are dependent on a particular GSIM parameter. We develop a method to invert GSIM parameters with large uncertainties from the Fourier coeffi-

cient estimates; thus providing a better constraint on the GSIM. A thorough observability analysis is carried out using multiple metrics to determine which Fourier coefficients can be estimated from tracking data. For all the Fourier models and different satellite shapes, only a few coefficients need to be estimated and some higher order coefficients need to be modeled.

One of the primary goals of this work is provide a way to estimate atmospheric densities that are unbiased by the drag-coefficient. Leveraging the Fourier drag-coefficient models and the framework to invert GSIM parameters from the Fourier coefficient estimates, an algorithm is developed to simultaneously estimate local atmospheric densities along the orbit and the time-varying drag-coefficient for satellites with attitude variations. We demonstrate significant improvements in the estimated densities over the nominal density model used in the filter with simulated and real tracking data. In particular, an improvement of around 29 % is obtained in the filter density estimates over NRLMSISE-00 w.r.t the High Accuracy Satellite Drag Model (HASDM) densities for Spire satellite POD and 49 % over JB2008. This methods provides a practical approach to decorrelate density and drag-coefficient biases and can be easily implemented in operational use.

Finally, the simple representation of the complex physics of gas-surface interactions using empirical parameters lends the developed Fourier drag-coefficient models very well for analytical theories of orbital motion in an atmosphere. All previous analytical formulations have assumed a constant drag-coefficient in their derivations. We re-derive the original King-Hele theory with a time-varying representation of the drag-coefficient using our Fourier models. We demonstrate improvements in prediction of orbital elements with our modification, especially proving that the argument of perigee undergoes secular changes for satellites with planes of asymmetry whereas the original theory derives the change to be zero. The developed theory can be used for applications such as preliminary mission analyses and deriving densities using TLE data.

The methods developed in this work can be further improved for implementation in operational use. A direct application of the study on aliasing effects is the quantification of these effects for the special perturbations catalog that uses a 36×36 geopotential which we show to be inadequate when estimating nongravitational force coefficients. In this work, we inverted the fractional

coverage parameter and velocity ratio from the Fourier coefficient estimates to better constrain the DRIA model. The set of GSIM parameters that are the primary contributors to the drag-coefficient uncertainty and can be estimated from the Fourier coefficients needs to be identified. Additionally, other GSIMs with different scattering dynamics and energy/momentum transfer parameters should be investigated since the drag-coefficient variation can vary significantly between different GSIMs. In particular, it needs to be analyzed whether any particular GSIM lends itself better to the framework of simultaneous density and drag-coefficient estimation. As observed in one of the simulated cases in chapter 7, the density estimates are highly dependent on the tuning parameters, especially the noise levels in the GMP process. It was shown that modifying the noise levels between iterations may prove to be useful during times of higher geomagnetic activity. The particular tuning parameters that should be used in the method should be analyzed. Machine-learning methods can be applied to train the tuning parameters of the Gauss Markov process over varying satellite orbits and atmospheric conditions using the SET HASDM database. Techniques such as adaptive DMC can be used to dynamically change the noise levels during the filtering process. The validation of the method done using Spire POD as measurements might introduce errors due to violation of the uncorrelated white noise assumption in the Kalman filter. In future work, datasets with raw GPS measurements should be utilized for validation of the method. The analytical theory developed in this paper is independent of the underlying physical model for the drag-coefficient being used. Therefore, future developments in drag-coefficient modeling can be used to improve estimates of the Fourier coefficients, especially at higher altitudes, that can be then used in this theory to increase fidelity of orbital element predictions. Moreover, the theory can be easily supplemented with other modifications developed in literature such as extensions to accommodate generic atmospheric density models and adapting the theory to non-singular elements, to provide a complete analytical theory for a satellite in an atmosphere. Additionally, the averaged equations for OFF and BFF models can be used in semi-analytical theories of satellite orbit propagation by considering the slow variation of the Fourier coefficients due to their dependence on the semi-major axis and eccentricity that will be addressed in future work.

Bibliography

[1] A. Albertella, F. Migliaccio, and F. Sansó. The Aliasing Effect in Coefficients Estimation. In R.H. Rapp, F. Sansò (eds) Determination of the Geoid. International Association of Geodesy Symposia, volume 106, pages 10–15. Springer, 1991.

[2] Salvatore Alfano, Daniel Oltrogge, Holger Krag, Klaus Merz, and Robert Hall. Risk assessment of recent high-interest conjunctions. Acta Astronautica, 184:241–250, 2021.

[3] Yaakov Bar-Shalom, X.-Rong Li, and Thiagalingam Kirubarajan. Estimation with Applications to Tracking and Navigation, chapter 5.6. Wiley-Interscience Publication, 2001.

[4] W.N. Barker, W.J. Casali, and R.N. Wallner. Earth gravitational error budget for space control. Advances in the Astronautical Sciences, 93:351–370, 1996. Proceedings of AAS/AIAA Spaceflight Mechanics Meeting, Austing, TX, February 12-15, 1996.

[5] G.A. Bird. Molecular Gas Dynamics and Direct Simulation of Gas Flows. Clarendon Press, 1994.

[6] Bruce R. Bowman, Kent W. Tobiska, Frank A. Marcos, Cheryl Y. Huang, Chin S. Lin, and William J. Burke. A New Empirical Thermospheric Density Model JB2008 Using New Solar and Geomagnetic Indices . AIAA/AAS Astrodynamics Specialist Conference, 2008.

[7] Sean Bruinsma. The DTM-2013 Thermosphere Model. Journal of Space Weather and Space Climate, 5(A1), 2015.

[8] Sean Bruinsma. The DTM-2013 thermosphere model. Journal of Space Weather and Space Climate, 5(22), 2015.

[9] Sean Bruinsma, Claude Boniface, Eric K. Sutton, and Mariangel Fedrizzi. Thermosphere modeling capabilities assessment: geomagnetic storms. Journal of Space Weather and Space Climate, 11(12), 2021.

[10] Roland Brun, Peter Reichert, and R. Hans Künsch. Practical identifiability analysis of large environmental simulation models. Water Resources Research, 37(4):1015–1030, 2001.

[11] C.J. Capon, B. Smith, M. Brown, R. Abay, and R.R. Boyce. Effect of ionospheric drag on atmospheric density estimation and orbit prediction. Advances in Space Research, 63(8):2495–2505, 2019.

[12] C.C. Chao, G.R. Gunning, K. Moe, S.H. Chastain, and T.J. Setteceri. An Evaluation of Jacchia 71 and MSIS 90 Atmosphere Models with NASA ODERACS Decay Data. Journal of the Astronautical Sciences, 45(2):131–142, 1997.

[13] Qiujie Chen, Yunzhong Shen, Olivier Francis, Wu Chen, Xingfu Zhang, and Houze Hsu. Tongji-Grace02s and Tongji-Grace02k: High-Precision Static GRACE-Only Global Earth's Gravity Field Models Derived by Refined Data Processing Strategies. Journal of Geophysical Research: Solid Earth, 123:6111–6137, 2018.

[14] Z. Chen. Local observability and its application to multiple measurement estimation. IEEE Trans. Ind. Electron., 38(6):491–496, 1991.

[15] Minkang Cheng, John C. Ries, and Byron D. Tapley. Assessment of the solar radiation model for GRACE orbit determination. Advances in the Astronautical Sciences, 129:501–510, 2008.

[16] Yunfei Chu and Juergen Hahn. Generalization of a Parameter Set Selection Procedure Based on Orthogonal Projections and the D-Optimality Criterion. Process Systems Engineering, 58(7):2085–2096, 2012.

[17] Paul G. Constantine and Eric Dow. Dynamic Model Compensation for Near-Earth Satellite Orbit Determination. AIAA Journal, 13(3):343–349, 1975.

[18] Paul G. Constantine and Eric Dow. Active subspace methods in theory and practice: applications to kriging surfaces. SIAM Journal on Scientific Computing, 36(4):A1500–A1524, 2014.

[19] G.E. Cook. Satellite Drag Coefficients. Planetary and Space Science, 13(10):929–946, 1965.

[20] National Research Council. Solar and Space Physics: A Science for a Technological Society. The National Academies Press, Washington D.C., 2013.

[21] Leland E. Cunningham. On the computation of the spherical harmonic terms needed during the numerical integration of the orbital motion of an artificial satellite. Celestial Mechanics, 2:207–216, 1970.

[22] George Dakermanji, Micheal Burns, and Leonine Lee. The Global Precipitation Measurement (GPM) Spacecraft Power System Design and Orbital Performance . 11th European Space Power Conference 2016, 2016.

[23] Silvia Daun, Jonathan Rubin, Yoram Vodovotz, Anirban Roy, Robert Parker, and Gilles Clermont. An ensemble of models of the acute inflammatory response to bacterial lipopolysaccharide in rats: Results from parameter space reduction. Journal of Theoretical Biology, 253:843–853, 2008.

[24] BL Decker. World Geodetic System 1984. Technical report, Defense Mapping Agency, April 1986.

[25] Eelco Doornbos. Thermospheric Density and Wind Determination from Satellite Dynamics. PhD thesis, Delft University of Technology, 2011.

[26] Eelco Doornbos, Sean Bruinsma, B. Fritsche, G. Koppenwallner, P. Visser, J. Van Den IJssel, and J. de Teixeira de Encarnação. Air Density and Wind Retrieval Using GOCE Data – Final Report. ESA contract 4000102847/NL/EL, GOCE+ Theme 3, TU Delft, 2014.

[27] Douglas P. Drob, John T. Emmert, John W. Meriwether, Makela J. Jonathan, Eelco Doornbos, Mark Conde, Gonzalo Hernandez, John Noto, Katherine A. Zawdie, Sarah E. McDonald, Joe D. Huba, and Jeff H. Klenzing. An update to the Horizontal Wind Model (HWM): The quiet time thermosphere. Earth and Space Science, 2(7):301–319, 2015.

[28] D.P. Drob, J.T. Emmert, G. Crowley, J.M. Picone, G.G. Shepherd, W. Skinner, P. Hays, R.J. Niciejewski, M. Larsen, C.Y. She, J.W. Meriwether, G. Hernandez, M.J. Jarvis, D.P. Sipler, C.A. Tepley, M.S. O'Brien, J.R. Bowman, Q. Wu, Y. Murayama, S. Kawamura, I.M. Reid, and R.A. Vincent. An empirical model of the Earth's horizontal wind fields: HWM07. Journal of Geophysical Research, 113, 2008.

[29] J.T. Emmert. Thermospheric Mass Density: A Review . Advances in Space Research, 56:773–824, 2015.

[30] J.T. Emmert, J.M. Picone, J.L. Lean, and S.H. Knowles. Global change in the thermosphere: Compelling evidence of a secular decrease in density. Journal of Geophysical Research, 109(A2), 2004.

[31] Elena Fantino, Roberto Flores, and Amna Adheem. Accurate and Efficient Propagation of Satellite Orbits in the Terrestrial Gravity Field. In Proceedings of the 70th International Astronautical Congress (IAC), 2019.

[32] William M. Folkner, James G. Williams, Dale H. Boggs, Ryan S. Parks, and Petr Kuchynka. The Planetary and Lunar Ephemerides DE430 and DE431. IPN progress report, Jet Propulsion Laboratory, February 2014.

[33] L. Fraiture. The information dilution theorem. ESA Journal, 10(4):381–386, 1986.

[34] Stefan Frey, Camilla Colombo, and Stijn Lemmens. Extension of the king-hele orbit contraction method for accurate, semi-analytical propagation of non-circular orbits. Advances in Space Research, 64:1, 17, 2019.

[35] Alex M. Friedman and Carolin Frueh. Determining characteristics of artificial near-Earth objects using observability analysis. Acta Astronautica, 144:405–421, 2018.

[36] Jeroen L. Geeraert. Multi-Satellite Orbit Determination Using Interferometric Observables with RF Localization Applications. PhD thesis, University of Colorado Boulder, 2017.

[37] A. Gelb. Applied Optimal Estimation. The MIT Press, 1974.

[38] Bruce P. Gibbs. Advanced Kalman Filtering, Least-Squares and Modeling. John Wiley & Sons, 2011.

[39] D.J. Gondalech and R. Linares. Real-time thermospheric density estimation via two-line element data assimilation. Space Weather, 18(2), 2020.

[40] D.J. Gondalech and R. Linares. Real-Time Thermospheric Density Estimation via Radar and GPS Tracking Data Assimilation. Space Weather, 19(4), 2021.

[41] Frank O. Goodman and Harold Y. Wachman. Formula for Thermal Accommodation Coefficient. M.I.T. Fluid Dynamics Research Laboratory Report, Massachusetts Institute of Technology, February 1966.

[42] J.C. Gregory and P.N. Peters. A Measurement of the Angular Distribution of 5 eV Atomic Oxygen Scattered off a Solid Surface in Earth Orbit. Proceedings of the 15th International Symposium on Rarefied Gas Dynamics, 1:641–656, 1987.

[43] I.K. Harrison and J.J. Swinerd. A free molecule aerodynamic investigation using multiple satellite analysis. Planetary and space science, 44(2):171–180, 1996.

[44] M.D. Hejduk and D.E. Snow. The Effect of Neutral Density Estimation Errors on Satellite Conjunction Serious Event Rates. Space Weather, 16(7):849–869, 2018.

[45] Siamak G. Hesar. A Framework for Precise Orbit Determination of Small Body Orbiting Spacecraft. PhD thesis, University of Colorado Boulder, 2016.

[46] Siamak G. Hesar, Daniel J. Scheeres, and Jay W. McMahon. Precise Model for Small-Body Thermal Radiation Pressure Acting on Spacecraft. Journal of Guidance, Control, and Dynamics, 40(10):2432–2441, 2017.

[47] Siamak G. Hesar, Daniel J. Scheeres, and Jay W. McMahon. Precise Solar Radiation Pressure Models for Small-Body Orbiters: Applications to OSIRIS-REx Spacecraft. Journal of Guidance, Control, and Dynamics, 40(7):1638–1650, 2017.

[48] D.R. Imbro, Mildred M. Moe, and K. Moe. On fundamental problems in the deduction of satellite densities from satellite drag. Journal of Geophysical Research, 80(5):3077–3086, 1975.

[49] W.M. Kaula. Theory of satellite geodesy. 1966.

[50] G.M. Keating, R.H. Tolson, and M.S. Bradford. Evidence of long term global decline in the Earth's thermospheric densities apparently related to anthropogenic effects. Geophysical Research Letters, 27(10):1523–1526, 2000.

[51] Desmond King-Hele. Theory of satellite orbits in an atmosphere. Butterworths, 1964.

[52] Desmond King-Hele. Satellite orbits in an atmosphere: theory and applications. Blackie, 1987.

[53] G. Koppenwallner. Comment on Special Section: New Perspectives on the Satellite Drag Environments of Earth, Mars and Venus. Journal of Spacecraft and Rockets, 45(6):1324–1327, 2008.

[54] A.J. Krener and K. Ide. Measures of unobservability. In Proceedings of the 48th IEEE Conference on Decision and Control, 2009 Held Jointly with the 2009 28th Chinese Control Conference, pages 6401–6406.

[55] Jason M. Leonard, Felipe G. Nievinski, and George H. Born. Gravity Error Compensation Using Second-Order Gauss–Markov Processes. Journal of Spacecraft and Rockets, 50(1):217–229, 2013.

[56] R.J. Licata, P.M. Mehta, K.W. Tobiska, and S. Huzurbazar. Machine-Learned HASDM Model with Uncertainty Quantification. 16 Sep 2021.

[57] Jer-Chyi Liou and N.L. Johnson. Earth Satellite Population Instability: Underscoring the Need for Debris Mitigation. National Aeronautics and Space Administration, 2005.

[58] Sabrina Livadiotti, N.H. Crisp, P.C.E Roberts, S.D. Worrall, V.T.A Oiko, S. Edmondson, S.J. Haigh, C. Huyton, K.L. Smith, L.A. Sinpetru, B.E.A Holmes, R.M. Becedas, J. Domìnguez, V. Cañas, S. Christensen, A. Mølgaard, J. Nielsen, M. Bisgaard, Y.A. Chan, G.H. Herdrich, F. Romano, S. Fasoulas, C. Traub, D. Garcia, Almiñana, S. Rodriguez-Donaire, M. Sureda, D. Kataria, B. Belkouchi, A. Conte, J.S. Perez, R. Villain, and R. Outlaw. A review of gas-surface interaction models for orbital aerodynamic applications. Progress in Aerospace Sciences, 119, 2020.

[59] Biao Lu, Christoph Förste, Franz Barthelmes, Svetozar Petrovic, Frank Flechtner, Zhicai Luo, Bo Zhong, Hao Zhou, Xiaolong Wang, and Tangting Wu. Using real polar terrestrial gravimetry data to overcome the polar gap problem of GOCE - the gravity field model IGGT_R1C. GFZ Data Services, 2018.

[60] D.M. Lucchesi. Reassessment of the Error Modelling of Nongravitational Perturbations on LAGEOS II and Their Impact in the Lense-Thirring Determination. Part I. Planetary and Space Science, 49:447–463, 2001.

[61] Berit Floor Lund, Hans E. Berntsen, and Bjarne A. Foss. Methods for Parameter Ranking in Nonlinear, Mechanistic Models. In IFAC Proceedings Volumes, volume 28, pages 578–583, 2005.

[62] Berit Floor Lund and Bjarne A. Foss. Parameter ranking by orthogonalization—Applied to nonlinear mechanistic models. Automatica, 44:278–281, 2008.

[63] F. Lyard, F. Lefevre, T. Letellier, and O. Francis. Modelling the global ocean tides: modern insights from FES2004. Ocean Dynamics, 56(5-6):394–415, 2006.

[64] G. March, P.N. Doornbos, and P.N.A.M Visser. High-fidelity geometry models for improving the consistency of CHAMP, GRACE, GOCE and Swarm thermospheric density data sets. Advances in space research, 63:213–238, 2019.

[65] T. Matsuo, M. Fedrizzi, T.J. Fuller-Rowell, and M.V. Codrescu. Data assimilation of thermospheric mass density. Space Weather, 10(5):569–588, 2012.

[66] C.A. McLaughin, Steve Mance, and Travis Lechtenberg. Drag Coefficient Estimation in Orbit Determination. Journal of the Astronautical Sciences, 58(3):513–530, 2011.

[67] C. A. McLaughlin, A. Hiatt, and T. Lechtenberg. Precision Orbit Derived Total Density. Journal of Spacecraft and Rockets, 48(1):166–174, 2011.

[68] Jay W. McMahon and Daniel J. Scheeres. New Solar Radiation Pressure Force Model for Navigation. Journal of Guidance, Control, and Dynamics, 33(5):1418–1428, 2010.

[69] Jay W. McMahon and Daniel J. Scheeres. Improving Space Object Catalog Maintenance Through Advances in Solar Radiation Pressure Modelling. Journal of Guidance, Control, and Dynamics, 38(8):1366–1381, 2015.

[70] J.W. McMahon, D. Farnocchia, D. Scheeres, and Chesley S. Understanding Kaula's Rule for Small Bodies. In 47th Lunar and Planetary Science Conference, 2016.

[71] Piyush M. Mehta, Craig A. McLaughin, and Eric K. Sutton. Drag coefficient modeling for grace using Direct Simulation Monte Carlo. Advances in Space Research, 52(12):2035–2051, 2013.

[72] Piyush M. Mehta, Andrew Walker, Earl Lawrence, Richard Linares, David Higdon, and Josef Koller. Modeling satellite drag coefficients with response surfaces. Advances in Space Research, 54:1590–1607, 2014.

[73] Piyush M. Mehta, Andrew Walker, Eric K. Sutton, and Humberto C. Godinez. New density estimates derived using accelerometers on board the CHAMP and GRACE satellites. Space Weather, 15:558–576, 2017.

[74] P.M. Mehta and R. Linares. A methodology for reduced order modeling and calibration of the upper atmosphere. Space Weather, 15(10):1270–1287, 2017.

[75] P.M. Mehta and R. Linares. A new transformative framework for data assimilation and calibration of physical ionosphere-thermosphere models. Space Weather, 16(8):1086–1100, 2018.

[76] P.M. Mehta, R. Linares, and E.K. Sutton. A quasi-physical dynamic reduced order model for thermospheric mass density via Hermitian space-dynamic mode decomposition. Space Weather, 16(5):569–588, 2018.

[77] Kenneth Moe and Mildred M. Moe. Gas Surface Interactions and Satellite Drag Coefficients. Planetary and Space Science, 53(8):793–801, 2005.

[78] Kenneth Moe, Mildred M. Moe, and Carl J. Rice. Simultaneous Analysis of Multi-Instrument Satellite Measurements of Atmospheric Density. Journal of Spacecraft and Rockets, 41(5):849–853, 2004.

[79] Kenneth Moe, Mildred M. Moe, and Stephen D. Wallace. Drag Coefficients of Spheres in Free Molecular Flow. Advances in the Astronautical Sciences, 93(1):391–406, 1996.

[80] Mildred M. Moe and Louis C. Tsang. Drag coefficients for Cones and Cylinders According to Schamberg's Model. AIAA Journal, 11(3):396–399, 1973.

[81] Mildred M. Moe, Steven D. Wallace, and Kenneth Moe. Recommended Drag Coefficients for Aeronomic Satellites. The Upper Mesosphere and Lower Thermosphere: A Review of Experiment and Theory, 87:349–356, 1995.

[82] Olliver Montenbruck and Eberhard Gill. Satellite Orbits: Models, Methods and Applications. Springer, 2000.

[83] NASA. Orbital Debris Quarterly News, 25(1), 2021.

[84] National Research Council. Continuing Kepler's Quest: Assessing Air Force Space Command's Astrodynamics Standards. The National Academies Press, Washington D.C., 2012.

[85] F. Nievinski, Brandon Yonko, and G. Born. Improved orbit determination using second-order gauss-markov process. Advances in the Astronautical Sciences, 140, 2011.

[86] S. Nocilla. The surface re-emission law in free molecular flow. In 3rd Symposium Rarefied Gas Dynamics, 1962.

[87] Mette S. Olufsen and Johnny T. Ottesen. A practical approach to parameter estimation applied to model predicting heart rate regulation. Journal of Mathematical Biology, 67(1):39–68, 2008.

[88] C. Pardini, L. Anselmo, K. Moe, and M.M. Moe. Drag and Energy Accommodation Coefficient During Sunspot Maximum. Advances in Space Research, 45(45):638–650, 2010.

[89] Nikolaos K. Pavlis, Simon A. Holmes, Steve C. Kenyon, and John K. Factor. The development and evaluation of the Earth Gravitational Model 2008 (EGM2008). Journal of Geophysical Research, 2012.

[90] David Perez and Ricardo Bevilacqua. Neural Network based calibration of atmospheric density models. Acta Astronautica, 110:58–76, 2015.

[91] Gérard Petit and Brian Luzum. IERS Conventions. IERS Technical Note No. 36, 2010.

[92] J.M. Picone, J.T. Emmert, and J.L. Lean. Thermospheric densities derived from spacecraft orbits: Accurate processing of two-line element sets. Journal of Geophysical Research, 110, 2005.

[93] J.M. Picone, A.E. Hedin, D.P. Drob, and A.C. Aikin. NRLMSISE-00 Empirical Model of the Atmosphere: Statistical Comparisons and Scientific Issues. Journal of Geophysical Research, 107(A12):2035–2051, 2002.

[94] M. D. Pilinski, B. M. Argrow, and S. E. Palo. Semi-empirical Model for Satellite Energy-Accommodation Coefficients. Journal of Spacecraft and Rockets, 47(6):951–957, 2010.

[95] Marcin D. Pilinski, Brian M. Argrow, and Scott E. Palo. Semi-Empirical Model for Satellite Energy-Accommodation Coefficients. Journal of Spacecraft and Rockets, 47(6):951–956, 2010.

[96] Marcin D. Pilinski, Brian M. Argrow, Scott E. Palo, and Bruce R. Bowman. Semi-Empirical Satellite Accommodation Model for Spherical and Randomly Tumbling Objects. Journal of Spacecraft and Rockets, 50(3):556–571, 2013.

[97] H. Poincaré. Les Méthodes Nouvelles de la Mécanique Céleste, volume 1. Dover Reprint, 1960.

[98] A.D. Poularikas. The Handbook of Formulas and Tables for Signal Processing. CRC Press LLC, Boca Raton, 1999.

[99] David Mostaza Prieto, Benjamin P. Graziano, and Peter C.E. Roberts. Spacecraft Drag Modelling. Progress in Aerospace Sciences, 64:56–65, 2014.

[100] Vishal Ray and Daniel J. Scheeres. A drag coefficient model to track variations due to attitude and orbital motion. Journal of Guidance, Control and Dynamics, 43(10):1915–1926, 2020.

[101] Vishal Ray and Daniel J. Scheeres. Gravitational Force-Model Aliasing with Non-Gravitational Force Coefficients in Dynamic Prediction. Journal of Guidance, Control and Dynamics, 43(10):1984–1997, 2020.

[102] Vishal Ray and Daniel J. Scheeres. King-Hele orbit theory for periodic orbit and attitude variations. Monthly Notices of the Royal Astronomical Society, 501:1168–1187, 2020.

[103] Vishal Ray, Daniel J. Scheeres, Siamak G. Hesar, and Matthew Duncan. A drag coefficient modeling approach using spatial and temporal Fourier expansions for orbit determination. Journal of the Astronautical Sciences, 67(3):1139–1168, 2020.

[104] Vishal Ray, Daniel J. Scheeres, and Marcin Pilinski. Inverting gas-surface interaction parameters from Fourier drag-coefficient estimates for a given atmospheric model. Advances in Space Research, 68(4):1902–1927, 2021.

[105] Justin E. Register. Contribution of individual forces to orbit determination accuracy. Advances in the Astronautical Sciences, 114:1819–1838, 2003.

[106] Orbital Debris Research, Development Interagency Working Group of the National Science, and Technology Council. National Orbital Debris Research and Development Plan. Technical report, 2021.

[107] J. Ries, S. Bettadpur, R. Eanes, Z. Kang, U. Ko, C. McCullough, P. Nagel, N. Pie, S. Poole, T. Richter, H. Save, , and B. Tapley. Development and Evaluation of the Global Gravity Model GGM05, CSR-16-02. Technical report, Center for Space Research, University of Texas at Austin, 2016.

[108] J. Ries, S. Bettadpur, R. Eanes, Z. Kang, U. Ko, C. McCullough, P. Nagel, N. Pie, S. Poole, T. Richter, H. Save, , and B. Tapley. The Combined Gravity Model GGM05C. GFZ Data Services, 2016.

[109] Christopher W. T. Roscoe, Jacob D. Griesbach, Jason J. Westphal, Dean R. Hawes, and John P.. Carrico Jr. Force Modeling and State Propagation for Navigation and Maneuver Planning for CubeSat Rendezvous, Proximity Operations, and Docking. In Advanced Maui Optical and Space Surveillance Technologies (AMOS) Conference, Wailea, Maui, Hawaii, 2013.

[110] Howard Saltsburg, Joe N. Smith, and Milton Rogers. Fundamentals of Gas Surface Interactions. Academic press, New York, U.S.A, 1967.

[111] R. Schamberg. A New Analytic Representation of Surface Interaction for Hyperthermal Free Molecular Flow. Academic press, Santa Monica, California, 1959.

[112] D.J. Scheeres, S.G. Hesar, S. Tardivel, M. Hirabayashi, D. Farnocchia, J.W. McMahon, S.R. Chesley, O. Barnouin, R.P. Binzel, W.F. Bottke, M.G. Daly, J.P. Emery, C.W. Hergenrother, D.S. Lauretta, J.R. Marshall, P. Michel, M.C. Nolan, and K.J. Walsh. The geophysical environment of Bennu. Icarus, 276:116–140, 2016.

[113] L.H. Sentman. Free Molecule Flow Theory and Its Application to the Determination of Aerodynamic Force. Lmsc-448514, ad 265-409, Lockheed Missiles and Space company, 1961.

[114] R.K. Sharma. Analytic approach using ks elements to near-earth orbit predictions including air drag. Proc. R. Soc. Lond., A 433:121, 130, 1991.

[115] Ken Shoemake. Animating rotations with quaternion curves. In SIGGRAPH '85: Proceedings of the 12th annual conference on Computer graphics and interactive techniques, pages 245–254, 1985.

[116] Nathan Stacey and Simone D'Amico. Adaptive and dynamically constrained process noise estimation for orbit determination. IEEE Transactions on Aerospace and Electronic Systems, 57(5):2920–2937, 2021.

[117] M.F. Storz, B.R. Bowman, M.J.I Branson, S.J. Casali, and W.K. Tobiska. High Accuracy Satellite Drag Model (HASDM). Advances in Space Research, 36:2497–2505, 2005.

[118] J. Sanz Subirana, J.M. Juan Zornoza, and M. Hernandez-Pajares. Transformations between time systems. `https://gssc.esa.int/navipedia/index.php/Transformations_between_Time_Systems`, 2011. [Online].

[119] Furong Sun, Robert B. Gramacy, Benjamin Haaland, Earl Lawrence, and Andrew Walker. Emulating satellite drag from large simulation experiments. SIAM/ASA Journal on Uncertainty Quantification, 7(2), 2019.

[120] E.K. Sutton. A new method of physics-based data assimilation for the quiet and disturbed thermosphere. Space Weather, 10(5):736–753, 2018.

[121] E.K. Sutton, Jeffrey P. Thayer, Marcin D. Pilinski, Shaylah P. Mutschler, Thomas E. Berger, Vu Nguyen, and Dallas Masters. Toward Accurate Physics-Based Specifications of Neutral Density Using GNSS-Enabled Small Satellites. Space Weather, 19(6), 2021.

[122] Eric K. Sutton. Normalized Force Coefficients of Satellites with Elongated Shapes. Journal of Spacecraft and Rockets, 46(1):112–116, 2009.

[123] B.D. Tapley, J. Ries, S. Bettadpur, D. Chambers, M. Cheng, F. Condi, and S. Poole. The GGM03 Mean Earth Gravity Model from GRACE. In EOS Transactions AGU, volume 88(52). Fall Meet. Suppl., Abstract G42A-03, 2007.

[124] Byron D. Tapley, Bob E. Schutz, and George H. Born. Statistical Orbit Determination, chapter 6. Elsevier Academic Press, 2004.

[125] Jeffrey P. Thayer, Kent W. Tobiska, marcin D. Pilinski, and Sutton Eric K. Remaining issues in upper atmosphere satellite drag. Space Weather Effects and Applications, pages 111–140, 2021.

[126] K.W. Tobiska, B.R. Bowman, D. Bouwer, A. Cruz, K. Wahl, M. Pilinski, P.M. Mehta, and R.J. Licata. The SET HASDM density database. Space Weather, 2021.

[127] D.A. Vallado. An analysis of state vector propagation using different flight dynamics programs. Advances in the Astronautical Sciences, 121, 2005. Proceedings of the 15th AAS/AIAA Space Flight Mechanics Meeting, Copper Mountain, CO, January 23–27 2005.

[128] David Vallado. Fundamentals of Astrodynamics and Applications, chapter 3. Microcosm Press and Springer, 3 edition, 2007.

[129] David A. Vallado and David Finkleman. A Critical Assessment of Satellite Drag and Atmospheric Density Modelling. Acta Astronautica, 95:141–165, 2014.

[130] N.X. Vinh, J.M. Longuski, A. Busemann, and R.D. Culp. Analytic theory of orbit contraction due to atmospheric drag. Acta Astronautica, 6(5-6):697, 723, 1979.

[131] Andrew Walker, Piyush Mehta, and Joseph Koller. Drag Coefficient Model Using the Cercignani–Lampis–Lord Gas–Surface Interaction Model. Journal of Spacecraft and Rockets, 51(5):1544–1563, 2014.

[132] Andrew Walker, Piyush M. Mehta, and Josef Koller. The Effect of Different Adsorption Models on Satellite Drag Coefficients. Advances in the Astronautical Sciences , 150(AAS 13-746), August 2013.

[133] Y.M. Wang, J.L. Lean, and N.R. Sheeley Jr. Modeling the Sun's magnetic field and irradiance since 1713. The astrophysical journal, 625(1):522–538, 2005.

[134] H.G. Wengel. Tide-generating potential for the earth. In Wilhelm, H. and Zürn, W. and Wenzel, H.G., editor, Tidal Phenomena, volume 66. Springer, Berlin, 1997.

[135] James R. Wright and James Woodburn. Simultaneous Real-Time Estimation of Atmospheric Density and Ballistic Coefficient. Technical report, Analytical Graphics, Inc., 2004.

[136] Philipp Zingerle, Jan Martin Brockmann, Roland Pail, Thomas Gruber, and Martin Willberg. The polar extended gravity field model TIM_R6e. GFZ Data Services, 2019.

[137] Philipp Zingerle, Roland Pail, Thomas Gruber, and Xanthi Oikonomidou. The experimental gravity field model XGM2019e. GFZ Data Services, 2019.

Appendix A

Integrals required for analytical BFF model

The following integrals are needed to compute the analytical BFF coefficients in chapter 6.

$$\begin{aligned}\int_0^{2\pi} e^{-\gamma^2 s^2}\cos n\psi d\psi &= \int_0^{2\pi} e^{-s^2\mathcal{C}^2\cos^2\psi}\cos n\psi d\psi \\ &= e^{-\frac{s^2\mathcal{C}^2}{2}}\int_0^{2\pi} e^{-\frac{s^2\mathcal{C}^2}{2}\cos 2\psi}\cos n\psi d\psi \\ &= \frac{e^{-\frac{s^2\mathcal{C}^2}{2}}}{2}\int_0^{4\pi} e^{-\frac{s^2\mathcal{C}^2}{2}\cos x}\cos\frac{nx}{2}dx.\end{aligned} \tag{A.1}$$

The integral is then given by

$$\int_0^{2\pi} e^{-\gamma^2 s^2}\cos n\psi d\psi = \begin{cases} 2\pi e^{-\frac{s^2\mathcal{C}^2}{2}} I_k(-\frac{s^2\mathcal{C}^2}{2}), & n=2k, k\in\mathbb{Z}^{\geq} \\ 0, & n=2k+1, k\in\mathbb{Z}^{\geq}, \end{cases} \tag{A.2}$$

where I_k is the modified Bessel integral of the first kind. Based on the above result and using $\cos A\cos B = \frac{1}{2}(\cos(A+B)+\cos(A-B))$, the following integral is computed,

$$\begin{aligned}&\int_0^{2\pi}\gamma e^{-\gamma^2 s^2}\cos n\psi d\psi = \\ &\begin{cases} \pi\mathcal{C}e^{-\frac{s^2\mathcal{C}^2}{2}}[I_{k+1}(-\frac{s^2\mathcal{C}^2}{2})+I_k(-\frac{s^2\mathcal{C}^2}{2})], & n=2k+1, k\in\mathbb{Z}^{\geq} \\ 0, & n=2k, k\in\mathbb{Z}^{\geq}. \end{cases}\end{aligned} \tag{A.3}$$

The next integral is computed as follows,

$$\begin{aligned}
&\int_0^{2\pi} \operatorname{erf}(s\gamma)\cos n\psi d\psi = \int_0^{2\pi} \operatorname{erf}(s\mathcal{C}\cos\psi)\cos n\psi d\psi \\
&= [\operatorname{erf}(s\mathcal{C}\cos\psi)\int \cos n\psi d\psi]|_0^{2\pi} - \int_0^{2\pi} [\frac{d}{d\psi}\operatorname{erf}(s\mathcal{C}\cos\psi)\int \cos n\psi d\psi]d\psi \\
&= [\operatorname{erf}(s\mathcal{C}\cos\psi)\frac{\sin n\psi}{n}d\psi]|_0^{2\pi} + \int_0^{2\pi} [\frac{2}{\sqrt{\pi}}e^{-s^2\mathcal{C}^2\cos^2\psi}s\mathcal{C}\sin\psi\frac{\sin n\psi}{n}]d\psi \\
&= \frac{s\mathcal{C}}{n\sqrt{\pi}}\int_0^{2\pi}[e^{-s^2\mathcal{C}^2\cos^2\psi}(\cos(n-1)\psi - \cos(n+1)\psi)]d\psi,
\end{aligned} \tag{A.4}$$

for $n > 0$. For $n = 0$, $\int_0^{2\pi} \operatorname{erf}(s\cos\psi)d\psi = 0$. The final form of the integral can be evaluated by using Eq. A.2,

$$\begin{aligned}
&\int_0^{2\pi} \operatorname{erf}(\gamma s)\cos n\psi d\psi = \\
&\begin{cases}
\frac{2\sqrt{\pi}}{2k+1}s\mathcal{C}e^{-\frac{s^2\mathcal{C}^2}{2}}\left[I_k(-\frac{s^2\mathcal{C}^2}{2}) - I_{k+1}(-\frac{s^2\mathcal{C}^2}{2})\right], & n = 2k+1, k \in \mathbb{Z}^{\geq} \\
0, & n = 2k, k \in \mathbb{Z}^{\geq},
\end{cases}
\end{aligned} \tag{A.5}$$

Using Eq. A.5, the following integrals can be computed.

$$\begin{aligned}
&\int_0^{2\pi} \gamma(1+\operatorname{erf}(s\gamma))\cos n\psi d\psi = \\
&\int_0^{2\pi} \frac{\mathcal{C}}{2}[1+\operatorname{erf}(s\mathcal{C}\cos\psi)][\cos(n+1)\psi + \cos(n-1)\psi]d\psi,
\end{aligned} \tag{A.6}$$

$$\begin{aligned}
&\int_0^{2\pi} \gamma(1+\operatorname{erf}(s\gamma))\cos n\psi d\psi = \\
&\begin{cases}
\mathcal{C}\pi, & n = 1 \\
\sqrt{\pi}\mathcal{C}^2 s e^{-\frac{s^2\mathcal{C}^2}{2}}\left[\frac{I_k(-\frac{s^2\mathcal{C}^2}{2}) - I_{k+1}(-\frac{s^2\mathcal{C}^2}{2})}{2k+1}\right. & \\
\left. + \frac{I_{k-1}(-\frac{s^2\mathcal{C}^2}{2}) - I_k(-\frac{s^2\mathcal{C}^2}{2})}{2k-1}\right], & n = 2k, k \in \mathbb{Z}^{\geq} \\
0, & n = 2k+1, k \in \mathbb{Z}^{+},
\end{cases}
\end{aligned} \tag{A.7}$$

and,

$$\int_0^{2\pi} \gamma^2(1+\mathrm{erf}(s\gamma))\cos n\psi d\psi = \int_0^{2\pi} \mathcal{C}^2[1+\mathrm{erf}(s\mathcal{C}\cos\psi)]\left[\frac{1}{2}\cos n\psi + \frac{\cos(n+2)\psi+\cos(n-2)\psi}{4}\right]d\psi, \tag{A.8}$$

$$\int_0^{2\pi} \gamma^2(1+\mathrm{erf}(s\gamma))\cos n\psi d\psi = \begin{cases} \mathcal{C}^2\pi, & n=0 \\ \dfrac{\mathcal{C}^2\pi}{2}, & n=2 \\ 0, & n=2k, k\in\mathbb{Z}^+-\{1\} \\ \sqrt{\pi}\mathcal{C}^3 s e^{-\frac{s^2\mathcal{C}^2}{2}}\left[\dfrac{I_k(-\frac{s^2\mathcal{C}^2}{2})-I_{k+1}(-\frac{s^2\mathcal{C}^2}{2})}{2k+1}\right. & \\ \left.+\dfrac{I_{k+1}(-\frac{s^2\mathcal{C}^2}{2})-I_{k+2}(-\frac{s^2\mathcal{C}^2}{2})}{2(2k+3)}\right. & \\ \left.+\dfrac{I_{k-1}(-\frac{s^2\mathcal{C}^2}{2})-I_k(-\frac{s^2\mathcal{C}^2}{2})}{2(2k-1)}\right], & n=2k+1, k\in\mathbb{Z}^{\geq} \end{cases} \tag{A.9}$$

Appendix B

Comparison of geopotential models for orbit determination

This chapter demonstrates that the differences between the different state-of-the-art geopotential models are negligible for the purposes of the aliasing analysis in chapter 4 by analyzing orbit determination and prediction results for GRACE-B satellite. The same data used in Section 5.4 is processed here. Nine geopotential models are chosen arbitrarily from the most recent models in International Centre for Global Earth Models (ICGEM) database[1] for comparison purposes - XGM2019e [137], TIM_R6e [136], IGGT_R1C [59], Tongji-Grace02k [13], GGM05C [108], GGM05G [107], GGM05S [107], EGM2008 [89] and GGM03S [123]. The initial state from the precision orbit data is propagated using the gravitational models truncated at order 180 along with the other forces in Section 5.4. The norm of the position errors between the propagated states and the precision orbit data at the end of four days are plotted in Fig. B.1 (a) for all the gravitational models. Orbit determination is carried out using all the gravitational models, similar to Section 5.4, and the estimated states are predicted for the next three days after the one-day data-arc. The prediction errors are plotted in Fig. B.1 (b). It can be seen that both the propagation and prediction errors are within a few meters of each other for all gravitational field models except propagation errors for IGGT_R1C. Therefore, the results of this work are not significantly affected by the choice of the geopotential model and the qualitative trends hold for most other state-of-the-art models.

[1] `http://icgem.gfz-potsdam.de/tom_longtime`

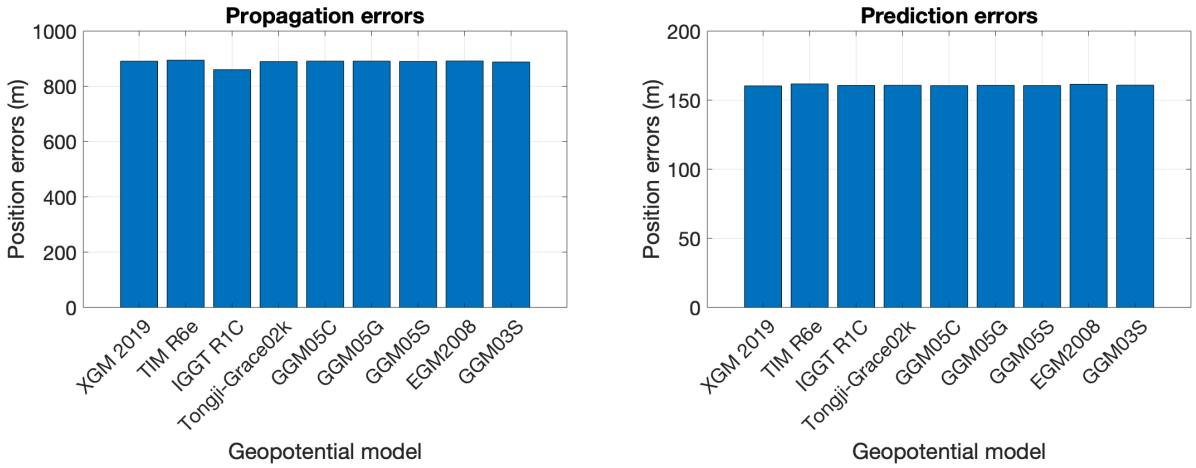

(a) (b)

Figure B.1: (a) Error between propagated states and precision orbit data; (b) Error between predicted states (propagated estimated states) and precision orbit data

Appendix C

Parameter values for computation of tidal perturbations

C.1 Fundamental arguments of nutation theory

The fundamental arguments of nutation theory required to compute the Doodson arguments in section 3.4.4.1 can be calculated as follows

$$l = (134.96340251 + (1717915923.2178T + 31.879200T^2 + 0.051635T^3 - 0.0002447T^4)/3600)\pi/180$$

$$lp = (357.52910918 + (129596581.0481T - 0.553200T^2 + 0.000136T^3 - 0.00001149T^4)/3600)\pi/180$$

$$F = (93.27209062 + (1739527262.847800T - 12.7512T^2 - 0.001037T^3 + 0.00000417T^4)/3600)\pi/180$$

$$D = (297.85019547 + (1602961601.209T - 6.3706T^2 + 0.00659300T^3 - 0.00003169T^4)/3600)\pi/180$$

$$Om = (125.04455501 - (6962890.543100T + 7.472200T^2 + 0.007702T^3 - 0.00005939T^4)/3600)\pi/180$$

C.2 Nominal Love numbers

Nominal Love numbers to be used in eq. (3.32) are given in

Table C.1: Nominal Love numbers

n	m	Re k_{nm}	Im k_{nm}	k^+_{nm}
2	0	0.30190	0.0	-0.00089
2	1	0.29830	-0.00144	-0.00080
2	2	0.30102	-0.00130	-0.00057
3	0	0.093	-	-
3	1	0.093	-	-
3	2	0.093	-	-
3	3	0.094	-	-

Table C.2: In-phase and out-of-phase amplitudes for corrections to k_{21} to be used in eq. (3.34). The units of the amplitudes are 10^{-12}

Doodson number	A_{ip}	A_{op}
55,565	16.6	-6.7
55,575	-0.1	0.1
56,554	-1.2	0.8
57,555	-5.5	4.3
57,565	0.1	-0.1
58,554	-0.3	0.2
63,655	-0.3	0.7
65,445	0.1	-0.2
65,455	-1.2	3.7
65,465	0.1	-0.2
65,655	0.1	-0.2
73,555	0.0	0.6
75,355	0.0	0.3
75,555	0.6	6.3
75,565	0.2	2.6
75,575	0.0	0.2
83,655	0.1	0.2
85,455	0.4	1.1
85,465	0.2	0.5
93,555	0.1	0.2
95,355	0.1	0.1

Table C.3: In-phase amplitudes for corrections to k_{21} to be used in eq. (3.35) with $m = 2$. The units of the amplitudes are 10^{-12}. The out-of-phase amplitudes are zero.

Doodson number	A_{ip}
245,655	-0.3
255,555	-1.2

Table C.4: In-phase and out-of-phase amplitudes for corrections to k_{21} to be used in eq. (3.35) with $m = 1$. The units of the amplitudes are 10^{-12}

Doodson number	A_{ip}	A_{op}
125,755	-0.1	0.0
127,555	-0.1	0.0
135,645	-0.1	0.0
135,655	-0.7	0.1
137,455	-0.1	0.0
145,545	-1.3	0.1
145,555	-6.8	0.6
147,555	0.1	0.0
153,655	0.1	0.0
155,445	0.1	0.0
155,455	0.4	0.0
155,655	1.3	-0.1
155,665	0.3	0.0
157,455	0.3	0.0
157,465	0.1	0.0
162,556	-1.9	0.1
163,545	0.5	0.0
163,555	-43.4	2.9
164,554	0.6	0.0
164,556	1.6	-0.1
165,345	0.1	0.0
165,535	0.1	0.0
165,545	-8.8	0.5
165,555	470.9	-30.2
165,565	68.1	-4.6
165,575	-1.6	0.1
166,455	0.1	0.0
166,544	-0.1	0.0
166,554	-20.6	-0.3
166,556	0.3	0.0
166,564	-0.3	0.0
167,355	-0.2	0.0
167,365	-0.1	0.0
167,555	-5.0	0.3
167,565	0.2	0.0
168,554	-0.2	0.0
173,655	-0.5	0.0
173,665	-0.1	0.0
175,445	0.1	0.0
175,455	-2.1	0.1
175,465	-0.4	0.0
183,555	-0.2	0.0
185,355	-0.1	0.0
185,555	-0.6	0.0
185,565	-0.4	0.0
185,575	-0.1	0.0
195,455	-0.1	0.0
195,465	-0.1	0.0